LBL-23804

Lawrence Berkeley Laboratory
UNIVERSITY OF CALIFORNIA

Materials & Chemical Sciences Division

The Effect of Additives on the Reactivity of Palladium Surfaces for the Chemisorption and Hydrogenation of Carbon Monoxide: A Surface Science and Catalytic Study

T.G. Rucker
(Ph.D. Thesis)

June 1987

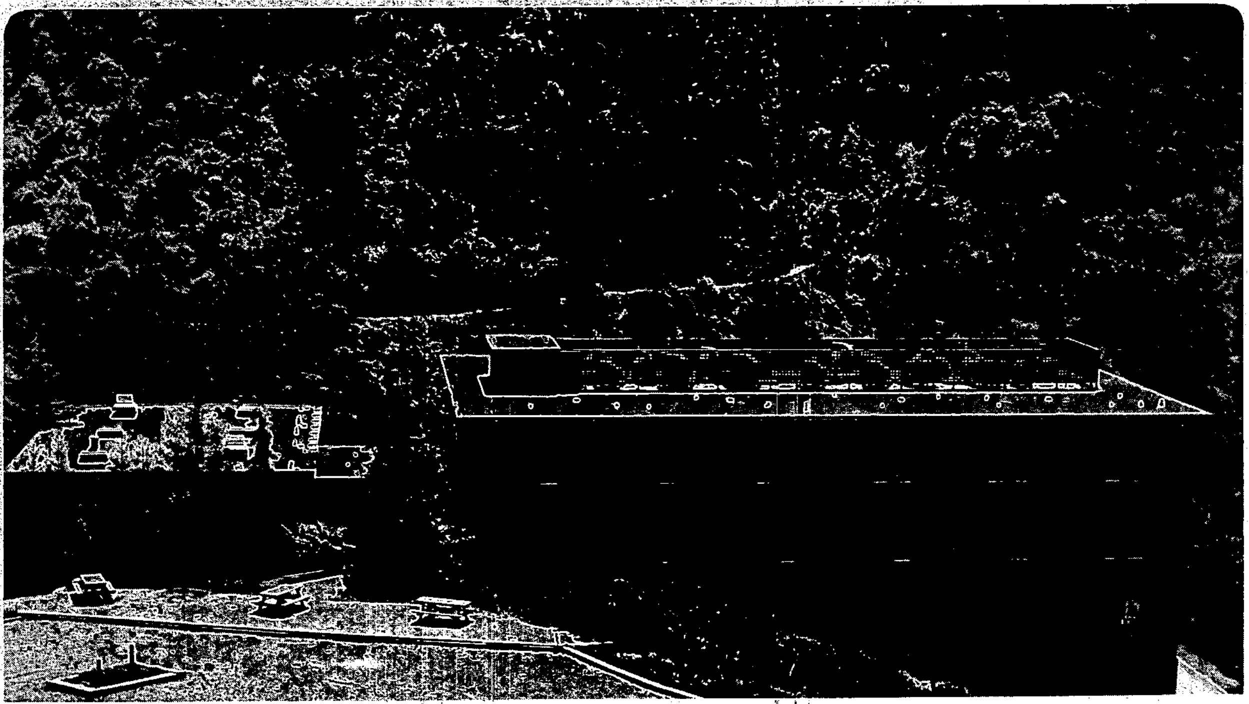

Prepared for the U.S. Department of Energy under Contract DE-AC03-76SF00098

LBL-23804

The Effect of Additives on the Reactivity of Palladium Surfaces for the Chemisorption and Hydrogenation of Carbon Monoxide: A Surface Science and Catalytic Study.

Thomas George Rucker

LBL--23804

Ph.D. Thesis

DE87 014685

Lawrence Berkeley Laboratory
University of California
Berkeley, California 94720

June 1987

This work was supported by the U.S. Department of Energy under Contract Number DE-AC03-76SF00098.

MASTER

DISTRIBUTION OF THIS DOCUMENT IS UNLIMITED

The Effect of Additives on the Reactivity of Palladium Surfaces for the Chemisorption and Hydrogenation of Carbon Monoxide: A Surface Science and Catalytic Study.

Thomas George Rucker

Abstract

This thesis research has studied the role of surface additives on the catalytic activity and chemisorptive properties of palladium single crystals and foils. The effect of sodium, potassium, silicon, phosphorus, sulfur and chlorine on the bonding of carbon monoxide and hydrogen and on the cyclotrimerization of acetylene on the (111), (100) and (110) faces of palladium has been investigated in addition to the role of TiO_2 and SiO_2 overlayers deposited on palladium foils in the CO hydrogenation reaction.

The surface characterization and catalytic reactions were performed in a combined ultra-high vacuum/ high pressure chamber equipped with the standard surface analytical techniques. The chamber included a new high pressure isolation cell mounted inside the chamber capable of attaining pressures of 1800 psi.

On palladium, only in the presence of oxide overlayers (TiO_x, SiO_x), are methane or methanol formed from CO and H_2. The maximum rate of methane formation is attained on palladium foil where 30% of the surface is covered with titania. Methanol formation can be achieved only if the TiO_x/Pd surface is pretreated in 50 psi of oxygen at 550°C prior to the reaction. Temperature Programmed Desorption and X-ray Photoelectron Spectroscopy results and kinetic studies suggest that methane forms on a stable mixed TiO_x/Pd catalytic site whereas methanol, which is produced only during the first few minutes of the reaction, forms on an unstable heavily oxidized TiO_x/Pd surface.

The additives (Na, K, Si, P, S, & Cl) affect the bonding of CO and hydrogen

and the cyclotrimerization of acetylene to benzene by structural and electronic interactions. The structural interaction induced by the additives are evidenced by surface reconstruction, changes in palladium ensemble size, site blocking and changes in the CO bonding configuration on palladium. The electronic interaction involves the donation or withdrawal of electron density from the additives based on their electronegativites relative to palladium. In general, the electron donating additives increase the desorption temperature of CO and increase the rate of acetylene cyclotrimerization and the electron withdrawing additives decrease the desorption temperature of CO and decrease the rate of benzene formation from acetylene.

Contents

List of Figures

List of Tables

ACKNOWLEDGEMENTS

There are many people I wish to thank who have made my four years at Berkeley scientifically challenging and personally fulfilling. My research advisor, Gabor A. Somorjai, has allowed me the freedom to pursue projects independently, while still always being there to suggest the right experiments and directions. It is from him that I have learned how to approach research projects: to look at the 'big picture' and concentrate on understanding the chemistry and science. He has always been ready and willing to help.

Many thanks also to my co-workers, Tom Gentle and Mark Logan who taught me the basics of surface science and Sabrina Fu who will continue the tradition of CO + H_2 chemistry. The Somorjai group members, past and present, especially José Carrazza, Dan Strongin, Dave Godbey and Simon Bare have been extremely helpful in scientific problems and more importantly have become lifelong friends.

Were it not for the expertise of our group technicians, Dan Colomb and Keith Franck, who were always ready to quickly fix all those broken pieces and build new parts for the chamber, this project would have taken many more years and the chamber would not be a pretty site.

The help of Dan Strongin and Steven Rucker in proofreading this thesis is gratefully acknowledged. Special thanks also to Craig Shaefer for a copy of RPLOT and always being willing to answer my countless questions and help in getting the program running on the computer.

My family (Steven, Janet, Donald, Craig and Mimi) and my fiancée Libby have been a constant source of love and help that is greatly appreciated.

My deepest thanks go to my parents. Were it not for their constant love, support and encouragement this thesis and the culmination of my education which it represents would never have been realized. It is to them that I dedicate this thesis.

This work was supported by the Office of Basic Energy Sciences, U.S. Department of Energy, under Contract No. DE-AC03-76SF00098.

für meine Eltern,
Daisy and Klaus

Chapter 1

INTRODUCTION

In the early decades of catalysis research, little was known about the interaction of multicomponent catalysts, and hence, many industrial catalysts were developed with an *ad hoc* approach. Advances in physical chemistry, solid-state physics, instrumental analysis and computer applications spurred by the growth of the electronics and aerospace industries led to the development of numerous techniques with which we can probe the small concentrations of molecules and atoms on catalyst surfaces ($\sim 10^{15}$ molecules/cm^2 compared to a solid block of $\sim 10^{22}$ molecules/cm^3, $10,000,000$ times less).

In a heterogeneous catalytic reaction, the following sequence of steps are typically involved.

1. Adsorption of reactant molecules on the catalyst.
2. Surface Diffusion.
3. Formation of intermediates and products.
4. Product desorption.

All of these steps depend strongly on the structural and electronic nature of the catalyst surface. Historically, catalysts have been doped with additives, dispersed on various 'inert' supports and subjected to pretreatment conditions to increase activity, selectivity and stability. How and why these steps alter the basic catalytic steps has only in the past few years started to be understood.

This research uses a wide variety of surface sensitive techniques to study catalytic systems and the interaction between the metals, supports and additives. In particular, the influence of oxide overlayers (TiO_x, SiO_x) deposited on palladium on the CO hydrogenation reaction and the influence of surface additives (sodium, potassium, silicon, phosphorus, sulfur, chlorine) on the chemisorption (CO, H_2) and catalytic ($C_2H_2 \rightarrow C_6H_6$) behavior of palladium single crystals are investigated. By understanding how adsorbates modify chemical (binding, composition, oxidation state) and structural features of catalysts, and which steps in the catalytic reaction sequence they perturb, one would be able to selectively deposit adlayers on a surface and accurately control not only the catalytic behavior, but also the electronic and mechanical properties.

Practical catalysts consist of millions of small particles dispersed on high surface area (100 m^2/gram) supports (usually oxides)[1]. Many techniques have been developed to study these systems including (Fourier Transform) Infrared Absorption, Mossbauer and Extended X-ray Absorption Fine Structure, and these have all yielded much information [1]. An inherent difficulty in studying the structure, composition and oxidation states of dispersed catalysts is their anisotropy. With a large number of binding sites it is difficult to determine which sites are catalytically active. This complexity has led scientists to model the working catalyst with simpler systems to answer these fundamental questions.

In this research, the model system is a 1 cm^2 palladium single crystal or foil which has been doped with a surface additive. Through a systematic comparison of the effects of each additive on the activity of clean palladium, the catalyst can be characterized.

1.1 The Catalytic Hydrogenation of Carbon Monoxide

Since the first report of the catalytic hydrogenation of carbon monoxide to methane over a nickel catalyst in 1902 by Sabatier and Senderens, this reaction has been extensively studied[2]. In 1913 a patent was issued to Badische Analin und Soda Fabrik (BASF) for a process to form hydrocarbons and oxygenates from CO and H_2 using alkali doped oxides of cobalt and osmium (Pressures $>$ 100 atm, T= 350°C)[3]. Ten years later, another patent was issued to BASF for methanol formation using a zinc oxide and chromium oxide catalyst. In 1926, Fischer and Tropsch formed higher hydrocarbons at atmospheric pressures and lower temperatures over a catalyst of iron and cobalt containing potassium carbonate and copper as promoters[4,5,6,7]. Germany during World War II produced 100,000 barrels of synthetic fuels per day using a modified version of this catalyst (cobalt, thoria, magnesium oxide and kieselguhr (diatomaceous earth), 1 - 10 atm)[8,9,10,11,12,13]. After the war, research continued, but was virtually halted a few years later in the presence of inexpensive foreign oil. Presently, only in South Africa (SASOL) is the syn gas reaction commercially active. In the early seventies, with the increasing cost of crude oil, the applications and feasibility were again discussed and research was restarted in developing selective and active catalysts.

1.1.1 Thermodynamics

Hydrocarbons are thermodynamically favored over CO and H_2 at lower temperatures. Figure 1.1 shows the standard free energies of formation of hydrocarbons and alcohols from CO and H_2 with water as a by-product. The reactions of primary interest in this research are:

$$\begin{aligned} CO + 3H_2 &\rightleftharpoons CH_4 + H_2O \\ CO + 2H_2 &\rightleftharpoons CH_3OH \end{aligned}$$

Since at low temperatures the reactions become kinetically limited, reaction rates are maximized in the temperature range between 500 -700K for methane and 400 - 550K for methanol. By Le Chatelier's principle, higher pressures enhance product formation in associative reactions. Figure 1.2 show the pressure dependence for methanol synthesis. To increase the yield of methanol and methane pressures of 20 atm or higher are desirable.

1.1.2 Metal - Oxide Systems

Numerous catalysts for methane and methanol formation exist. Nickel is an excellent methanation catalyst [14] and zinc chromate - copper chromate an excellent catalyst for methanol synthesis. Palladium has been reported to form methane [15] or methanol [16] selectively or to be inactive [17]. The major difference in these reports is the support on which the palladium is impregnated. This system is one example where the support is acting as a promoter or co-catalyst.

Previously, the oxide supports used in catalysis were considered inert substrates with high surface area. By dispersing the metal on these supports a high surface to volume ratio could be achieved, thereby exposing a high percentage of the expensive metal atoms to the reactants. In the late 1950's numerous research groups discovered that the catalytic activity of metals is strongly influenced by the support. Schwab *et al.* found that the activation energy of decomposition of formic acid on nickel was dependent on the type of oxide present[18,19]. They found that addition of n-type additives to nickel on alumina increased the activation energy while p-type dopants decreased the activation energy. Another influence of the oxide supports was to change the chemisorptive properties of metals. Tauster and co-workers found suppression of CO and H_2 chemisorption after high temperature reduction (773 K) of various oxide supports[20,21,22]. TiO_2, Nb_2O_5, V_2O_3, Ta_2O_5 showed a large suppression whereas SiO_2, Al_2O_3, Sc_2O_3, HfO_2, MgO, ZrO_2

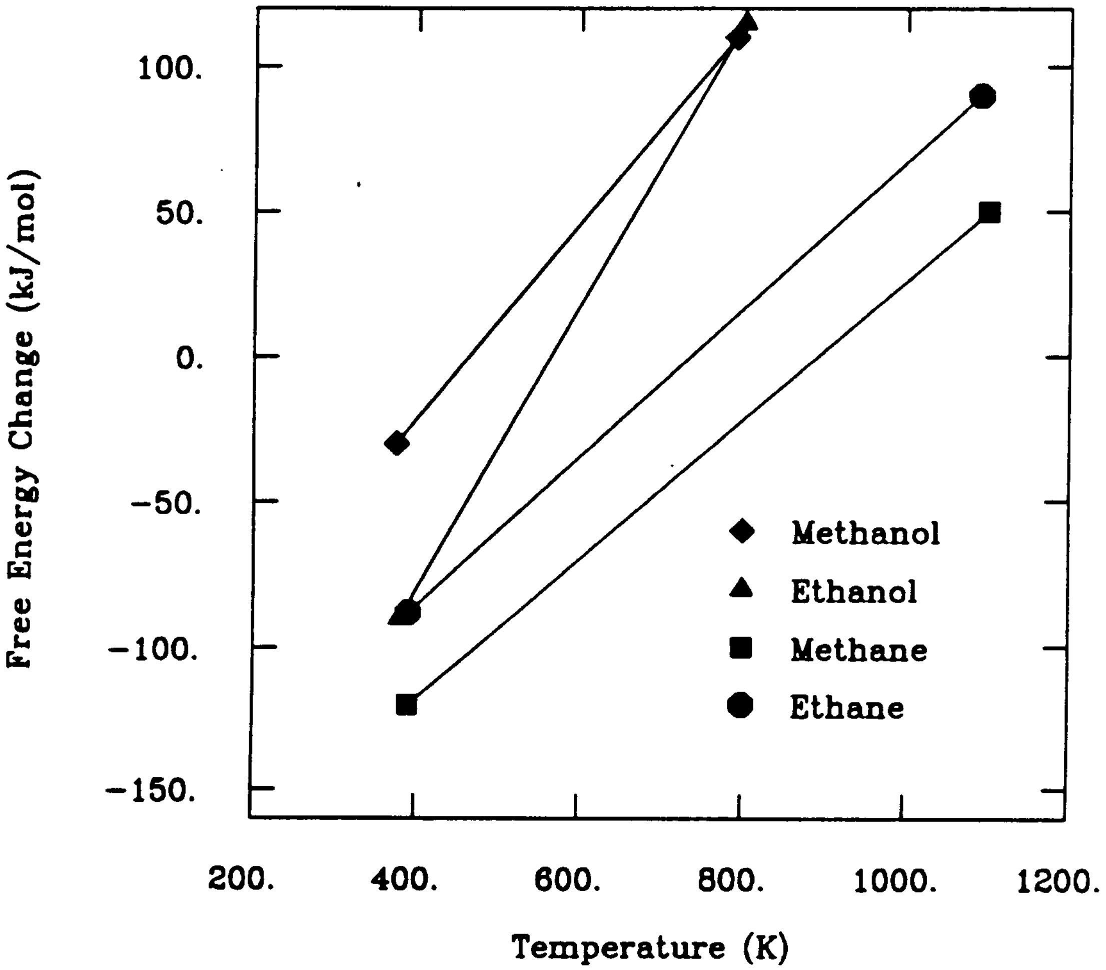

Figure 1.1: Free Energies of Formation for Products in the CO + H_2 reaction.

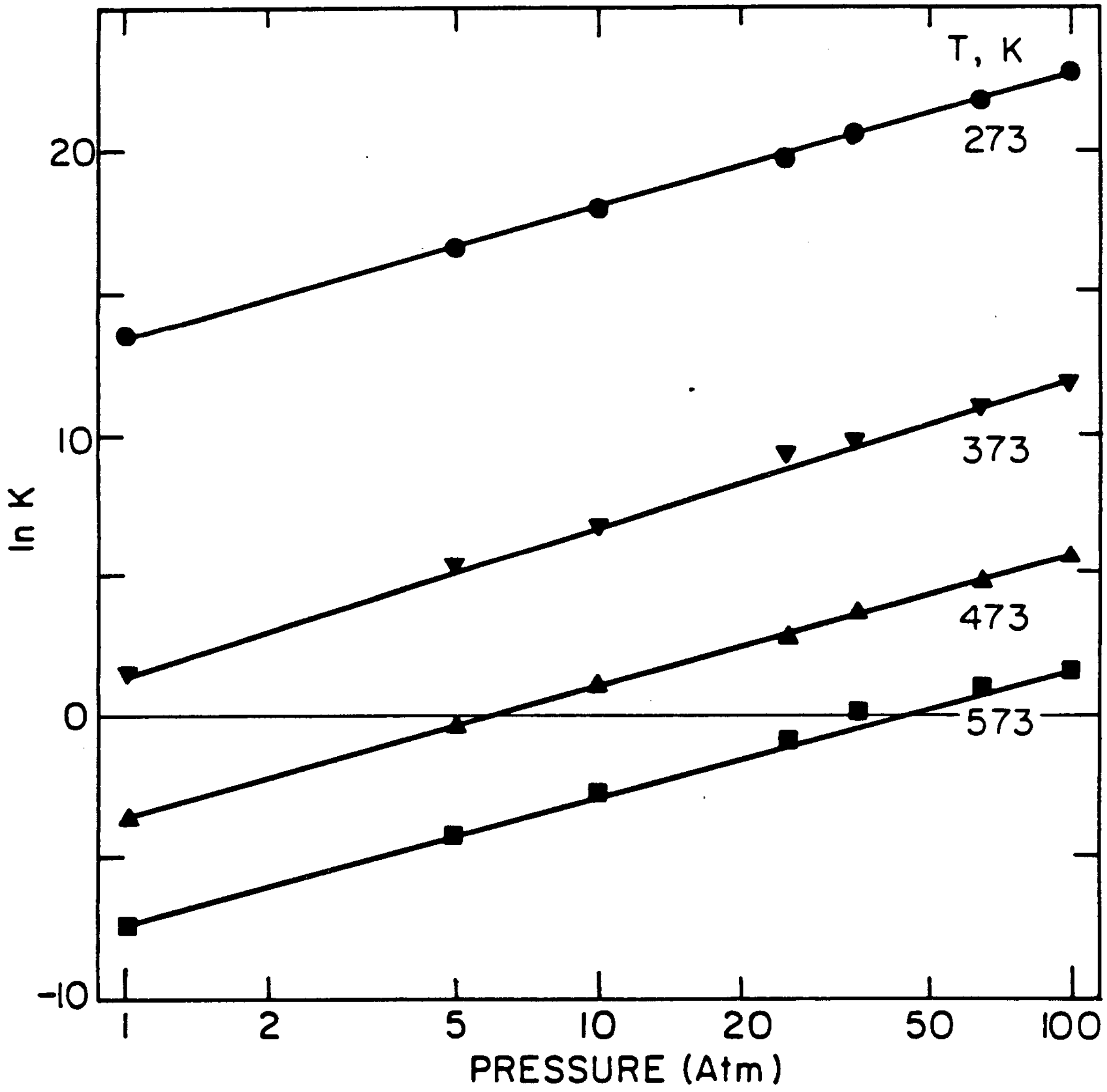

Figure 1.2: Pressure Dependence for Methanol Formation.

and Y_2O_3 had very little effect. Tauster found that more easily reducible oxides interacted more with the metal to reduce CO and H_2 chemisorption. Numerous research groups have found a strong correlation between the oxide supports and catalytic activity and selectivity. Bell *et al.* studied the activity of palladium in the CO hydrogenation reaction and found the following order in methanol activity: $La_2O_3 >> ZrO_2 > ZnO \approx MgO > TiO_2 > Al_2O_3 \approx SiO_2 >>$ carbon black, and the following order for methane activity: $TiO_2 \approx ZrO_2 > La_2O_3 > Al_2O_3 > SiO_2 \approx$ carbon black $> MgO > ZnO$[23]. The rate enhancement has been attributed to numerous factors, including the formation of mixed metal - metal oxides sites [24,25] and the formation of metal ions [26].

1.2 Metal - Additives

Small concentrations of surface additives drastically modify the activity and selectivity of metals in catalytic reactions. In some instances (K on Fe/Al_2O_3 in ammonia synthesis) the additives enhance the rate of product formation, whereas in other systems (S on Fe and Pd in CO hydrogenation) the additives poison the reaction or change the product distribution (S on Pt-Re in hydrocarbon reforming). Even though it has been known for close to 150 years that dopants are catalytically important, the nature of the interaction between the additive and metal is not well understood [27].

It has been reported that these additives have numerous effects including acting as active components or co-catalysts, limiting coking and structurally changing the catalyst. However, the majority of the studies have only looked at the macroscopic changes induced by the additives, and have not probed their fundamental relationship on the atomic scale.[1] In this thesis LEED, $\Delta\Phi$, AES, reaction studies and the chemisorption of H_2, CO and C_2H_2, are used to study on the atomic

---

[1] A comprehensive survey of metal-additive systems is presented in the references[28,29,30,31].

scale how the additives, potassium, sodium, silicon, phosphorus, sulfur and chlorine deposited on palladium single crystals ((111),(100) & (110)), alter the metal's catalytic, structural and electronic properties.

1.3 Perovskites

Numerous studies have shown that oxidized metals are catalytically active in the CO hydrogenation reaction [32,33,34]. Instead of depositing additives on a metal surface, it is possible to alter a metal's catalytic activity and stability by exposing it to a different chemical environment. One example is to bond the metal in an oxide matrix which can stabilize the metal in a higher oxidation state. Perovskite compounds (ABO_3) are one such class of compounds where in the bulk the metal cation (B) is surrounded by 6 oxygen and 8 metal cations (A).

In this thesis a survey of the activity of perovskite compounds ($LaMnO_3$, $LaCrO_3$, $LaFeO_3$, $LaRhO_3$) in the CO hydrogenation reaction is presented. The metal is enclosed in an oxide matrix which can modify the activity and product distribution relative to an undoped foil. XPS and kinetic studies are used to understand the catalytic behavior of the perovskite compounds.

References

[1] C. N. Satterfield. *Heterogeneous Catalysis in Practice.* McGraw-Hill, 1980.

[2] P. Sabatier and J. B. Senderens. *C. R. Acad. Sci. Paris* **134** (1902) 514.

[3] Badische Anilin und Sodafabrik. *D. R. P. 293,787* (1913) .

[4] F. Fischer and H. Tropsch. *Brennst.-Chem.* **7** (1926) 97.

[5] F. Fischer and H. Tropsch. *D. R. P. 411,216* (1922) .

[6] F. Fischer and H. Tropsch. *Brennst.-Chem.* **4** (1923) 276.

[7] F. Fischer and H. Tropsch. *D. P. R. 484,337* (1925) .

[8] H. Pichler. *Brennst.-Chem.* **19** (1938) 226.

[9] H. Pichler. *Ges. Abh. Kenntn. Hohle* **13** (1957) 417/74.

[10] H. Pichler. *Adv. Catal.* **4** (1952) 271.

[11] H. Kolbel. *Chem. Ing. Tech* **29** (1957) 505.

[12] H. Kolbel and D. Hanus. *Chem. Ing. Tech.* **46** (1974) 1042.

[13] J. H. Storch, N. Golumbic, and R. B. Anderson. *The Fischer-Tropsch & Related Synthesis.* Wiley, 1951.

[14] M. A. Vannice. *Catal. Rev. Sci. Eng.* **14** (1976) 153.

[15] J. F. Schultz, F. S. Karn, and R. B. Anderson. *Bureau of Mines Report of Investigation* **6974** (1967) .

[16] M. L. Poutsma, L. F. Elek, P. A. Ibarbia, A. P. Risch, and J. A. Rabo. *J. Catalysis* **52** (1978) 157.

[17] R. Kratel. PhD thesis, Technische Hochschule, Berlin-Charlottenburg, 1937.

[18] G. M. Schwab, J. Block, W. Muller, and D. Schultze. *Naturwissenschaften* **44** (1957) 582.

[19] G. M. Schwab, J. Block, and D. Schultze. *Angew. Chem.* **71** (1958) 101.

[20] S. J. Tauster, S. C. Fung, and R. L. Garten. *J. Am. Chem. Soc.* **100** (1966) 2173.

[21] S. J. Tauster and S. C. Fung. *J. Catalysis* **55** (1978) 29.

[22] S. J. Tauster, S. C. Fung, R. T. K. Baker, and J. A. Horsley. *Science* **211** (1981) 1121.

[23] R. Hicks. PhD thesis, U. C. Berkeley, Berkeley, CA., 1984.

[24] J. D. Bracey and R. Burch. *J. Catalysis* **86** (1984) 384.

[25] R. Burch and A. R. Flambard. *J. Catalysis* **78** (1982) 389.

[26] E. K. Poels, E. H. van Broekhoven, W. A. A. van Barneveld, and V. Ponec. *React. Kinet. Catal. Lett.* **18** (1981) 223.

[27] W. Dobereiner. *Pogg. Ann.* **64** (1845) 94.

[28] M. Shelef, K. Otto, and N. C. Otto. *Adv. Catal.* **27** (1978) 311.

[29] E. B. Maxted. *Adv. Catalysis* **3** (1951) 129.

[30] B. Imelik. *Metal-Support and Metal-Additive Effects in Catalysis.* Elsevier, 1982.

[31] C. H. Bartholowmew, P. T. Agrawal, and J. R. Katzer. *Advances in Catalysis,* pages 135 – 170. Academic Press, 1982.

[32] P. R. Watson and G. A. Somorjai. *J. Catalysis* **74** (1982) 282.

[33] P. R. Watson and G. A. Somorjai. *J. Catalysis* **72** (1981) 347.

[34] G. A. Somorjai. *Chemistry in Two Dimensions.* Cornell University Press, Ithaca, New York, 1981.

Chapter 2

EXPERIMENTAL

2.1 Introduction

This research project has centered on studying catalytic reactions on well characterized low surface area (1 cm^2) transition metal single crystal and polycrystalline surfaces to correlate surface composition and structure (determined in UHV) to catalytic behavior (high pressure conditions), and to determine the effect of surface additives on chemical bonding. This chapter describes in detail the experimental apparatus , techniques and procedure .

By analyzing the samples in UHV the surface remained clean from background gas contamination. Using the kinetic gas law it can be determined that at 1×10^{-6} torr the surface would become saturated with background gases in 1 second, assuming a sticking coefficient of unity. By performing the surface analysis at 1×10^{-10} torr, the surface remained relatively free (less than 10% of the surface covered) of adsorbates for ~1000 seconds. Also, for the electron spectroscopy techniques UHV is necessary.

To mimic the high pressure - high temperature conditions used in industrial reactions, the sample, after surface characterization, is enclosed in an isolation cell. This small volume ~128 cm^3 cell is pressurized with the reactant gases, the sample is heated and the product distribution monitored with a gas chromatograph. The reaction can be stopped, and the reaction cell evacuated and opened to UHV without exposing the sample to the ambient atmosphere [1,2].

2.2 Experimental Equipment

2.2.1 Combined High Pressure/Low Pressure Chamber

This section describes the design of a new high pressure isolation cell mounted inside an ultra-high vacuum (UHV) chamber capable of attaining pressures of 1800 psi (122 atm). This pressure range allows modeling of many industrially important reactions, including CO hydrogenation, ammonia synthesis and hydrocarbon reforming. Many commercial reactions are operated at pressures over 500 psi. Thermodynamics dictates that product formation for some reactions is enhanced at higher pressures. Also, at higher pressures, different mechanisms may exist which lead to different product distributions than at lower pressures because of larger surface concentrations of weakly adsorbed molecules. In ammonia synthesis higher conversions are obtained by performing the reaction at higher pressures (>1500 psi). In the Fischer-Tropsch (Syn Gas) reaction, recent studies in our laboratory found a significant increase (from 65% to 90%) in the alcohol selectivity of K_2CO_3 promoted MoS_2 in a pressure range of 500 to 1500 psi H_2 with a constant CO pressure of 500 psi [3]. A schematic of the high pressure/UHV system is shown in Figure 2.1 and photographs of the front and back are shown in Figure 2.2 and Figure 2.3. The primary components are the manipulator (to which the sample is attached), the high pressure cell mounted inside the UHV chamber, a gas circulation pump and gas chromatograph for reaction product analysis. The components of the high pressure system (manipulator and cell) are described in detail below. (see Appendix A)

Various constraints are imposed on the design of the high pressure cell and

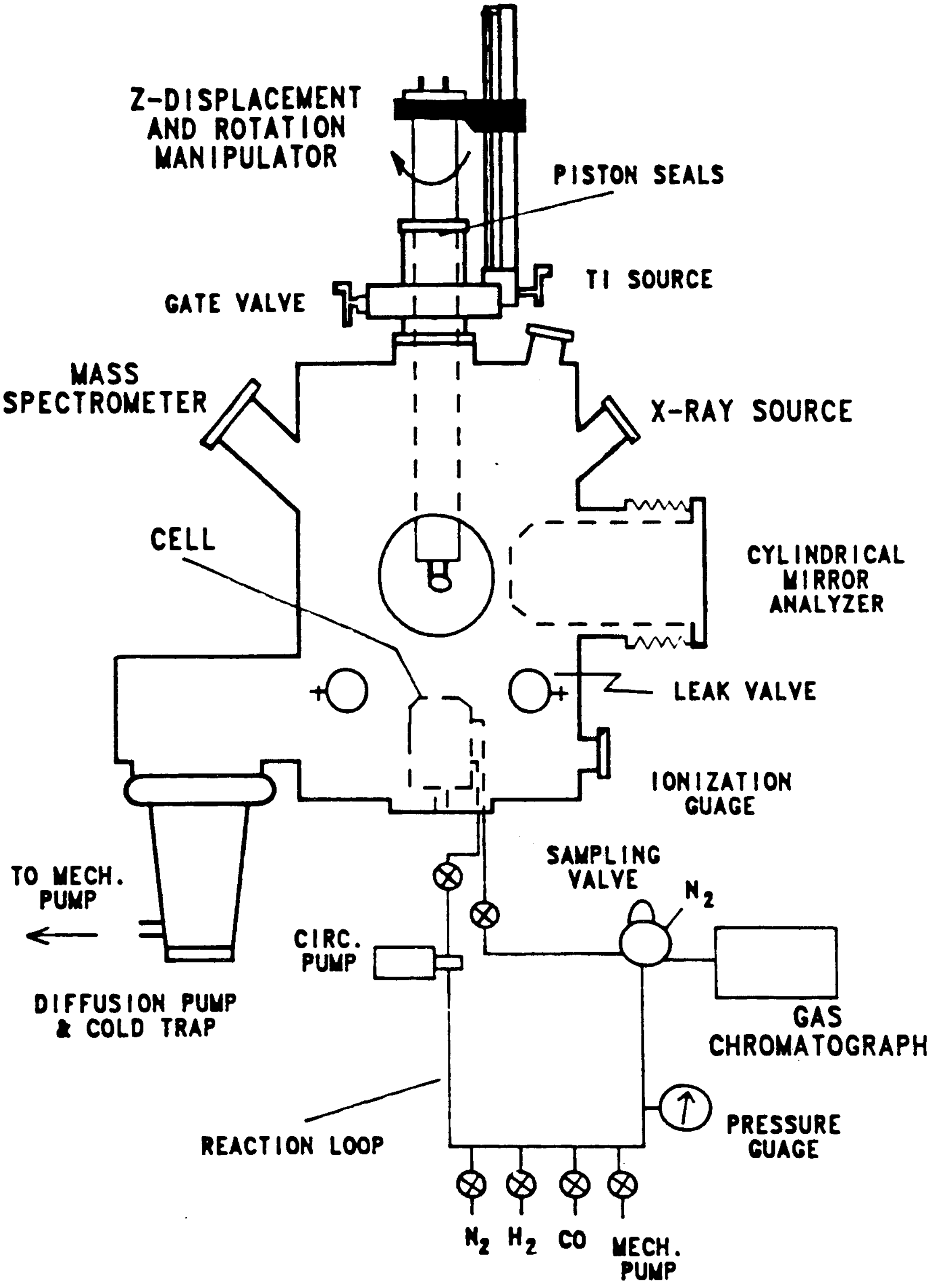

Figure 2.1: Schematic of Combined High Pressure - Low Pressure System

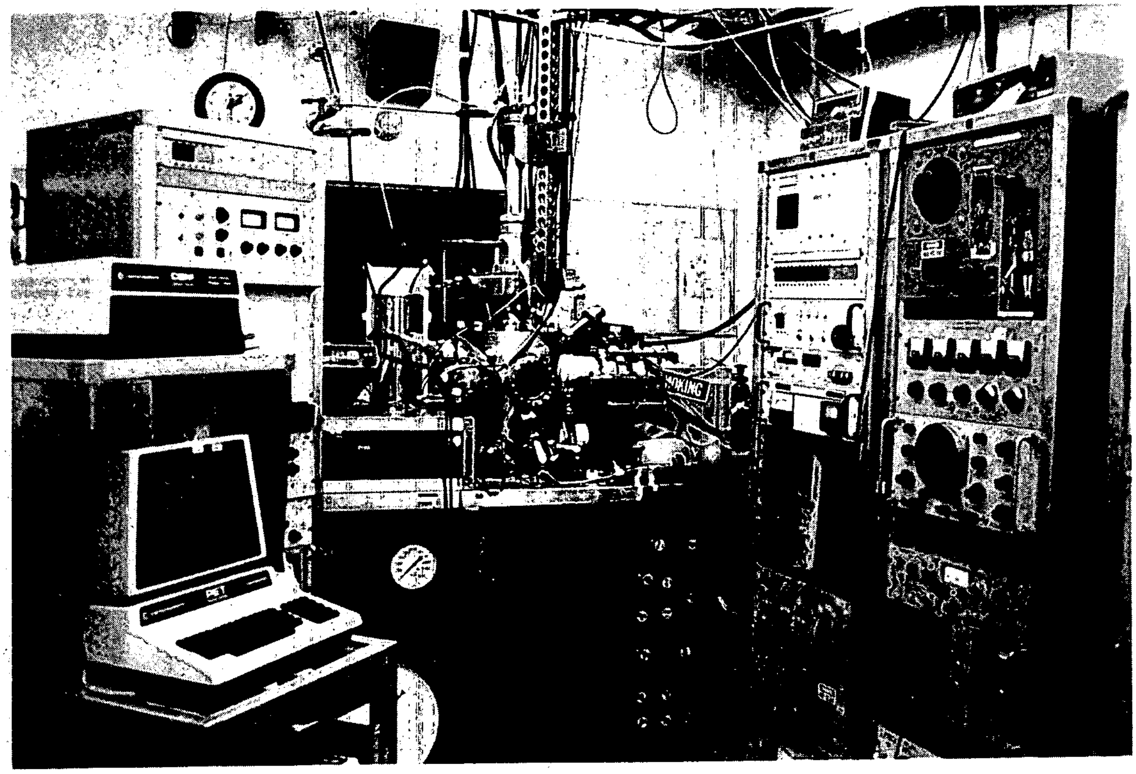

XBB 876-5031

Figure 2.2: Photograph of Front of High Pressure - Low Pressure Chamber

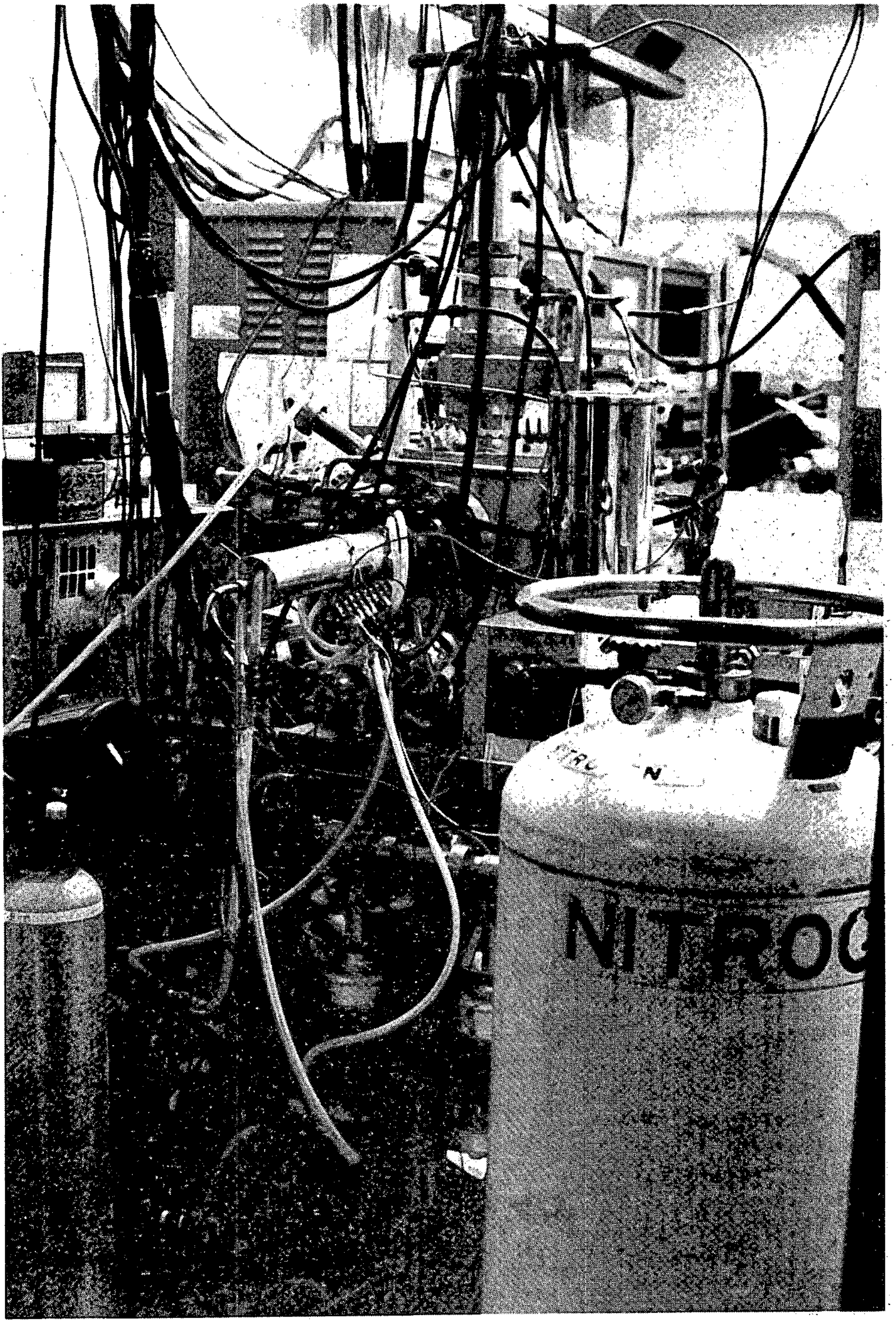

XBB 876-5033

Figure 2.3: Photograph of Back of High Pressure - Low Pressure Chamber

the manipulator. The cell should have a seal capable of maintaining UHV in the chamber during reactions with 10^5 torr of reactants. After a reaction, the cell should pump down rapidly (within minutes) to UHV. The total unit has to fit comfortably inside a 10 liter UHV chamber and also allow use of all of the surface science equipment (x-ray and electron sources, electron energy analyzer and mass spectrometer). The volume of the cell has to be minimized for two reasons. First, since the catalyst surface area is $\sim$1 cm^2, the ratio of sample surface area to cell volume must be maximized to enhance detectability of reaction products. Second, during reactions, products and reactants adsorb on the walls of the cell and slowly outgas when the cell is opened to UHV, increasing the chamber base pressure. The sample should be easily mountable on the manipulator to facilitate sample changes. The cell and sample support must be catalytically inactive at the reaction temperatures to which they are exposed.

The major limitation in reaching high pressures ($>$ 350 psi) in the previous isolation cells was the manipulator-to-cell sealing surface. The copper gasket-knife edge seal fails above 350 psi of reactant gas. This new apparatus uses a sealing surface with differentially pumped o-rings, which is tight to over 1800 psi of reactant gas. Other improvements in design include smaller cell volume, easier manipulator-cell alignment, and a simplified sealing mechanism.

a) MANIPULATOR

The manipulator, shown in Figure 2.4, is composed of two sections: a solid stainless steel bulkhead with thermocouple and electrical feedthroughs to which the sample is attached and a 1m long stainless steel transfer probe. This unit has both vertical and 360° rotational motion with the sample mounted on the central chamber axis.

The manipulator is raised and lowered by a vertical translator mounted on the chamber. To prevent exposure of the chamber to the atmosphere during sample

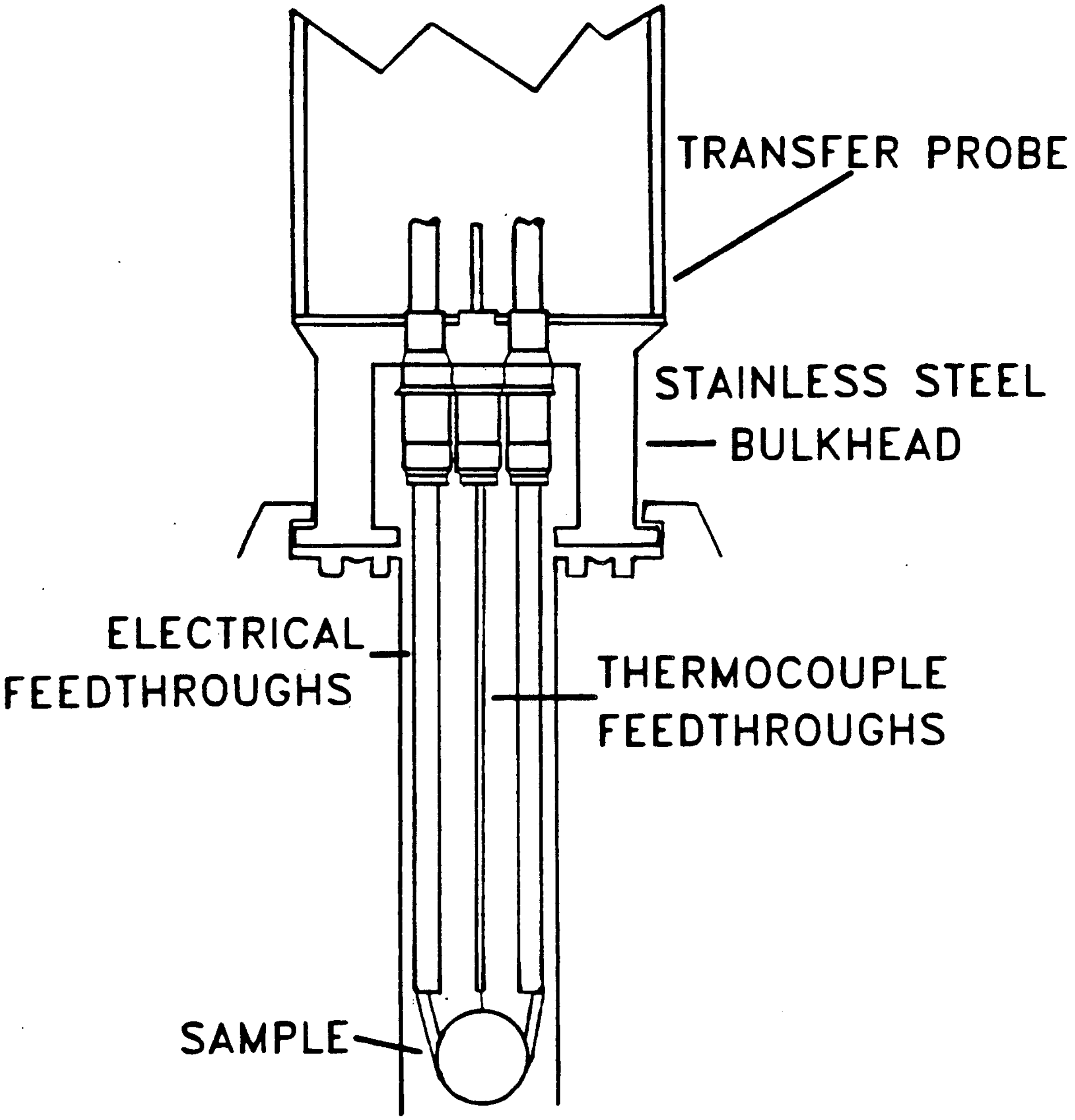

XBL 871-366

Figure 2.4: Diagram of manipulator showing electrical and thermocouple feedthroughs used to regulate the crystal temperature.

changes a load lock is mounted on the chamber (Figure 2.1). The seal between the manipulator and chamber, located above the load lock gate valve, consists of two differentially pumped piston seals which are very lightly lubricated with diffusion pump oil to allow the manipulator to slide easily.

The bulkhead has two 150 amp copper feedthroughs and two thermocouple feedthroughs welded in with the ceramic insulator inside the cell. The sample is spotwelded to 20 mil gold wire which in turn is spotwelded to the copper feedthroughs. Sample temperature was monitored by either a platinum/platinum-10% rhodium or a chromel/alumel thermocouple. Thermocouple accuracy was checked by visually observing the minimum temperature of optical emission ($\sim$ 785K). On the topside of the electrical feedthroughs copper tubes were soldered on which carry in liquid nitrogen for cooling and current for sample heating. The sample could be cooled to $\sim$ 80K and heated to 1000K without heating the copper supports. Air was passed through these tubes during normal use to keep the bulkhead and copper feedthroughs from heating during sample heating and reactions. The tubes and thermocouple wires run the length of the 2.5′ diameter polished transfer probe welded to the bulkhead. The other end of the probe is capped to allow evacuation of the transfer probe to cool samples without condensation on the outside of the probe. The copper tubes and thermocouple have vacuum tight connections through this cap.

b) CELL

The manipulator is lowered and inserted into the high pressure cell (Figure 2.5) to complete a micro-batch reactor. This cell (18 cm × 7.5 cm), mounted inside the chamber on the bottom center, has a piston-actuated seal which grasps the manipulator in a bayonet mount. The sealing surface of the cell consists of two differentially pumped viton o-rings seated in dove-tail grooves on the top flat surface. Pressurizing the piston through the air-in line pulls down the outer housing which in turn pulls the manipulator's flat sealing surface tightly against the o-rings. A nitrogen sealing pressure of at least one-half the reaction gas pressure is needed for a tight seal. When the nitrogen pressure is released, the spring forces the piston and outer housing up.

The inner cell is mounted on a 1 cm diameter pedestal which holds the cell firmly while still allowing 1-2 mm lateral flexibility for manipulator-cell alignment.The cell has cavities for the sample (9 cm × 2.5 cm) and piston (6 cm × 5 cm). This cell has connections for reactant gas in and out, nitrogen for pressurizing the piston, and for differential pumping between the o-rings and the volume below the piston. The volume under the piston is pumped as an extra precaution to eliminate the possibility of nitrogen leaking into the chamber during a reaction.

The vacuum system in which this high pressure cell was mounted consisted of a stainless steel belljar ($\sim$ 40 liter internal volume) built at the Lawrence Berkeley Laboratory. The chamber which had a base pressure of 1×10^{-9} torr (after 24 hr bakeout, 150° C) was pumped by an 6 liter liquid nitrogen trapped (Torr Vacuum Products LNB-62) oil diffusion pump (Varian VHS-6). This chamber was also equipped with:

- A double pass cylindrical mirror analyzer (CMA) for electron energy analysis (AES, XPS, $\Delta\phi$) mounted on bellows (Built by K. Franck).
- A dual filament 15 kV x-ray source mounted on bellows [4].
- Two CRT-electron guns for AES (one glancing incidence and one inside the CMA).
- A quadrupole mass spectrometer (EAI Quad 240) for residual gas analysis and TPD.
- An ion sputtering gun (Varian 981-2043) for Ar^+ sputter cleaning the sample surface.

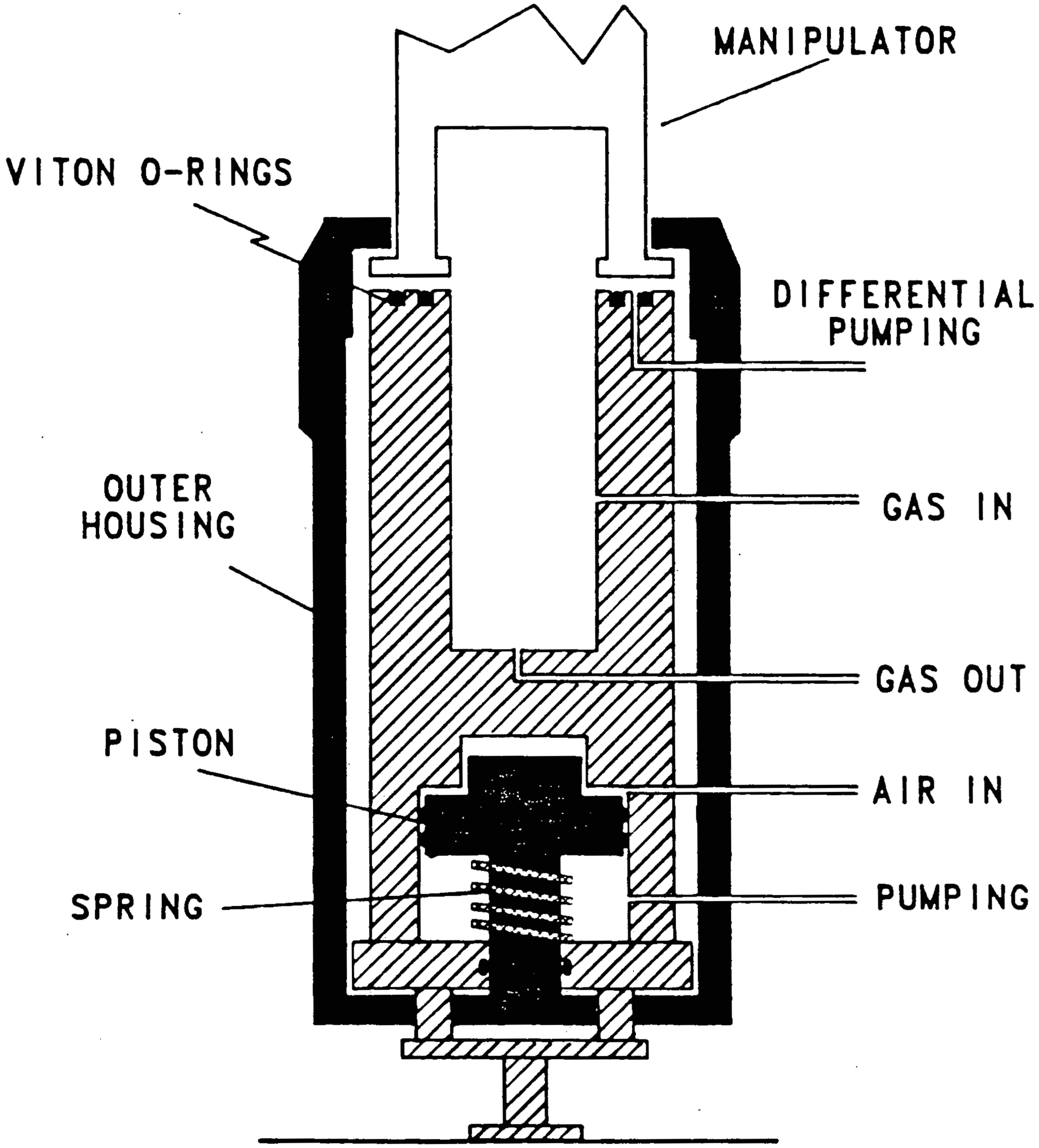

Figure 2.5: Diagram of internal high pressure cell mounted on the bottom of the chamber. Nitrogen forces the piston down which in turn pulls down the outer housing and grabs the manipulator in the bayonet mount, tightly sealing the flat bottom of the manipulator against the viton o-rings on the cell.

- Three variable rate leak valves (Varian 951-5106) for controlled addition of gases into the chamber.
- A nude ion gauge (Varian 971-5008) for measuring chamber pressure.
- Resistive dosers for potassium (Saes Getters) and Ti.

The high pressure batch reactor included:

- Two gas circulation pumps
    1. A teflon rotor micropump (Micropump 120-000-100) for pressures <100 psi.
    2. A positive displacement diaphragm pump (Whitey LP10) for pressures >100 psi.
- Two pressure gauges
    1. Pressures < 400 torr (Wallace & Tiernan 61C-1D-0410).
    2. Pressures > 400 torr (Heise H3J547).
- A gas chromatograph (HP 5793) and peak integrator (HP 3390) to determine product yields and distributions. Columns were 1/8 inch stainless steel tubing packed with either Poropak N, Q, QS, Chromosorb 103 or 102.
- A 6 port GC sampling valve (Nitronic-60) for pressures up to 7000 psi.
- A liquid nitrogen trapped (Varian M2) oil diffusion pump (Varian VHS-2) for evacuating the loop down to $\sim 10^{-5}$ torr.

2.2.2 Low Pressure Chamber

The second system used in this research was an ion-pumped chamber with a base pressure between 1×10^{-10} to 5×10^{-11} torr (Figure 2.6). This lower pressure facilitated TPD and LEED experiments. This bell-jar (Varian) was equipped with:

- Five 140 liter/sec triode ion pumps (Varian 912-7000).
- A titanium sublimation pump (Varian).
- A four grid LEED optics for LEED, AES and work function measurements.
- A multiplexed quadrupole mass spectrometer (UTI 100c) with programmable peak selector (UTI) for TPD and residual gas analysis.
- An offset manipulator to hold the sample.
- An ion sputter gun (781-2454) for Ar^+ sputter cleaning the sample surface.
- A glancing angle CRT electron gun for AES.
- A single pass cylindrical mirror analyzer for energy analysis (AES).
- Two variable rate leak valves for controlled addition of dosing gases into the chamber.

2.3 Experimental Techniques

To understand the interaction of adsorbates on surfaces and their influence on catalytic reactions, a wide variety of surface sensitive techniques are available. These analytical techniques yield information on chemical composition (Auger Electron

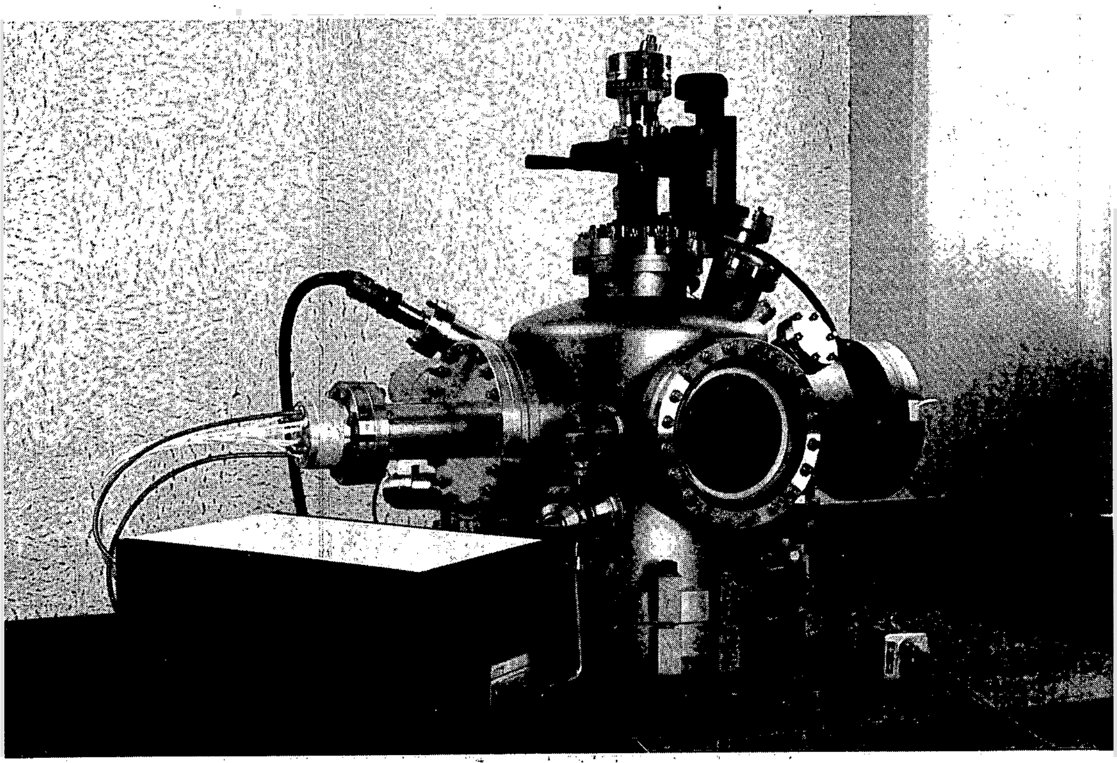

XBB 790-14004

Figure 2.6: Photograph of the System used for Low Pressure TPD Studies

Spectroscopy), oxidation states (X-ray Photoelectron Spectroscopy), surface structure (Low Energy Electron Diffraction), surface - adsorbate bond strengths (Temperature Programmed Desorption) and surface electron density (Work Function).

Some of these techniques achieve surface sensitivity by using electrons in the 10 - 1000 eV energy range. Figure 2.7 shows the short mean free path in solids for electrons in this range. Figure 2.8 shows a schematic of the energy distribution of electrons when a surface is bombarded by a monoenergetic beam of electrons. At low energy are the secondary electrons whose position and intensity reflect changes in work function, followed by auger electrons, electrons which have lost energy to the plasmons and phonons and then the elastically scattered electrons at the incident beam energy.

This section briefly describes each technique used in this research, the type of information obtained and the experimental equipment and procedure used.

2.3.1 Auger Electron Spectroscopy

Auger Electron Spectroscopy (AES) named after P. Auger is used to obtain detailed information on the chemical composition of the uppermost (2 - 5) layers of the sample surface [5]. In this technique a beam of high energy electrons (2000 eV) incident on the sample ionizes atoms to form core level holes (Figure 2.9). The core holes are filled by outer shell electrons and the energy is transmitted in a radiationless process to a secondary electron. This secondary electron or Auger electron is emitted from the atom with an energy

$$E(SVV) = E_S - E_1 - (E_2 + e\phi_{spect}) \tag{2.1}$$

where E_S is the energy of the core level electron, E_1 the energy of the outer shell electron which fills the core hole, E_2 the energy of the auger electron and ϕ_{spect} the spectrometer work function. From this, it can be seen that the kinetic energy of the auger electron is independent of the incident beam energy, and dependent

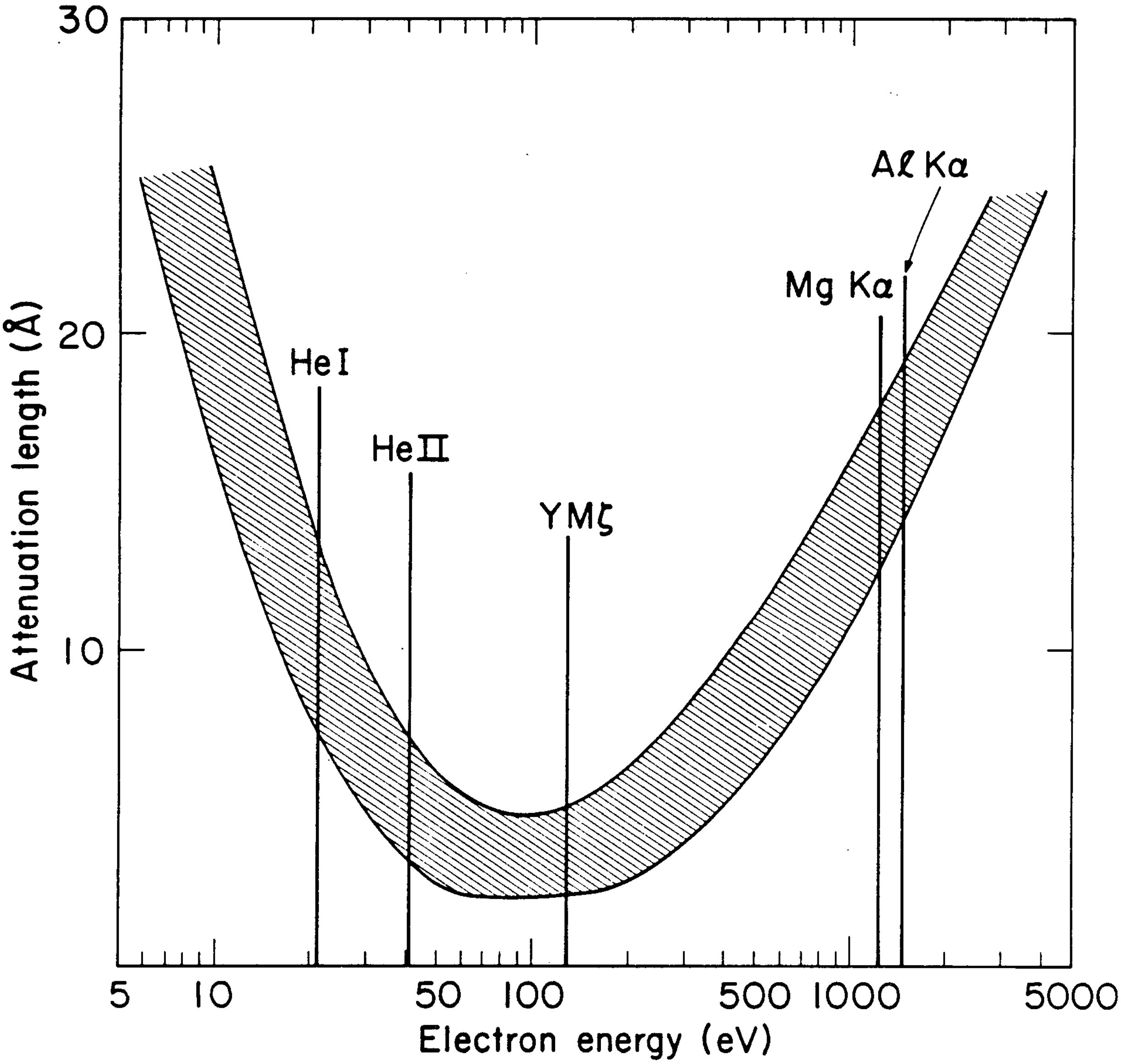

Figure 2.7: This figure show the mean free path of electrons in solids. Electrons in the range of 100 - 1000 eV are the most surface sensitive.

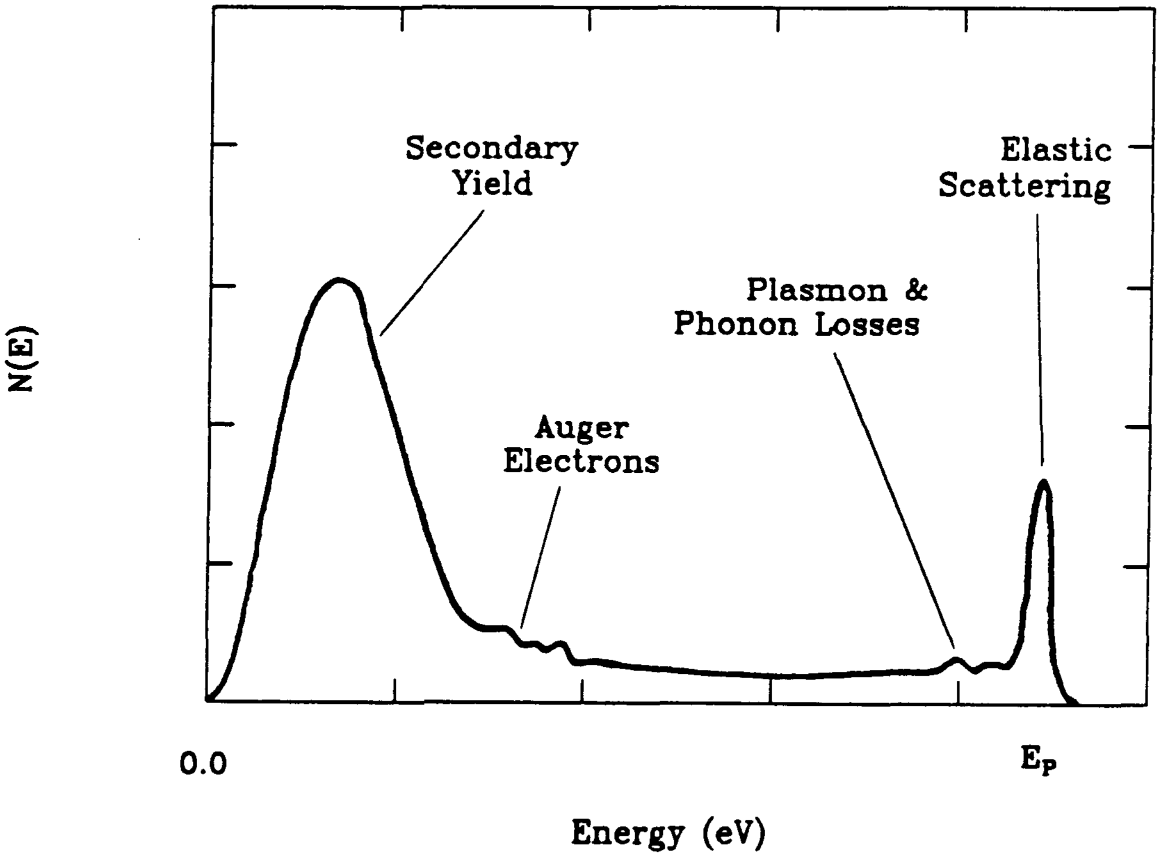

Figure 2.8: The energy distribution of electrons scattered from a surface bombarded with a beam of electrons is shown here. At low energy are the secondary electrons, followed by the Auger electrons and then the elastically scattered electrons at the primary beam energy.

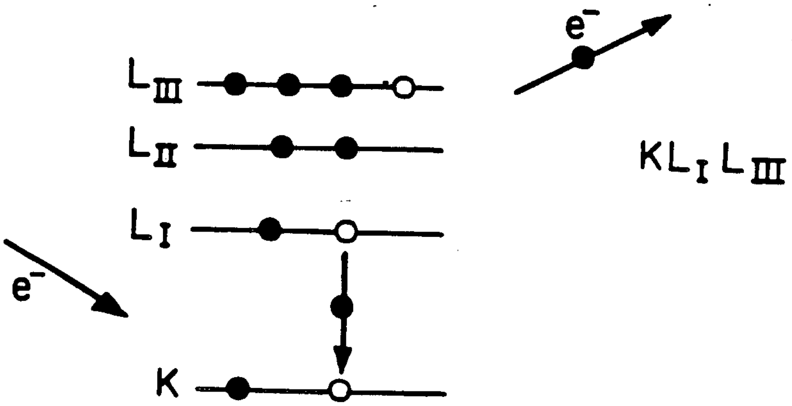

Figure 2.9: A schematic of the Auger process.

only on the element and binding state. Instead of an auger electron emission the excited state ion can undergo an x-ray emission, however the probability for this process is low for lighter elements and energies below $\sim$ 500 eV [6].

The energy of the auger electron (or any electron) can be measured readily with a wide variety of electron energy analyzers: Retarding Field Grid Analyzer (RFA), Cylindrical Mirror Analyzer (CMA), 127° Analyzer and Concentric Hemispherical Analyzer (CHA). A double pass CMA (shown diagrammatically in Figure 2.10) was used in this work. Energy analysis is accomplished by three filters arranged in series - one hemispherical retarding grid and two cylindrical mirror analyzers. There is also an internal aperture, which affects energy resolution and luminosity, to achieve maximum sensitivity for either XPS or AES. The second harmonic of the modulation voltage was detected as a function of the ramp voltage using a phase sensitive lock-in amplifier. The second harmonic corresponds to the first derivative of the auger spectrum.

A typical auger spectrum (phosphorus-doped palladium) is shown in Figure 2.11. Spectra acquisition time is 2 - 3 minutes. Quantitative data on relative surface composition can be determined by AES. Since the N(E) curve can be approximated to be gaussian, the peak-to-peak height (I_x) of the differentiated auger line (in the dN(E)/dE curve) is proportional to the surface concentration. This peak height is very sensitive to many parameters (beam energy, modulation, etc.) so comparison from spectrum to spectrum is not reproducible. However, comparisons or ratios within the same spectrum are valid. Surface coverages of additives in this work are determined by taking the ratio of the peak height for the additive and substrate, accounting for the ionization cross-section ($\Theta_x = (I_x/S_x)/(\sum_{i=1}^{n} I_i/S_i)$) [7,8].

AES can also be used to determine growth mechanisms of overlayers [9]. Elec-

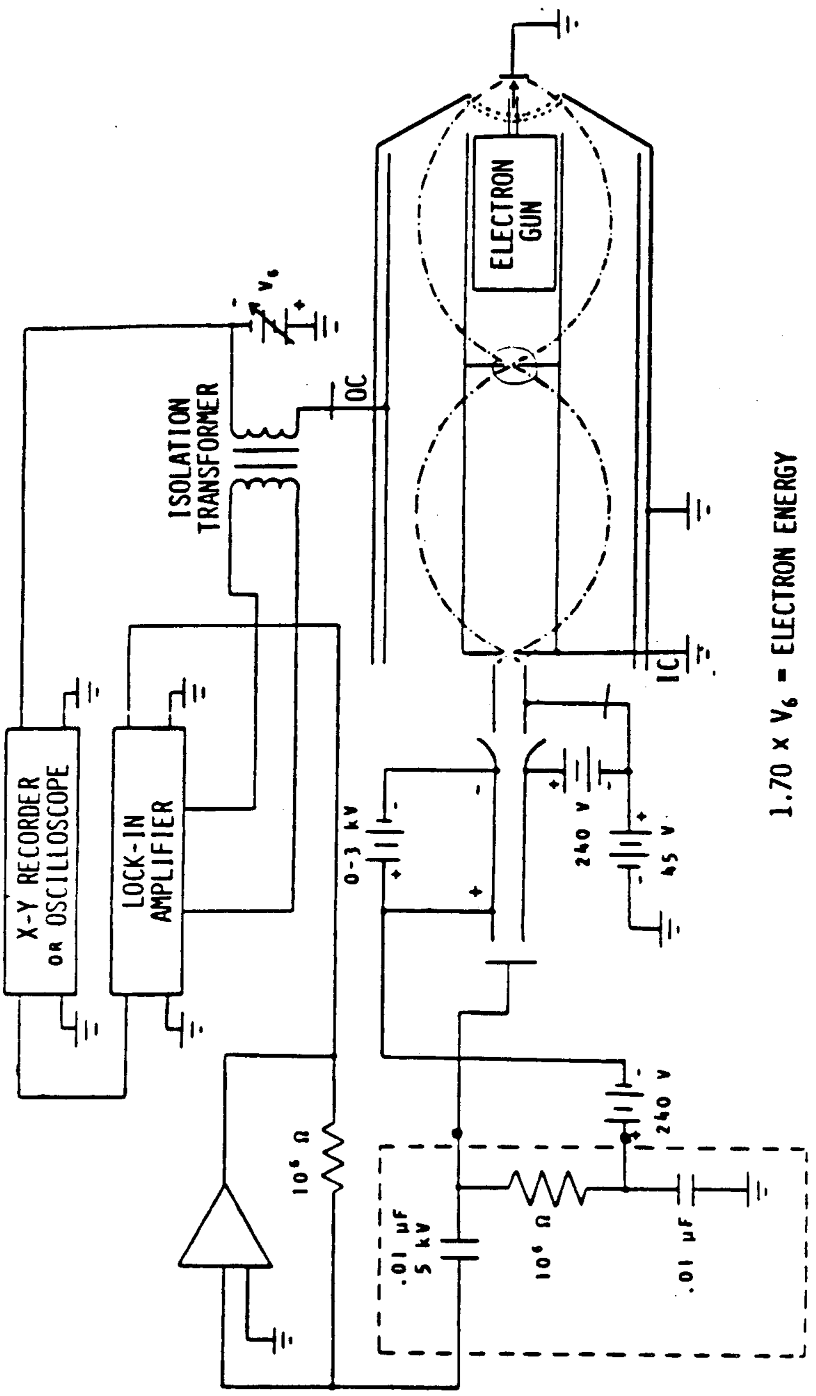

Figure 2.10: Schematic of a double pass cylindrical mirror analyzer.

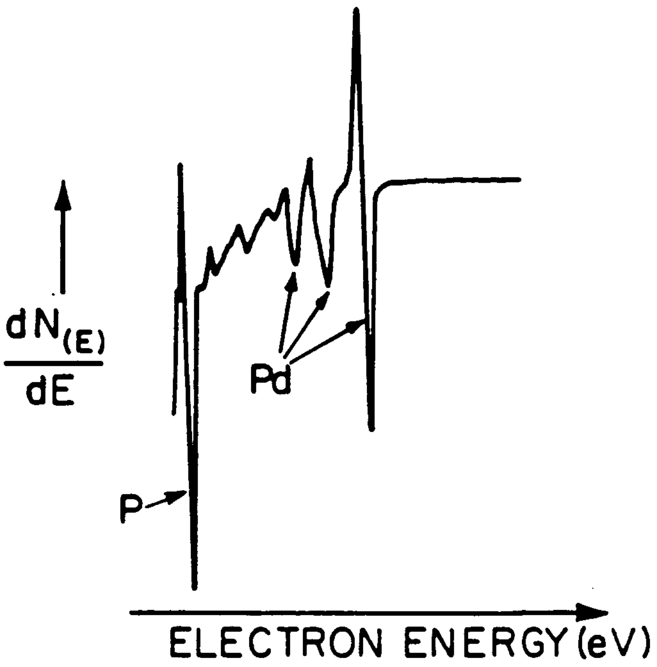

Figure 2.11: AES spectrum of a phosphorus-doped palladium single crystal.

trons emitted from a surface are attenuated (α)

$$\alpha = I/I_o = exp(-h/\lambda cos\phi) \tag{2.2}$$

depending on the mean free path of the electron (λ) and the thickness of the overlayer (h). For a surface covered by a fraction of monolayer (Θ) the intensity of the substrate peak will be a combination of the uncovered surface and the attenuated signal of the covered surface:

$$I = I_o\Theta\alpha + I_o(1-\Theta). \tag{2.3}$$

For two monolayers the substrate signal is attenuated by α^2, for three layers by α^3 and so forth. Therefore, for a layer by layer growth mechanism there is a sharp break in the uptake curves at the completion of each layer whereas for three dimensional growth there is an exponential decay in the substrate signal. Figure 2.12 shows the three growth mechanism which can be differentiated by this analysis. These three mechanisms are: layer by layer (Frank - Van der Merwe), layer followed by three dimensional (Stranski - Krastinov) and three dimensional (Volmer - Weber).

2.3.2 X-ray Photoelectron Spectroscopy

From the 1905 hypothesis by Einstein [10] that the energy of an ejected electron could be calculated as the energy difference between the incident photon ($h\nu$) and the binding energy of the target electron, has evolved the technique of X-ray Photoelectron Spectroscopy (XPS) (also called Electron Spectroscopy for Chemical Analysis (ESCA)). Subsequent work by Siegbahn and coworkers developing sensitive photoelectron spectrometers (sources and detectors) opened this field to many applications and a tremendous amount of both experimental and theoretical work has accumulated in the past 30 - 40 years [11,12,13,14,15,16,17,18,19]

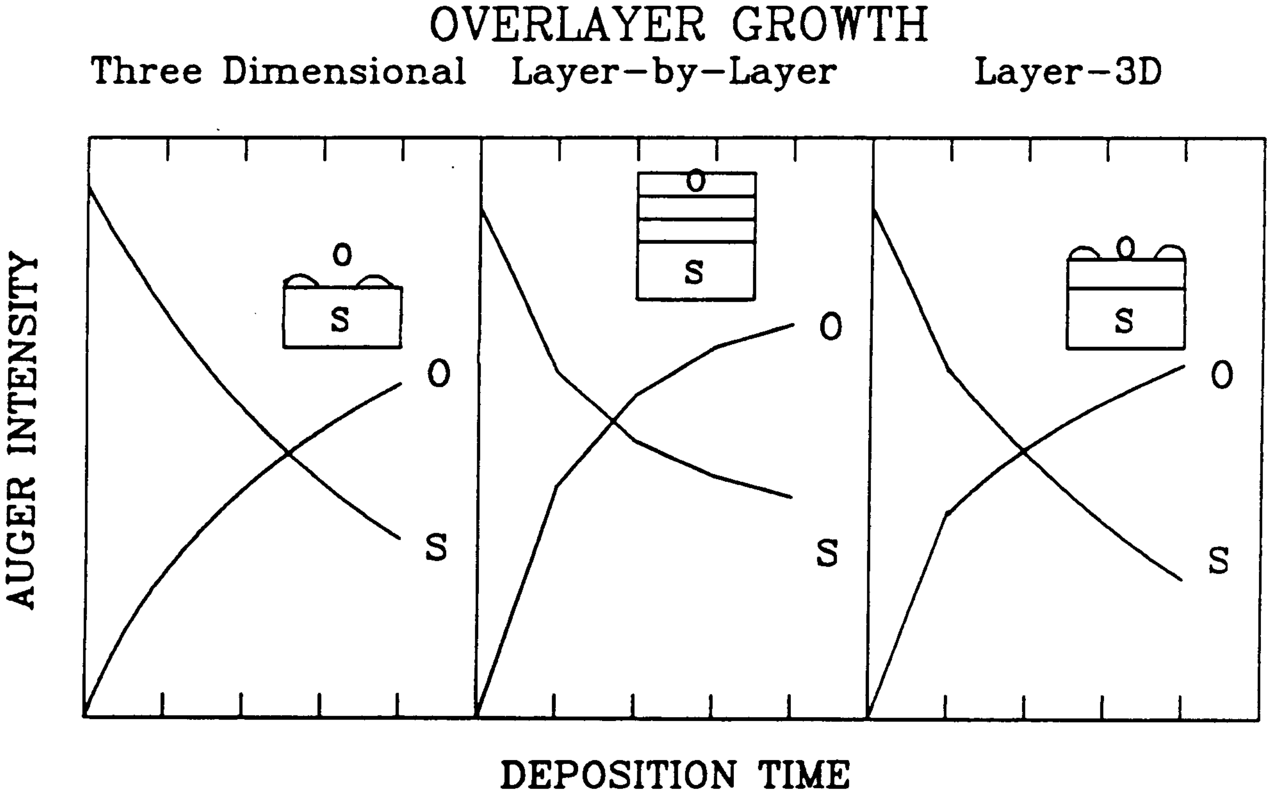

Figure 2.12: There are three general mechanisms for overlayer growth: Layer by layer, layer folllowed by three dimensional and three dimensional.

Conceptually, the experimental procedure for XPS is straightforward. Electrons from a filament (thoriated tungsten) impinge on a magnesium or aluminum anode (biased at 15 kV) giving rise to either Al(Kα) (1486.6 eV, .85 eV FWHM) or Mg(Kα)(1253.6 eV, .7 eV FWHM) x-rays (Figure 2.13). These x-rays, after passing through a 1 μm Al window (to eliminate electrons), strike the sample surface, causing photoemission of both core and valence level electrons [4]. The kinetic energy distribution of these electrons is measured by the CMA and a plot of the detected signal (counts from the channeltron) against kinetic energy is obtained. Figure 2.14 shows a schematic representation of this technique and a typical spectrum obtained for titania decorated palladium. The kinetic energy is converted to binding energy using a modified Einstein equation

$$E_B = h\nu - E_K - \phi_{spect}, \tag{2.4}$$

where ϕ_{spect} is the work function of the spectrometer. All the experimentally obtained binding spectra were referenced to a standard, either the gold $f_{7/2}$ (84.0 ± 0.1 eV) or the carbon 1s (285.0 eV). From this shift, the spectrometer work function was determined to be approximately 3.5 eV.

These full scans gave only qualitative information on surface composition. In order to obtain the exact chemical shifts the region around a specific elemental peak was scanned with a higher resolution (lower pass energy)[17]. [1] Quantitative information can be determined by measuring peak area and using the elemental

---

[1] Electrons are filtered in the CMA by applying a potential across the inner and outer cylinders (V_R , V_M). To maintain constant instrumental resolution across the spectrum, the following relationship holds:

$$\Delta E_{sp}/eV_{pass} = K$$

where ΔE_{sp} is the instrumental resolution, K is a constant and eV_{pass} the pass (kinetic) energy of the electrons in the CMA which can be expressed as:

$$eV_{pass} = (V_R - V_M)/\left(1.3 ln \left(\frac{Radius_{outer\ cyl.}}{Radius_{inner\ cyl}} \right) \right).$$

From these two equations the instrumental resolution was determined to be $\Delta E_{sp} = .007 \times eV_{pass}$. By decreasing the pass energy the instrumental resolution can be increased.

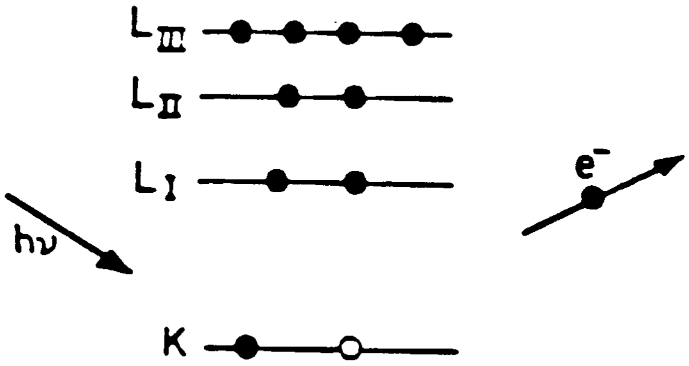

Figure 2.13: Schematic representation describing the formation of x-rays.

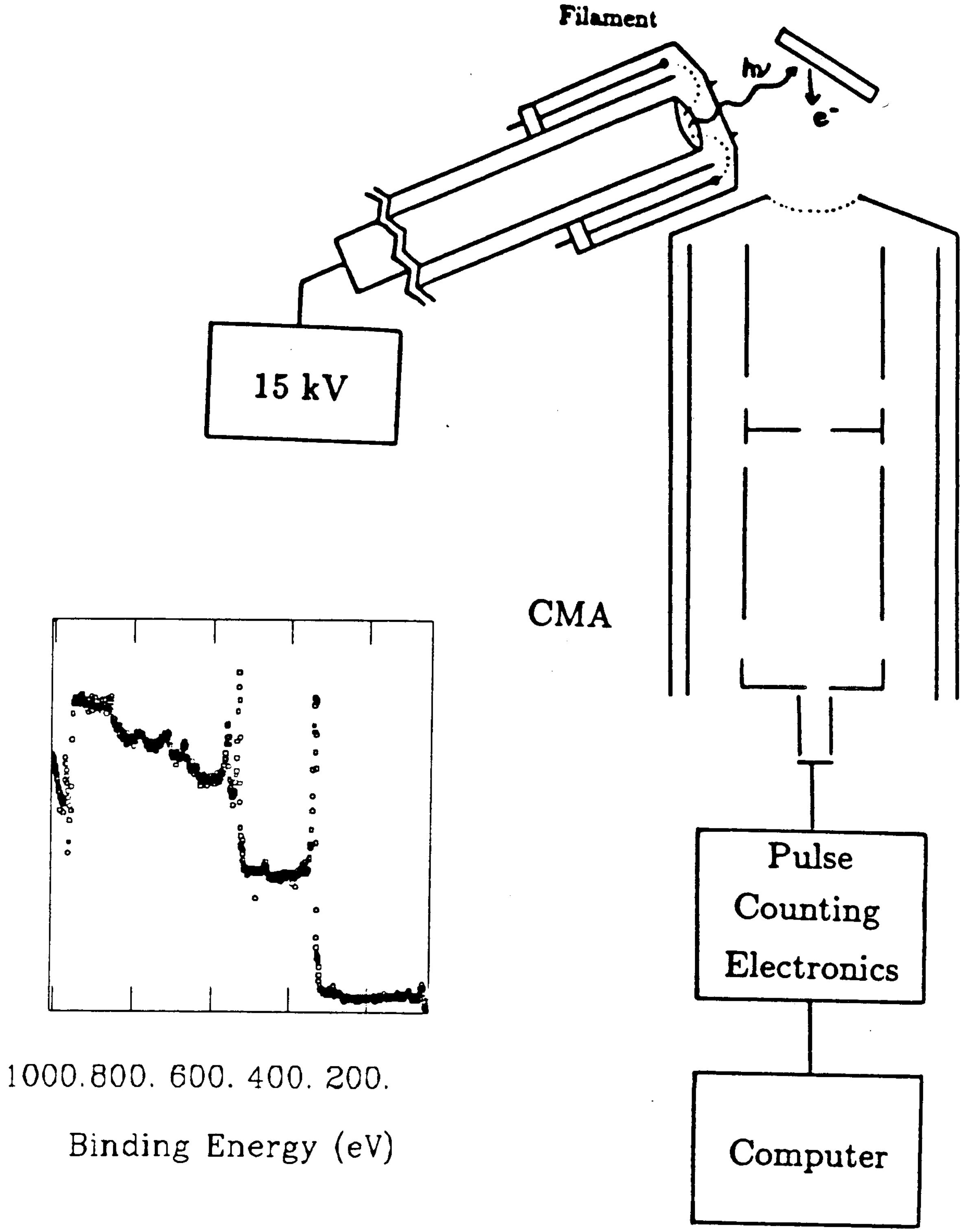

Figure 2.14: Schematic representation of the equipment needed to obtain an XPS spectrum and a typical spectrum.

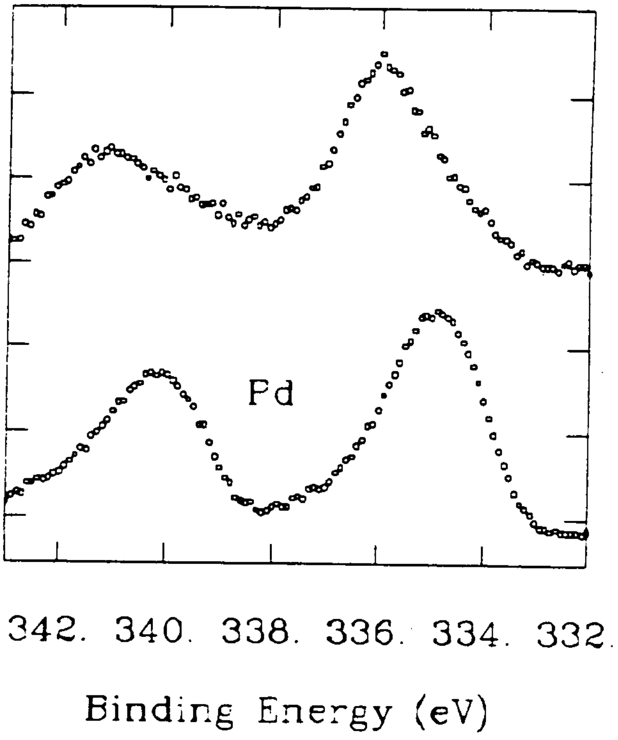

Figure 2.15: The Pd 3d peaks have different binding energies depending on the oxidation state. This figure shows the Pd 3d peaks for a clean and oxidized sample.

scaling factor which is related to the probability of photoemission (ionization cross section).

A simple classic electrostatic model shows that as the charge of the atom is increased, the electrons are held more tightly (i.e. higher binding energy). Figure 2.15 shows the 3d peaks of palladium and palladium oxide. A 1.6 eV shift to higher binding energy is seen for the oxide. Comparison of this shift to shifts of compounds with known composition enables the assignment of oxidation states (Pd^{+2} in this example). Table 2.1 summarizes the binding energies and corresponding oxidation states for the metals used in this work [17].

Line shapes and splitting also contain much information on the chemical environment of the element. The major factor causing peak splitting is spin-orbit

Metal	Binding Energy (eV)			
	0	+2	+3	+4
Pd	335.1	336.2		340.0
Ti	453.9	454.5		458.4
Si	98.5			103.5
Rh	307.0		309-311	
Co	777.9		779-782	
Fe	706.8		709-712	
Cr	574.0		576-580	

Table 2.1: Binding energies for the metallic and oxidized transition metals used in this research

coupling. When the orbital angular momentum quantum number l is greater than zero, the electron spin couples with l to yield two substrates $j = l + 1/2$ and $j = l - 1/2$, with the second having lower binding energy. The peak shape (width, asymmetry) are influenced by many factors, including spectrometer and x-ray source resolution, unresolved satellites, many-electron effects and lifetime broadening [13].

2.3.3 Temperature Programmed Desorption

Temperature Programmed Desorption (TPD) yields information on adsorbate - surface bond strengths, stoichiometric UHV reaction products and mechanisms and also on adsorbate - adsorbate interactions. Additionally, using CO, this technique could be used to titrate for surface cleanliness and adsorbate coverages.

Experimentally, a surface is dosed with a gas and then heated at a constant heating rate. A mass spectrometer detects desorbing fragments, and a plot of mass intensity as a function of temperature is obtained. Figure 2.16 shows three typical TPD traces. In case I, a molecule is adsorbed on the surface, M, and molecularly desorbs at a temperature, T. The temperature is directly proportional to the substrate - adsorbate bond strength, and as the surface composition or structure is varied, the maximum can shift. An example of reversible molecular desorption represented by this trace is CO on palladium. Case II presents the decomposition of molecule ABC on the surface. Only fragments A and B desorb, with fragment C remaining bound to the surface. From this type of trace mechanistic routes of decomposition can be determined as well as molecule-surface bonding geometries. An example of adsorption with decomposition is thiophene on palladium, where the sulfur remains bound to the surface and H_2 and C_4 molecules desorb. The third type of system for which TPD is useful is for UHV reactions. Molecule AB adsorbs on the surface, reacts to form C, and C desorbs from the surface. An example is the cyclotrimerization of acetylene to form benzene on palladium.

As mentioned earlier, TPD is used to determine adsorbate - surface bond strength or activation energies of desorption. There have been numerous analytical methods proposed in the literature [20,21,22,23], but the one used for this work is the Redhead method [24]. In this method, the rate of desorption per unit area is

$$Rate = \nu_n \sigma^n exp\left(\frac{-E}{RT}\right) \tag{2.5}$$

where n = order of the desorption reactions

σ = surface coverage (molecules/cm^2)

ν_n = rate constant

E = activation energy of desorption (cal/mole)

Assuming a linear heating rate, $T = T_0 + \beta t$, this rate equation can be expressed

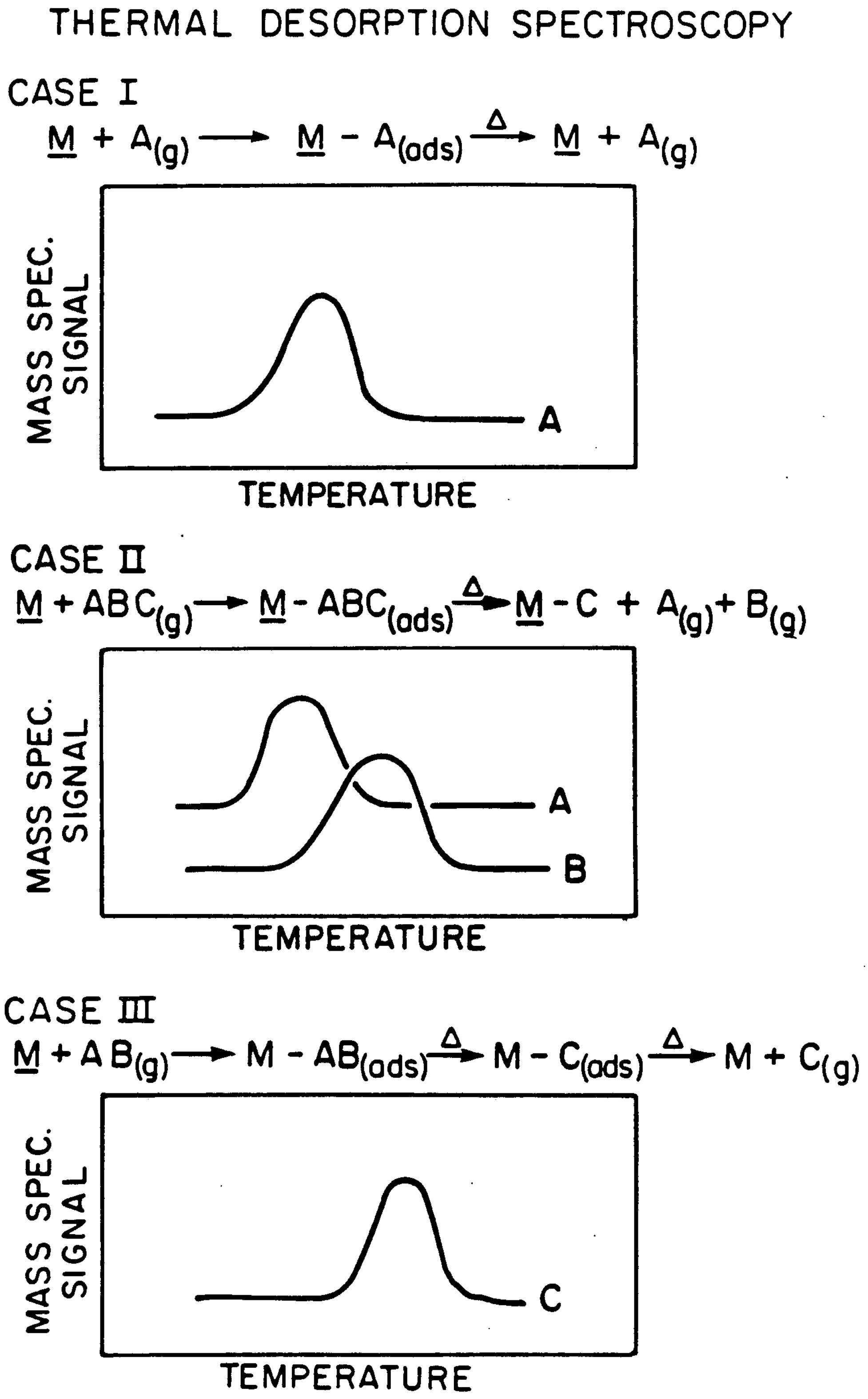

Figure 2.16: This figure shows three temperature programmed spectra.

as:

$$\frac{E}{RT_P^2} = \left(\frac{\nu_1}{\beta}\right) exp\left(\frac{-E}{RT_P}\right) \qquad n = 1 \tag{2.6}$$

$$= \left(\frac{2\sigma_P \nu_2}{\beta}\right) exp\left(\frac{-E}{RT_P}\right) \qquad n = 2 \tag{2.7}$$

$$= \left(\frac{\sigma_0 \nu_2}{\beta}\right) exp\left(\frac{-E}{RT_P}\right) \qquad n = 2$$

With σ_0 as the initial surface coverage and σ_P as the surface coverage at T = T$_P$. The first order rate equation can be simplified to:

$$\frac{E}{RT_P} = ln\left(\frac{\nu_1 T_P}{\beta}\right) - 3.64 \tag{2.8}$$

assuming $10^{13} > \nu_1/\beta > 10^8$ $({}^\circ K^{-1})$. Experimentally, in a first order trace the peak position is invariant with coverage and in a second order desorption process, the peak maximum decreases with increasing coverage. A decreasing peak maximum with increasing coverage may also signify a first order process where the activation energy is dependent on coverage. Redhead presents two methods to distinguish these cases. The simplest method is to plot log($\sigma_0 T_P^2$) against 1/T$_P$ with a second order fixed activation energy reaction yielding a straight line.

2.3.4 Work Function

Electrons are prevented from leaving a surface by a potential energy barrier commonly referred to as the work function ($\Delta\Phi$). The work function is defined as the potential energy difference between the Fermi level and the vacuum level. As the addition of adsorbates alter the surface composition this energy difference is decreased (increased) if the additives donate (withdraw) electron density from the surface. Changes in surface electron density affect the bonding of small molecules to the surface, product distributions, and yields in high pressure catalytic reactions.

Common methods for work function measurements include the Kelvin probe (vibrating capacitor), thermionic emission and photoelectron spectroscopy (UPS). With the Kelvin probe, two conductors are brought into contact so that their Fermi energies line up, causing an electrostatic potential gradient between the two metals. If the identity of one metal is known, the size of the potential difference allows the work function of the other metal to be determined. In UPS the energy at which the valence electrons are first detected is the work function. These absolute values of work functions, however, vary widely.

Only relative changes in work function were measured in this work. There are two very simple methods to accomplish this. In one technique, the onset of the secondary electron cascade is measured[25,26]. The crystal is biased -10 volts and in the auger mode the energy range from 0 - 25 eV is scanned. As the surface coverage of additives is increased the onset will change up to 2 - 3 eV. The second technique yields information on relative trends. An incident beam of electrons (from AES gun) produces a large flux of secondary electrons which can either be emitted from the surface or flow to ground through an ammeter (Figure 2.17). The current to ground varies linearly with the work function. Even though this measured current is caused by the electrons which cannot be emitted into vacuum, directly relating these values to changes in the work function is very difficult. It should be noted that all these work function measurements give an average value for the whole sample.

2.3.5 Low Energy Electron Diffraction

Low Energy Electron Diffraction (LEED) is a surface crystallographic technique used to determine the structure of clean solid surfaces and of monolayers of adsorbates, atomic and molecular. In particular LEED reveals the size and orientation of adsorbate unit cells, and with dynamical calculations (I-V analysis) LEED can

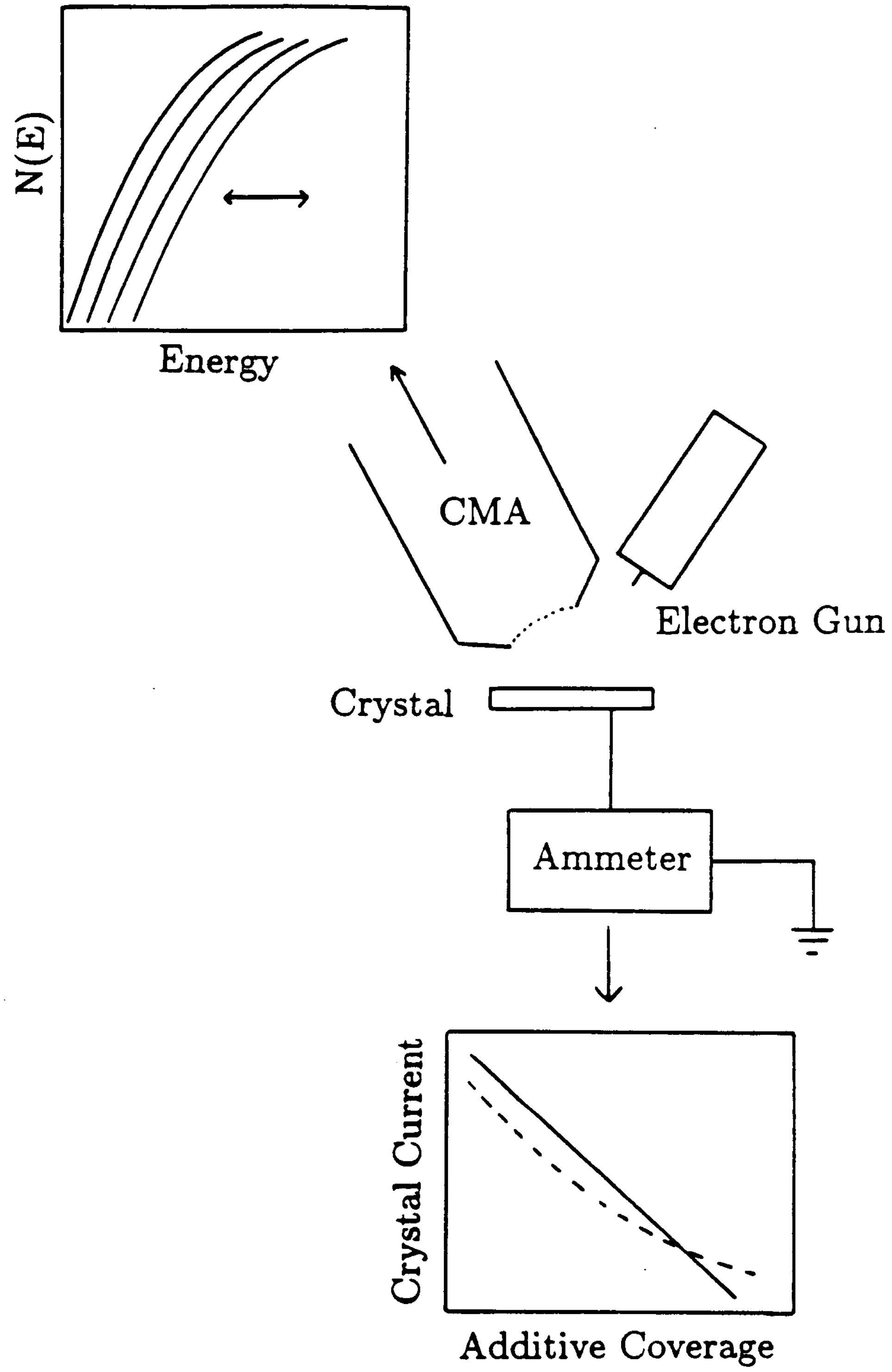

Figure 2.17: Schematic of the two work function measurement techniques used. In one method, the onset of the secondary electron cascade is measured, and in the second technique the current to ground is measured.

help determine bond lengths and adsorbate bonding sites [27,28].

In LEED, electrons with a narrow energy bandwidth diffract off single crystals and impinge on a phosphorescent screen, yielding a characteristic pattern of bright spots. These spots are due to the wave interferences from the electrons scattered by atom cores, which is expressed in the de Broglie equation $\lambda = h/mv$. From the Bragg diffraction law, we know if the primary wave strikes the surface with an incident angle φ_o, back-scattered waves occur in the directions φ which satisfy the condition

$$d(sin\varphi - sin\varphi_o) = n\lambda \tag{2.9}$$

where d is the lattice spacing and n is the integer denoting the order of diffraction. For normal incidence beams this equation can be simplified to

$$sin\varphi = \frac{1}{d_{hk}}\sqrt{\frac{150}{U}} \tag{2.10}$$

where U is the beam energy and d_{hk} (Å), the distance between parallel rows of scatterers in the [h,k] direction. Electron beams with energies of 15 - 400 eV and with de Broglie wavelengths of .5-4 Å are used in LEED to make the technique surface sensitive.

The sharpness and intensity of the spots is related to the degree of ordering, with less ordered systems producing fainter spots and higher background intensity. LEED is only sensitive ordering of domains larger than ~100Å^2.

Figure 2.18 shows a schematic representation of the experimental setup, with the elastically scattered electrons filtered by an RFA and accelerated onto the screen. Also shown is a typical LEED pattern photographed through the viewport. The LEED patterns photographed on the phosphor screen represent reciprocal space and must be converted to real space to obtain the structural information. The larger the unit cell, the closer the first diffraction maxima will be located to the surface normal. A detailed procedure is outlined in numerous publications[5,28].

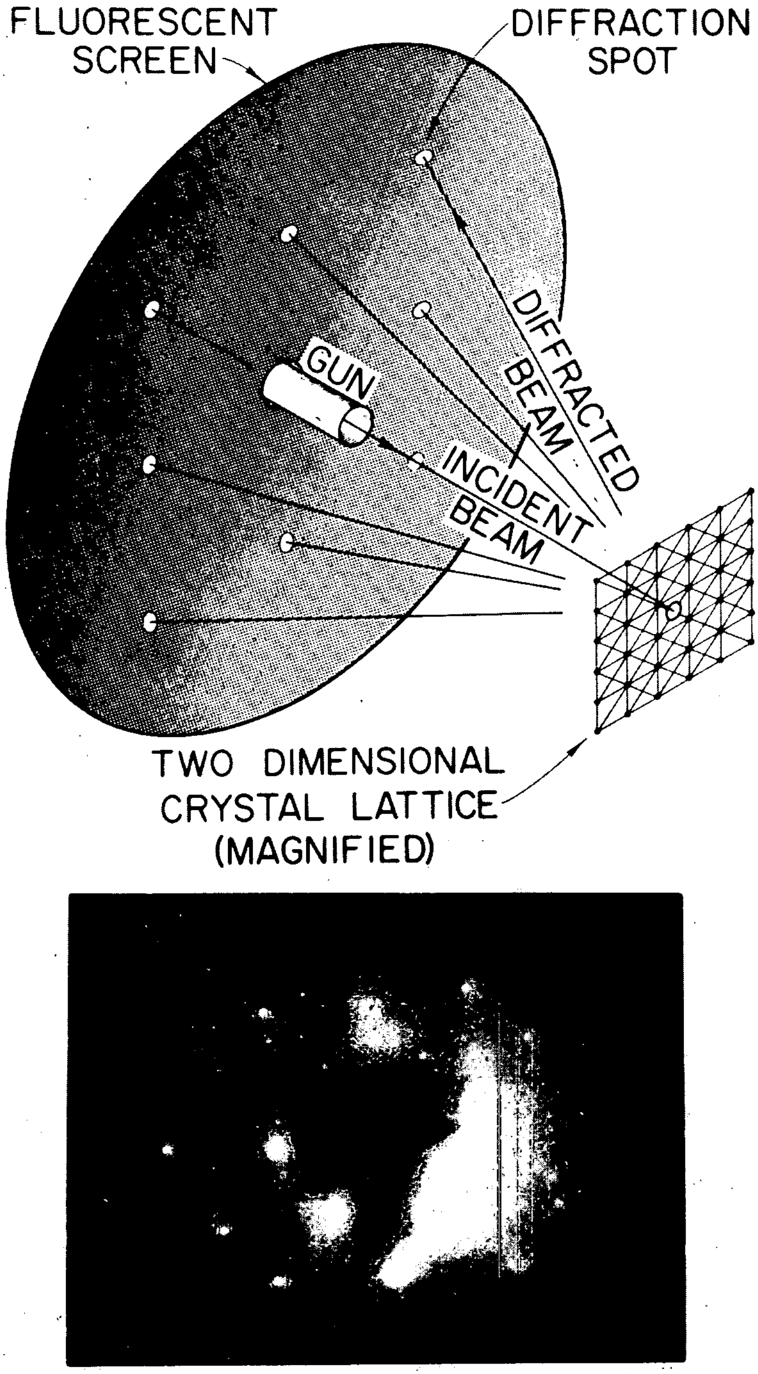

XBB 708-3583B

Figure 2.18: Experimental setup for LEED: A monoenergetic beam of electrons diffracts from the surface and is detected on the phosphor screen. The pattern is photographed through the viewport.

Sample	Source	Impurities	Cleaning Procedure
Pd	Materials Res. Corp. Lawrence Liv. Lab.	C, S	Oxygen 5×10^{-6} torr, 500° C Ar^+ Sputter, 500° C, Anneal
Au	Engelhard	C, S, Ca	Oxygen 5×10^{-6} torr, 450° C Ar^+ Sputter, 500° C
$LaRhO_3$ $LaFeO_3$ $LaCrO_3$ $LaMnO_3$ $LaCuO_3$	Dr. K. Seiber	C	Heat in 5×10^{-6} torr O_2

Table 2.2: Catalyst Samples, Source, Impurities and Cleaning Procedures

2.4 Experimental Procedure

2.4.1 Surface Preparation

All samples used were either single crystals, foils or powders. Palladium single crystals were spark erosion cut to a thin disk (~ 0.3 - 0.9 mm thick) from stock single crystal rods. Laue x-ray back diffraction was used to verify orientation (± .5°). The crystals were then polished to a mirror finish using standard metallurgical procedures. The samples were dipped in acid, water, acetone and ethanol prior to mounting on the manipulator and insertion into the UHV system. Figure 2.19 shows the three low miller index planes of palladium used in this research ((111), (100) & (110)).

Since slight changes in surface composition and structure markedly affect the surface chemistry, it was very important to clean the surface thoroughly before experiments. Table 2.2 summarizes the major contaminants and cleaning procedure for the palladium samples. In general, these cleaning procedures consisted of Ar^+ sputtering (1×10^{-4} torr Ar, 20 mA) and oxygen treatment (5×10^{-6}

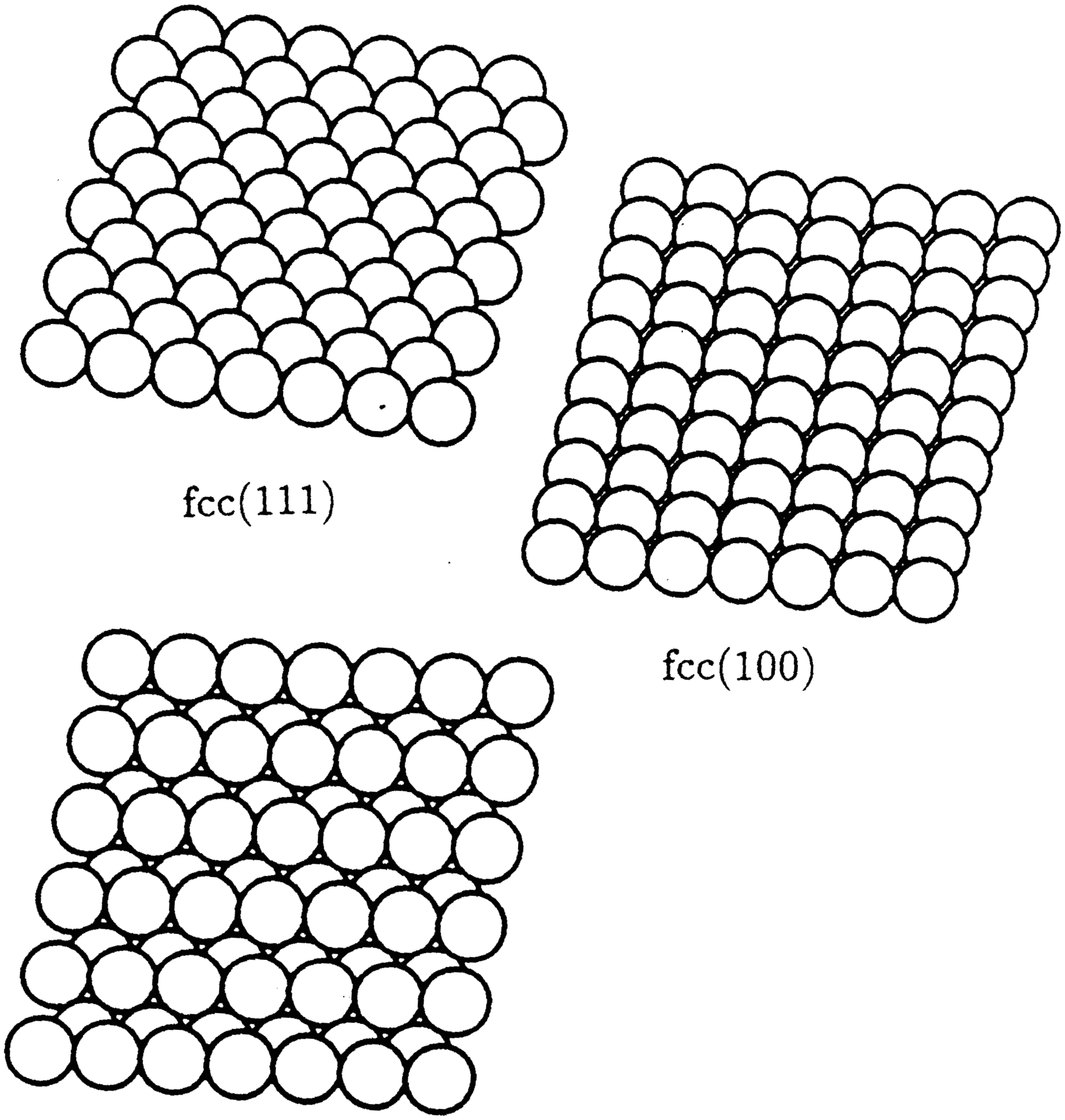

fcc(111)

fcc(100)

fcc(110)

Figure 2.19: The three Low Miller Index Planes of Palladium.

to 5×10^{-7} torr, 500-600°C). The most effective cleaning procedure was a combination of both treatments. For single crystals, the surface was heated at 600 - 700°C for 3 - 5 minutes until a sharp LEED pattern was visible, to anneal out the structural damage from sputtering. The extent of carbon contamination was the most difficult to determine since the carbon and a palladium auger peak (270 eV) overlap. However, in the presence of small amounts ($> 3\%$) of carbon, this peak broadened and the ratio of the three characteristic palladium auger peaks changed from the clean ratio of 1:2:10.

After cleaning, the surfaces were dosed with the desired concentration of additives. Coverages were determined by the equation:

$$\Theta_x = \frac{I_x/S_x}{\sum_{i=1}^{n} I_i/S_i} \tag{2.11}$$

where I is the intensity and S the sensitivity of the auger peaks. Sensitivity factors were obtained from the Phi Auger Manual [7] (Pd=.8, K=.8, Si=.35, P=.55, S=.8, Cl=1.05, Ti=.45, O=.5). The peaks measured were the most intense auger peaks for each element (Pd=330 eV, K=252 eV, Na=990 eV, Si=90 eV, P=120 eV, S=152 eV, Cl=181 eV, Ti=387 eV, O=512 eV). This method is accurate at low concentration ($<30\%$) and at higher concentrations if $\sum_{i=1}^{n} I_i/S_i$ is constant.

Potassium and sodium were dosed from a resistively heated SAES Getter[2] which consisted of a powdered mixture of potassium chromate or sodium chromate and a zirconium - 16% aluminum alloy getter enclosed in a tantalum dispenser. Phosphorus was deposited by dosing the surface with phosphine and heating to 450°C. Elemental silicon was deposited from silane, sulfur from hydrogen sulfide and chlorine from chlorine gas. A titanium doser was produced by wrapping 20 mil titanium wire around 20-30 mil tungsten wire and resistively heating the tungsten to white hot (> 1300°C). A tantalum shield was placed in front of the titanium source to inhibit dosing of the sample support wires and manipulator. To form

---

[2] SAES Getters SpA, Via Gallarate 215, I20151, Milano, Italy

the titania and silica oxide overlayers on the palladium, the treated surfaces were heated to 500°C in 5×10^{-6} torr of oxygen. Further oxidation was accomplished by heating the samples in 50 psi of oxygen to 500 - 600°C.

2.4.2 UHV Experiments

In the UHV experiments the sample was cleaned, dosed with the surface adatoms and characterized by Auger Electron Spectroscopy. The sample was then rotated to face the gas doser, exposed to the CO, H_2 or C_2H_2 for the desired time and pressure, and then rotated to face the mass spectrometer. The mass spectrometer was outfitted with a tantalum shield to reduce the signal from gases not desorbing from the crystal face. The crystal was heated at a linear rate ($\sim$ 25°/sec) and the desorbing fragments analyzed with the mass spectrometer.

2.4.3 High Pressure Experiments

In a typical reaction study, the $\sim$ 1 cm^2 catalyst sample is cleaned and characterized by AES, LEED and XPS. The manipulator is lowered and then rotated 45° to latch it into the high pressure cell. After the manipulator and cell are tightly sealed, by pressurizing the piston (500 psi N_2) and thereby activating the clamping mechanism, the differential pumping between the o-rings is started. At this point the cell is opened to the loop to complete the micro-batch reactor (total volume 150 cm^3). The unit is filled with the desired amount of reactant gases (up to 1800 psi) which are circulated by a positive displacement circulation pump. The sample is then resistively heated and the product yield and distribution monitored with a gas chromatograph. At reaction pressures over 20 atm, sample heating becomes difficult due to heat conduction by the gases. Depending on the sample and reactant gases 80 - 90 amps maybe necessary to heat the 1 cm^2 sample to 400°C. After the reaction, the unit is evacuated with a mechanical pump and oil-diffusion pump to $\sim 1 \times 10^{-6}$ torr ($\sim$ 30 min.). The differential pumping is stopped and the cell is

Chemical	**Supplier**	**Purity**	**Impurities**
H_2	Matheson	99.99	
CO	Matheson	99.95	CH_4,C_2
N_2	LBL	99.99	Ar, H_2O
O_2	LBL	99.99	CO
Ar	LBL	99.958	CH_4, CO_2
C_2H_2	Matheson	99.6	acetone
K	Saes Getter		
Na	Saes Getter		
SiH_4	Matheson	99.99	
PH_3	Matheson	99.999	
H_2S	Matheson	99.5	
Cl_2	Matheson	99.96	

Table 2.3: Supplier, Purity and Impurities of Chemicals used.

isolated from the rest of the loop. After releasing the piston pressure and rotating the manipulator 45°, the manipulator is raised to align the sample with the UHV surface analytical tools and fully characterized. The chamber pressure increased to 5×10^{-7} torr when opening the loop, but then slowly return to $\sim 5 \times 10^{-9}$ torr after 2 - 3 hours. During periods when many reactions are run, the chamber base pressure increases to 2×10^{-8} torr.

Reaction rates are determined with the following formula:

$$Rate(\frac{molecules}{site \cdot sec}) = \frac{(\# \ GC \ Counts)(8 \times 10^{12} \frac{molec.}{count})}{(\# \ Carbons)(3 \times 10^{15} \frac{sites}{cm^2})(area \ cm^2)(time)} \tag{2.12}$$

2.5 Chemicals

In table 2.3 are listed the materials and chemicals used in these experiments, their source , impurities and special purification steps.

H_2 and CO were passed through a liquid nitrogen cooled molecular sieve trap to remove the hydrocarbons and metal carbonyls (in CO). C_2H_2 was passed through a dry ice/acetone bath to remove the acetone stabilizer. For the UHV experiments, C_2H_2 was also purified using freeze - pump - thaw cycles.

References

[1] D. W. Blakely, E. I. Kozak, B. A. Sexton, and G. A. Somorjai. *J. Vac. Sci. Tech.* **13** (1976) 1091.

[2] A. L. Cabrera, N. D. Spencer, E. Kozak, P. W. Davies, and G. A. Somorjai. *Rev. Sci. Instrum.* **53** (1982) 1889.

[3] X. Youchang, B. M. Naasz, and G. A. Somorjai. *Appl. Catal.* **27** (1986) 233.

[4] O. Ganschow and P. Steffens. *J. Vac. Sci. Tech.* **21:3** (1982) 999.

[5] G. Ertl and J. Kuppers. *Low Energy Electrons and Surface Chemistry.* Verlag Chemie, 1974.

[6] W. Banbynek. *Rev. Mod. Phys.* **44** (1972) 716.

[7] P. N. Palmberg, G. E. Riach, R. E. Weber, and N. C. MacDonald. *Handbook of Auger Electron Spectroscopy.* Physical Electronics Ind., 1972.

[8] S. Mroczkowski and D. Lichtman. *Surf. Sci.* **131** (1983) 159.

[9] T. E. Gallon. *Surf. Sci.* **17** (1969) 486.

[10] A. Einstein. *Ann. Phys.* **17** (1905) 132.

[11] D. Briggs. *Handbook of X-ray and Ultraviolet Photoelectron Spectroscopy.* Heydon and Son, 1977.

[12] R. Joyner. *Surf. Sci.* **63** (1977) 291.

[13] D. A. Shirley. *Topics in Applied Physics: Photoemission in Solids I*, page 165. Springer - Verlag, Berlin, 1978.

[14] J.C. Fuggle, E. Unbach, D. Menzel, K. Wandelt, and C. R. Brundle. *Solid State Comm.* **27** (1978) 65.

[15] J. H. Lunsford. *Spectroscopy in Heterogen. Catalysis*, pages 267–321 (Chpt. 8). Academic Press, 1979.

[16] F. Delannay. *Charat. of Heterogen. Catalysts.* Marcel Dekker, 1984.

[17] C. D. Wagner. *J. Elect. Spectros & Related Phenom.* **32** (1983) 99.

[18] D. W. Turner, C. Baker, A. D. Baker, and C. R. Brundle. *Molecular Photoelectron Spectroscopy.* Interscience, 1970.

[19] D. Briggs and M. P. Seah. *Practical Surface Analysis by Auger and X-ray Photoelectron Spectroscopy.* Wiley, 1983.

[20] C. M. Chan, R. Aris, and W. H. Weinberg. *Applic. Surf. Sci.* **1** (1978) 360.

[21] D. A. King. *Surf. Sci.* **47** (1975) 403.

[22] J. L. Falconer and R. J. Madix. *J. Catalysis* **48** (1977) 262.

[23] E. Habenschaden and J. Kuppers. *Surf. Sci.* **138** (1984) L147.

[24] P. A. Redhead. *Vacuum* **12** (1962) 203.

[25] R. A. Barker, T. E. Felter, S. Semancik, and P. J. Estrup. *J. Vac. Sci. Tech.* **17(3)** (1980) 755.

[26] A. G. Knapp. *Surf. Sci.* **34** (1973) 289.

[27] M. A. VanHove and S. Y. Tong. *Surface Crystallography by LEED.* Springer - Verlag, 1979.

[28] G. A. Somorjai. *Chemistry in Two Dimensions.* Cornell University Press, Ithaca, New York, 1981.

Chapter 3

PALLADIUM WITH OXIDE OVERLAYERS

3.1 Introduction

An increasing amount of evidence in recent years has proven that oxide supports, which have historically been believed only to disperse and increase the surface/volume ratio of metal catalysts, are actively involved in the catalytic process. Rather than merely inhibiting metal sintering, supports bond with metal atoms thereby forming mixed metal - oxide sites exhibiting catalytic activity which neither the metal nor oxide alone show. Numerous studies have probed this metal - support interaction [1,2].

Parallel studies have been undertaken to develop catalysts active in the synthesis gas ($CO + H_2$) reaction. Of particular interest is the formation of the simplest oxygenate, methanol. Using the Mobil ZSM-5 zeolite catalyst, methanol can be readily converted into gasoline-length hydrocarbons (C_5 - C_{11}). Commercially, methanol is formed from carbon monoxide and hydrogen on a mixed zinc - copper - chromium oxide catalyst [3].

Poutsma *et al.* reported that palladium supported on oxides is also active in methanol formation from CO and H_2 under the correct thermodynamic conditions

[4]. This discovery was quite surprising since previous groups had reported only methanation activity for palladium and the reported rates were orders of magnitude lower than on nickel, one of the best methanation catalysts. Numerous groups have studied supported palladium systems and their results are summarized in Tables 3.1 and 3.2. In general they found that the rate and yield of methane and methanol was critically dependent on the support. This suggests a mixed oxide - metal site as the catalytic reaction site.

Numerous investigators have seen an enhancement of the activity of Group VIII metals in the CO hydrogenation reaction when supported on titania rather than on silica or alumina. Evidence suggests that this rate increase is due to the presence of small islands of the oxide which have migrated onto the metal from the support. Recent work has shown comparable hydrocarbon formation rates with TiO_2 promoted Pt-Black, Pd/SiO_2 and Rh/SiO_2 as with the titania-supported Pt, Pd and Rh.

The palladium - oxide system is excellent for studying not only the mechanism of methane and methanol formation, but also the role of oxides in catalytic processes. Palladium powders and foils (this study) show no activity in the CO hydrogenation reaction. Only in the presence of an oxide overlayer are methane or methanol formed. Palladium also does not dissociatively adsorb CO, and the formation of methanol seems to be the result of the hydrogenation of molecular CO.

Instead of using palladium impregnated on supports as all the previous groups have done, we deposited the oxide (titania or silica) onto a palladium foil. With this configuration the surface is more homogeneous and easier to characterize. Several other groups have studied the effect of oxides on Pt, Ni and Rh foils and single crystals. For example, Demmin *et al.* found a 10 kcal/mol decrease in the activation energy for the CO hydrogenation reaction and an enhancement in rate on titania-covered platinum [5]. Chung *et al.* (for Ni(111)) found a maximum in the methanation rate at a titania coverage of 7.5% of a monolayer [6], and Levin *et al.* found a minimum in the activation energy and a maximum in the methanation rate at a titania coverage of $\Theta_{Ti} = .20$ [7]. This approach can be useful in studying the interaction between metals and oxides.

The research goals addressed in this study are:

- To Characterize the growth and properties of oxide overlayers (titania,silica) on palladium. (*Three-dimensional for Ti*)
- To activate palladium foils for methanol and methane formation. (*Maximum methane at Θ_{Ti} = .20, Methanol on oxidized titania surface only*)
- To determine the active sites in methanol and methane formation and the role of the oxides in the CO hydrogenation reaction. (*Mixed Pd-TiO_x,SiO_x site for methane, palladium oxide for methanol*)

3.2 Results

In order to characterize and understand the interaction between the oxides (silica, titania) and palladium, a wide variety of techniques were used. In this section, the catalytic activity of mixed palladium metal - oxide systems will be presented, followed by the results of experiments which help us understand the growth mechanism of oxide overlayers (AES, $\Delta\phi$), binding sites (CO chemisorption) and surface oxidation states (XPS).

3.2.1 Auger Characterization

Figure 3.1 shows the plot of the auger intensities of the palladium (330 eV) and titanium (360 eV) peaks as a function of titanium deposition time. The palladium

YEAR	SUPPORT	COMMENTS-CONCLUSIONS	AUTHORS
1925	unsupported	Ranked last in Group VIII in methanation activity	Fischer [8]
1937	black	In a survey of noble metal catalysts found Pd inactive (280-400°C, 100 atm)	Kratel [9]
1965	ThO_2/ kieselguhr	Low Activity, Traces of methane (250-300°C, 30-50 atm)	Eidus [10]
1967		$\geq$98% Methane (500°C, 21 atm $CO:H_2$ 1:3)	Schulz [11]
1974	Al_2O_3	Modest Methanation Rate 650°, 1 atm	Kertamus [12]
1975	η-Al_2O_3	Ru>Fe>Ni>Co>Rh>Pd>Pt>Ir (275°C, 1 atm)	Vannice [13]
1975	η-Al_2O_3, SiO2, black	Sizeable support effect η-Al_2O_3 > SiO_2 > black (80:2:1)	Vannice [14]
1978	SiO_2	High selectivity for methanol Used $PdCl_2$, (260-350°C, 150-15000 psi)	Poutsma [4]
1978	SiO_2	Studied Mechanism and role of C	Rabo [15]
1979	Al_2O_3	Only a factor of 3 less active than Ni Activity of alumina depend. on pretreatment	Vannice [16]
1980	variety	Support dependent	Ichikawa [17]
1981		Pd ions important for methane and methanol	Poels [18]
1981	SiO_2, Al_2O_3 Na-Y zeolite	M_2PdCl_4, M=alkali High selectivity	Kikuzoma [19]

Table 3.1: Previous studies on Palladium in the CO Hydrogenation Reaction.

YEAR	SUPPORT	COMMENTS-CONCLUSIONS	AUTHORS
1981	SiO_2 HY & Na-Y zeolite	Crystallite size important Support Effects	Fajula [20]
1983	SiO_2 w/ La, Mg	Pd ions active for MeOH	Driessen [21]
1983	Al_2O_3	Mechanism, kinetic studies CO dissociation is rate limiting step	Mori [22]
1983	TiO_2, SiO_2	No SMSI, interface active site	Bracey [23]
1984	SiO_2, La_2O_3	Support migrates onto metal Si no interaction, La_2O_3 interaction	Fleisch [24]
1984	ZnO	Metal - support interaction	Wehner [25]
1984	Al_2O_3, TiO_2	Oxide migration found using electron microscopy	Baker [26]
1984	SiO_2, La_2O_3	Used Laser Raman Spectros. to study Pd-oxide interface	Chan [27]
1984	SiO_2, La_2O_3	CO (suppressed) and H_2 (no effect) chemisorption studies	Hicks [28]
1984	La_2O_3 , ZrO_2, ZnO, MgO, TiO_2, Al_2O_3, SiO_2, black	Studied specific activity for methanol and methane activity	Hicks [29]
1985	Pr_6O_{11}, CeO_2, La_2O_3,Nd_2O_3	Prep. and characterization of Pd on rare earth oxides	Sudhaker [30]
1985	SiO_2, La_2O_3	Methanol mechanism independ. of support, methane mechanism support depend.	Hicks [31]
1986	SiO_2 w/ Li,Na,K,Rb,Cs	Studied CO & H_2 chemisorption	Rieck [32]

Table 3.2: Continuation of previous studies on Palladium catalysts in the CO Hydrogenation reaction.

curve shows an exponential decrease in intensity and the titanium peak shows a logarithmic increase, with neither curve showing sharp breaks in the slope. At a deposition time of approximately 18 minutes, the palladium peak decreased by a factor of two and the $\Theta_{Ti} = .4$

Annealing the titania-decorated foil to 650°C caused a sharp decrease in the Ti/Pd ratio. No titanium containing species were detected desorbing from the surface by the mass spectrometer, so the titania had to diffuse into the bulk (Figure 3.2). At this temperature, oxygen did desorb from the surface, indicating thermal decomposition of the titania. Continued annealing at this temperature resulted in an equilibrium ratio of Ti/Pd = .2 ($\Theta_{Ti} = .11$). Above 850°C the remaining titanium diffused into the bulk. Since it was very difficult to determine surface titania coverage after annealing, all reactions and UHV studies were performed on surfaces which were not heated above 550°C.

AES was also used to determine the extent of CO decomposition during reactions. There was no carbon buildup on an undecorated palladium foil after a CO + H_2 reaction. When either titania or silica was deposited onto the palladium, there was extensive carbon buildup during the reaction. This implies that the presence of these oxide overlayers provide binding sites where CO dissociates.

3.2.2 CO Hydrogenation Activity

To produce either methane or methanol in the CO + H_2 reaction on palladium, the metal had to be partially covered by an oxide overlayer. Figure 3.3 shows the relative amounts of methane formed on various palladium foils. All reactions were run at 300°C, using a 300 psi total pressure of a 2:1 - H_2:CO mixture. On the clean palladium foil and the oxidized foil (50 psi oxygen, 500°C (to oxidize the palladium)) negligible amounts of methane and no methanol formed. However, in the presence of silica or titania, methane formation increased 20-fold and 30-fold

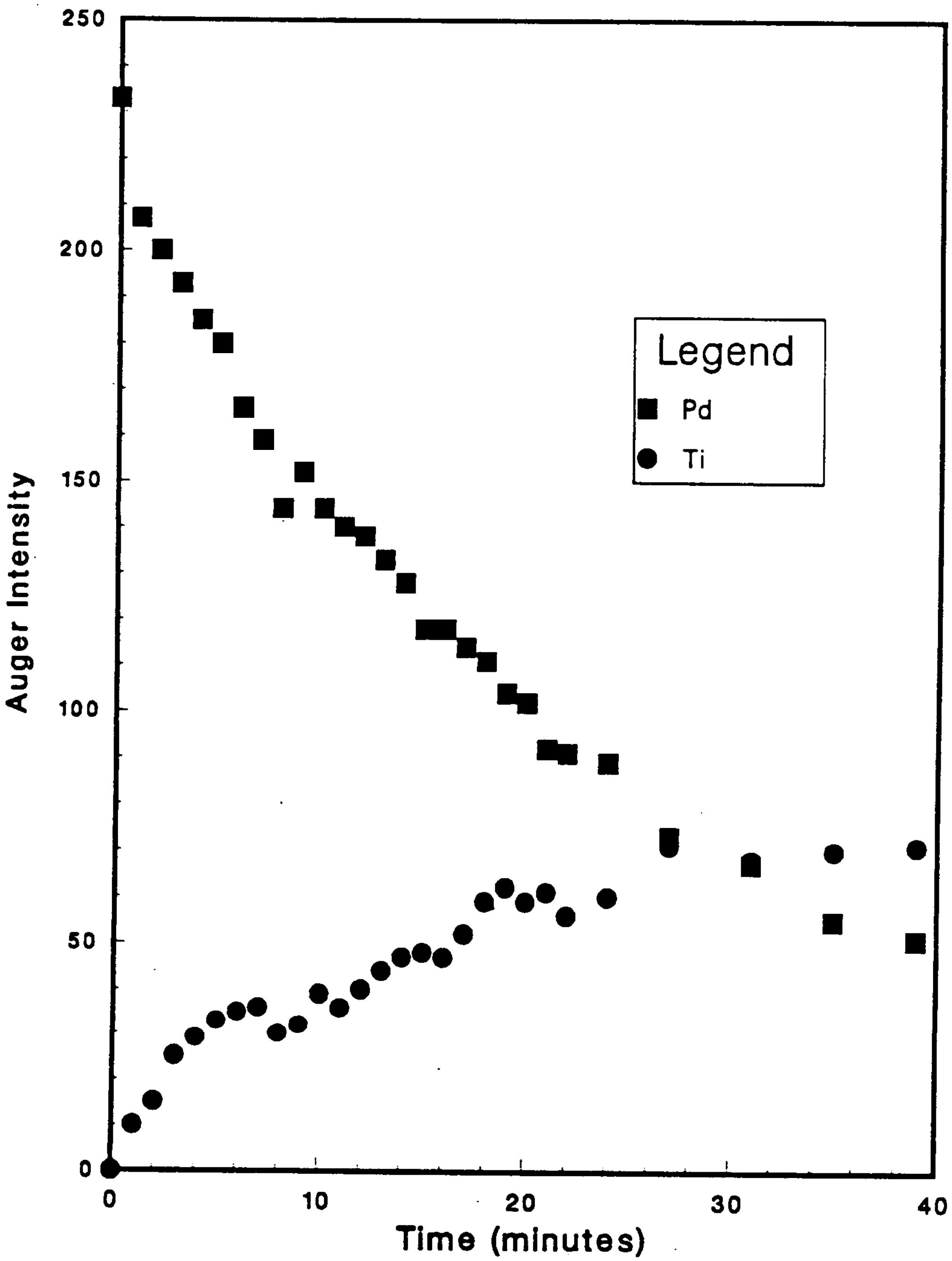

Figure 3.1: Auger intensities of the palladium (330 eV) and titanium (360 eV) peaks as a function of titanium deposition time. No breaks in the slope of either curve are evident.

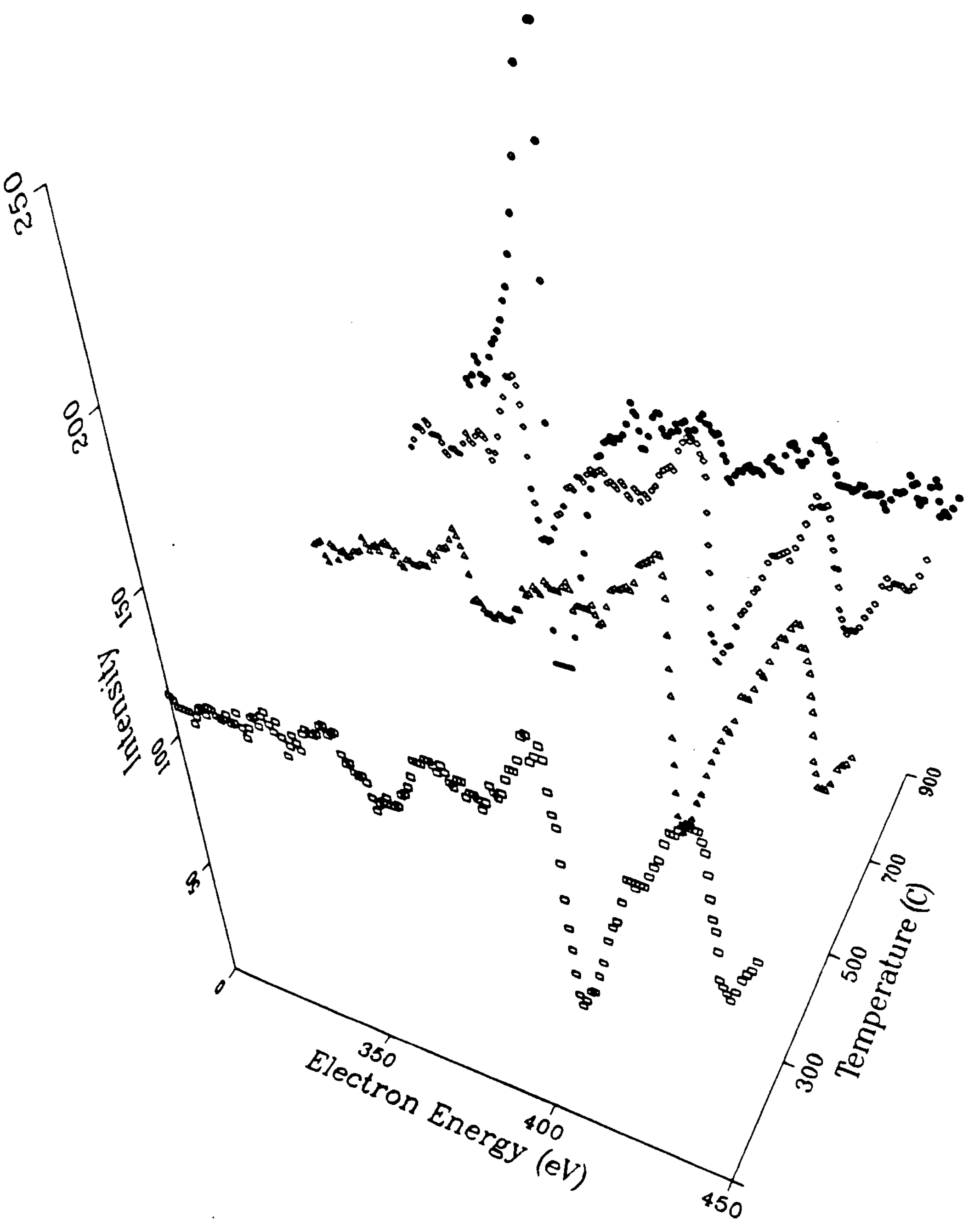

Figure 3.2: The surface concentration of titania as a function of temperature. At approx. 650°C, Ti starts to diffuse rapidly into the bulk and at approximately 900°C all the titania has disappeared into the bulk.

respectively. Annealing the sample to 650°C to diffuse the titania into the near surface region and induce Pd-Ti-O compound formation decreased the amount of methane formed by a factor of seven. To obtain the highest methane production rate, the oxide overlayers should be on the palladium surface.

None of the surfaces prepared in UHV ($< 5 \times 10^{-6}$ torr O_2)[1] showed activity for methanol formation. If the titania-decorated surface was pretreated in 50 psi of oxygen at 500 - 600°C before the reaction, methanol was detected but only during the first few minutes of the reaction (Figure 3.4). A second GC sample after 25 minutes showed no further increase in the amount of methanol. Conversely, over the three hour reaction on this surface, there was no decrease in the methanol in the reaction loop, implying that methanol did not decompose. Neither of the other two heavily oxidized surfaces, clean or silica showed any trace of methanol formation. In Figure 3.5 the rate of methane formation is plotted as a function of titania coverage. The methane formation rate is very dependent on titania coverage, showing a maximum at $\Theta_{Ti} = .18$. At higher titania coverages the rate decreases until methane formation ceases at titania coverages greater than $\Theta_{Ti} = .35$.

3.2.3 CO Chemisorption

CO dosed onto a clean palladium foil at room temperature desorbs at 210°C. At saturation CO coverages (1×10^{-7} torr, 50 sec) a low temperature shoulder at 110°C forms. In the presence of titania or silica overlayers, the shape and intensity of the CO desorption peak changes (Figure 3.6). For both doped surfaces the oxide is associated with a poorly resolved shoulder at about 300°C on the high temperature side of the CO maximum. This desorption peak remains even after repeated (8 - 10) CO TPD indicating a stable site.

---

[1] Background water vapor in the chamber oxidized the titania and silica. After UHV oxygen treatment, both silicon and titanium were completely oxidized.

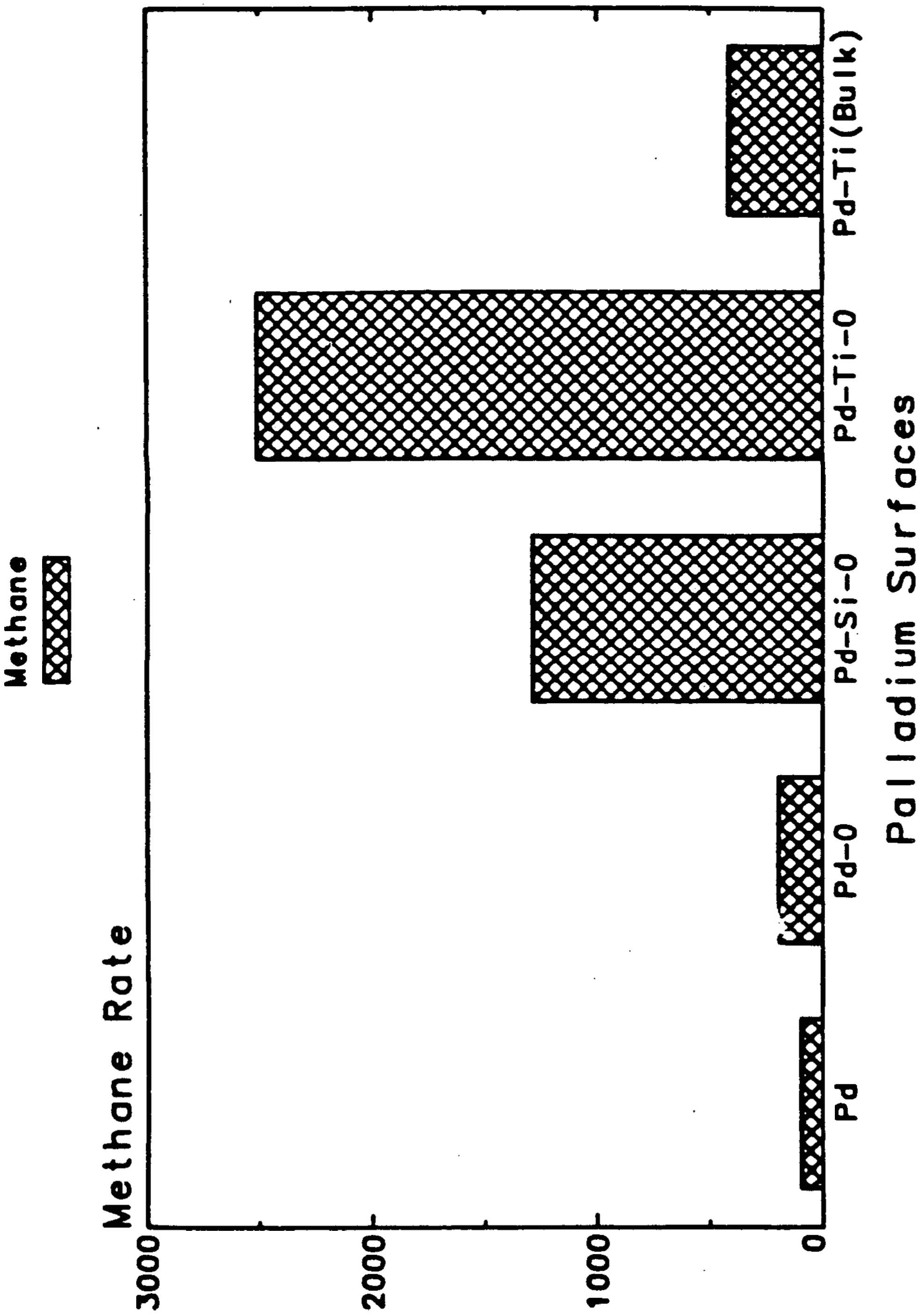

Figure 3.3: The relative amount of methane formed on the oxide-covered palladium foils in the CO hydrogenation reaction show that the titania-decorated surface is more active than the silica-decorated surface or a titania-covered surface which has been annealed. Clean and oxidized palladium form negligible amounts of methane.

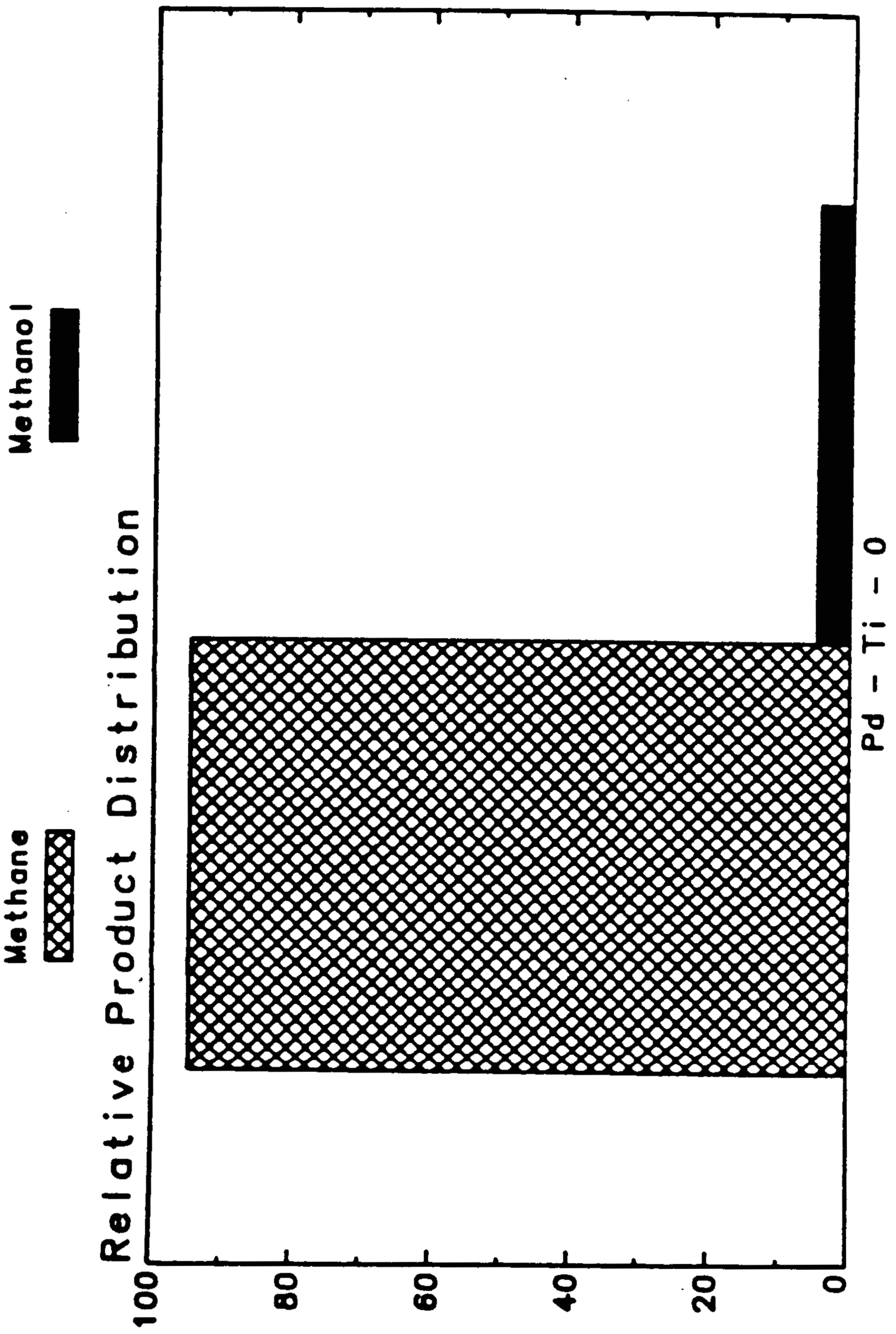

Figure 3.4: The relative amount of methanol formed on a heavily oxidized titania decorated palladium foil. This is the only surface from which methanol was detected.

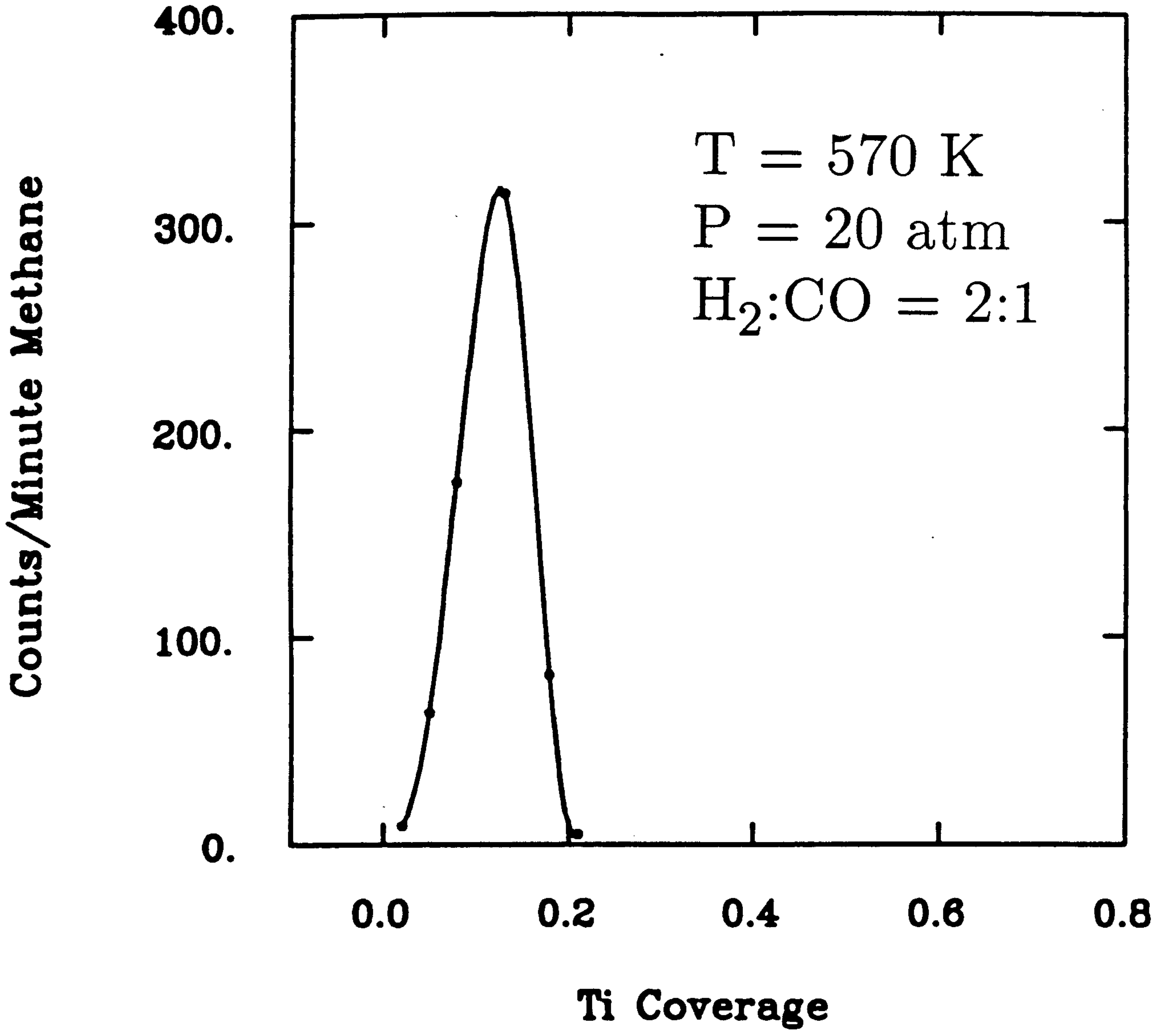

Figure 3.5: The rate of methane formation as a function of titania coverage is plotted here. At a titania coverage of Θ_{Ti}=.18, there is maximum in the rate.

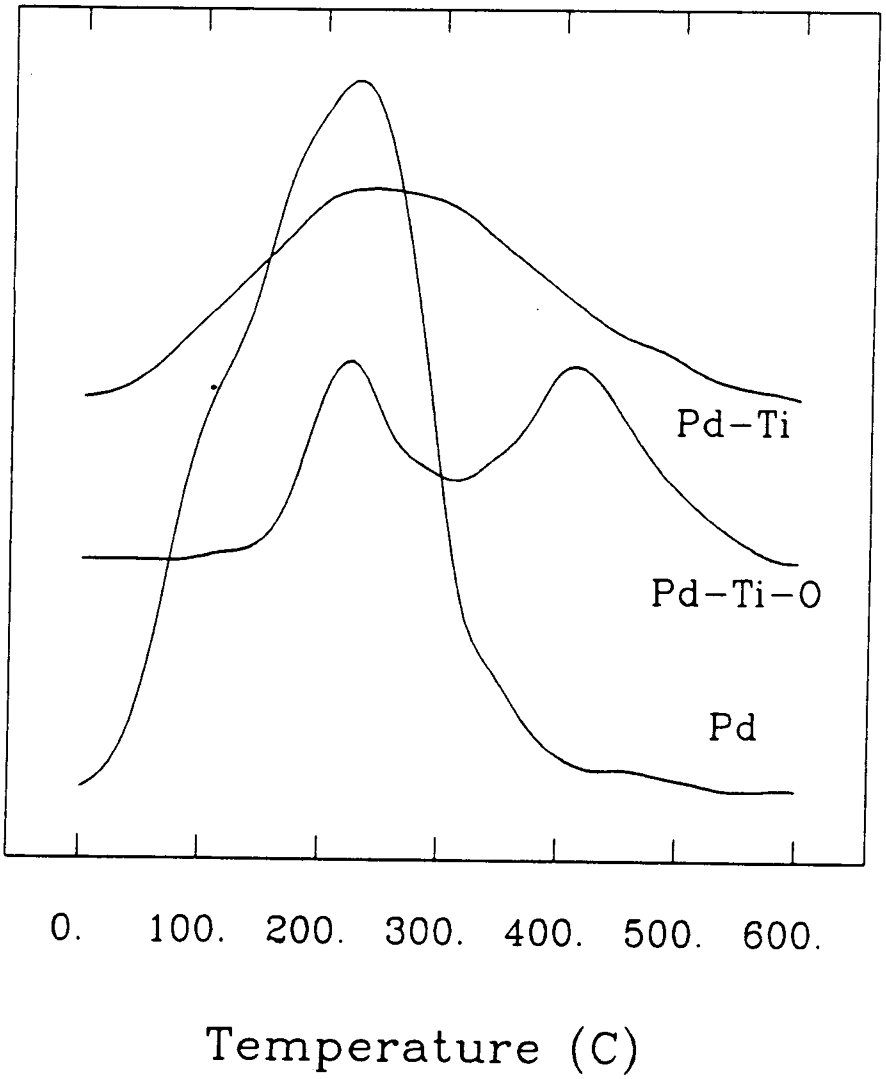

Figure 3.6: The addition of silica or titania onto palladium produces a new CO binding site as seen by the high temperature shoulder on the 200°C desorption peak of the clean surface. High pressure oxidation produces another high temperature (300°C) desorption state for CO.

After exposing the sample to high oxygen pressures (50 psi oxygen, 500 - 600°C) a new high temperature CO desorption maximum at 410°C was detected. On the clean and silica-doped foil, this CO peak is only detected for the first TPD, and for all subsequent CO TPD the trace obtained is similar to the UHV pretreated surface. Reoxidation at high pressures will again yield the high temperature binding site. On the titania-decorated surface, this high temperature site is stabilized relative to the other surfaces. This peak slowly diminishes in intensity after consecutive CO TPD and after 7 - 10 TPD resembles the UHV pretreated surface (Figure 3.7). The titania stabilizes the high temperature CO binding site relative to the clean or silica-covered surface. The titania-covered surface is also the only surface on which methanol forms.

Figure 3.8 shows the amount of CO that adsorbs on the palladium surface as a function of titania coverage. There is a sharp decrease in chemisorbed CO at low titania coverages and at a titania coverage of $\Theta_{Ti} = .6$, there is no further decrease in CO that bonds to the surface. CO TPD from a surface covered with multilayers of titania (no palladium peaks detected by AES) showed the same residual amount of CO desorbing as a surface with $\Theta_{Ti} \sim .6$. This residual CO is from the supports and back of the crystal, which was not dosed with TiO_x in the TPD experiments.

3.2.4 XPS Characterization

An extensive series of XPS studies were undertaken to understand the electronic interactions between the oxides and palladium. These include spectra before and after the various pretreatments and before and after reactions.

For all of the surfaces that formed methane, palladium was found to be in the metallic state. Figure 3.9 shows the palladium 3d peaks of a clean foil, of a surface freshly doped with titania and a surface heated to 400°C in 5×10^{-6} torr

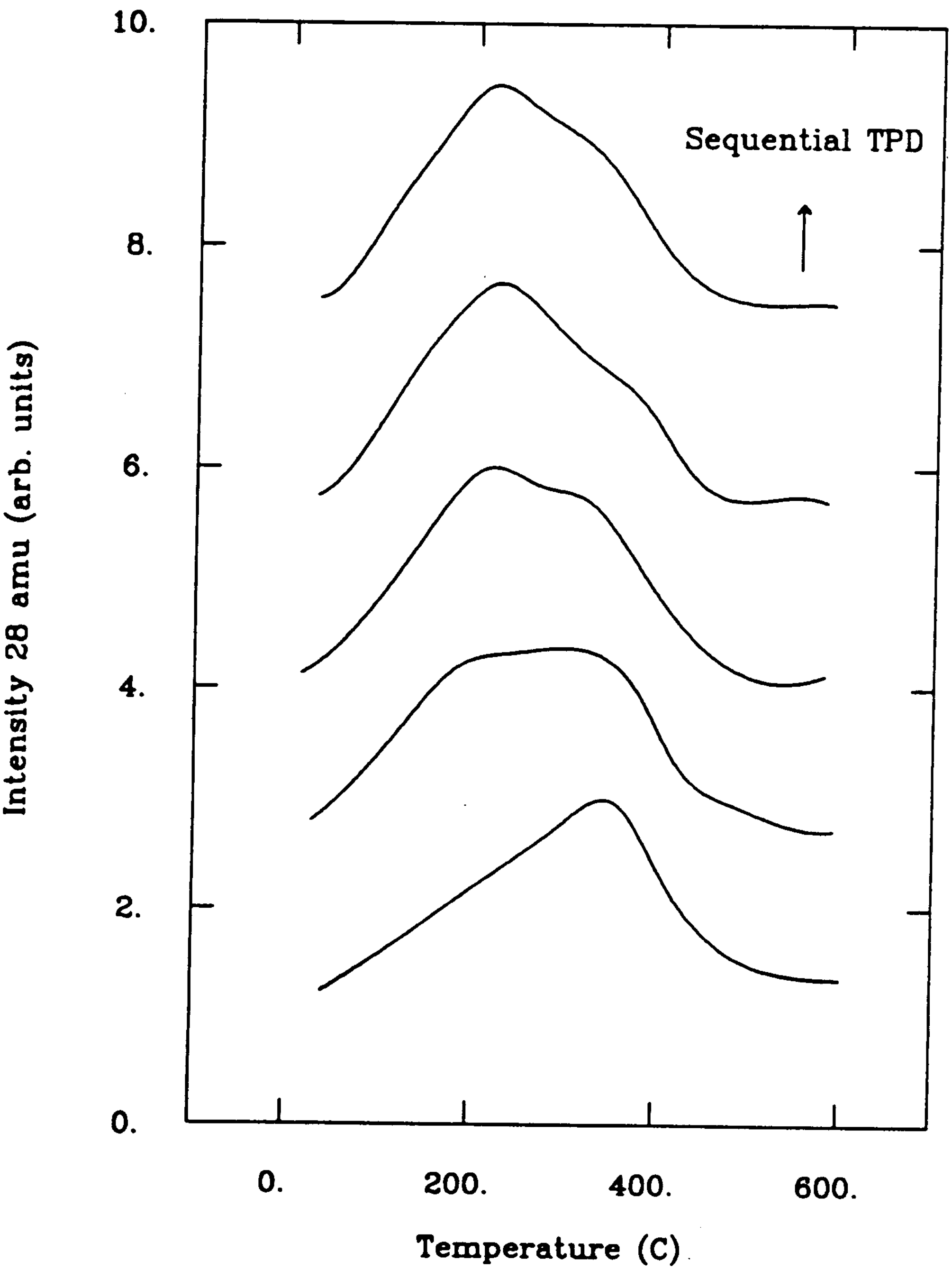

Figure 3.7: Only the presence of titania stabilizes the high temperature CO desorption state induced by oxidation. This figure shows the decrease in intensity of the peak in the presence of titania after sequential TPD. On the clean and silica-decorated surfaces, this site disappears after the first TPD.

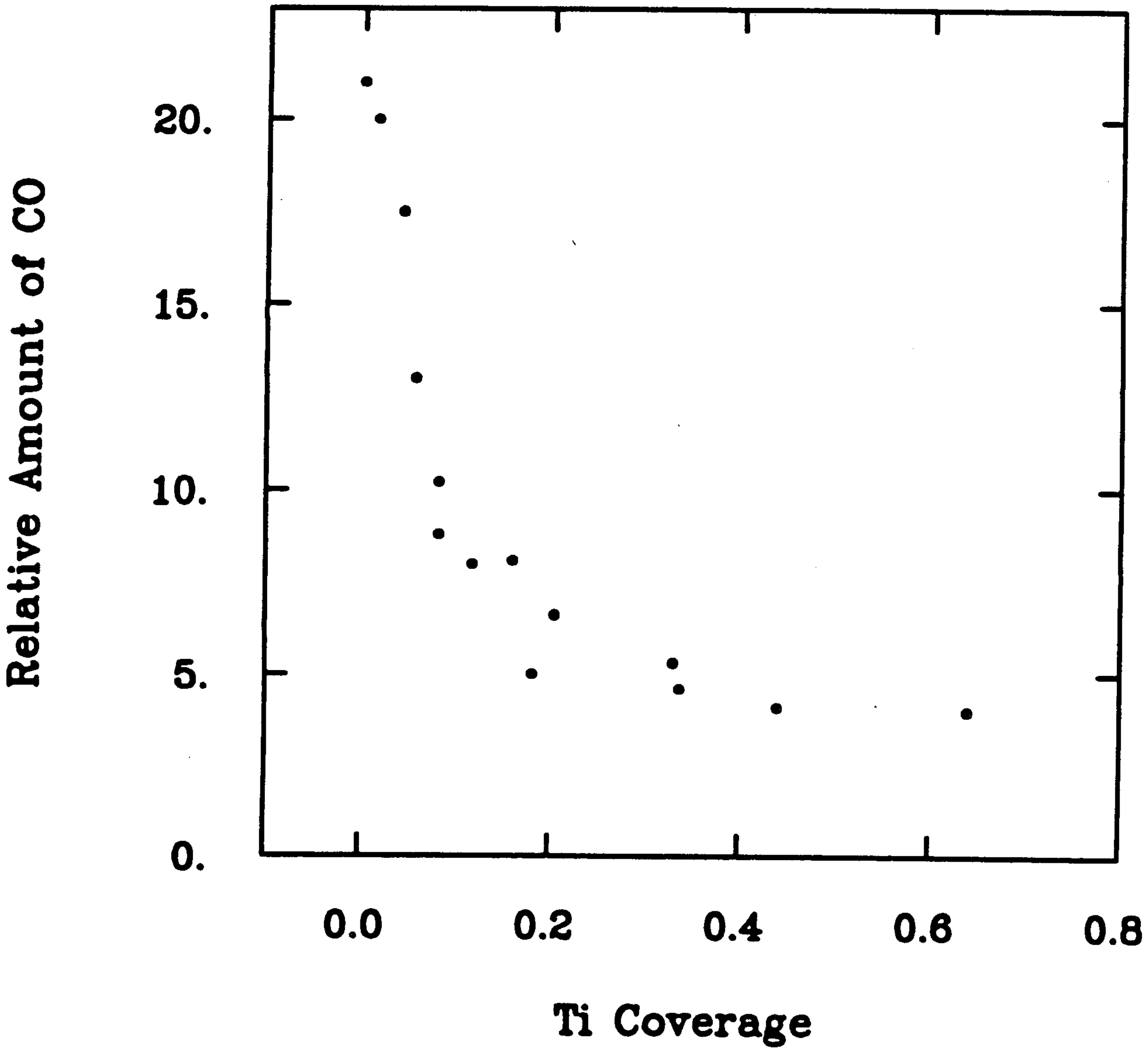

Figure 3.8: This figure shows the relative amount of CO desorbing from the surface as a function of titania coverage. Low titania coverages greatly suppress CO chemisorption.

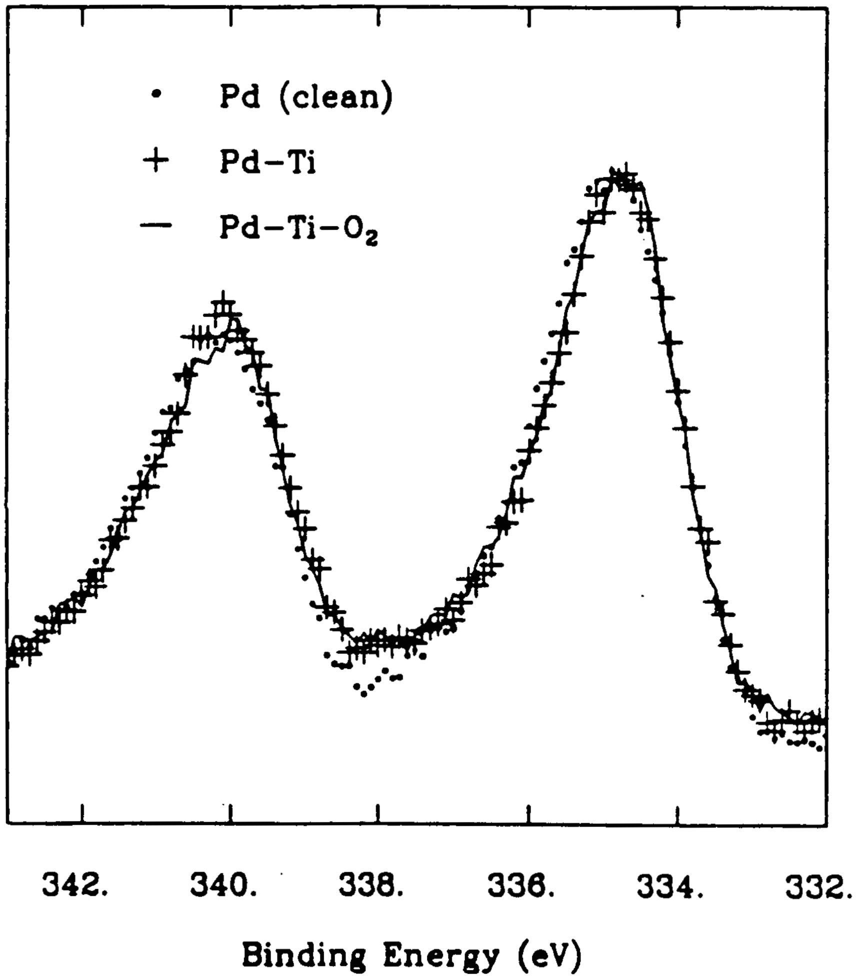

Figure 3.9: The XPS spectra of the palladium 3d peaks after titania deposition and UHV oxidation and heating are shown here. Under all conditions, the Pd remains in the metallic state.

oxygen. All three spectra are superimposable. For all heating/oxygen treatments attempted on this system there was no change in the shape or position of the palladium peaks. Similar results for the palladium were obtained with the silica-doped surface.

The titanium was in the +4 oxidation state under all pretreatment conditions and was also in the +4 state after all reactions. This does not preclude the possibility of the presence of Ti^{+3} species under reaction conditions which reoxidize to the +4 state during the high pressure cell evacuation. However, UHV hydrogen treatments did not reduce the titania. Ti^{+3} could be formed only when large Ti dosings (> 5 min) were done. In this case, metallic titanium deposited from the titanium doser, was covered by the second and third layers of titanium before it was completely oxidized. Even after these large doses the titanium oxidized to the +4 state within 20 minutes. After high pressure oxidations only Ti^{+4} was detected.

Silicon XPS showed two forms of silicon on the surface after dosing: elemental Si (~98.5 eV) and SiO_2 (~103 eV). Facile oxidation of the silane by the background gases formed some SiO_2 without oxygen treatments. After both UHV and high pressure oxidation, only the SiO_2 was detected. This oxide peak was also detected after reactions. The low ionization cross section made it difficult to determine the exact type of SiO_2 present on the palladium surface (Figure 3.10).

Changes in the XPS peak of oxygen are difficult to distinguish since it overlaps with the Pd 3p peak. Both the clean and titanium-doped surfaces showed an oxygen peak characteristic of a metal oxide, lower binding energy shoulder in Figure 3.11. The peak for OH groups falls underneath the palladium. The SiO_2 decorated surface shows a sharp peak which is a combination of SiO_2 and the Pd 3p peak. After a high pressure oxidation (50 psi oxygen, 500°C) the clean and titania covered surface show oxygen peaks corresponding to metal oxides and also a small shoulder attributable to OH groups (Figure 3.12). The silicon surface shows formation of SiO_2 and also OH groups but no indication of oxygen from a palladium oxide.

As mentioned in the CO hydrogenation section, methanol formed only on the heavily oxidized titania-decorated palladium foil. Figure 3.13 shows the Pd 3d peaks on the clean, silica- and titania-covered palladium foil after 50 psi oxidation. All three surfaces showed formation of the palladium oxide (+2). The temperature during the oxidation determined the extent of Pd^{+0} remaining. In general, for a

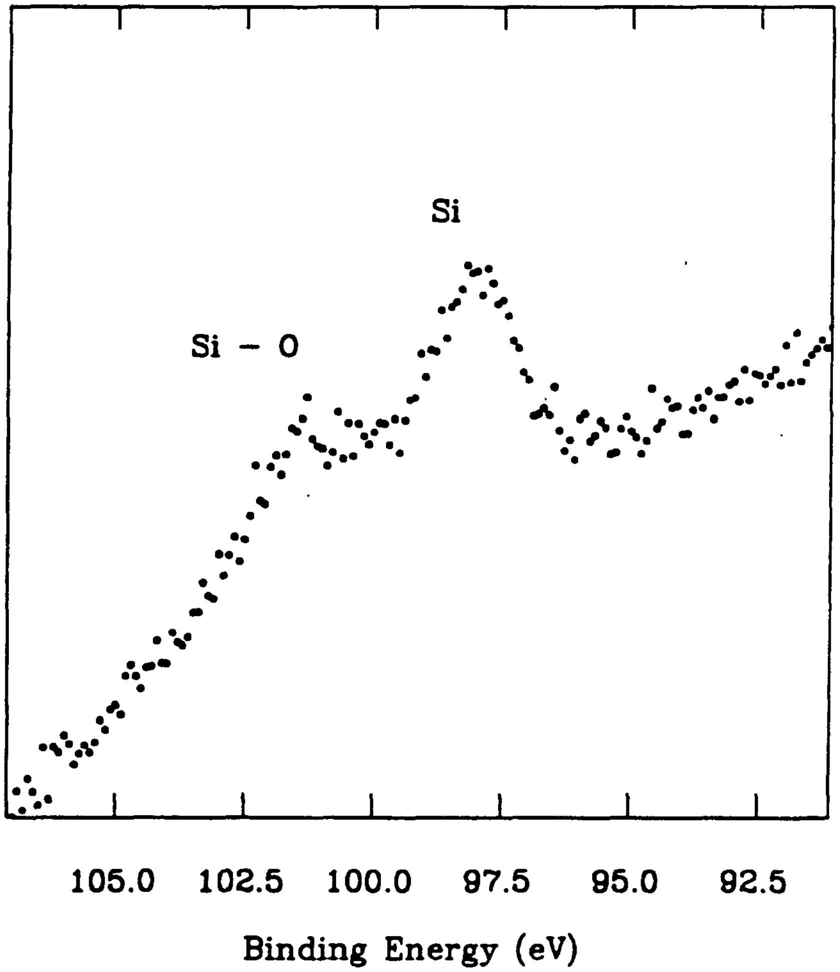

Figure 3.10: The silicon 3p XPS peaks are shown here. The low ionization cross section made it difficult to determine the exact type of SiO_2 present on the surface.

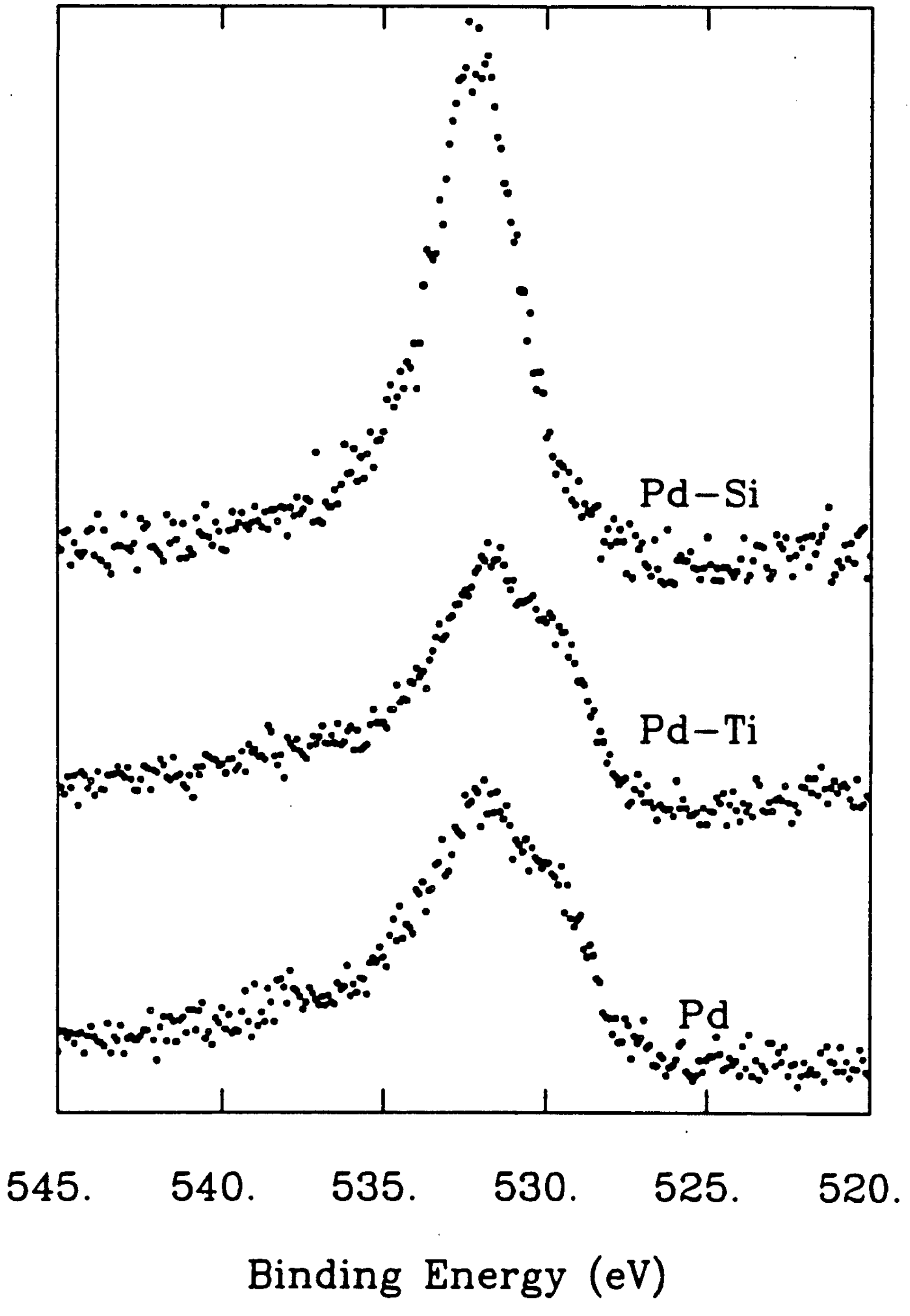

Figure 3.11: The oxygen and Pd 3p peaks are shown here after UHV oxide deposition and oxidation. For the clean and titania-decorated surface an oxide characteristic of a metal oxide is seen, and for the silica surface only an oxide characteristic of SiO_2 is seen.

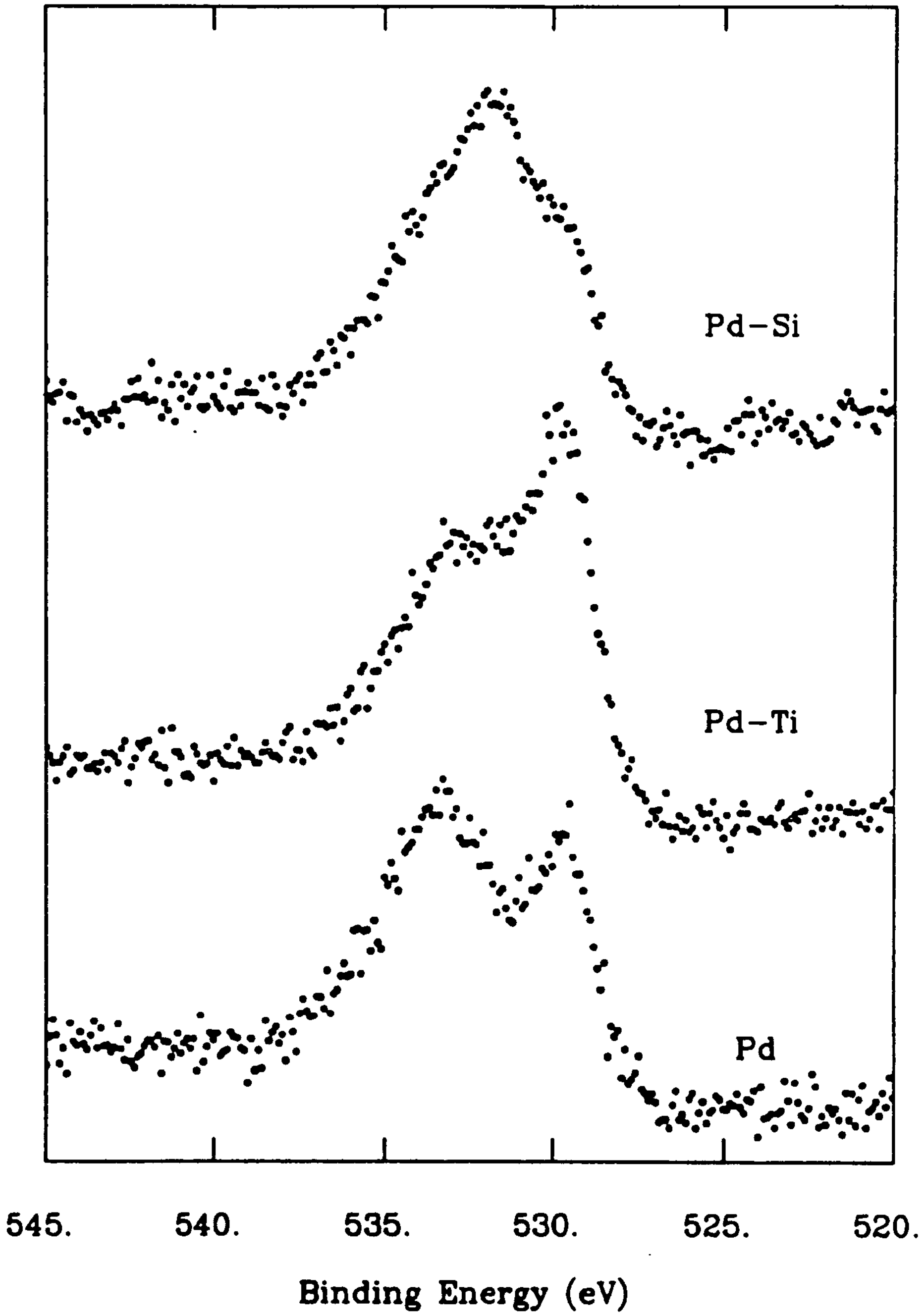

Figure 3.12: The XPS spectra of the oxygen and Pd 3p peaks are shown here after high pressure oxidation (50 psi). Oxygen peaks corresponding to metal oxides, and a shoulder attributable to OH groups are seen.

given temperature it was more difficult to completely oxidize the titania system, which involved oxidizing the topmost 4 - 6 atomic layers. The Pd 3d peak on the titania covered surface shows some metallic palladium in addition to palladium oxide which is the only peak seen on the clean and silica covered surfaces. This indicates that the titania blocks complete oxidation of the palladium surface region (XPS is sensitive to the top 4 - 6 atomic layers). The titania possibly limits or physically blocks oxygen diffusion into the near surface region or forms a stronger bond with the palladium that keeps the metal semi-metallic.

Figure 3.14 shows the Pd 3d peaks for the metallic and oxidized surface before and after reaction. In both cases, the surface is completely reduced to the metallic state after a reaction. This complete reduction was seen when the surface was examined after thirty minutes of reaction time while it was still actively producing methane.

The major difference between the surfaces that produce methanol and those that did not was the stability of the palladium oxide. To determine this stability two experiments were done. In one, the three surfaces were oxidized under the same high pressure conditions and then returned to UHV. The surfaces were then heated in 50 - 80°C increments and the ratio of Pd^{+0} to Pd^{+2} measured. Since the peaks overlapped, a curve fitting program was written which assumed a gaussian distribution peak shape and separated the two components.[2] Figure 3.15 shows the quality of fit obtained using this method. The undoped palladium - oxide sample decomposed at the lowest temperature ($\sim$ 420°C) followed by the silica-doped palladium ($\sim$ 500°C) and finally the titania-doped surface at $\sim$ 580°C (Figure 3.16). The titania stabilized the Pd^{+2} to higher temperatures relative to the other two surfaces, but all three surfaces were stable above reaction temperatures.

When the same high pressure oxidation and return to UHV was followed by

---

[2] Appendix B has the algorithm used and a program listing.

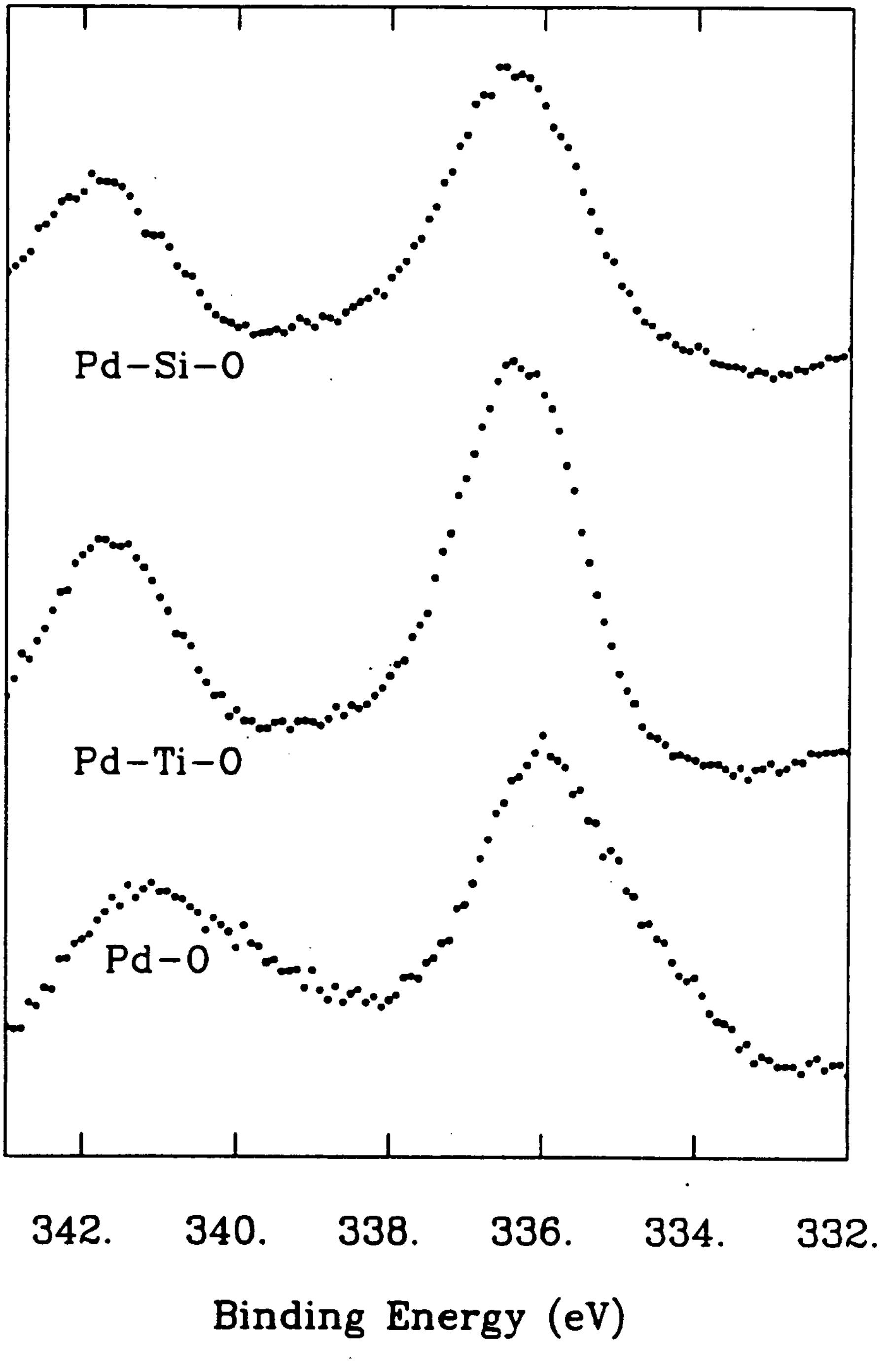

Figure 3.13: This figure shows the Pd 3d peaks of the clean, and silica- and titania-covered surface after a 50 psi oxidation. All three surfaces show oxidized palladium. The titania-decorated surface was the most difficult to oxidize.

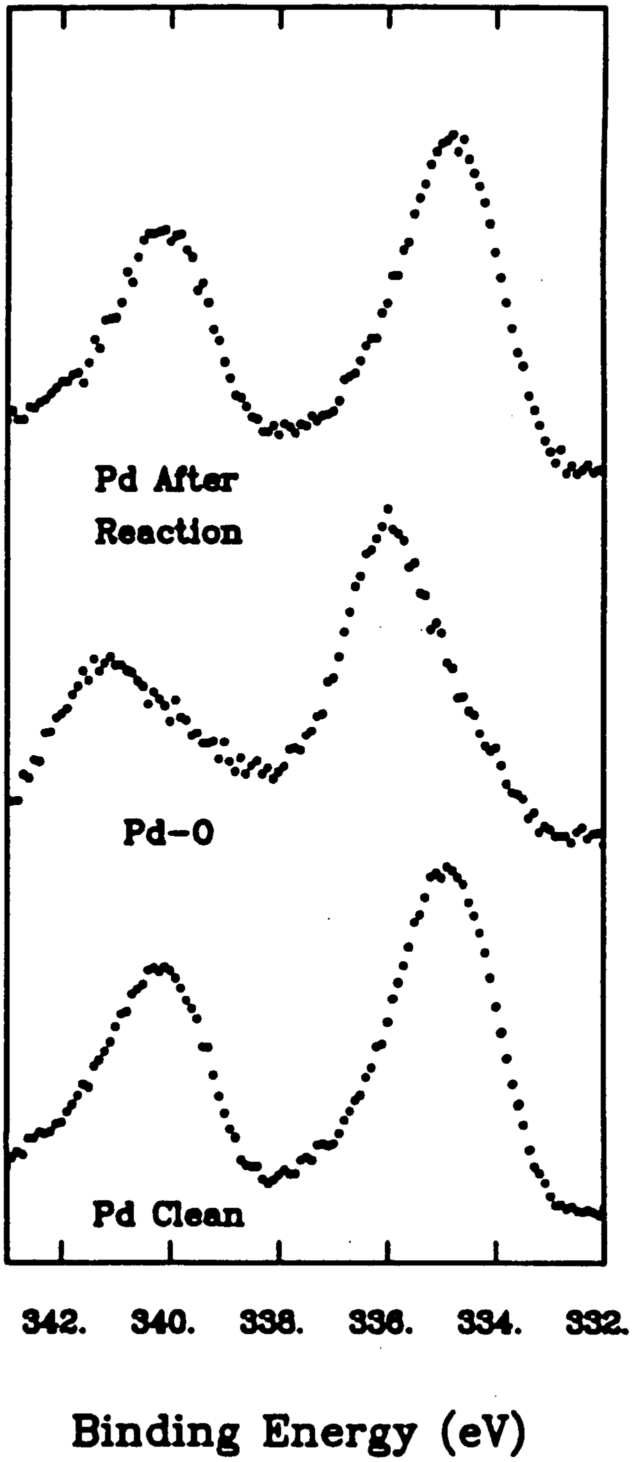

Figure 3.14: The palladium 3d peaks for a clean and oxidized titania-covered surface are shown before and after reaction. In all cases, the palladium is completely reduced to the metallic state after the reaction.

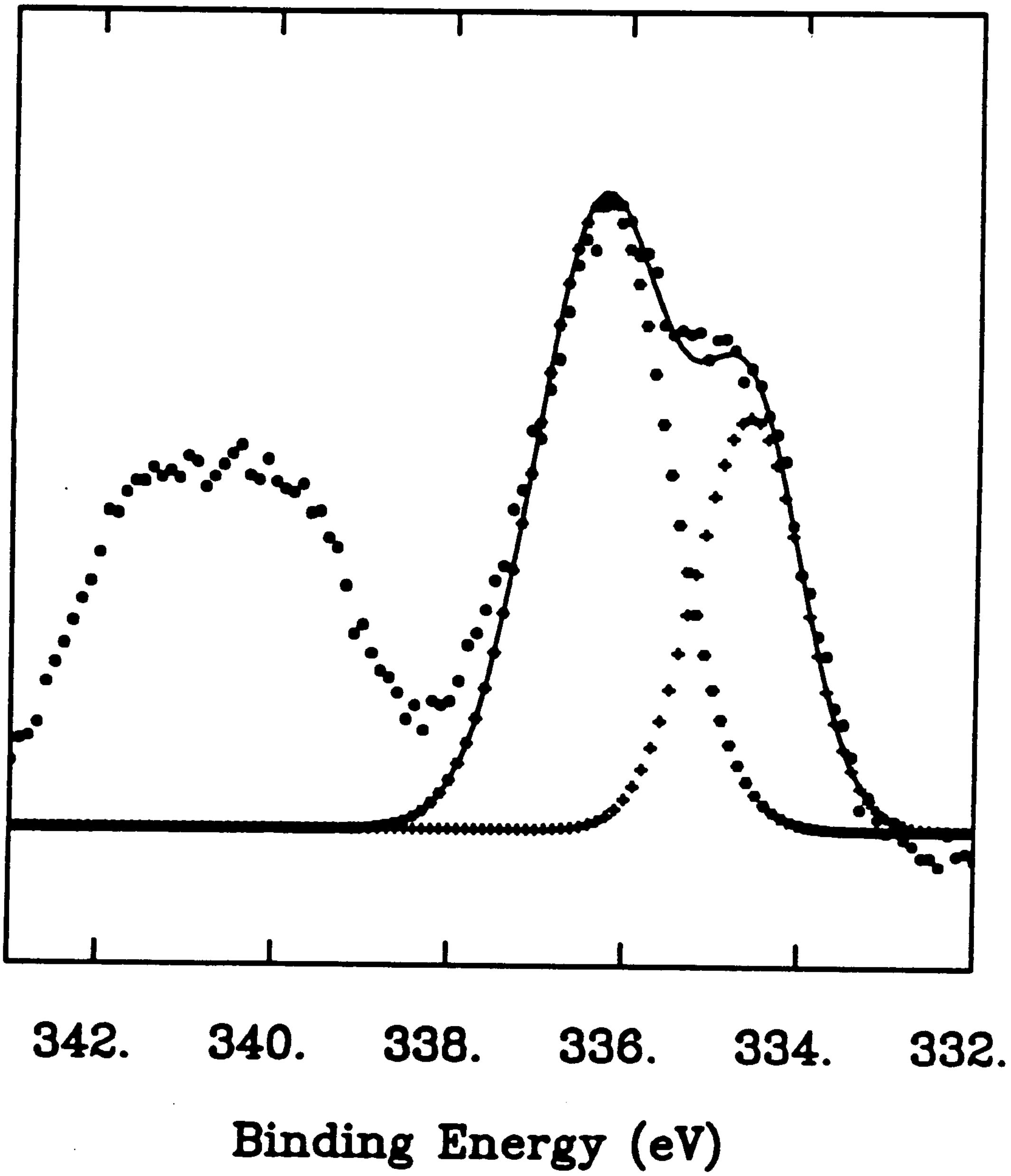

Figure 3.15: A sample of the quality of fit for the curve-fitting routine described in Appendix B is shown here.

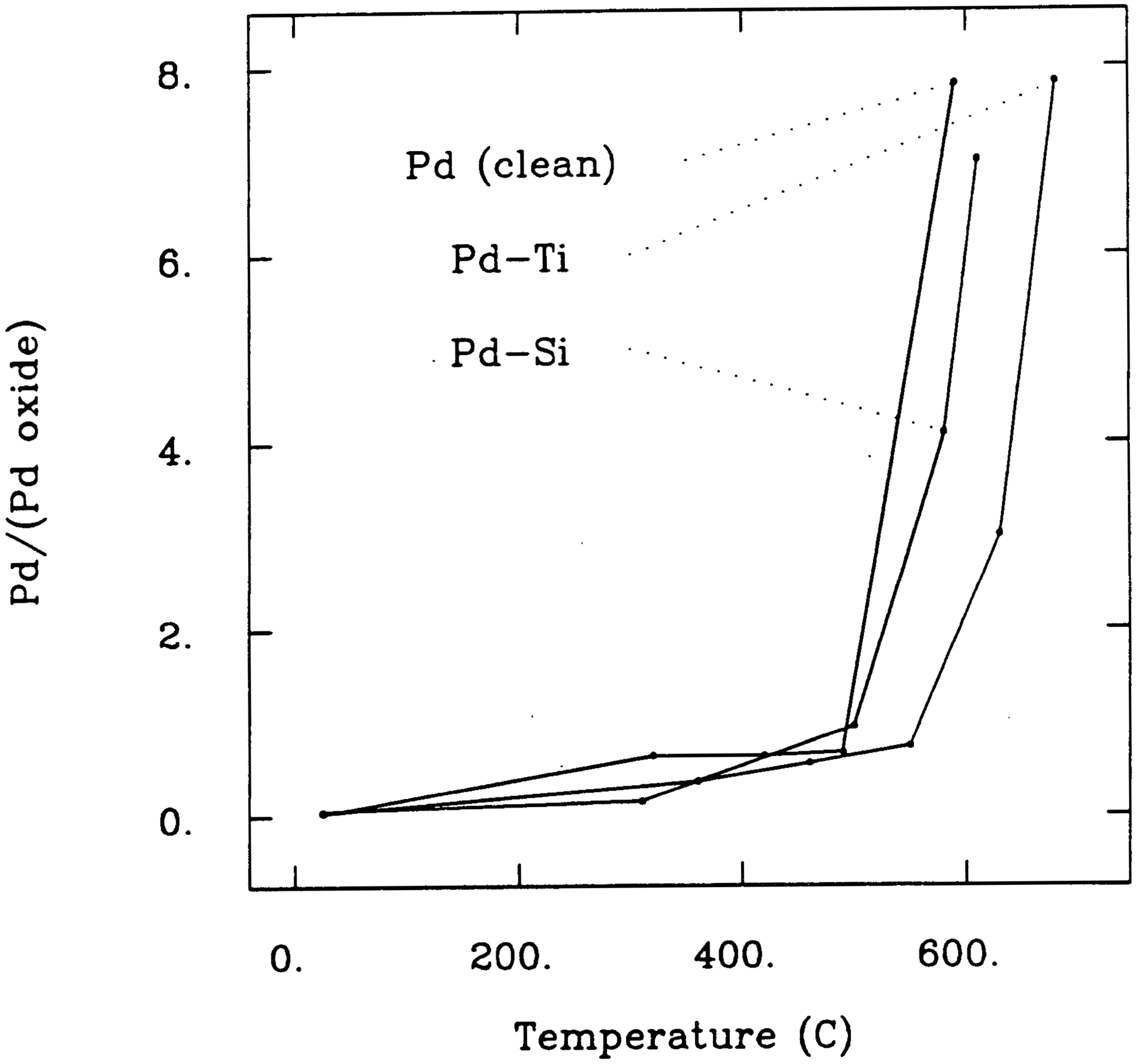

Figure 3.16: This figure shows the ratio of Pd/Pd oxide in the presence of oxide overlayers as a function of temperature. The titania-decorated surface is slightly more stable than the silica-doped and clean surfaces. The oxide on all three surfaces decomposes at approximately 500-600°C, far above reaction temperatures.

saturation exposures of hydrogen (5×10^{-6} torr, 200 sec), the stability changed dramatically (Figure 3.17). The undoped surface started to decompose ~ 200° lower in the presence of hydrogen, as did the silica covered surface (not pictured). The titania doped palladium still maintained the oxide up to almost 600°C. In the presence of hydrogen there was a large difference in oxide stability for the three surfaces.

3.2.5 Work Function Measurements

Measurements of work function changes and changes in crystal current were made to determine the average change in the surface electron density as a function of oxide coverage. Both oxides decrease the work function, indicating electron donation to the surface. Figure 3.18 shows the change in crystal current as function of silica and titania deposition time. For silicon, after 9 minutes of silane deposition (1×10^{-8} torr) there was no further decrease in the crystal current, indicating that the surface was saturated with silane and no further silane was adsorbing on the surface. The addition of titania linearly decreased the crystal current without reaching an asymptotic value, indicating multilayer adsorption. Interestingly, when studying the change in work function [3], there was a steep (1.3 eV) drop from the clean surface to a surface with a titania coverage of $\Theta_{Ti} = .2$ followed by a more gradual decline at higher titania coverages (Figure 3.19). At a titania coverage of $\Theta_{Ti} = .18$ there was a maximum in the methanation rate.

3.3 Discussion

The presence of oxide overlayers are necessary on palladium catalysts in the CO hydrogenation reaction for the formation of methane and methanol. In this section the interaction of these oxide overlayers with palladium will be discussed and

---

[3] Determined by measuring the onset in the secondary electron cascade.

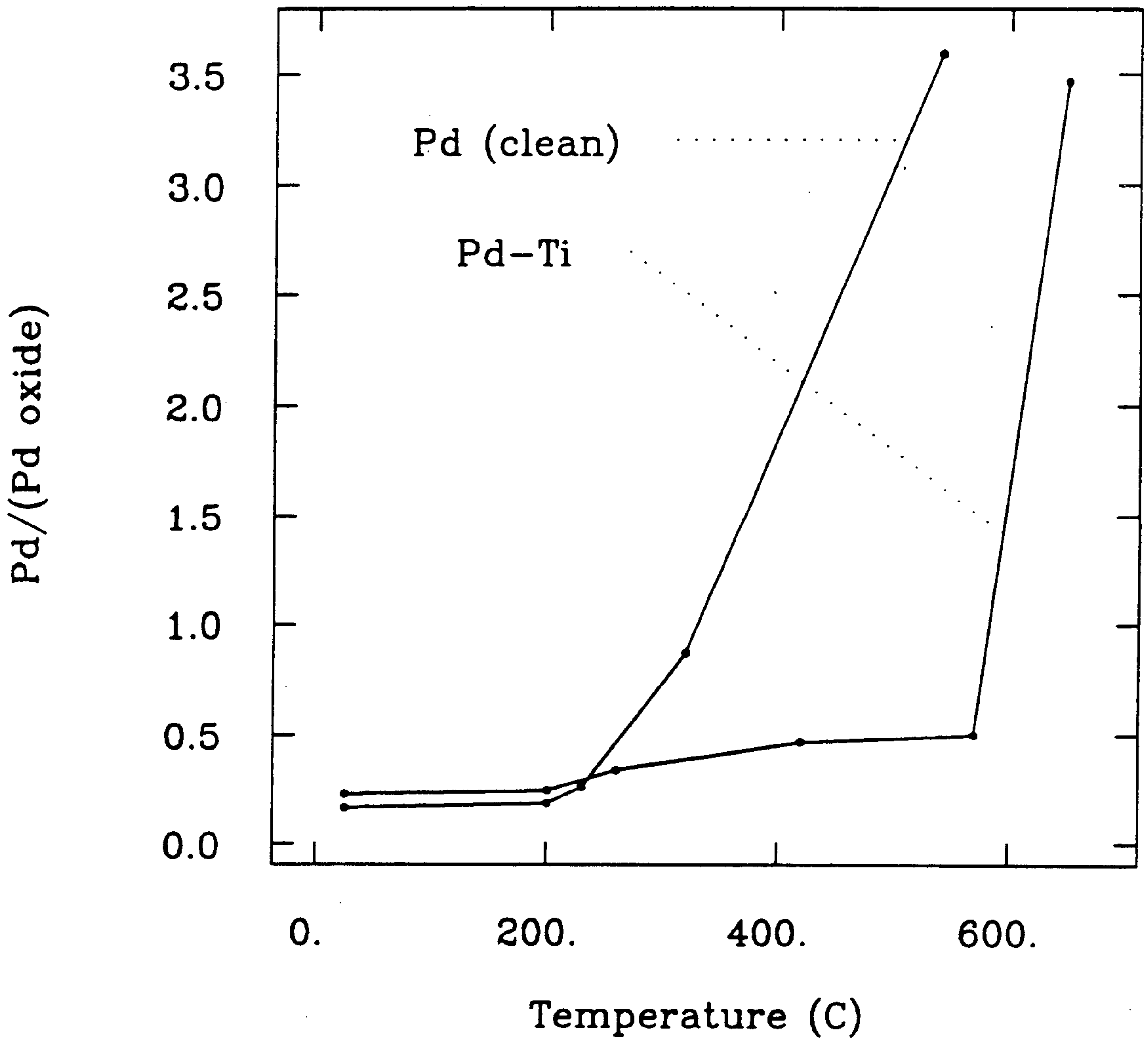

Figure 3.17: The figure shows the Pd/Pd oxide ratio on the clean and titania-decorated surfaces after high pressure oxidation followed by UHV hydrogen saturation as a function of temperature. The presence of titania greatly stabilizes the oxide relative to the other surfaces.(On the silica covered surface, the oxide starts to decompose around 220°C)

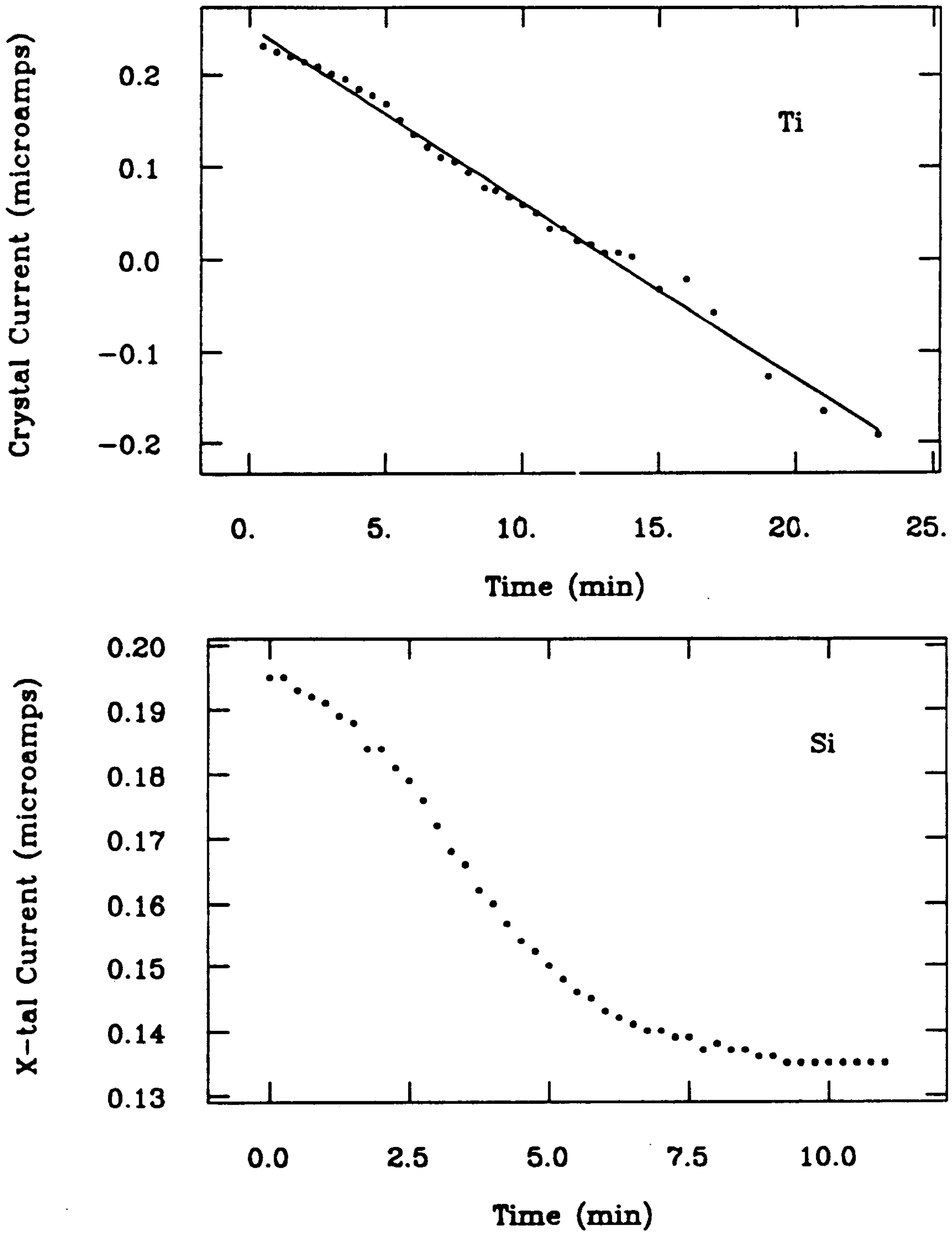

Figure 3.18: This figure shows the crystal current as a function of oxide deposition time. For titania there is continuous decrease showing growth of the overlayer, whereas for silica the surface becomes saturated and deposition stops.

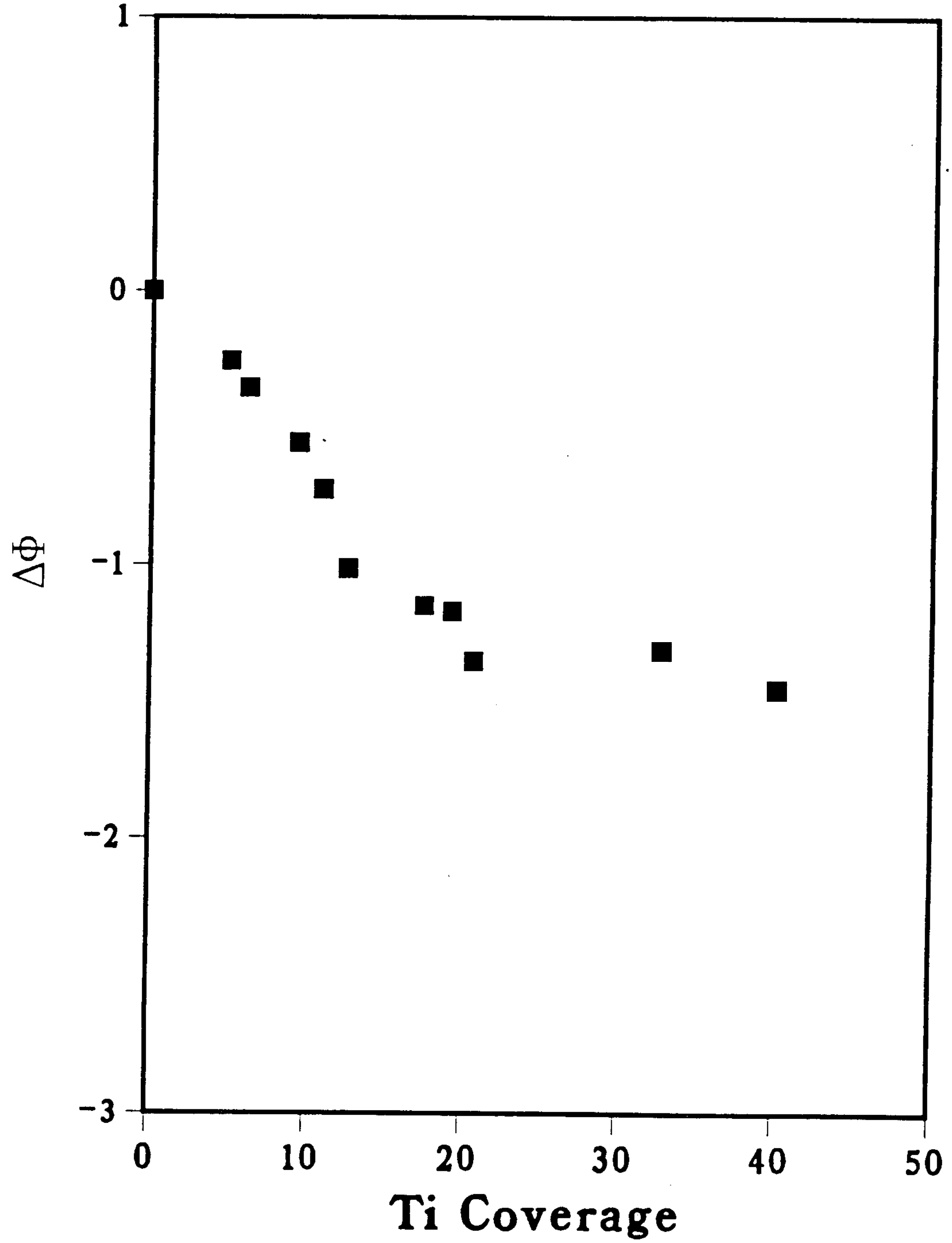

Figure 3.19: As titania is deposited, the surface work function decreases. Rapidly at first, up to a coverage of Θ_{Ti}=.2, then more gradually thereafter.

their role in the formation of methane and methanol from carbon monoxide and hydrogen.

3.3.1 Oxide Growth and Diffusion

Titania grows in a three-dimensional mechanism on palladium as determined from the AES uptake curves where the intensity of the palladium (330 eV) and titania (387 eV) peaks are plotted as a function of deposition time. As mentioned in Chapter 2, there are three overlayer growth mechanisms: Layer-by-layer (Frank - Van der Merwe), layer followed by three dimensional (Stranski - Krastanov) and three-dimensional (Volmer - Weber). The mechanism can be differentiated by the varying attenuation of the secondary electrons.

There is a strong thermodynamic driving force for the interaction of oxides (TiO_2, V_2O_5, ZrO_2, SiO_2) with palladium and other Group VIII metals. From the transition metal bonding model proposed by Brewer, the partially full d orbitals (or p for silicon) interact with the almost full d orbitals of the Pt group metals to form compounds of exceptional stability [33,34]. Both Pd_xTi_y and Pd_xSi_y are stable compounds. For Pt_3Ti and Pt_8Ti, Mechter and Worrel calculated the Gibbs free energy to be -17.8 kcal/g-atom and -8.20 kcal/g-atom at 1150 K [35]. The strength of the Pd-Ti bond is further evidenced by the stability of Ti during heating at 920 K ($\Theta_{Ti} = .10$) and the high temperature needed to completely diffuse the titania into the bulk (> 1000 K). However, in these studies, the catalytic activity of the sample was highest when the titania was on the surface and not heated to temperatures at which a strong Pd-Ti or Pd-Si surface compound would form. The active site is most likely a mixed Pd - TiO_2 or Pd - SiO_2 site, where the oxide is decorated on top of the palladium surface.

3.3.2 Catalysis and Chemisorption

Decorating the palladium foil with silica or titania overlayers produced a very selective methanation catalyst, with the titania-covered surface twice as active as the silica-covered surface. Since annealing the sample to temperatures at which the oxides diffuse into the bulk decreases their catalytic activity, it is necessary that these oxides remain dispersed on the catalyst surface. This suggests that a 'bulk' Pd-Ti-O is not the active species but rather a mixed Pd-TiO_x site (or Si). The lower methanation rates on the silica surface may be due in part to the lower activation barrier for bulk diffusion. Some of the silica AES intensity used to measure the surface coverage may be attributable to near surface region silicon, so that the actual concentration of silicon on the surface is lower than measured.

The CO chemisorption results show that the presence of the oxide overlayers produces different CO binding sites on the surface. A new high temperature shoulder (250°C) on the CO desorption trace is present on both the silica- and titania-covered surfaces, both which produce methane. This site is stable for repeated CO TPD. After high (50 psi) pressure oxygen treatments a new high temperature peak at 410° C is detected which implies a third CO binding site. This peak disappears by the second consecutive CO TPD after the oxidation on the clean and silica-covered surfaces, but only gradually decreases over 7 - 10 CO TPD in the presence of titania. The presence of titania stabilizes this site. It should also be noted that the titania-doped surface is the only surface on which methanol is detected. Therefore, this site may be indicative of a site that activates CO to form methanol, and the site represented by the shoulder indicative of a site at which CO reacts to form methane.

Other metals showed similar changes in catalytic behavior after oxide deposition, however their CO TPD results differ from those found in this study. Raupp *el al.* [36] and Levin *et al.* [7] reported a 90 K and 60 K decrease in the CO desorption temperature on Ni and Rh respectively, and attributed the decrease to a shift in the CO bonding from bridging to an on-top site. The difference of these studies could indicate that different CO bindings sites are active in producing methane on the different metals. Undecorated rhodium foil is active in forming methane from CO and H_2, whereas metallic palladium is essentially inactive. The CO on palladium is possibly tilted towards the oxide, with some bonding between the CO π bond and the TiO_2. This type of bonding configuration, similar to that seen for CO on a potassium-covered palladium single crystal ((111) or (100) Chapt. 4) would facilitate CO dissociation. EELS or IR spectroscopy would answer this question.

The Pd-Ti system shows a sharp decrease in the amount of CO chemisorbed as a function of titania coverage. This indicates that each titania molecule blocks more than one CO binding site and that the titania is well dispersed on the surface, forming only very small islands. Figure 3.20 shows the number of free palladium atoms (not adjacent to a titania atom) on a surface as a function of titania coverage. This Monte Carlo simulation shows that, with high dispersion, one titania atom will affect numerous palladium atoms and that even at low coverages the majority of the palladium atoms are adjacent to a titania. If the titania formed large islands this decrease in CO chemisorption would be more gradual and linear (dotted line). Calculations by Feibelman and Hansmann have demonstrated that changes in chemisorptive properties due to ionic centers can extend over a few metal atoms [37]. Ko and Gorte reported a linear decrease in CO coverage for the Pt/TiO_2 system and concluded the TiO_2 simply blocks adsorption sites [38,39,40]. Their titania coverage calibration was not corrected for AES elemental sensitivities. If this difference is taken into account their results and results by Levin *et al.* on Rh concur with this study, that titania is well dispersed and influences the CO bonding capabilities of multiple Pd atoms.

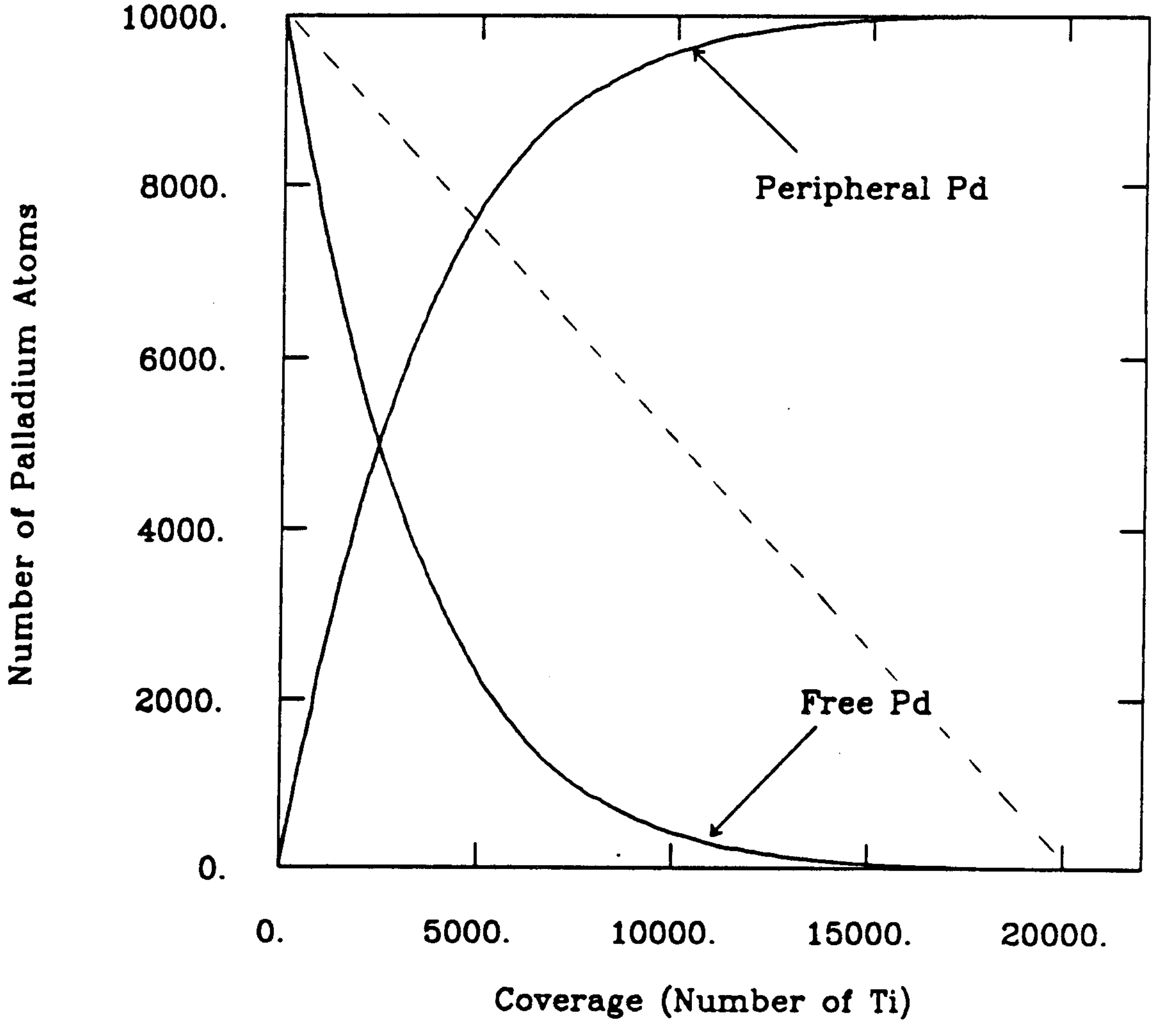

Figure 3.20: From a Monte Carlo growth simulation it can be seen that, for high titania dispersion on the surface, at low coverages almost every palladium atom is adjacent to a titania, whereas in a clustered growth (dashed line) a larger percentage of the palladium atoms are not adjacent to titania atoms.

Since the auger uptake curves did not have any sharp discontinuities in their slope which would signify completion of one monolayer, CO titration had to be used to determine at which point the palladium was completely covered. From the CO uptake curves, at Ti coverages higher than $\Theta_{Ti} = .60$ there is no further decrease in the amount of chemisorbed CO [4]. At this coverage all palladium is covered by titania.

Comparing the plot of the methanation rate on the Pd-Ti system to the CO chemisorption plot, it can be seen that if $\Theta_{Ti} = .6$ is considered the completion of 'one monolayer', the maximum in the methanation rate occurs when approximately one-third of the surface is covered with titania ($\Theta_{Ti} = .18$). At this coverage, assuming well-dispersed titania, there would be a maximum number of mixed Pd-TiO_x sites.[5] This also supports the proposal that methane forms on a mixed Pd-TiO_x or Pd-SiO_x site.

The XPS spectra of the Pd-TiO_x and Pd-SiO_x samples on which methane forms, show no shift in the Pd 3d peaks relative to metallic palladium. For all silica and titania coverages and under all UHV oxidation and heating conditions there was no variation in the position or shape of the Pd 3d peaks.[6] XPS of the titania peaks showed titanium in the +4 oxidation state. It has been reported that titania reduction is facilitated when the titania is deposited on metals capable of dissociatively adsorbing hydrogen, whereas titania alone is not easily reduced. This suggests that the Pd - Ti interaction (bonding, charge transfer) is rather weak compared to Rh-Ti interaction seen by Levin *et al.*[7]. Also, the diffusion of the hydrogen into the bulk may be more energetically favorable than the reduction of titania. Titania deposited on gold has also been found not to reduce easily [41].

---

[4] The residual CO desorbing is from the back of the crystal

[5] Determined from Monte Carlo growth simulation program. Similar results were obtained by Levin [41].

[6] One caveat: It is difficult to discern changes in surface oxidation state when the bulk is the same element. The surface features could be 'washed out' by the bulk peak.

Levin *et al.* found in the Rh/TiO_2 system that the metal catalyzes the reduction of the titania and that this interface between the metal and Ti^{+3} is the active site in methane formation [7]. The enhancement of the metal's catalytic and chemisorptive properties is due to an electronic interaction in which electron density is transferred from the Ti^{+3} to the metal. They found a correlation between the percentage of Ti^{+3} on the catalyst surface and the expected number of periphery (Ti^{+3} adjacent to Rhodium) sites.

Work function measurements in our study showed a rapid decrease in the work function up to a titania coverage of $\Theta_{Ti} = .2$ followed by a more gradual decrease. This rapid decrease can be attributed to an additional metal - titanium interaction which at $\Theta_{Ti} = .2$ reaches a maximum, the point at which the number of metal - oxide interface sites could be considered a maximum. No XPS evidence of titanium reduction after deposition on the palladium foil was found. Levin found that titania on gold showed similar behavior. It is possible that the electronic interaction between the palladium and titania is insufficient to keep the titania reduced under UHV conditions or in the presence of small quantities of oxidizing agents. Under 200 psi of hydrogen (reaction conditions) the titania may well be reduced to Ti^{+3}, and reoxidized during the loop evacuation.

Comparing AES from the samples before and after reaction, there was a large carbon buildup after reaction on the oxide decorated surfaces whereas the clean palladium catalyst had negligible amounts of carbon. On the oxide doped foils the palladium peak was attenuated to a larger degree than the titania and silica peaks, showing that the hydrocarbon species were bound to the palladium and that the reaction products were not formed on the oxide overlayer.

These results suggest that the mixed metal - oxide interface is the catalytically active site in methane formation. Figure 3.21 shows a possible binding configuration for the CO from which it next could dissociate or be hydrogenated. More studies are necessary to determine accurately the exact CO bonding and elementary reaction steps leading to methane. This mixed site scheme on the decorated palladium foil is similar to ideas proposed by Bracey *et al.* [23] and Ichikawa *et al.* [17] for supported palladium catalysts. Furthermore, methane is the predominant product on supports which are considered inert by themselves.

Interestingly, only the titania-decorated surface pretreated with 50 psi of oxygen at 500- 600°C was active in forming methanol from CO and H_2, but only for a few minutes ($<$ 10 minutes). XPS showed formation of palladium oxide after this treatment, but the same palladium +2 state was seen on the other surfaces on which no methanol formed. Similar to the CO chemisorption state on the oxide, the titania stabilizes the palladium oxide. In the presence of hydrogen the titania still stabilizes the oxide at high temperatures ($\sim$ 550°C) whereas on the other surfaces the oxide starts decomposing at 200°C. This suggests that methanol formation is dependent on the presence of a palladium ion, which only the titania is capable of stabilizing for a few minutes under reaction conditions.

Methanol and methane form through two different and independent pathways. CO TPD traces and kinetic data suggest that two distinct types of palladium catalyze the two reactions. On the highly oxidized surface the methanol shows no decrease in concentration indicating that it neither decomposes nor converts into methane. On the Pd-Ti-O sample that produces methane it is quite possible that initially only methanol is produced, and as the palladium is reduced, methane starts forming. This agrees very well with the supported palladium systems where, in general, either methane or methanol are selectively formed. Fajula *et al.* [20] have also proposed two distinct routes for methane and methanol but attributed the differences to crystallite size. The crystallite size only determines the number of mixed metal - oxide sites necessary for product formation, but the nature of the site determines if methane or methanol will form.

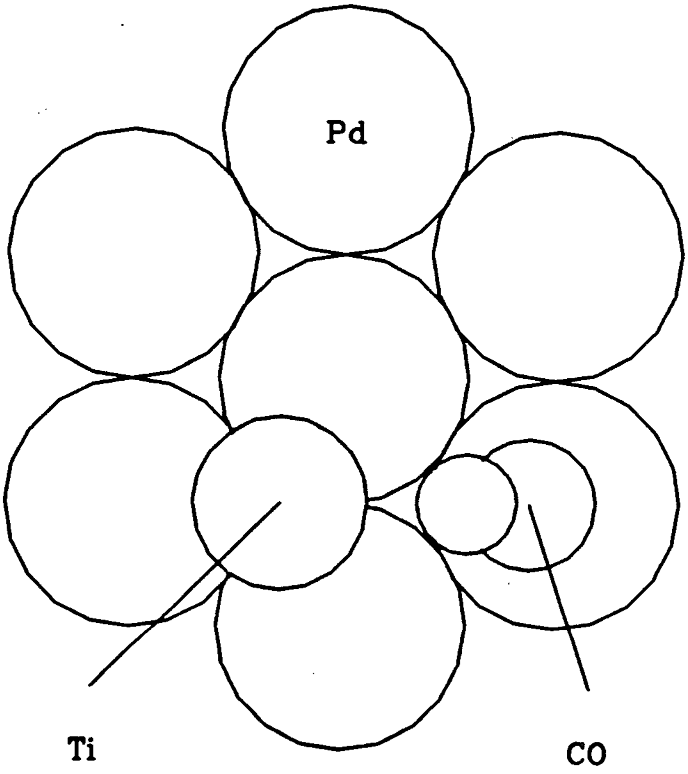

Top View

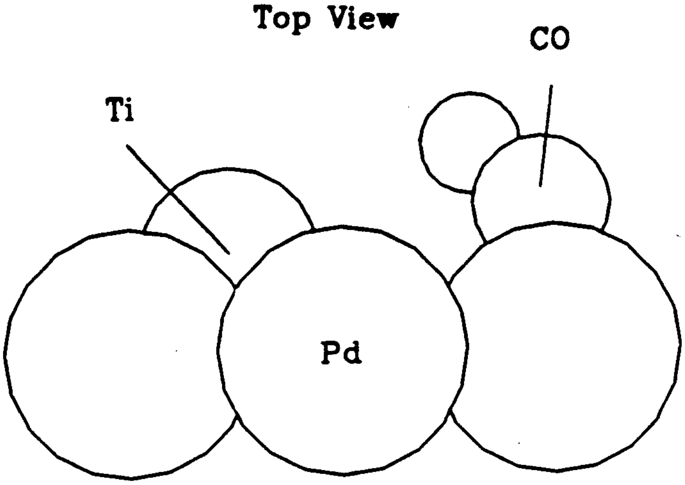

Side View

Figure 3.21: This figure shows some possible CO binding configurations in the presence of oxide overlayers in the CO hydrogenation reaction.

The differences in activity seen by various research groups (Bell and Poels [28,18]) for the activity of Pd/SiO_2 in methanol formation seems to be due to their use of $PdCl_2$ to impregnate the catalyst. An oxychloride species may help stabilize a palladium ion.

There are numerous well-documented examples of catalysts where support interactions drastically reduce the chemisorption of CO and hydrogen, but enhance the catalytic activity in the $CO + H_2$ reaction. In particular, titania, which is an easily reducible oxide has been observed to have this effect, commonly referred to as strong metal support interaction (SMSI). In the Pd/TiO_2 system SMSI is not involved. The sample shows activity in the CO hydrogenation reaction without the ~700°C pre-reduction necessary on the other catalysts exhibiting this type of behavior. On the contrary, heating the sample to these high temperatures caused the titania to diffuse into the bulk and near surface region, lowering the catalytic activity. Our results are in agreement with studies by Bracey and Burch [23] who have studied palladium supported on TiO_2 and SiO_2 and find no evidence for an SMSI effect.

3.4 Conclusions

The following points summarize the results found in the study of the effect of oxide overlayers on the chemisorptive and catalytic behavior of palladium foils in the CO hydrogenation reaction. Figure 3.22, a flow chart, correlates the treatment conditions and changes in chemical activity.

- Palladium foils decorated with SiO_x and TiO_x overlayers produce methane. This activity has been attributed to a mixed metal - oxide interface site.
- Palladium decorated with TiO_x (oxidized to 50 psi) produces methanol for a short period of time. This activity has been attributed to a Pd^{+n} ion which is stable in the presence of TiO_x.

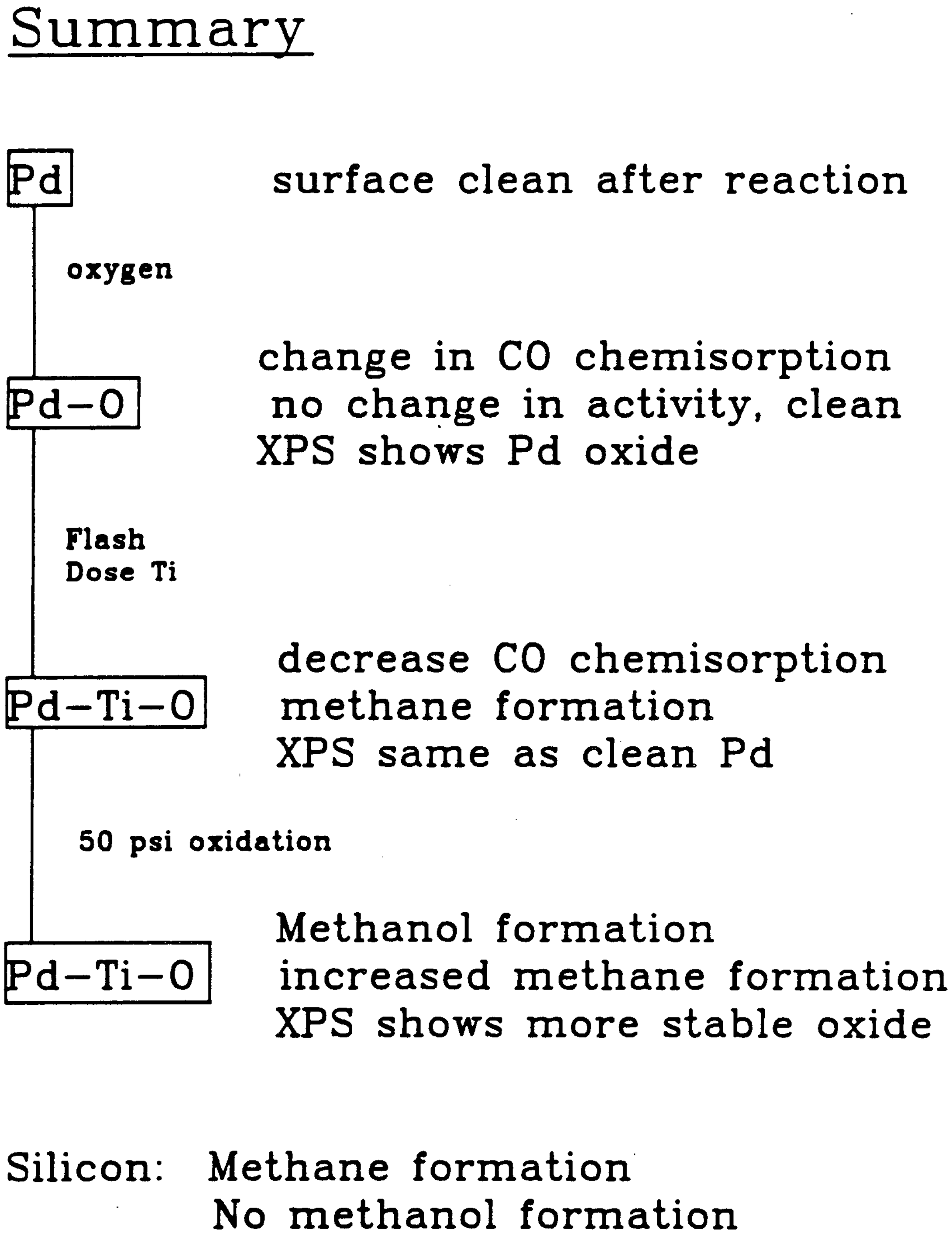

Figure 3.22: Flow chart correlating treatments and changes in catalytic activity.

References

[1] F. Solymosi. *Catal. Rev.* **1** (1967) .

[2] S. J. Tauster, S. C. Fung, and R. L. Garten. *J. Am. Chem. Soc.* **100** (1966) 2173.

[3] C. N. Satterfield. *Heterogeneous Catalysis in Practice.* McGraw-Hill, 1980.

[4] M. L. Poutsma, L. F. Elek, P. A. Ibarbia, A. P. Risch, and J. A. Rabo. *J. Catalysis* **52** (1978) 157.

[5] R. A. Demmin, C. S. Ko, and R. J. Gorte. *J. Phys. Chem.* **89** (1985) 1151.

[6] Y. M. Chung, G. Xiong, and C. C. Kao. *J. Catalysis* **85** (1984) 237.

[7] M. E. Levin, M. Salmeron, A. T. Bell, and G. A. Somorjai. *Surf. Sci.* **169** (1986) 123.

[8] F. Fischer, H. Tropsch, and P. Dilthey. *Brennst.-Chem.* **6** (1925) 265.

[9] R. Kratel. PhD thesis, Technische Hochschule, Berlin-Charlottenburg, 1937.

[10] Y. T. Eidus, B. K. Nefedov, M. A. Besprozvannyi, and Y. V. Pavlov. *Bull. Acad. Sci. USSR Div. Chem. Sci.* (1965) 1129.

[11] J. F. Schultz, F. S. Karn, and R. B. Anderson. *Bureau of Mines Report of Investigation* **6974** (1967) .

[12] N. J. Kertamus and G. D. Woolbert. *Prepr. Amer. Chem. Soc. Div. Fuel Chem.* **19(5)** (1974) 33.

[13] M. A. Vannice. *J. Catalysis* **37** (1975) 449.

[14] M. A. Vannice. *J. Catalysis* **49** (1975) 129.

[15] J. A. Rabo, A. P. Risch, and M. L. Poutsma. *J. Catalysis* **53** (1978) 295.

[16] M. A. Vannice and R. L. Garten. *Ind. Eng. Chem. Prod. Res. Dev.* **18** (1979) No. 3.

[17] M. Ichikawa. *Bull. Chem. Soc. Chem. Commun.* (1978) 566.

[18] E. K. Poels, E. H. van Broekhoven, W. A. A. van Barneveld, and V. Ponec. *React. Kinet. Catal. Lett.* **18** (1981) 223.

[19] *Faraday Soc.*

[20] F. Fajula, R. Anthony, and J. H. Lunsford. *J. Catalysis* **73** (1982) 237.

[21] J. M. Driessen, E. K. Poels, J. P. Hindermann, and V. Ponec. *J. Catalysis* **82** (1983) 26.

[22] T. Mori, H. Masuda, H. Imai, A. Miyamoto, R. Hasebe, and Y. Murakami. *J. Phys. Chem.* **87** (1983) 3648.

[23] J. D. Bracey and R. Burch. *J. Catalysis* **86** (1984) 384.

[24] T. H. Fleisch, R. Hicks, and A. T. Bell. *J. Catalysis* **87** (1984) 398.

[25] P. S. Wehner, G. C. Tustin, and B. L. Gustafson. *J. Catalysis* **88** (1984) 246.

[26] R. T. K. Baker, E. B. Prestridge, and G. B. McVicker. *J. Catalysis* **89** (1984) 422.

[27] S. Chan and A. T. Bell. *J. Catalysis* **89** (1984) 433.

[28] R. Hicks, Q. Yen, and A. T. Bell. *J. Catalysis* **89** (1984) 498.

[29] R. Hicks and A. T. Bell. *J. Catalysis* **91** (1985) 104.

[30] C. Sudhakar and M. A. Vannice. *Applied Catalysis* **14** (1985) 47.

[31] R. Hicks, A. Chin, and A. T. Bell. *J. Catalysis* **90** (1984) 205.

[32] J. S. Rieck and A. T. Bell. *J. Catalysis* **96** (1985) 88.

[33] L. Brewer. *Acta Met.* **15** (1967) 553.

[34] L. Brewer and P. R. Wengert. *Metall. Trans.* **4** (1973) 83.

[35] P. T. Meschter and W. L. Worrell. *Metall. Trans A* **7A** (1977) 299.

[36] G. B. Raupp and J. A. Dumesic. *J. Phys. Chem.* **88** (1984) 660.

[37] P. J. Feibelman and D. R. Hamann. *Surf. Sci.* **149** (1985) 48.

[38] C. S. Ko and R. J. Gorte. *J. Catalysis* **90** (1984) 59.

[39] C. S. Ko and R. J. Gorte. *Surf. Sci.* **161** (1985) 597.

[40] C. S. Ko and R. J. Gorte. *Surf. Sci.* **155** (1985) 296.

[41] M. Levin. PhD thesis, U. C. Berkeley, Berkeley, CA., 1987.

Chapter 4

PALLADIUM-ADDITIVES

4.1 Introduction

Surface additives (potassium, sodium, silicon, phosphorus, sulfur and chlorine) are present on many catalysts and greatly influence product distributions in many reactions, including CO hydrogenation, ammonia synthesis, steam reforming, hydrogenolysis and D_2 exchange [1,2,3]. However, the nature of the promoting or poisoning effect is not well understood. The two major types of interactions the additives exhibit are either structural or electronic (ligand, chemical). For example, alumina prevents sintering of iron in the ammonia synthesis reaction and is considered a structural interaction, and potassium in the CO hydrogenation reaction increases the specific activity of each site. This thesis shows that additives can both chemically and structurally modify the bonding of small molecules (H_2, CO and C_2H_2) to palladium single crystals.

More specifically, the questions this chapter addresses are:

1. How do surface additives interact with palladium single crystals?
2. How do surface additives modify adsorbate bonding?
3. How do surface additives modify palladium's catalytic activity?

These questions are answered by using a wide variety of surface analytical tools to probe the surface. One of these techniques is CO Temperature Programmed Desorption (TPD) which is a chemical probe sensitive to different binding sites and changes in surface electron density. Previous research has shown that different types of surface sites exhibit different chemistry and that differences in heats of adsorption of surface sites are related to their ability for bond breaking or forming required in catalysis. Using this technique in conjunction with LEED, Work Function measurements, TPD of other molecules (H_2 and C_2H_2), Electron Energy Loss Spectroscopy (EELS) and reaction studies, the interaction of the additives with the surface can be understood on an atomic level.

4.2 Results

4.2.1 Pd(111) - Na,Si,P,S,Cl - CO

CO TPD from clean Pd(111) single crystals showed a single peak maximum at 483K for low CO exposures (1×10^{-9} torr, 50 sec). At higher coverages (1×10^{-8} torr, 50 sec) the maximum shifted to 470K with a shoulder at 410K and at saturation coverages (2×10^{-8} torr, 50 sec) the peak had broadened to extend from 270K to 520K with maximum at 330K and 460K (Figure 4.1). Addition of Na, Si, P, S and Cl changed the desorption temperatures markedly. (Unless otherwise noted CO exposures were at 1×10^{-8} torr, 50 seconds.)

Addition of Na increased the desorption temperature of CO from 480K on the clean surface to 590K on the surface with $\Theta_{Na} = .35$ as shown in Figure 4.2. There was no change in the peak shape, but there was a 20% decrease in the peak area.

CO TPD for silane- and silicon-covered surfaces was different than for the sodium covered surface. Silane decomposed on palladium at 550K, at which point hydrogen from the silane desorbed. The silicon AES peak decreased in intensity and no gas-phase silicon fragments were seen in the mass spectrometer, suggesting

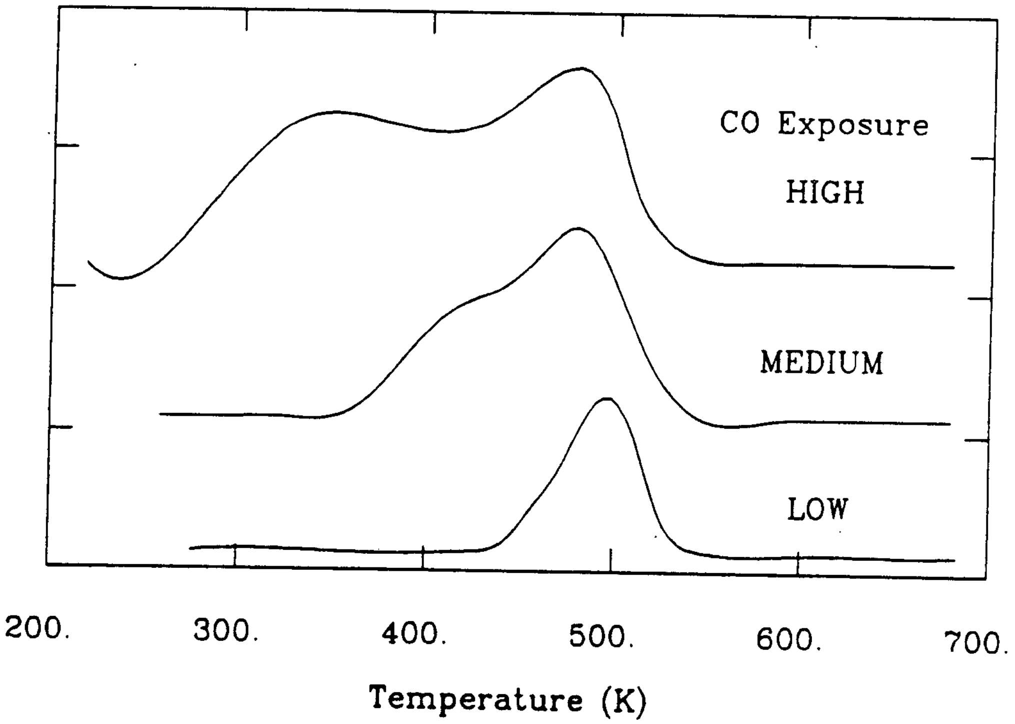

Figure 4.1: CO TPD from clean Pd(111) for low, medium and high CO exposures.

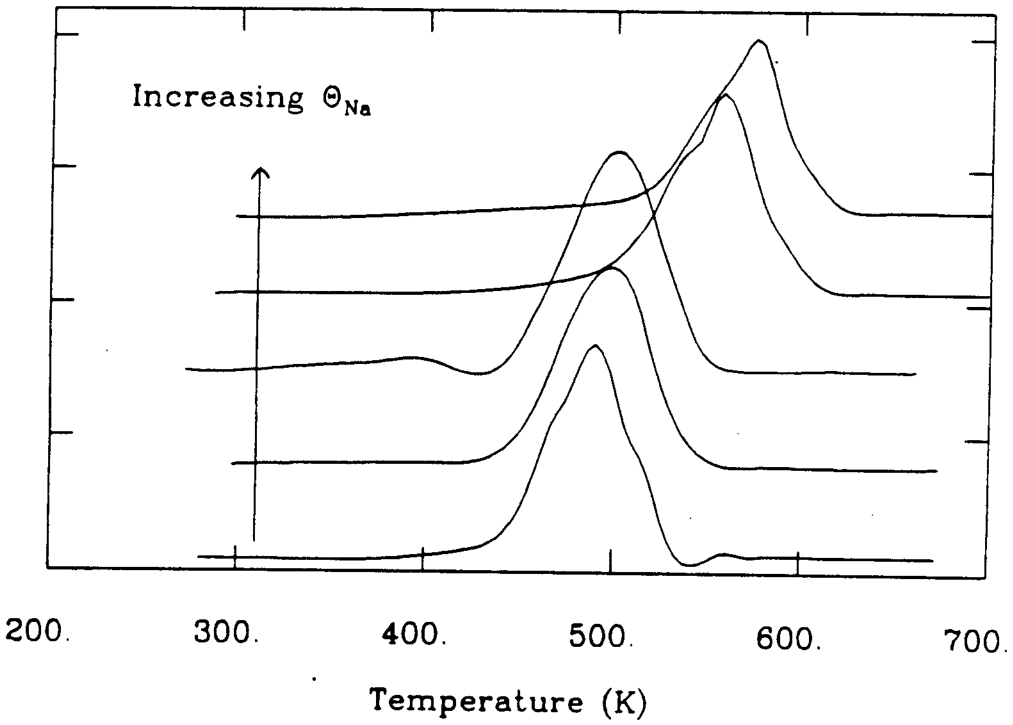

Figure 4.2: CO TPD from sodium-covered Pd(111) for low CO exposures.

that silicon diffused into the bulk. The CO desorption temperature increased as a silane dosed surface was heated repeatedly to 700K. Initially, CO desorbed in a broad peak ranging from 250K to 510K, with maximum at 270K and 390K. Subsequent CO TPD yielded a skewed peak centered at 390K. The third and all other CO TPD that followed for $\Theta_{Si} = .25$ yielded a larger and sharper peak centered at 435K. Sequential silane doses followed by heating shifted the CO desorption peak gradually from 480K ($\Theta_{Si} = 0$) to 420K ($\Theta_{Si} = .36$) (Figure 4.3). With these temperature flashes to 700K, $\Theta_{Si} = .36$ was the maximum obtainable coverage on the palladium surface.

The addition of phosphorus decreased the desorption temperature of CO relative to the Pd(111) surface. As coverages were incremented up to $\Theta_P = .3$ the desorption maximum continuously shifted from 480K ($\Theta_P = 0$) to 465K ($\Theta_P = .3$) (Figure 4.4). At a coverage of $\Theta_P = .35 - .40$ a new peak at 400K appeared, which increased in intensity with increasing phosphorus coverage. At a phosphorus coverage of $\Theta_P = .5$ the high temperature peak disappeared and only the low temperature peak remained, while it also shifted to 370K.

Increasing sulfur coverage decreased the desorption temperature of CO, decreased the peak area, and changed the peak shape as shown in Figure 4.5. At a coverage of $\Theta_S = .34$ the CO desorption shifted from 480K ($\Theta_S = 0$) to 440K with a 23% decrease in the peak area. At higher coverages $.34 < \Theta_S < .47$ a low temperature shoulder grew in and the peak maximum shifted to 380K ($\Theta_S = .43$). The maximum obtainable sulfur coverage ($\Theta_S = .47$) yielded a broad skewed peak,with a desorption maximum at 370K, extending from 300K to 430K.

Addition of chlorine, as in the case of sulfur, decreased the desorption temperature of CO from Pd(111) (Figure 4.6). At low coverages $0 < \Theta_{Cl} < .20$ the maximum was shifted from 480K to 445K, and a low temperature shoulder became evident. At coverages between $\Theta_{Cl} = .22$ and $\Theta_{Cl} = .39$ this shoulder developed

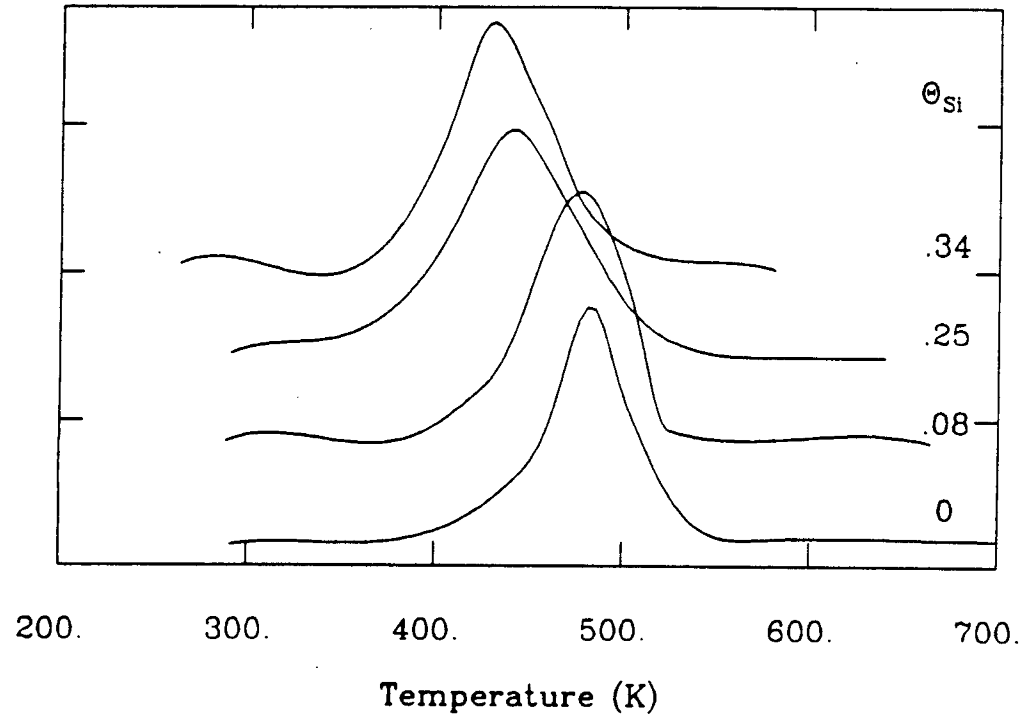

Figure 4.3: CO TPD from a silicon-covered Pd(111) surface for low CO exposures.

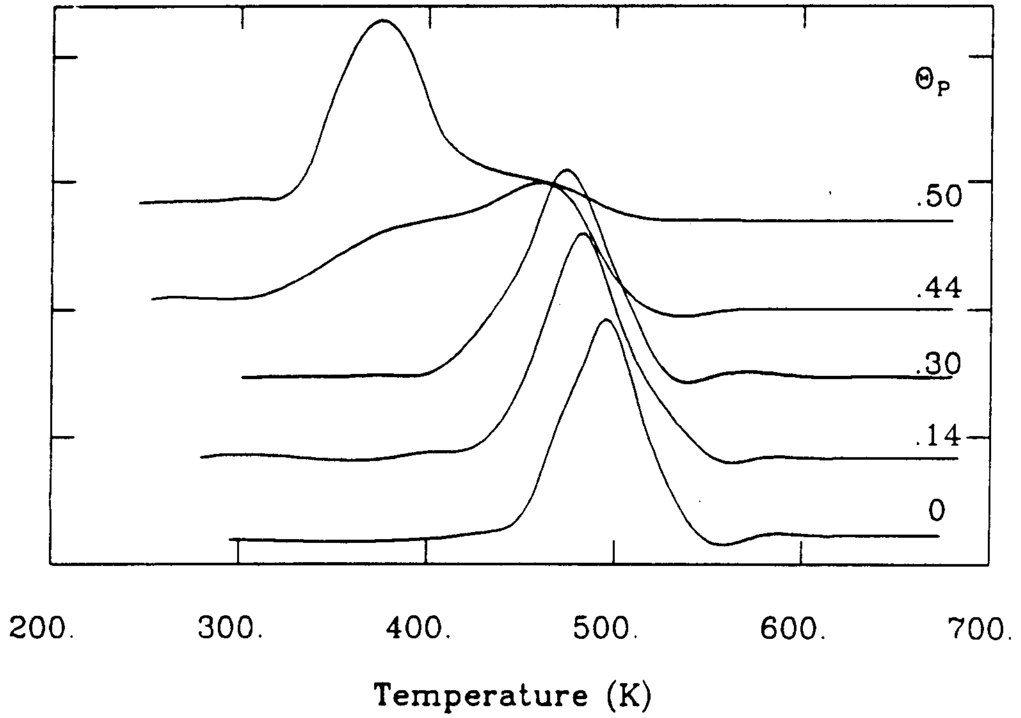

Figure 4.4: CO TPD from a phosphorus-covered Pd(111) surface for low CO exposures.

into a broad peak centered at 340K extending over a range of 150K.

4.2.2 Pd(111) - Si,P,S,Cl - H_2

Hydrogen desorbs from clean Pd(111), with a maximum rate at 310K in a single peak extending over a 100K range. The addition of the surface additives did not appreciably change the peak maximum or shape, but only decreased the amount of hydrogen that adsorbed on the surface. Figure 4.7 shows the relative change in desorbing hydrogen as a function of additive coverage. Chlorine showed the largest decrease in hydrogen chemisorption followed by sulfur, phosphorus and then silicon.

4.2.3 Pd(100) - K,Si,P,S,Cl - CO

CO TPD traces from clean Pd(100) surfaces show a single peak maximum at 470K at low coverages (1×10^{-9} torr, 50 sec) (Figure 4.8). Increasing CO exposures (1×10^{-8} torr, 50 sec) shifted the maximum to 420K with a low temperature shoulder at 390K. At saturation coverages (2×10^{-8} torr, 50 sec) the peak had a maximum at 420K with a well defined shoulder at 360K.

Potassium increased the CO desorption temperature maximum. At low potassium coverages ($\Theta_K = 0 \rightarrow .2$) the CO maximum shifts from 470K to 560 with broadening (Figure 4.9). At higher coverages ($\Theta_K > .35$) a sharp CO peak evolves at 620K. As the potassium concentration is increased this peak becomes larger relative to the 560K peak.

On the silicon covered surface the CO desorption maximum shifted to lower temperatures relative to clean Pd. Trace quantities of silicon ($\Theta_{Si} = .05$) shifted the maximum by 80° to 390K for low CO exposures. Medium CO exposures showed a maximum at 360K (Figure 4.10). Further additions of silicon ($.1 < \Theta_{Si} < .35$) gradually shifted the maximum down to 320K ($\Theta_{Si} = .35$) for low CO

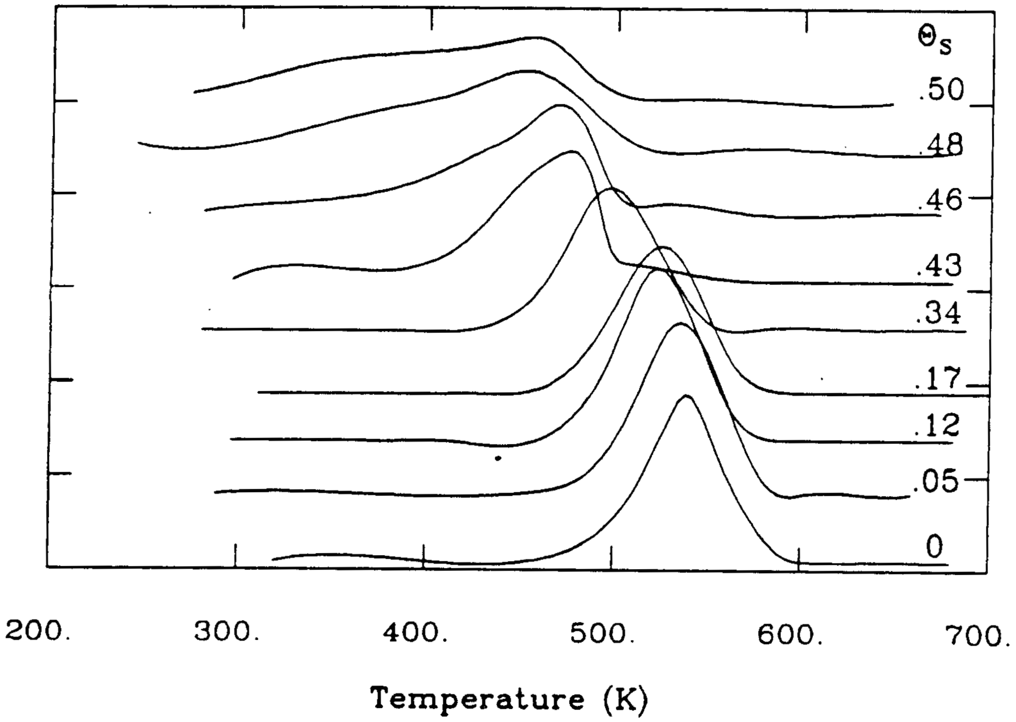

Figure 4.5: CO TPD from a sulfur-covered Pd(111) surface for low CO exposures.

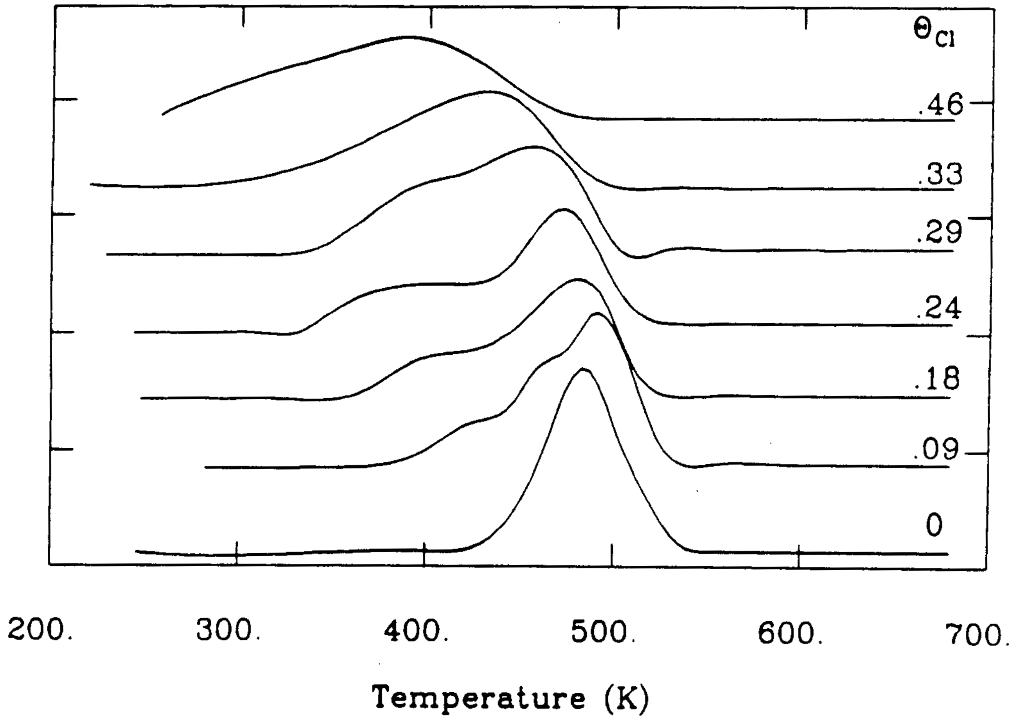

Figure 4.6: CO TPD from a chlorine-covered Pd(111) surface for low CO exposures.

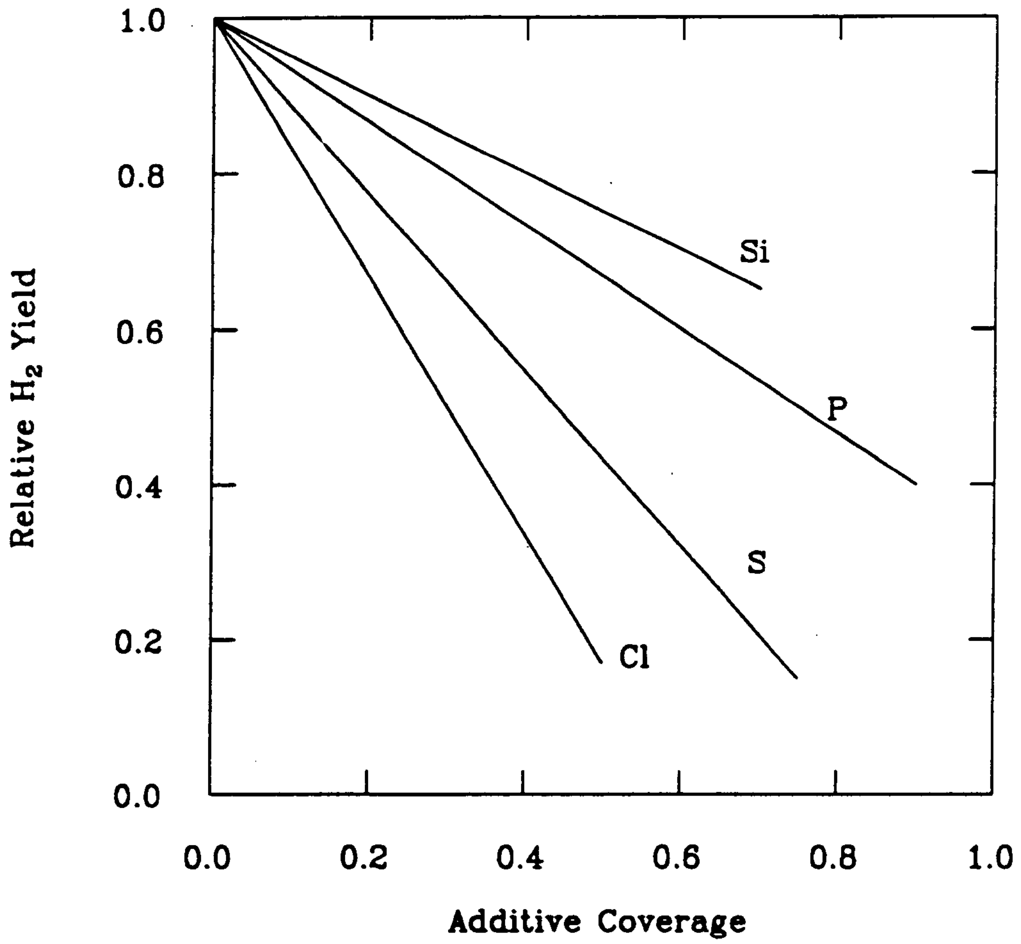

Figure 4.7: Relative amount of hydrogen desorbing from the additive-covered Pd(111) surface.

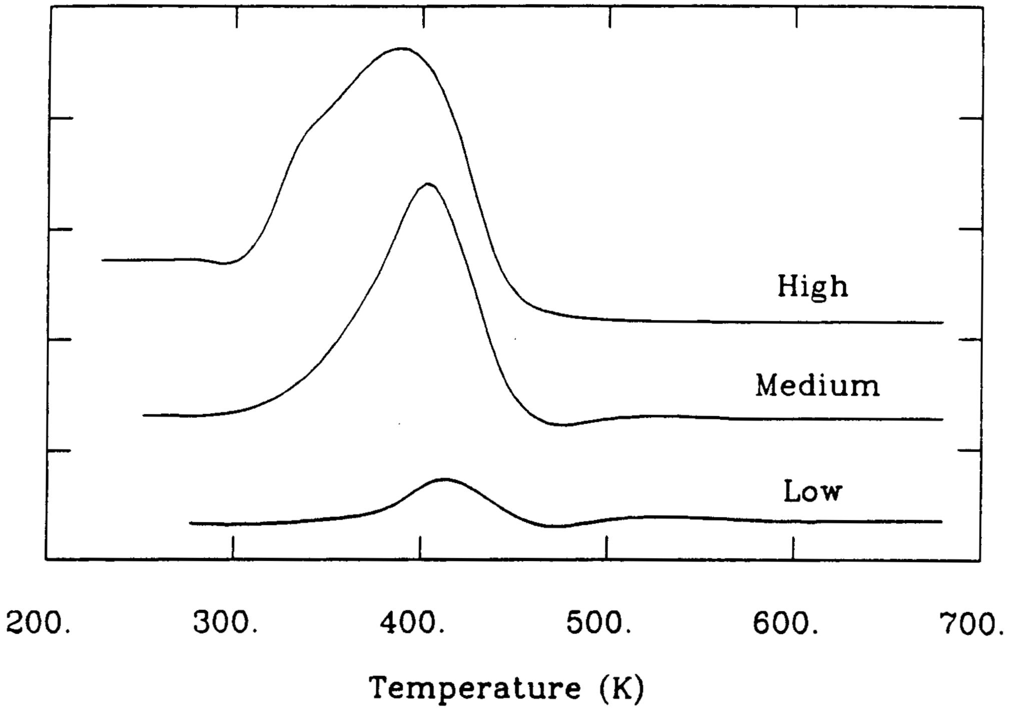

Figure 4.8: CO TPD from a clean Pd(100) surface for low, med and high CO exposures.

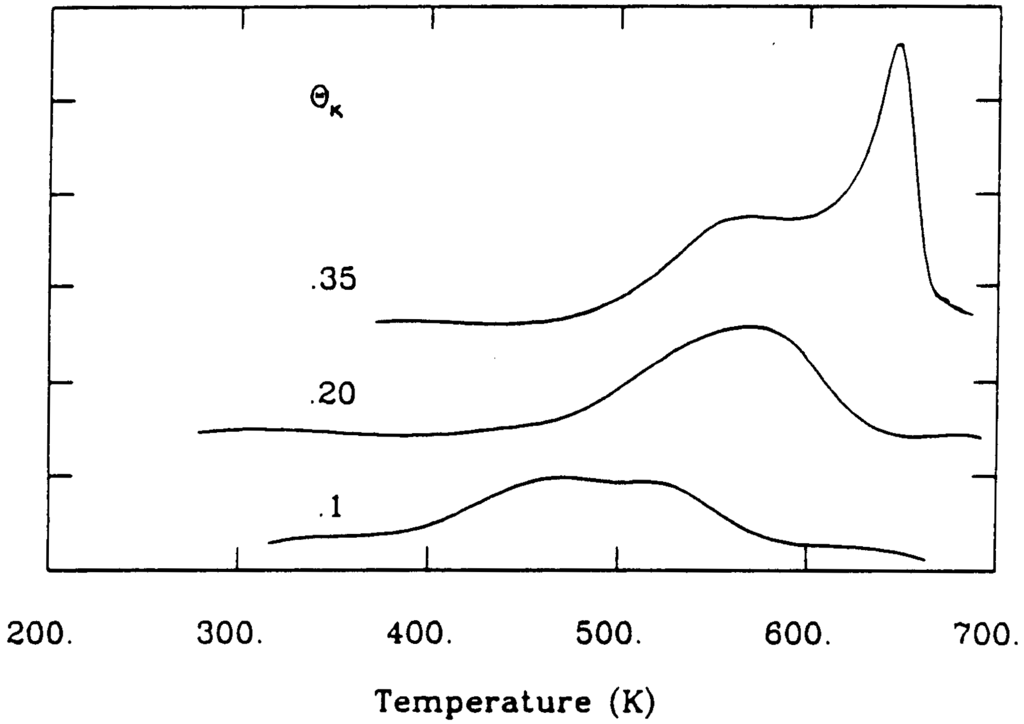

Figure 4.9: CO TPD from a potassium-covered Pd(100) surface for low CO exposures.

exposures (1×10^{-9} torr, 50 sec) and 260K at high (2×10^{-8} torr, 50 sec) exposures. No major changes in either the peak area or shape were observed.

Addition of phosphorus to the Pd(100) surface decreased CO desorption temperatures with peak broadening (Figure 4.11). At low coverages ($\Theta_P = .1$) the CO maximum were at 420K, 400K and 390K (340K shoulder) for low (1×10^{-9} torr, 50 sec), medium (1×10^{-8} torr, 50 sec) and high (2×10^{-8} torr, 50 sec) exposures of CO respectively. At higher coverages ($\Theta_P = .25$), the maximum was shifted to 370K for low CO exposures.

Sulfur lowered the CO desorption maximum, changed the peak shape and also decreased the amount of adsorbed CO (Figure 4.12). At low coverages , $0 < \Theta_S < .1$ the CO maximum were shifted to 420K, 390K and 380K for low, medium and high CO exposures. At sulfur coverages between $.1 < \Theta_S < .25$ a low temperature shoulder developed which evolved into the major peak centered at 330K, 310K and 310K for low (1×10^{-9} torr, 50 sec), medium (1×10^{-8} torr, 50 sec) and high high) CO exposures. For $\Theta_S > .25$ this new peak continued to shift to lower desorption temperatures reaching 240K at the maximum obtainable sulfur coverage of $\Theta_S = .6$.

Increasing chlorine concentration on the Pd(100) surface decreased the desorption temperatures of CO without changing peak shape up to $\Theta_{Cl} = .25$ (Figure 4.13). At $\Theta_{Cl} = .21$ the CO maximum at low CO exposures was shifted from 470K ($\Theta_{Cl} = 0$) to 310K ($\Theta_{Cl} = .21$). For higher CO exposures the maximum was shifted to 300K and 290K (1×10^{-8} torr, 50 sec and 2×10^{-8} torr, 50 sec doses respectively). At high chlorine coverages ($\Theta_{Cl} = .32$) all CO exposures yield the same double peak (195K and 285K) CO desorption trace.

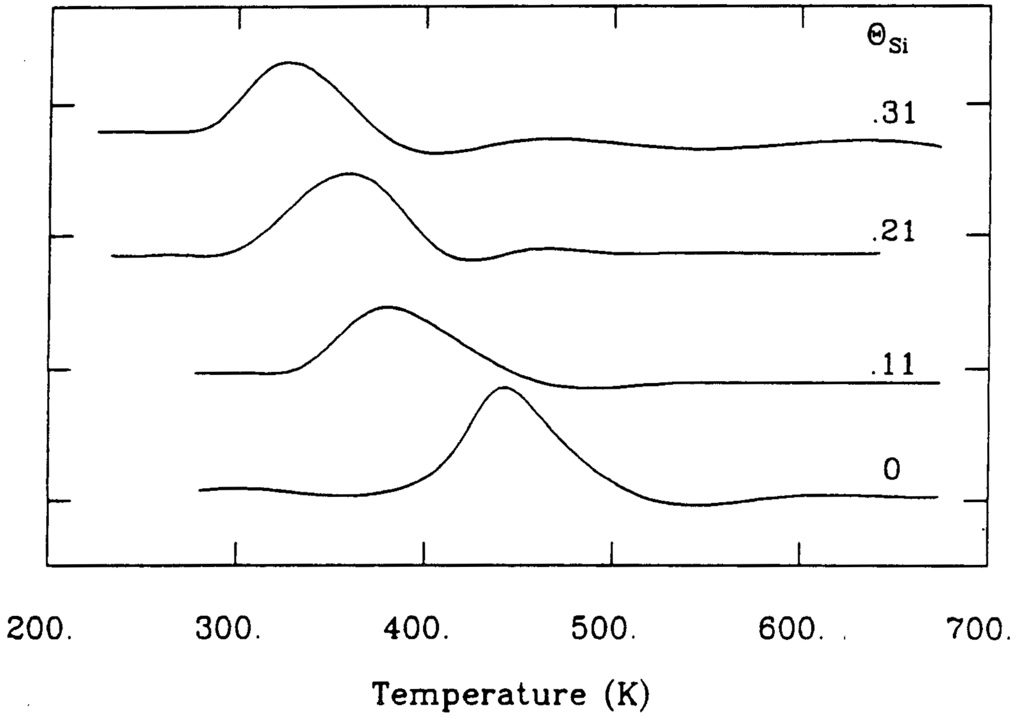

Figure 4.10: CO TPD from a silicon-covered Pd(100) surface for lo CO exposures.

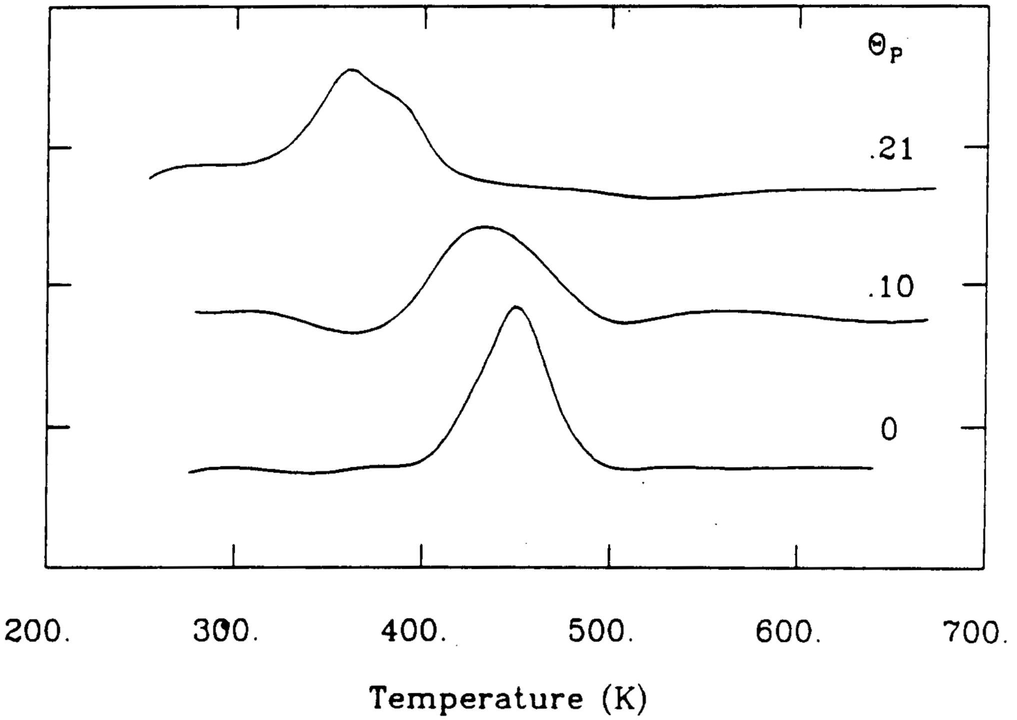

Figure 4.11: CO TPD from a phosphorus-covered Pd(100) surface for low CO exposures.

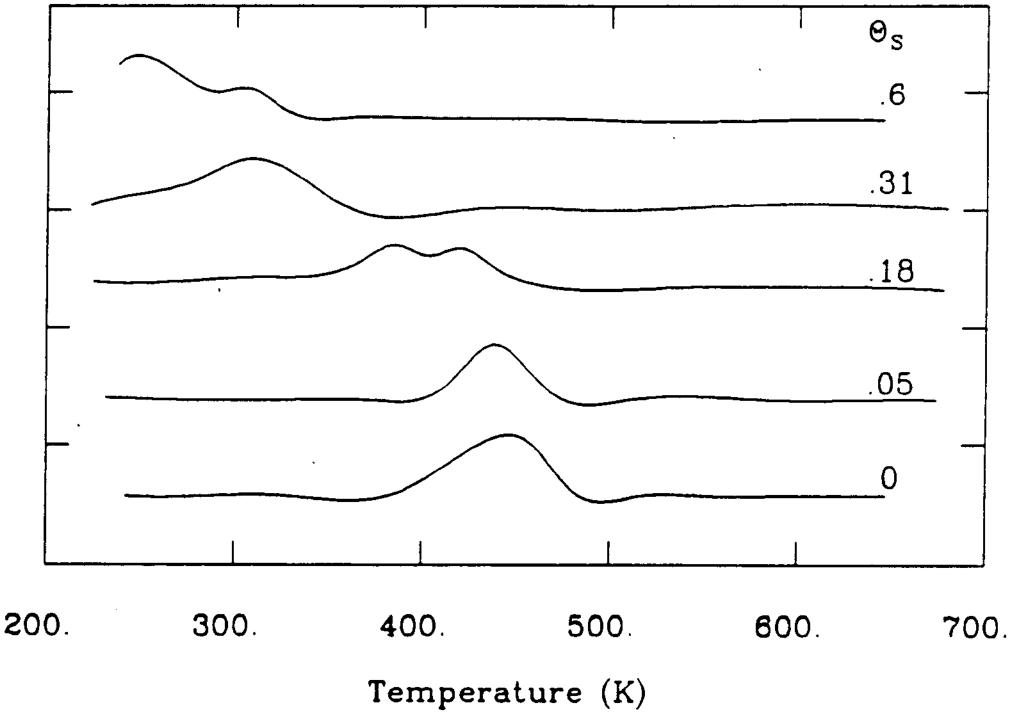

Figure 4.12: CO TPD from a sulfur-covered Pd(100) surface for low CO exposures.

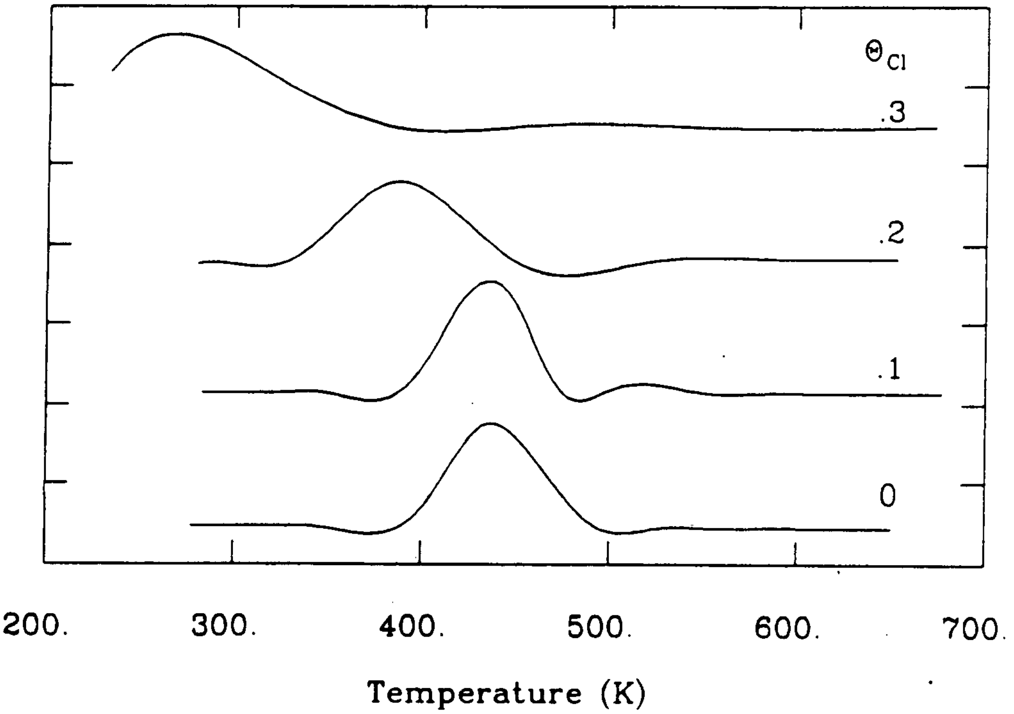

Figure 4.13: CO TPD from a chlorine-covered Pd(100) surface for low CO exposures.

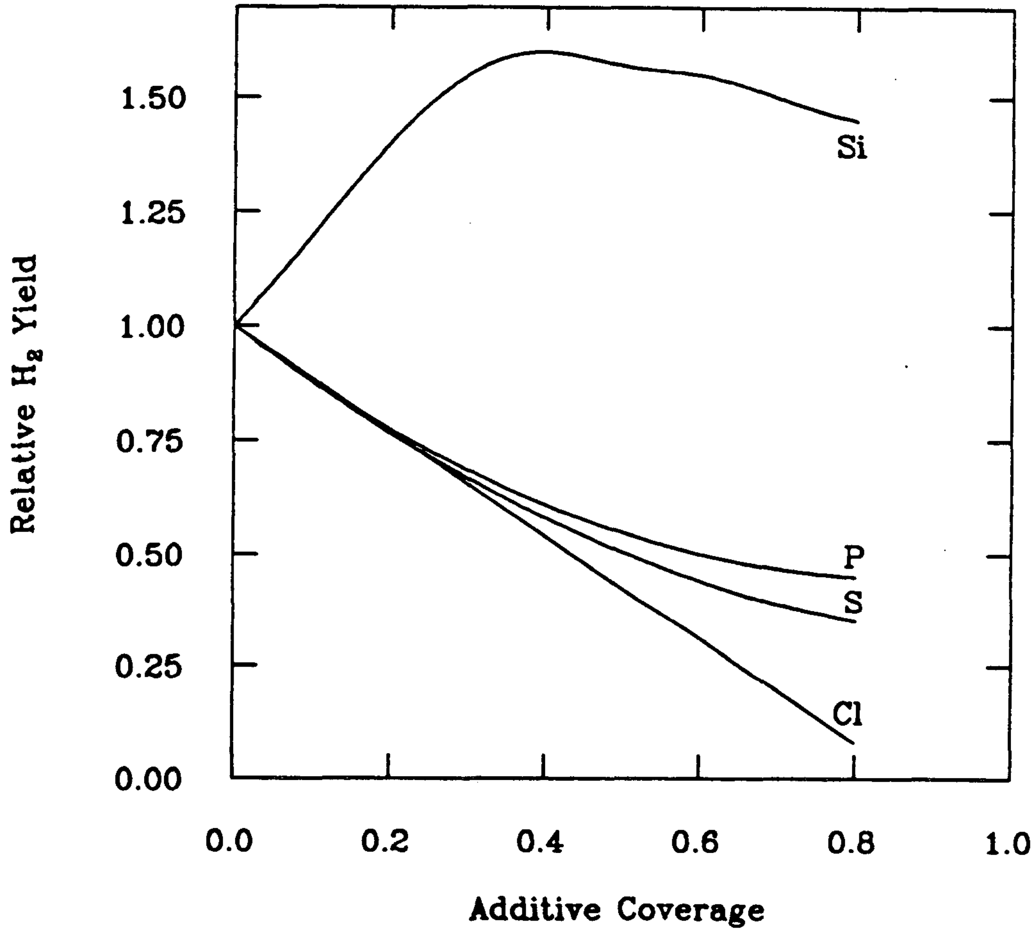

Figure 4.14: Relative amount of hydrogen desorbing from the additive-covered Pd(100) surface. Silicon increases the sticking coefficient of hydrogen whereas the other additives decrease the sticking coefficient on this palladium surface.

4.2.4 Pd(100) - Si,P,S,Cl - H_2

Figure 4.14 shows the relative amount of hydrogen desorbing from the additive covered Pd(100) surface. The desorption maximum at 310K of hydrogen from clean Pd(100) is independent of additive coverage. The addition of phosphorus, sulfur and chlorine decreased the amount of chemisorbed hydrogen (decreasing peak area), whereas silicon increased ($\Theta_{Si} = .4$) the amount of hydrogen by 60%.

4.2.5 Pd(110) - Na,Si,P,S,Cl - CO

The Pd(110) surface dosed with CO showed a single CO desorption maximum at 440K and 430K for low (1×10^{-9} torr, 50 sec) and medium (1×10^{-8} torr, 50 sec) coverages. At high CO exposures there was a maximum at 430K with a shoulder at 350K and also a new peak at 270K (Figure 4.15). Surface additives were found to modify CO bonding to the surface as outlined below.

Addition of sodium on the (110) surface decreased the desorption temperature of CO, in contrast to the Pd(111) and Pd(100) surfaces (Figure 4.16). At low coverages ($\Theta_{Na} < .2$) the maximum was shifted from 430K to about 400K with a slight (10%) decrease in peak area. At higher coverages ($\Theta_{Na} > .2$) a new low temperature desorption peak at 350K appears (original peak shifted to 385K)[1]. Similar results were observed for potassium on this surface.

Silicon on Pd(110) shifted the CO desorption maximum to lower temperatures (Figure 4.17) without changing the peak shape. At low CO exposures (1×10^{-9} torr, 50 sec) CO desorbs at 350K and for medium exposures the maximum is at 320K for a silicon coverage of $\Theta_{Si} = .44$. For these high silicon coverages, high CO exposures yielded a broad (200°) peak centered at 310K and skewed toward higher temperatures. At intermediate silicon coverages ($\Theta_{Si} = .20 - .30$) the CO maximum is at 370K with a shoulder at 285K, one-fifth as intense.

Phosphorus on the Pd(110) surface had little effect on CO chemisorption at any phosphorus coverage (Figure 4.18). At low CO exposures the CO maximum shifted from 430K to 410K. For medium exposures there were negligible changes in peak area and the desorption maximum shifted from 410K ($\Theta_P = 0$) to 400K ($\Theta_P = .53$). At high CO exposures the low temperature CO peak at 270K was shifted to higher temperature, yielding a broad 210° peak with maximum at 310K and 420K. Doubling this CO exposure (2×10^{-8} torr, 100 sec.) populated the low

---

[1] Electron beam-induced sodium desorption makes coverage determination difficult.

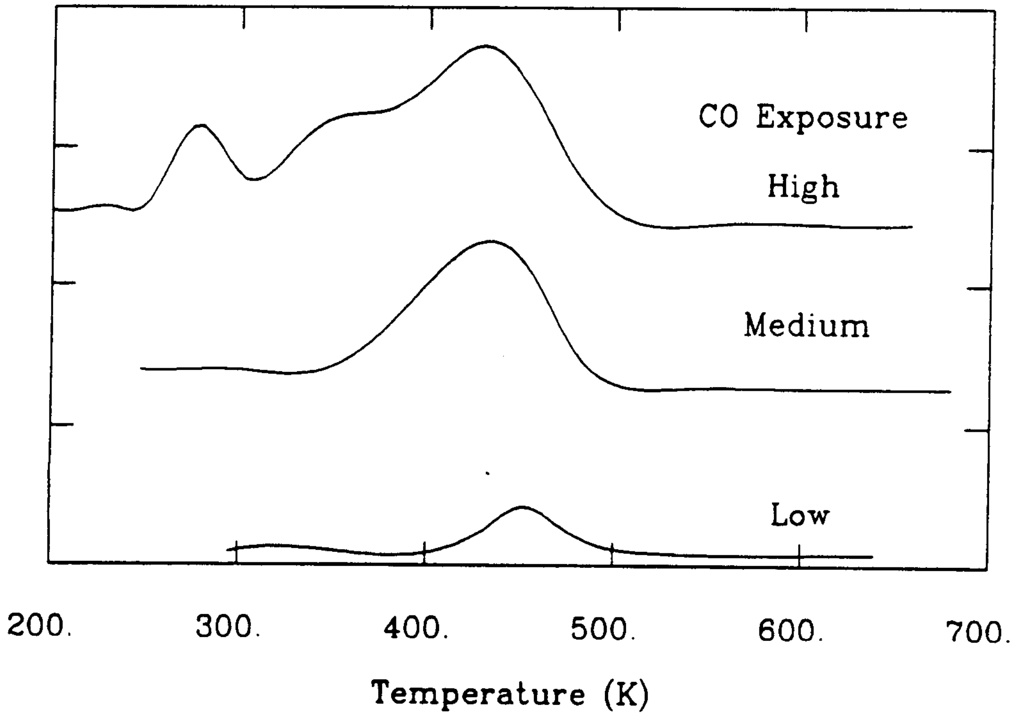

Figure 4.15: CO TPD from a clean Pd(110) surface for low CO exposures.

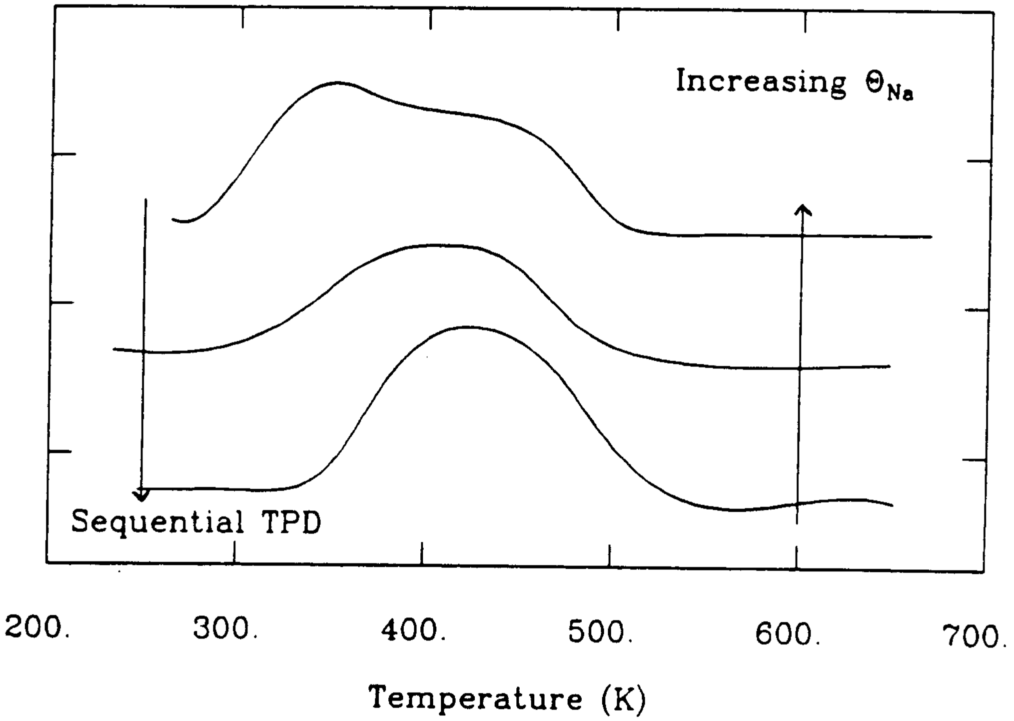

Figure 4.16: CO TPD from a sodium-covered Pd(110) surface for low CO exposures.

temperature side of the broad peak with a new peak at 260K.

Low sulfur coverages ($\Theta_S = 0 \rightarrow .39$) on the Pd(110) surface shift the CO desorption maximum 50K lower in temperature relative to the clean surface (Figure 4.19). At higher sulfur coverages a new low temperature CO desorption peak at 340K appears which increases in intensity relative to the high temperature (420K peak). Increasing sulfur coverages shift the peak to 270K ($\Theta_S = .5$).

The presence of chlorine adsorbed on Pd(110) changed the shape and temperature of CO TPD traces (Figure 4.20). For low CO exposures (1×10^{-9} torr, 50 sec) the peak maximum shifted from 430K to 320K with a peak twice as wide ($\Theta_{Cl} = 0 \rightarrow .32$). At coverages above $\Theta_{Cl} = .32$ this broad peak separated into two equivalent peaks centered at 270K and 330K. For medium CO exposures the maximum at 430K is shifted to 330K and becomes a shoulder on a peak approximately 1.5 times larger centered at 260K. Increasing CO exposures populated the low temperature 260K desorption peak.

4.2.6 Pd(110) - Si,P,S,Cl - H_2

The TPD of hydrogen on additive covered Pd(110) showed no temperature shifts, only peak area changes. Figure 4.21 shows the relative amount of hydrogen desorbing as a function of additive coverage. Silicon has the largest hydrogen chemisorption blocking effect, followed by chlorine, sulfur and phosphorus. It is interesting to note that silicon did not lie above phosphorus as would be expected from relative positions in the periodic table of the elements.

4.2.7 Pd(100) - K,Si,P,S,Cl - Work Function

To observe how the surface electronegativity changes with the addition of different adatoms to the surface, work function measurements were performed on Pd(100) (Figure 4.22). The decrease in work function is greatest for potassium, indicating

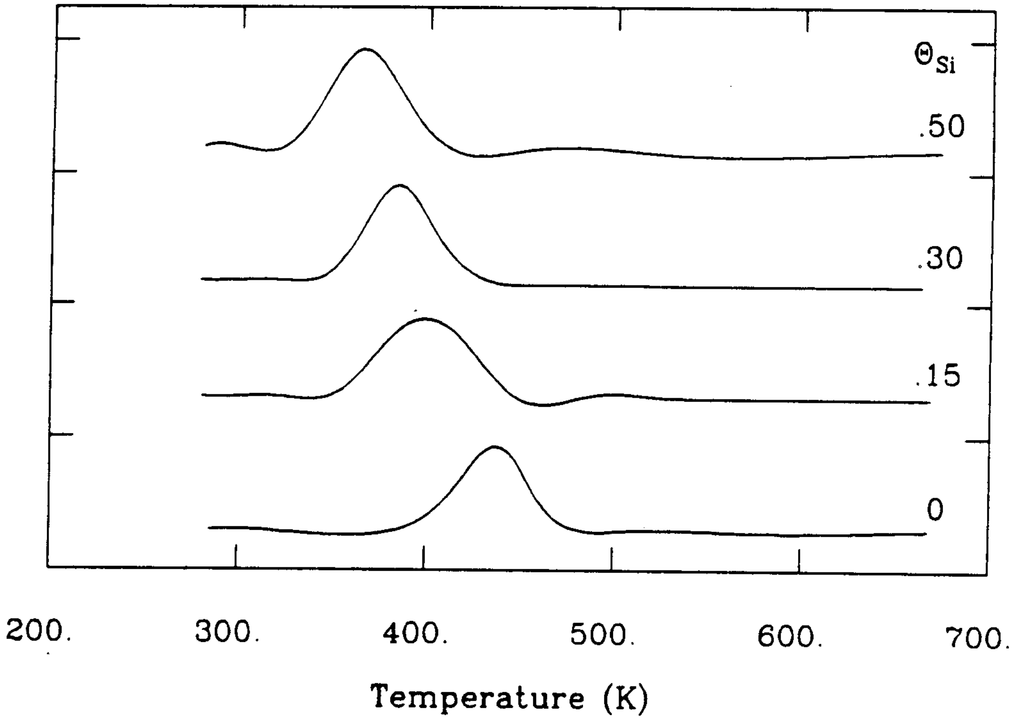

Figure 4.17: CO TPD from a silicon-doped Pd(110) surface for low CO exposures.

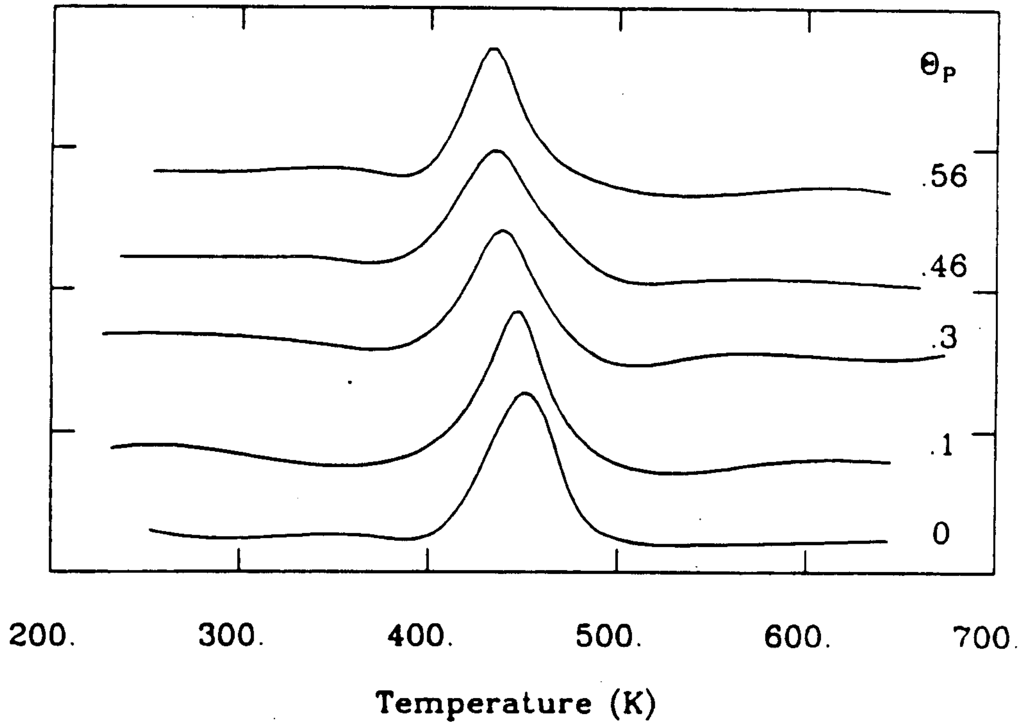

Figure 4.18: CO TPD from a phosphorus-covered Pd(110) surface for low CO exposures.

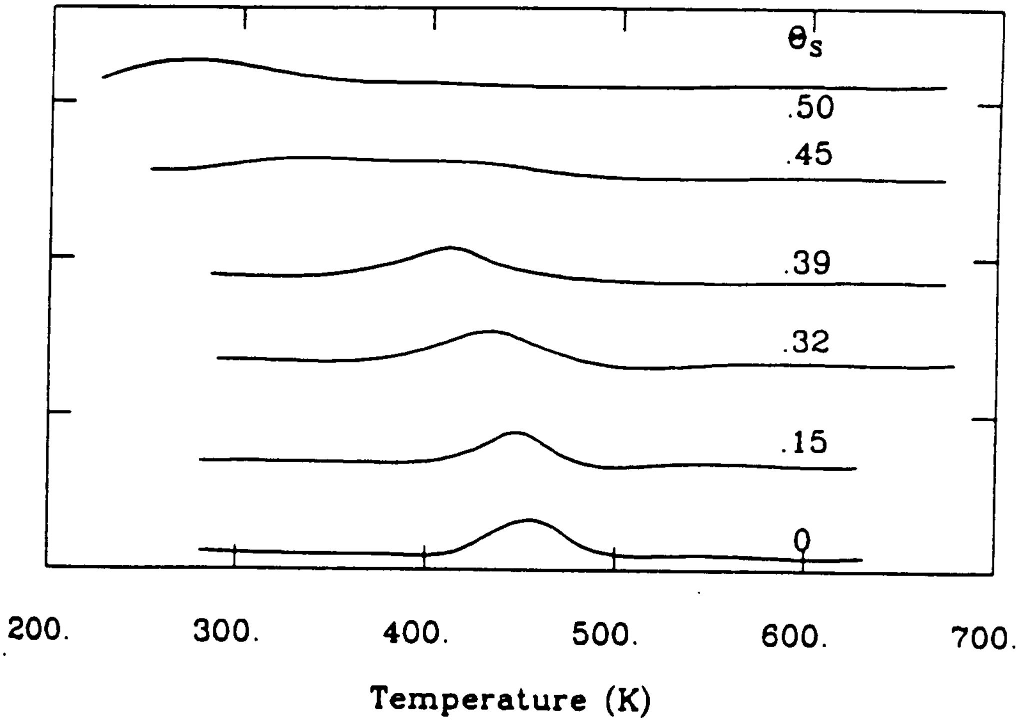

Figure 4.19: CO TPD from a sulfur-covered Pd(110) surface for low CO exposures.

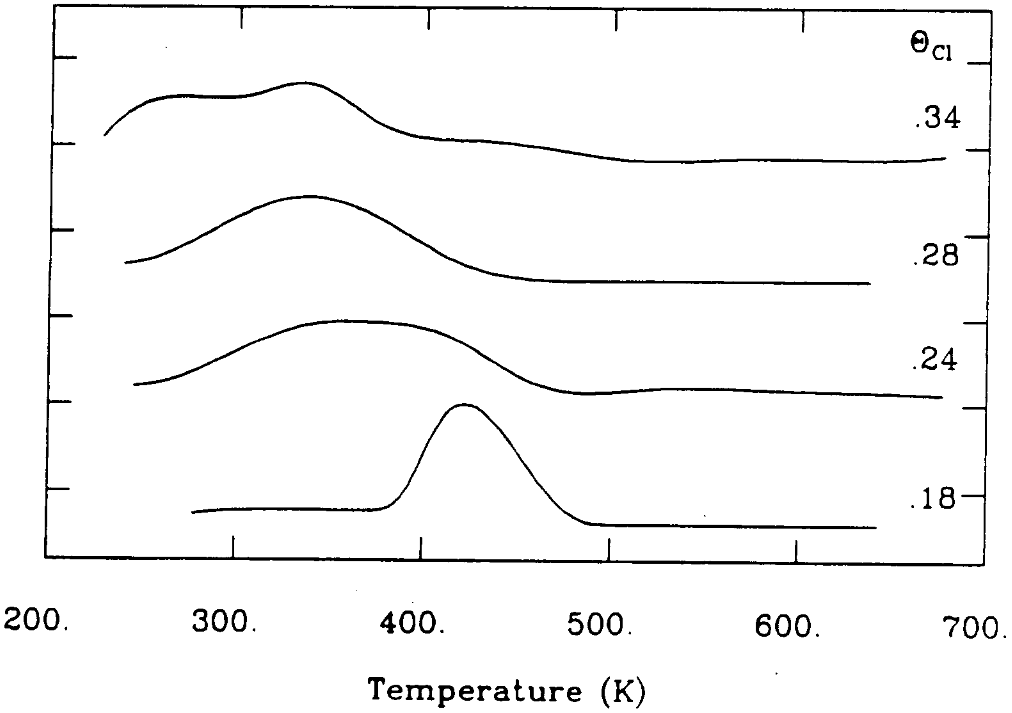

Figure 4.20: CO TPD from a chlorine-covered Pd(110) surface for low CO exposures.

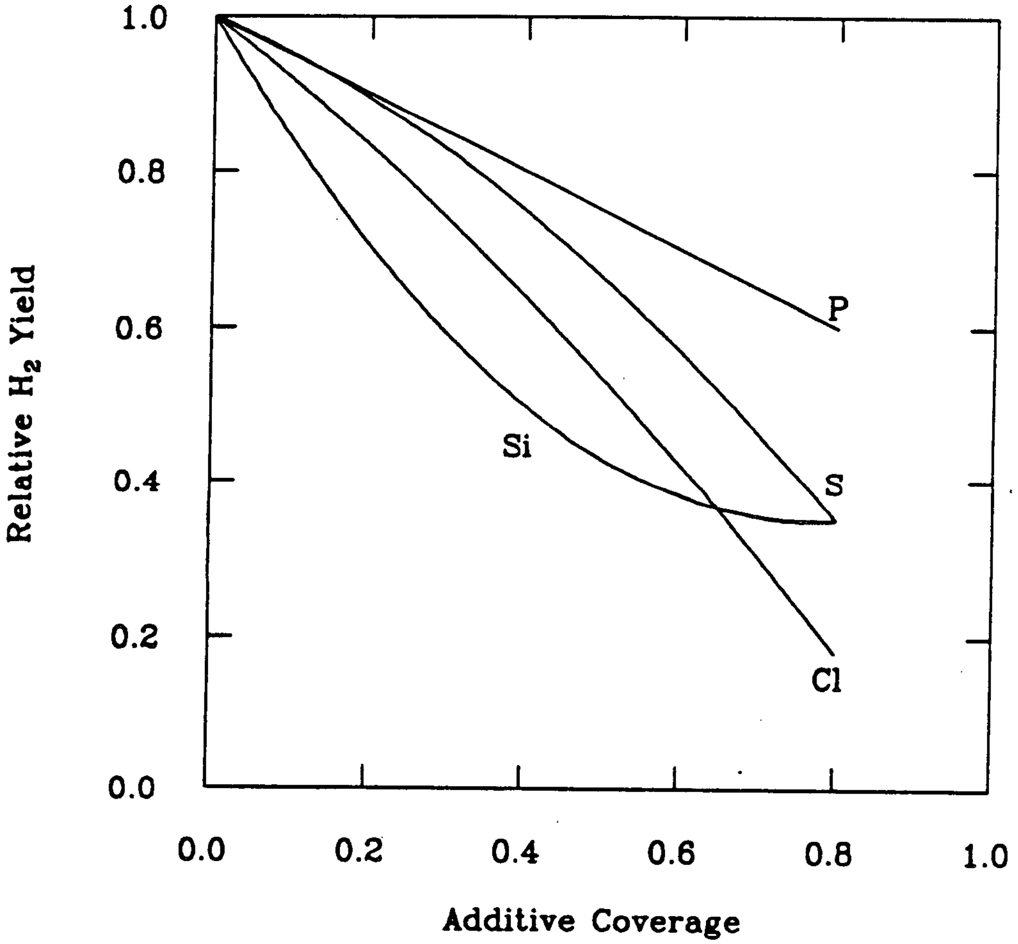

Figure 4.21: The relative hydrogen sticking coefficients on additive covered Pd(110) is shown here. Silicon has the largest hydrogen chemisorption blocking effect followed by chlorine, sulfur and phosphorus.

that it donates the most electron density to the surface per unit coverage, followed by silicon and then phosphorus. Conversely, sulfur increased the work function, implying that it withdraws electron density from the surface.

For silicon, heating the sample to 770K increased the work function by .75 eV (closer to clean Pd(100)), while only slightly decreasing the Pd-Si AES ratio (Figure 4.23). Since no silicon-containing fragments were distinguishable in the mass spectrum, the silicon diffused into the near-surface region of the crystal. This change in work function after sample flashing or annealing was not found for any other surface additive on Pd(100).

4.2.8 LEED

A study of surface ordering was undertaken in this research. Some of the additives were found to order on the palladium single crystal surfaces studied. A complete literature survey of K, Na, Si, P, S and Cl ordering on the Pd(111), (100) and (110) surfaces is presented in Table 4.1.

Phosphorus orders on both the (111) and (110) surfaces. On the (111) surface a $(\sqrt{7} \times \sqrt{7})R17^\circ$ structure forms at low coverages. The spots sharpen at higher coverages ($\Theta_P > .3$) (Figure 4.24). Ordered LEED patterns were also observed for the silicon-covered (100) and (110) surfaces (Figure 4.25). The streaking of the diffraction spots in one direction for silicon on the (110) surface indicate preferential ordering in one direction.

4.2.9 Pd(111) - S - CO (EELS)

Electron Energy Loss Spectroscopy (EELS) was used to study CO adsorbed on clean and sulfur modified Pd(111) surface. The EELS spectrum (Figure 4.26) of CO on the clean Pd(111) surface shows two peaks at 1835 and 325 cm^{-1} which can be assigned to the ν_{CO} and ν_{PdC} stretching modes. These frequencies indicate

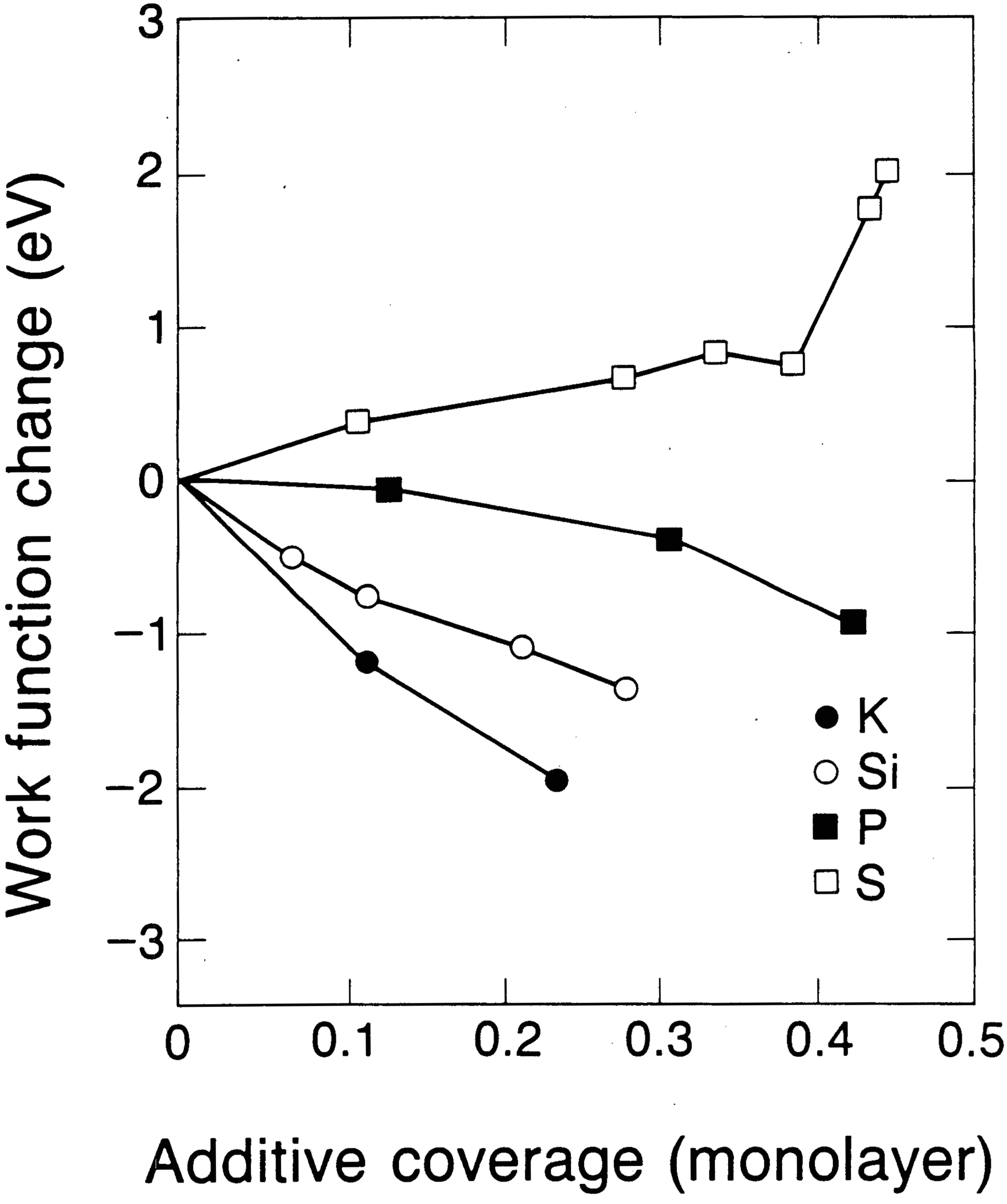

Figure 4.22: Work function changes on the Pd(100) surface in the presence of surface additives is shown here. In general they follow the trend that elements more electronegative than palladium withdraw electron density and increase the work function, and those more electropositive donate electron density and decrease the work function.

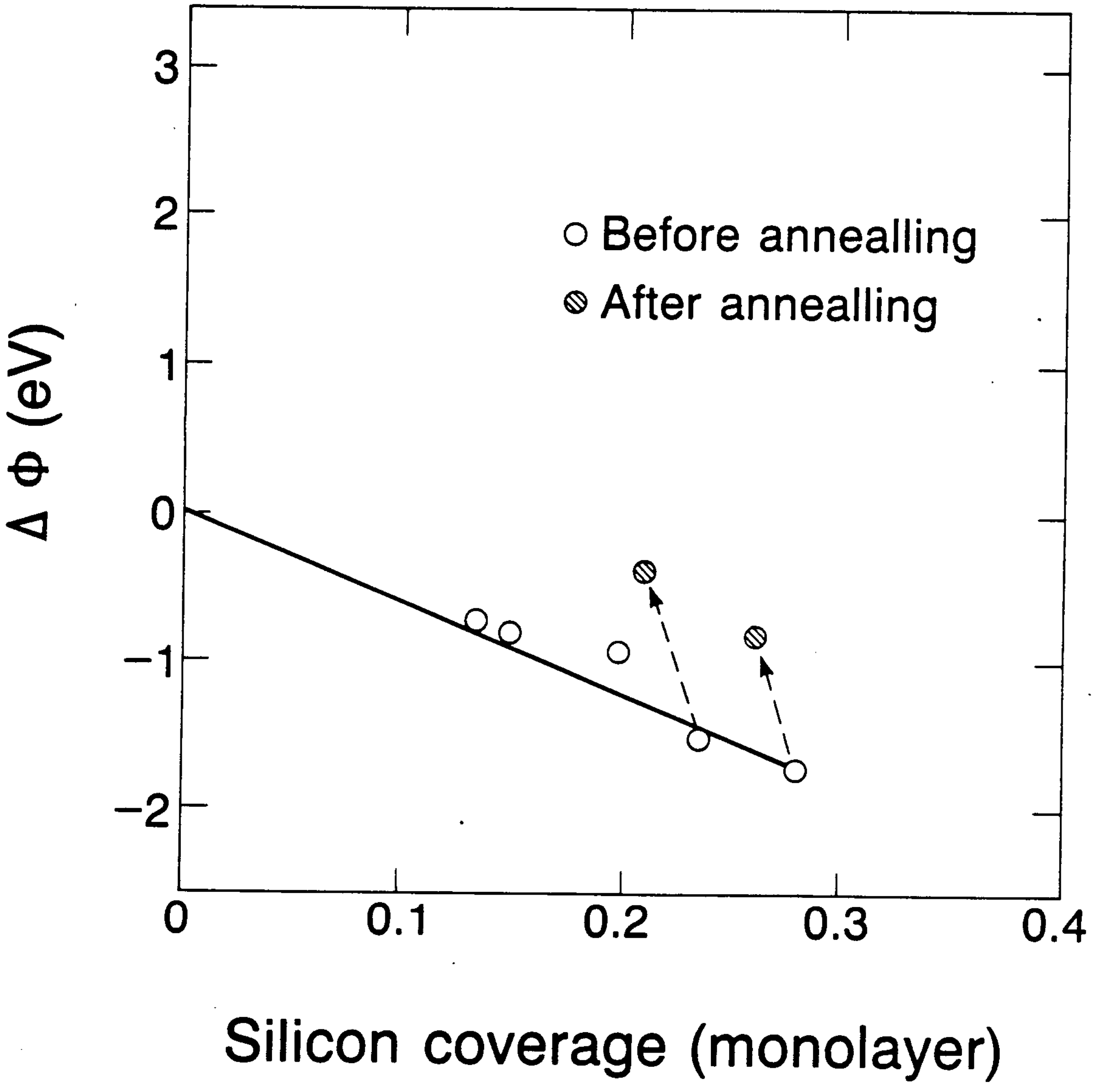

Figure 4.23: On the silicon-covered Pd(100) surface, heating the sample to 770K decreased the work function by .75 eV (closer to the clean surface), while only slightly decreasing the Pd-Si AES ratio.

Additive	**Surface**		
	(111)	**(100)**	**(110)**
CO	$(\sqrt{3} \times \sqrt{3})R30°$ [4]	$(4 \times 2)R45°$ [5]	$c(2 \times 2)$ [4] (4×2)
K, Na			(1×2) reconst.[6]
Si		**Ordered**	**Ordered**
P	$(\sqrt{7} \times \sqrt{7})\mathbf{R17°}$		**Ordered**
S	$(\sqrt{3} \times \sqrt{3})R30°$	(2×2) [7]	(2×3) [8] $c(2 \times 2)$ $c(8 \times 2)$ (3×2)
Cl	$(\sqrt{3} \times \sqrt{3})R30°$ [9] (3×3)		$c(16 \times 2)$ [10]

Table 4.1: LEED patterns for additives on palladium single crystals.

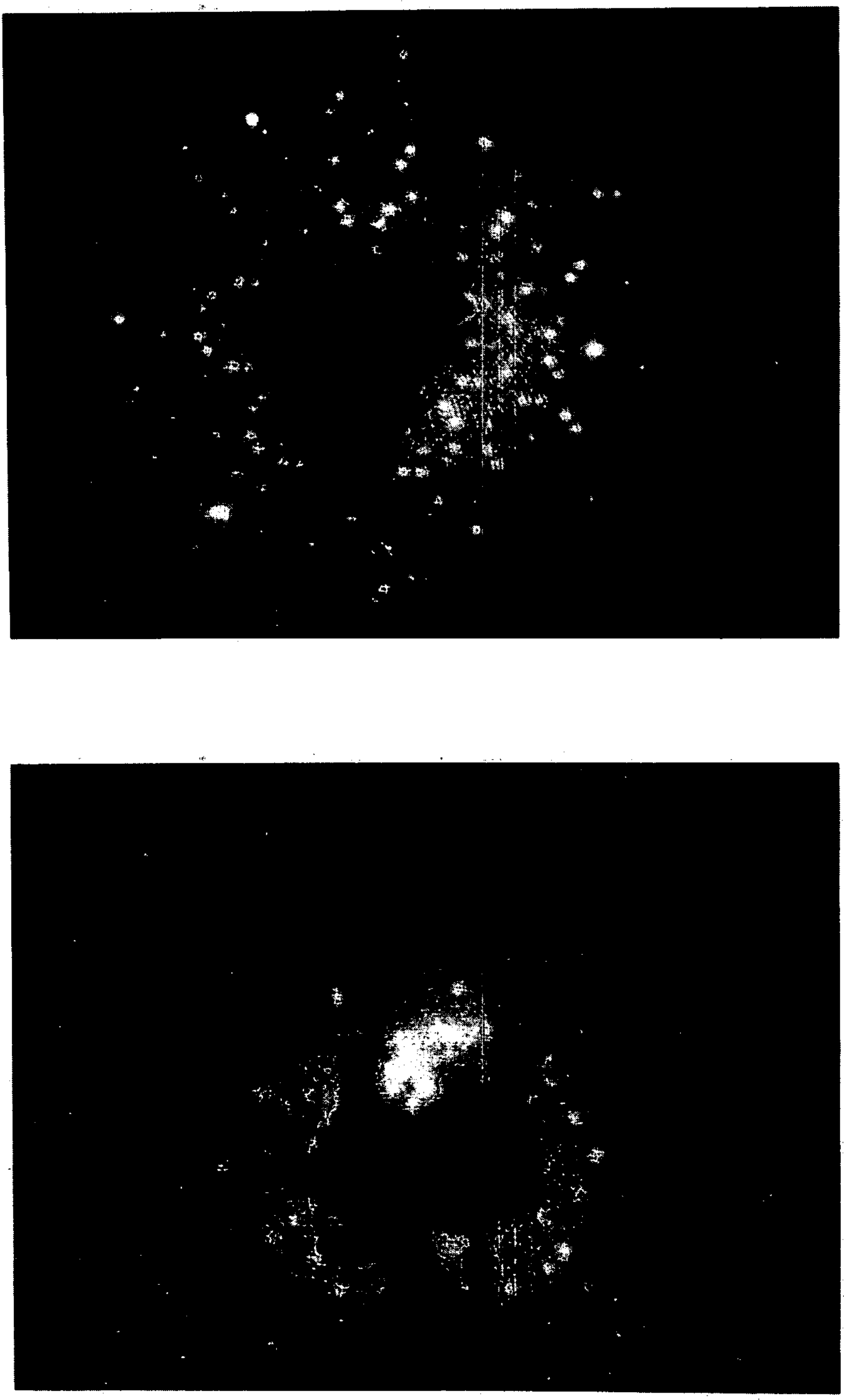

Figure 4.24: The LEED patterns of phosphorus on the (111) ($(\sqrt{7} \times \sqrt{7})R17°$) and (110) surface.

XBB 874-3311

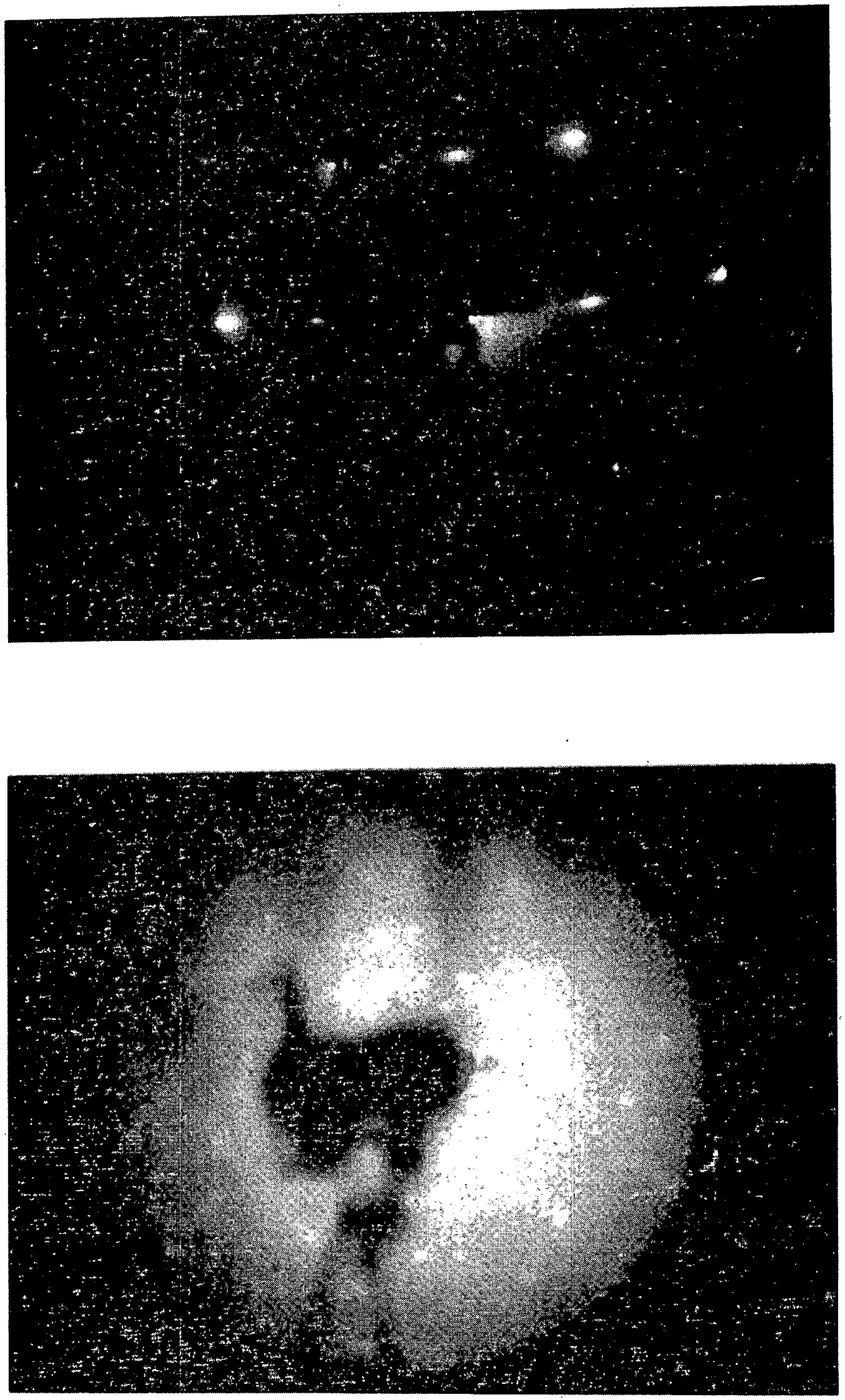

XBB 874-3314

Figure 4.25: LEED patterns of the clean and silicon-covered Pd(110) surface.

a bridged-site position for the molecule. When sulfur ($\Theta_S = .17$) is present on the surface, a new loss peak appears around 740 cm^{-1}, whereas the ν_{CO} frequency shifts down to 1755 cm^{-1}. At higher sulfur coverages this effect is more pronounced and a new low frequency peak can also be seen at 275 cm^{-1}. This latter peak can be assigned to a metal-sulfur stretching mode, similar to what is seen in sulfur-metal complexes [11].

The 740 cm^{-1} peak can be explained by a tilted CO molecule which would allow the δ_{MCO} motion to be EELS active. Some parent metal-carbonyl complexes show such vibrations around 700 cm^{-1} in the infrared spectra: 637 and 644 cm^{-1} for $Ni_2(\pi\text{-}C_5H_5)_2(\mu_2\text{-}CO)_2$ [12], 700 cm^{-1} for $Ru_6C(\mu_2\text{-}CO)(CO)_{16}$ [12] and 600 and 670 cm^{-1} for $Fe_2(\mu_2\text{-}CO)_3(CO)_6$ [13]. The formation of a SCO molecule can be ruled out by comparison to the frequencies of 859, 520 and 2062 cm^{-1} for the ν_{CS}, δ_{OCS} and ν_{CO} respectively [11].

4.2.10 Pd - K,Si,P,S,Cl - C_2H_2

The conversion of acetylene to benzene over palladium single crystals ((111), (100) and (110)) modified with submonolayer quantities of silicon, phosphorus, sulfur, chlorine and potassium has been studied under both ultra-high vacuum and atmospheric pressure conditions [14]. The reaction is structure-sensitive in both pressure regimes, and also proceeds on palladium films and palladium supported on alumina. In UHV the (111) face is the most active, followed by the (110) and (100) surfaces which are 1/8 and 1/20 as active respectively (Figure 4.27) [15]. At high pressures, the (111) and (100) surfaces have equal catalytic activity whereas the (110) face is one-fourth as active. If the percentage of open or active sites is taken into account the reaction exhibits the same structure sensitivity ordering as in UHV.[2]

---

[2] Percentage of open sites was determined by CO titrations. CO binds only to bare palladium and not to carbon overlayers

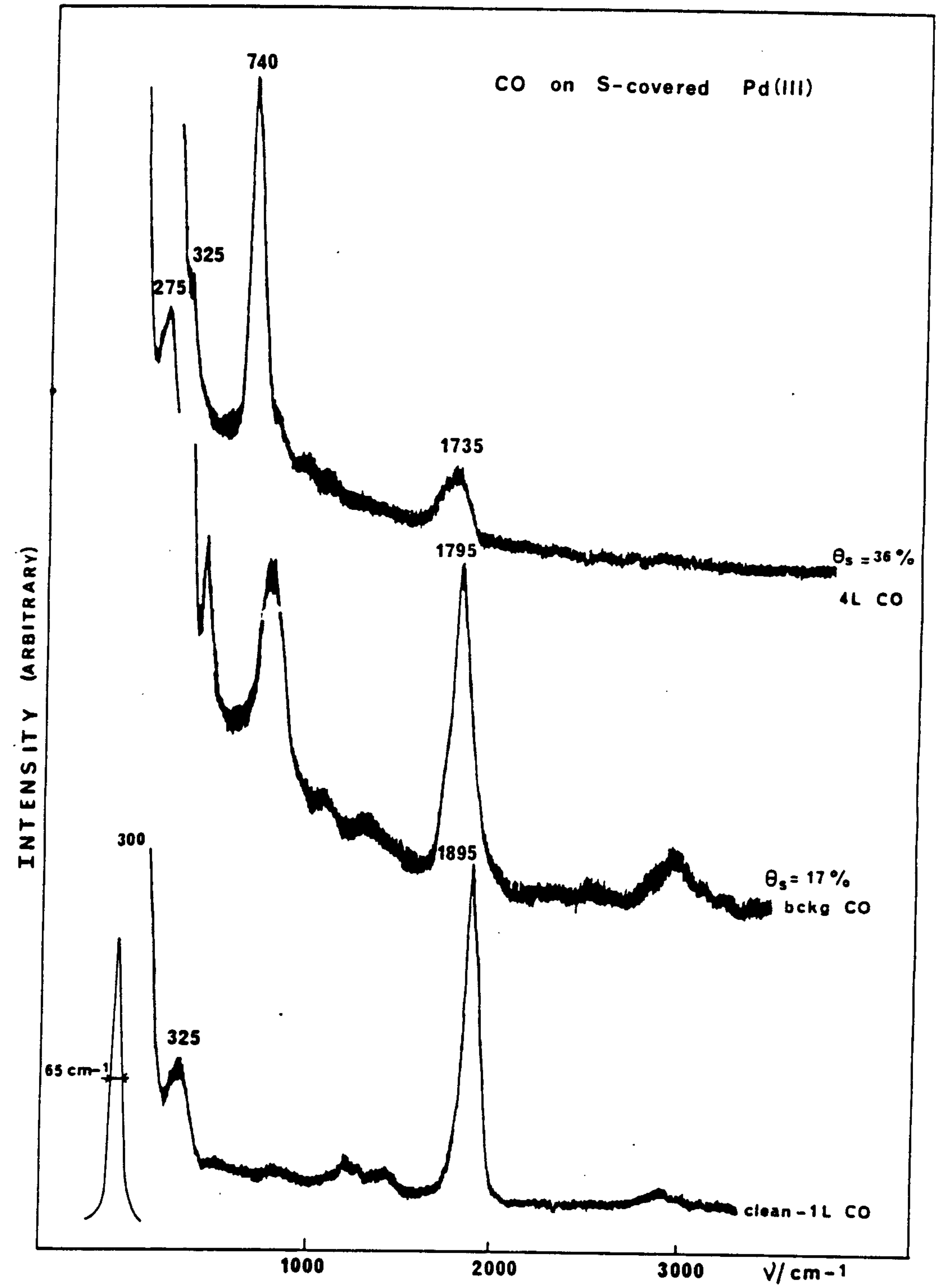

Figure 4.26: The EELS spectra of CO on sulfur-modified Pd(111) is shown here. At higher sulfur coverages new peaks grow in which can be assigned to new CO binding configurations.

At atmospheric pressures electron-donating additives enhanced the rate of benzene formation and electron-accepting additives reduced the rate [14]. It should be noted that on the (111) and (100) surfaces potassium increased benzene formation, whereas on the (110) surface potassium decreased benzene formation (Figure 4.28). It was found that potassium and silicon on the (100) surface reduced the amount of surface carbon that accumulated during the reaction and thereby increased the rate of benzene formation relative to the undoped surface (Figure 4.29). The trends at low pressures are presented in Figure 4.30). In general, potassium suppressed, silicon and phosphorus enhanced, and sulfur and chlorine left unchanged the benzene yield. In the presence of sulfur and chlorine the decomposition of acetylene and formation of ethylene were greatly suppressed in UHV. Sulfur-doped Pd(111) was a very selective catalyst for benzene formation from acetylene.

4.3 Discussion

A large amount of data has been presented which studied the effect of surface additives on small molecule bonding. From these results it can be seen that the additives exhibit varying and interesting structure-sensitive behavior. In this section the implications of these results to the fundamental understanding of the interaction of surface additives and their effect on surface bonding and catalytic activity are discussed.

4.3.1 Palladium - Additive Bonding

The strength of the palladium - additive surface bonds varied significantly. Sodium, chlorine and potassium formed much weaker bonds (as evidenced by TPD and AES after heating) than silicon, phosphorus and silicon. For the former additives the activation energy of desorption was lower than for silicon which had a lower activation energy for bulk dissolution. Sulfur and phosphorus were thermodynam-

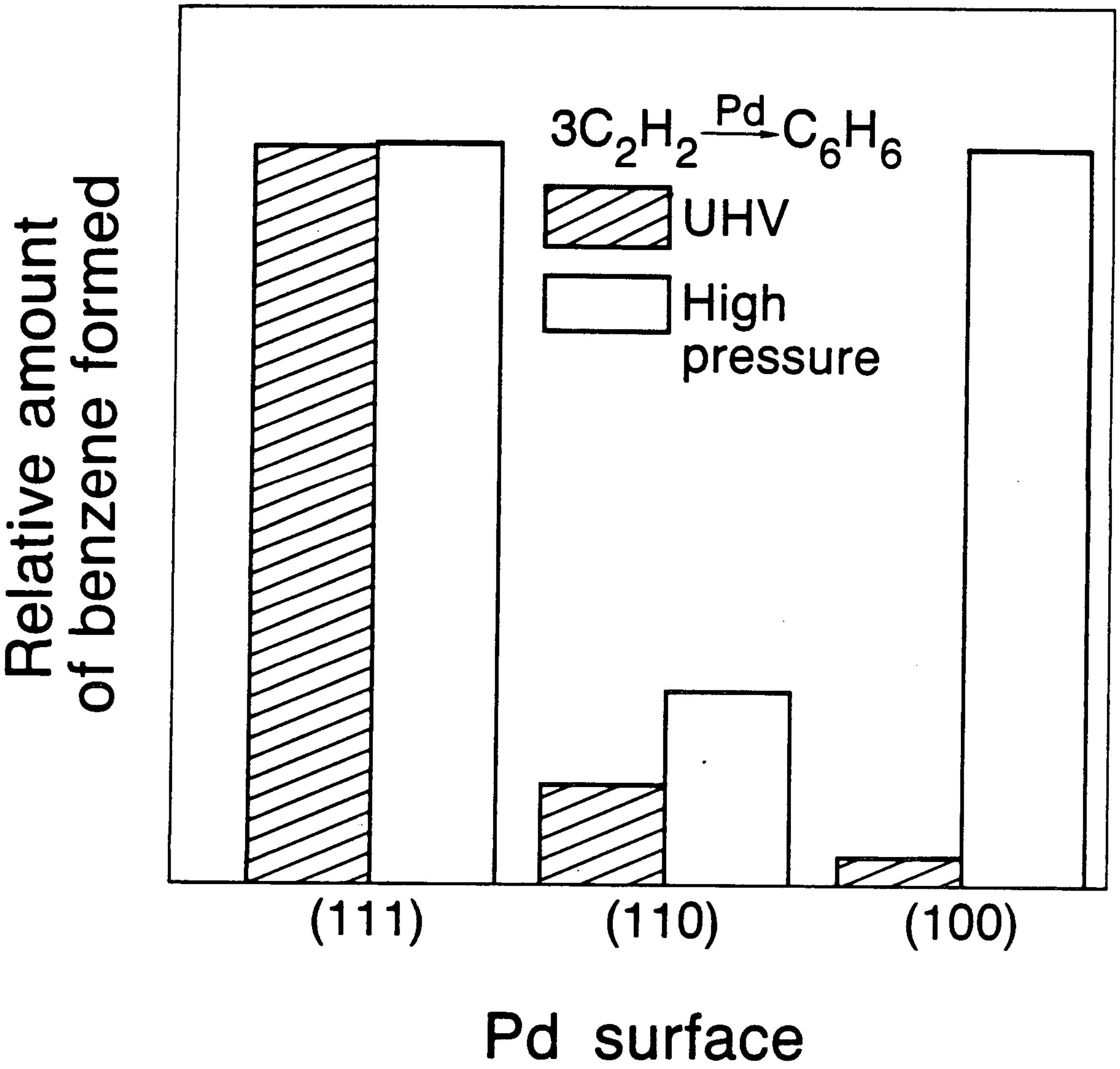

Figure 4.27: This figure shows the structure sensitivity of the acetylene cyclotrimerization reaction in UHV and at atmospheric pressures. In both pressure regimes the reaction is structure sensitive.

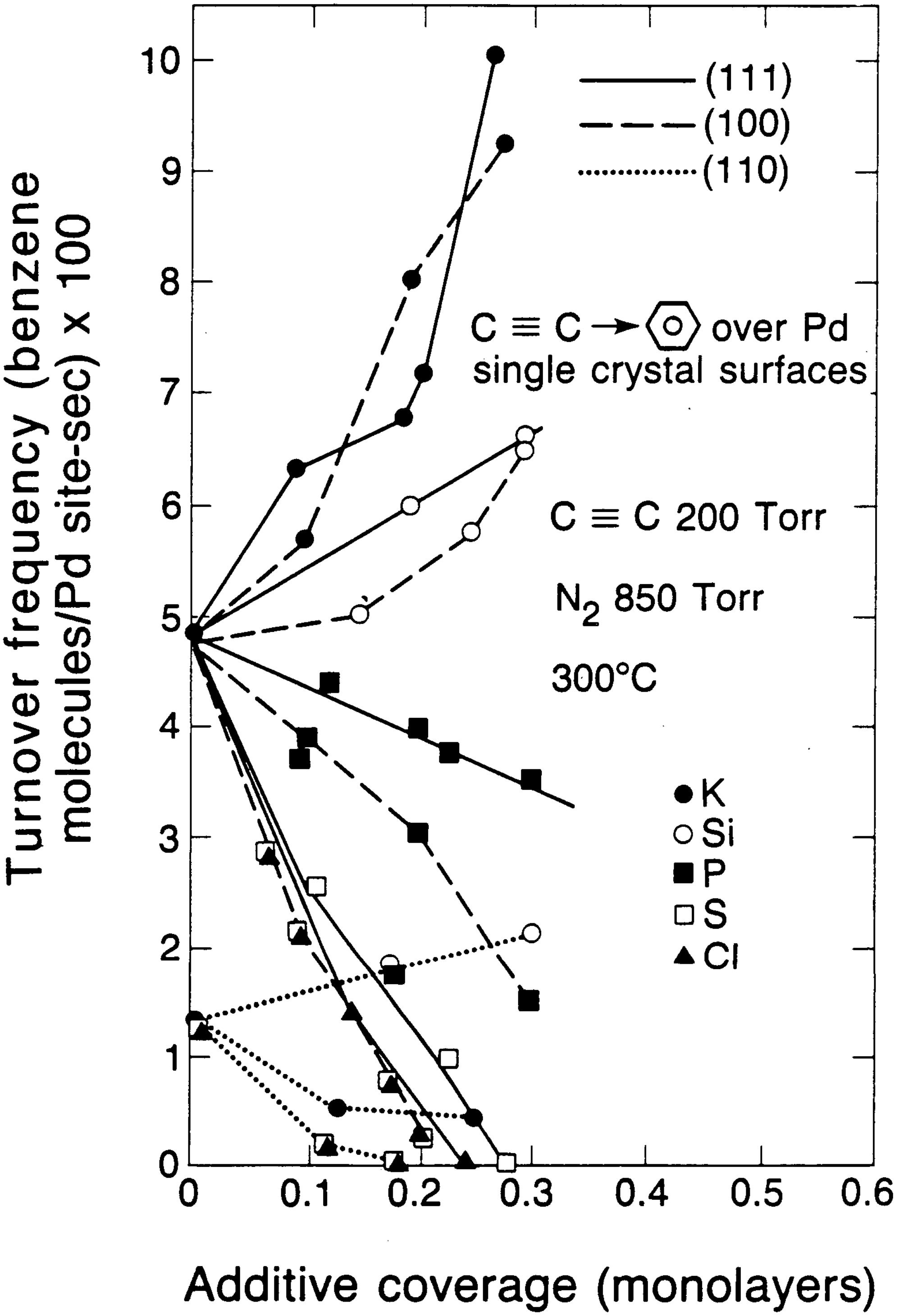

Figure 4.28: Reaction rates of the acetylene cyclotrimerization reaction in the presence of surface additives on the Pd(111), (100) and (110) surfaces at atmospheric pressures. In general, electron-donating additives enhance the rate and electron withdrawing-additives decrease the rate. Potassium on the (110) face is an exception.

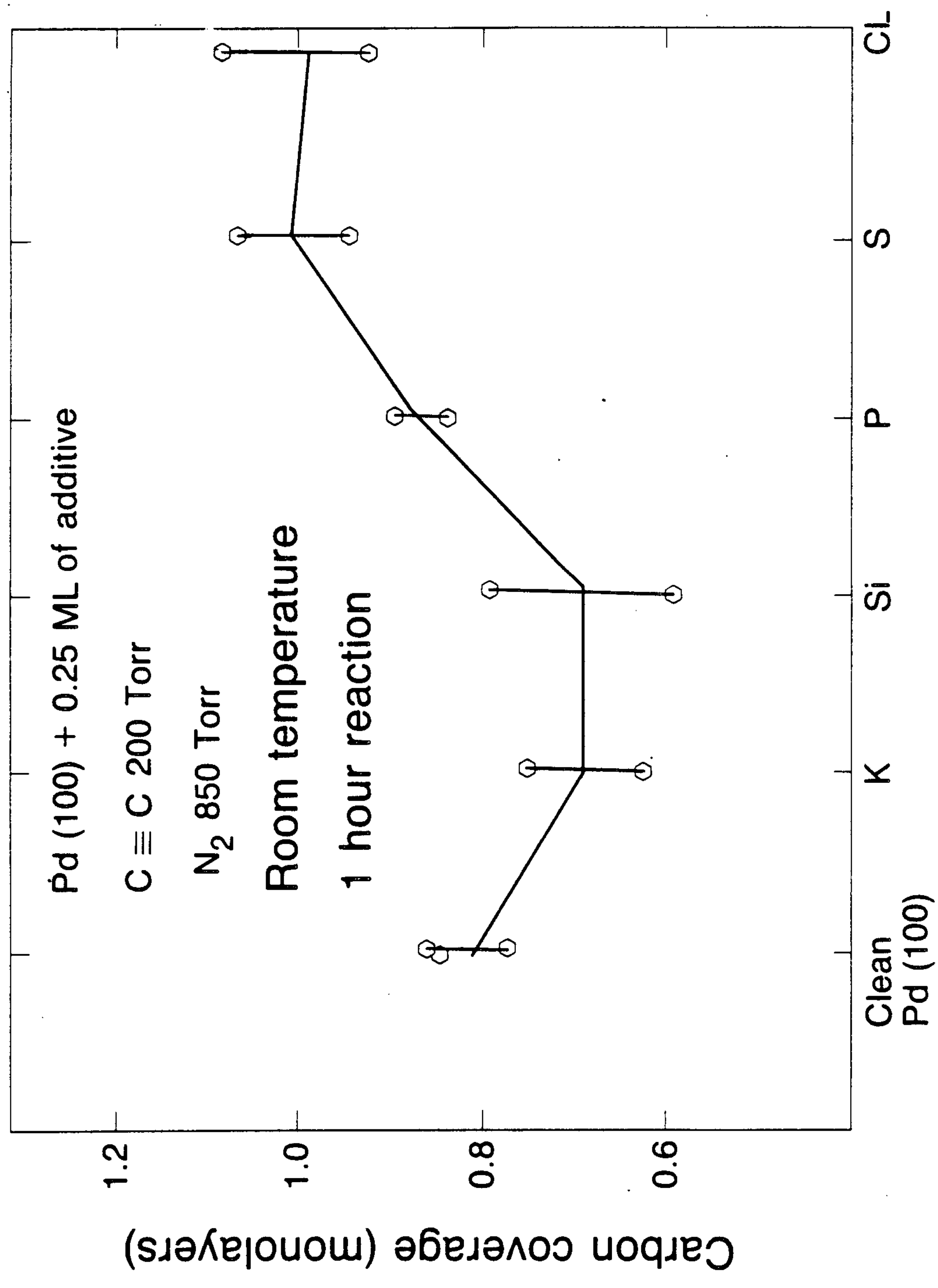

Figure 4.29: This figure shows the relative surface carbon coverage determined by CO titrations after the acetylene cyclotrimerization reaction in the presence of surface additives. Potassium and silicon on the Pd(100) surface reduced the amount of surface carbon buildup during a reaction. These two additives also increased the rate of benzene formation relative to the clean surface.

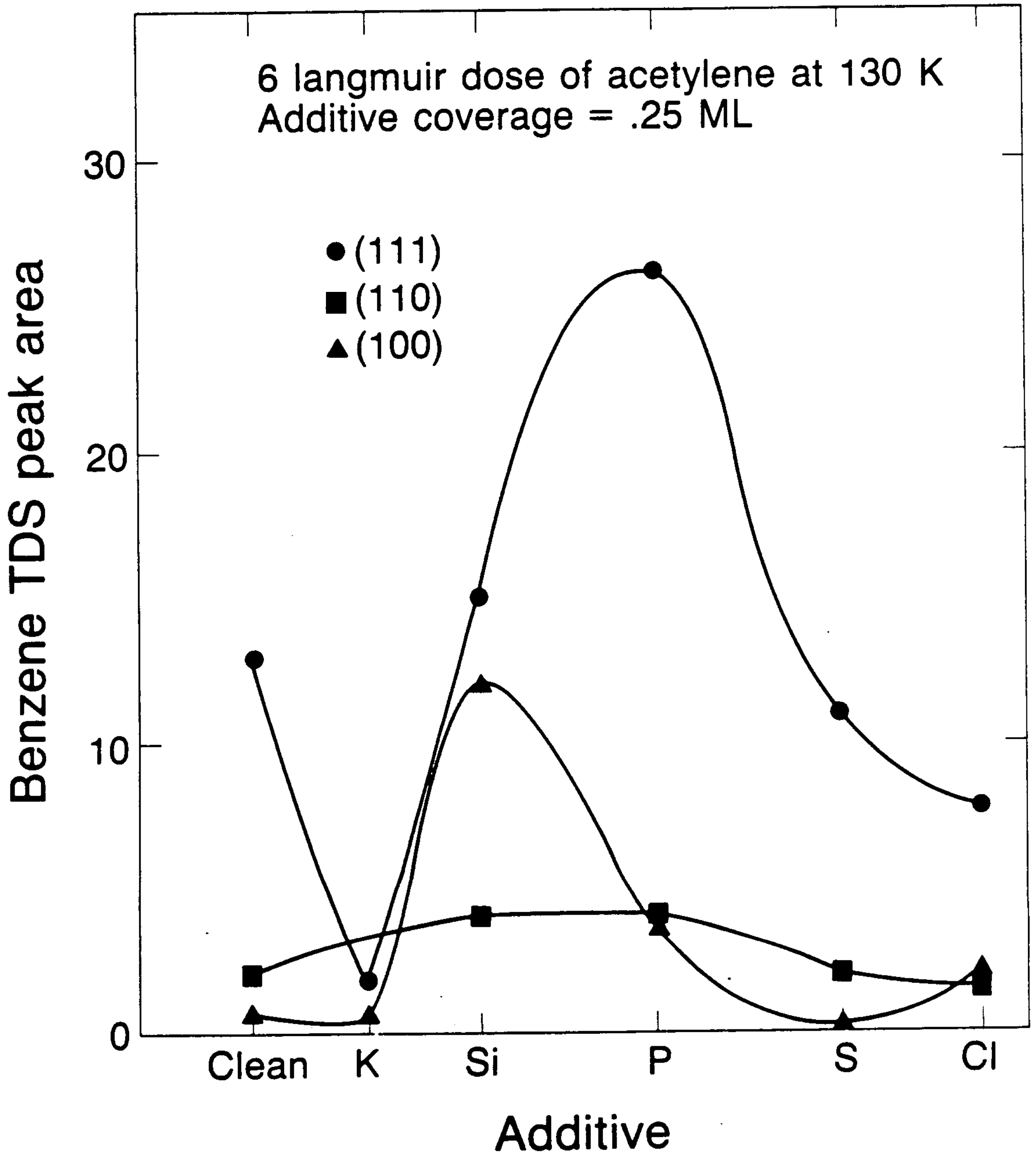

Figure 4.30: The amount of benzene formed in UHV on the additive covered surfaces is shown here. In general, potassium suppressed, silicon and phosphorus enhanced, and silicon and chlorine left unchanged the amount of benzene yield relative to the clean surface.

ically stable on the surface. This trend in the palladium additive bond strength correlates well to palladium complexes and bulk compounds. For example, $PdCl_2$ dissociates almost 400K lower than than PdS [16,17]. Also, palladium silicides are a well known class of bulk compounds.

The LEED work on these additives suggest that they are bound to the metal in high coordination sites: 3- or 4-fold hollow (each additive is bound to three of four palladium atoms). Surface compounds, due to their unique environment and different thermodynamic driving forces (minimizing surface free energy), have no direct analogies in bulk phase diagrams and have different coordination configurations than complexes. This makes it difficult to draw structural or stereochemical correlations. Studies have found potassium to be uniformly dispersed on metal surfaces [18,19] (except at multilayer coverages), whereas sulfur and chlorine form ordered islands at low coverages [20].

On the Pd(100) surface additives linearly change the work function. Potassium, silicon and phosphorus decreased the work function, indicating donation of electron density to the surface, whereas sulfur and chlorine (not pictured) increased the work function, implying withdrawal of electron density. These trends correspond to changes in work function for the Cl/Pd and K/Fe systems [9,10,21]. The work function changes observed correlate to the differences in Pauling electronegativities between the additives and palladium. Potassium (0.82) and silicon (1.9) are more electropositive than palladium (2.2) and donate electron density to the metal, decreasing the work function. Sulfur (2.6) and chlorine (3.2) are more electronegative, thus withdrawing electron density, thereby increasing the work function. Phosphorus (2.19) is essentially electroneutral with respect to palladium, but measurements indicate that it decreases the work function slightly. These changes clearly indicate that there is an electronic interaction between the additives and palladium.

4.3.2 CO Bonding on Clean Palladium

In recent years, many studies have investigated the adsorption of CO on clean palladium single crystals and foils using many techniques including LEED, EELS and IRRAS (infrared reflection absorption spectroscopy) [22,23,24,25,26,27]. The molecular simplicity and strong dipole has made this molecule an excellent surface sensitive probe. It is generally accepted that CO on most palladium surfaces occupies a bridge bonding site, that is, the carbon is bound to two palladium atoms. This is suggested by looking at the CO stretching frequency with either IR or EELS. The correlation between frequency and binding sites are classified as: > 2000 cm^{-1} - top site, 1700 - 2000 cm^{-1} - bridged and < 1700 cm^{-1} three or four fold hollow. On the clean Pd(111) surface a CO stretching frequency at 1835 cm^{-1} was found which is similar to the value of 1823 cm^{-1} reported by Bradshaw and Hoffman [28,29]. CO shows reversible molecular adsorption on all palladium surfaces. After TPD no evidence of carbon buildup was seen. Also, at high CO pressures (in the CO + H_2 reaction, 1:2, 300 psi total pressure, (see Chapter 3) there was no carbon overlayer buildup. CO has been reported to order on all three low Miller index planes used in this research. On the (111) surface a $(\sqrt{3}\times\sqrt{3})R30°$ forms, on the (100) face a (4 × 2)R45° forms and on the (110) face a c(2 × 2) at low coverages and a (4 × 2) at high coverages forms. High concentrations of CO on the surface have also been reported to change the bonding as evidenced by IR and heats of adsorption. This work and work by others found a 10 kcal/mol shift in heats of desorption between low and high CO surface coverages. Also the CO stretching frequency shifts from ~ 1800 cm^{-1} to 1950 cm^{-1} . Palazov *et al.* have studied palladium on silica and proposed that at high CO coverages a linear top site CO binding site evolves [30]. Theoretical calculations by Batra and Bagus have suggested that higher CO concentrations on the surface lead to direct intermolecular repulsion and reduction of backbonding via competition from neighbors [31].

Differences in CO bonding sites and the effect of surface additives can be better understood by seeing how CO bonds to metals. Figure 4.31 shows a molecular orbital diagram of CO and a metal atom. According to the Byholder model, CO binds to the metal 4d orbital through its 5σ molecular orbital to form a sigma bond [32,33]. The CO $2\pi^*$ antibonding orbitals also bond to metal 4d orbitals to form what is commonly referred to as the back-bonding or pi bond. The strength of the M-CO bond is determined by electron density in these bonds.

4.3.3 The Effect of Additives on CO Bonding

The extensive amounts of literature on the CO/Pd system shows that metal-CO bonding is well understood. Using this knowledge base we can use CO as a probe to better understand the effect of surface modifiers. Table 4.2 summarizes the changes in CO bonding induced by surface additives on the palladium (111), (110) and (100) faces.

The two generally accepted forms of additive interactions on surfaces are either electronic or structural. In the structural or site blocking interaction the additive physically hinders the adsorption of other molecules, whereas with an electronic interaction the charge density on the surface is altered to affect chemical bonding of molecules to the surface. Table 4.3 and Table 4.4 summarize the experimental and theoretical work by other groups which have studied the influence of additives. From these tables it can be seen that most groups have proposed that the additives either sterically or electronically change the chemisorption properties of the metal. However as will be discussed, it is necessary to invoke both types of interactions to completely explain the effect of surface additives on bonding and catalytic reactions. Surface additives form strong bonds with palladium as shown earlier. These additives block sites as evidenced by the decrease in CO chemisorption as

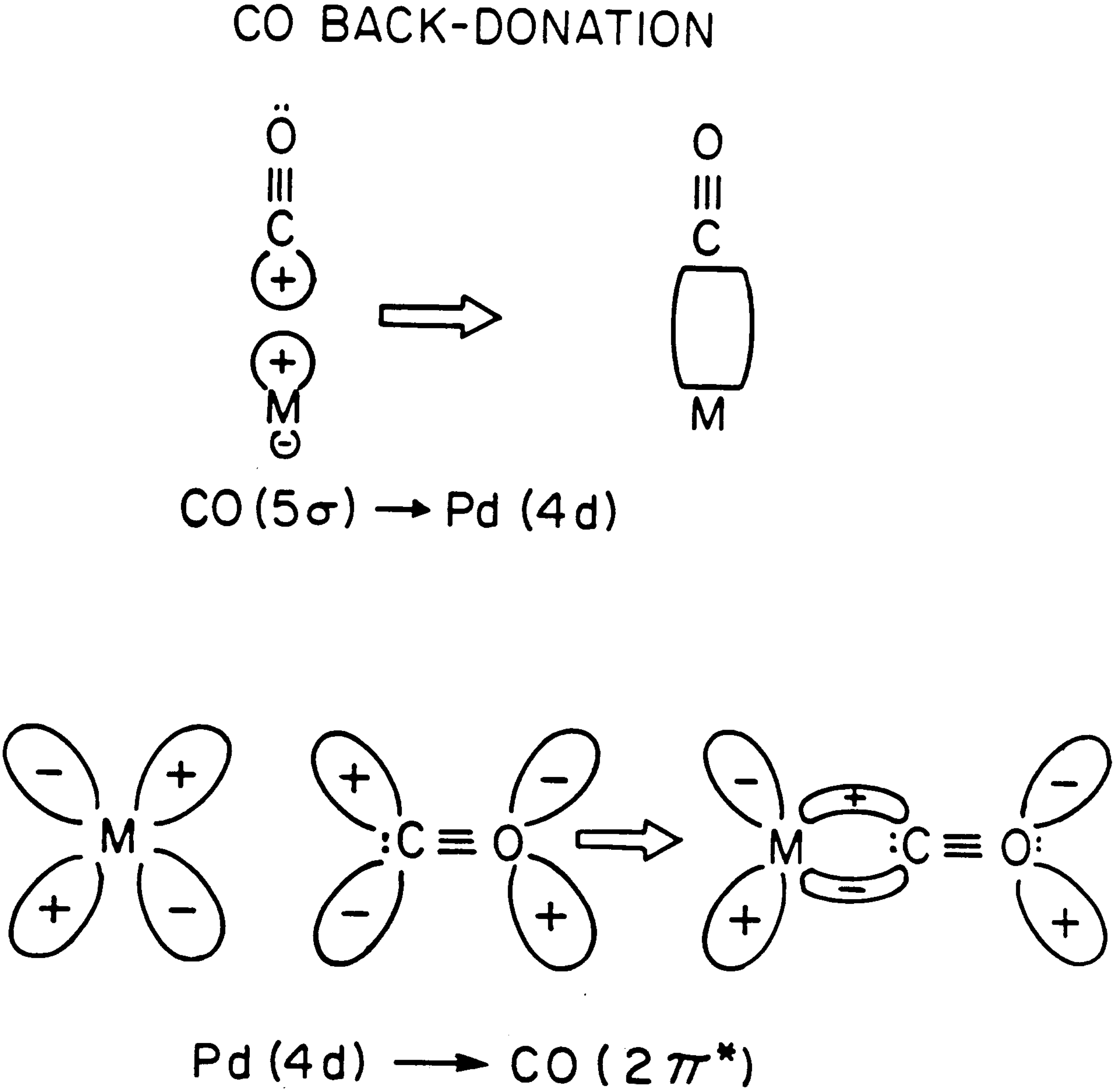

Figure 4.31: This figure shown a molecular orbital diagram of CO and a metal atom. The CO binds to the metal 4d orbitals through its 5σ molecular orbital to form a sigma bond, and through its $2\pi^*$ antibonding orbital to form what is commonly referred to as the back-bonding or pi bond.

Addit.	**(111)**	**(100)**	**(110)**
Clean	480K maximum, sharp 150K (sh) med. cover. 320K, high coverages	470K max. 420K (390K sh) (med) 420K,360K high cov.	450K Maximum Broad peak 430K at med. cover. 430K, 370K & 270K at high cover.
K, Na	Increase temp., shift. not much change in broadness	Increase Temp. new peak at higher Θ_K	Decrease Temp., new sites, broadening
Si	Gradual shift	Gradual shift, no broadening	Gradual shift, no broadening
P	20K shift followed by new peak at Θ_P=.35	Shift of 80K at Θ_P=.26 broadening poss. indicative of two peaks	Gradual shift 50K atΘ_P=.5
S	Shift 50K, new peak at Θ_S=.43	New peaks	Gradual shift Θ_S=.4 then new peak
Cl	Low cover. new peaks	Shifts - higher addit. cover. have larger shift	Gradual shift then new peak

Table 4.2: Summary of the CO TPD shifts on the additive-covered palladium faces

Substrate	Additive	Conclusions	Reference
Ni(100)	S	steric, local interactions	Gland [34]
Ni(100)	Cl, S, P	electronegativity	Kiskinova [35]
Ru(001)	Na	molec. reorientation of CO	Netzer [26]
Pd(110)	Na	LEED, surf. reconstruc.	Barnes *et al.* [6]
Ni, Pt, Pd (110)	Cl	LEED, TPD, $\Delta\Phi$	Erley [10]
Pd, Pt (111)	Cl	LEED, TPD, $\Delta\Phi$	Erley [9]
Pd(110)	S	LEED Equilibrium Configuration	Peralta [8] Madey [36]
Pd Foil	P	Pd-P compound	Sundram [37]
Pd(111),(110),(100)	K,Na,Si, P,S, Cl	Convolution of Electronic and Steric Interac.	This study

Table 4.3: Summary of some previous experimental studies of the interaction of additives on selected transition metals

a function of additive coverage. They change the bonding of CO to the surface as shown by changes in desorption temperature, formation of new CO desorption peaks and changes in stretching frequencies (determined by EELS). Since bonding involves sharing of electrons, the additives can also modify the distribution of surface electrons available for bonding with CO or any other adsorbate, in some or all of the possible binding sites.

The additives change the surface electron concentration (seen by $\Delta\Phi$) by withdrawing or donating electron density. On the (111) and (100) surfaces increasing the surface coverage of electronegative additives (Si, P, S, Cl) decrease the desorp-

Substrate	Additive	Conclusions	Reference
Trans. Metals	alkali,P,S,Cl,O	electrostatic interactions	Lang [38]
Trans. Metals	electronegative & electropositive	electrostatic interactions discuss structure sensitivity	Norskov [39]
Trans. Metals	alkali	electronic charge transfer	Albano [40]
Fe(100)	S,C,O	direct interaction between CO and additive	Benziger [41]
Ni(001)	S	electronic and geometric	Pendry [42]
Rh(001)	P,S,Cl,Li	electronic	Feibelman [43]

Table 4.4: Summary of some previous theoretical studies of the interaction of additives on selected transition metals

tion temperature of CO whereas electropositive additives (K, Na) increase the CO desorption temperature. Figure 4.32 shows the activation energies of desorption (calculated from the desorption temperature using the Redhead method [44]) of CO from additive covered Pd(111) and (110). Generally, the more electronegative an additive the larger is the decrease in the desorption temperature at a given coverage. From the Blyholder [32,33] CO bonding model discussed earlier, it can be seen that an electronegative adatom would withdraw electron density from the metal, thereby decreasing the 4d - $2\pi^*$ orbital density and weaken the metal - CO bond. Therefore, a lower desorption temperature corresponds to a weaker M-CO bond and a higher desorption temperature corresponds to a stronger M-CO bond. The rate of acetylene cyclotrimerization at high pressures also follows the general trend that more electronegative additives enhance the benzene yield. These promoting additives limit the decomposition or rate of polyacetylene formation (which block active sites) on the catalyst surface. Previous studies have found that electron withdrawing additives enhance the polymerization process by acidifying the metal surface [45].

There are many changes in bonding and catalytic activity of the additive-covered palladium surfaces which cannot be explained by a simple electron density arguement. Some examples are the increase on the CO desorption temperature and decrease in the acetylene cyclotrimerization rate on the potassium- and sodium-covered (110) surface in contrast to the other surfaces, the presence of new CO binding sites which grow in with increasing additive coverage (P on Pd(111)) and the differences in CO bonding for the same additive on different crystal faces.

Therefore, another form of additive interaction that needs to be considered is structural. Changes in surface structure or ensemble size (number of palladium atoms clustered together without additive) induces the largest shifts. The most striking example is with sodium- or potassium-doped surfaces. On the (110) surface, which undergoes restructuring [6], the CO desorption maximum shifts to lower temperatures, whereas on the (111) and (100) surface the desorption maximum shifts to higher temperatures. By charge transfer arguments, the desorption temperature should shift to higher temperatures on all three surfaces. Change in work function measurements show that on the (110) surface potassium does not donate as much electron density as on the (100) surface. (Figure 4.33). A reason for this difference might be that the more open surfaces have Fermi levels [46] closer to the potassium fermi level and that charge transfer is minimized [40]. Netzer *et al.* found for low sodium coverages and saturation CO coverages on Ru(001) that a fraction of the CO molecules undergo changes in bonding configuration - from linear to inclined [47]. The rearrangement of the surface and the minimal differences in electronic interaction of alkali metals on the three low Miller index planes suggest that a major determinant of CO bonding is structural.

This ensemble, or structure effect, is also evident on surfaces which do not

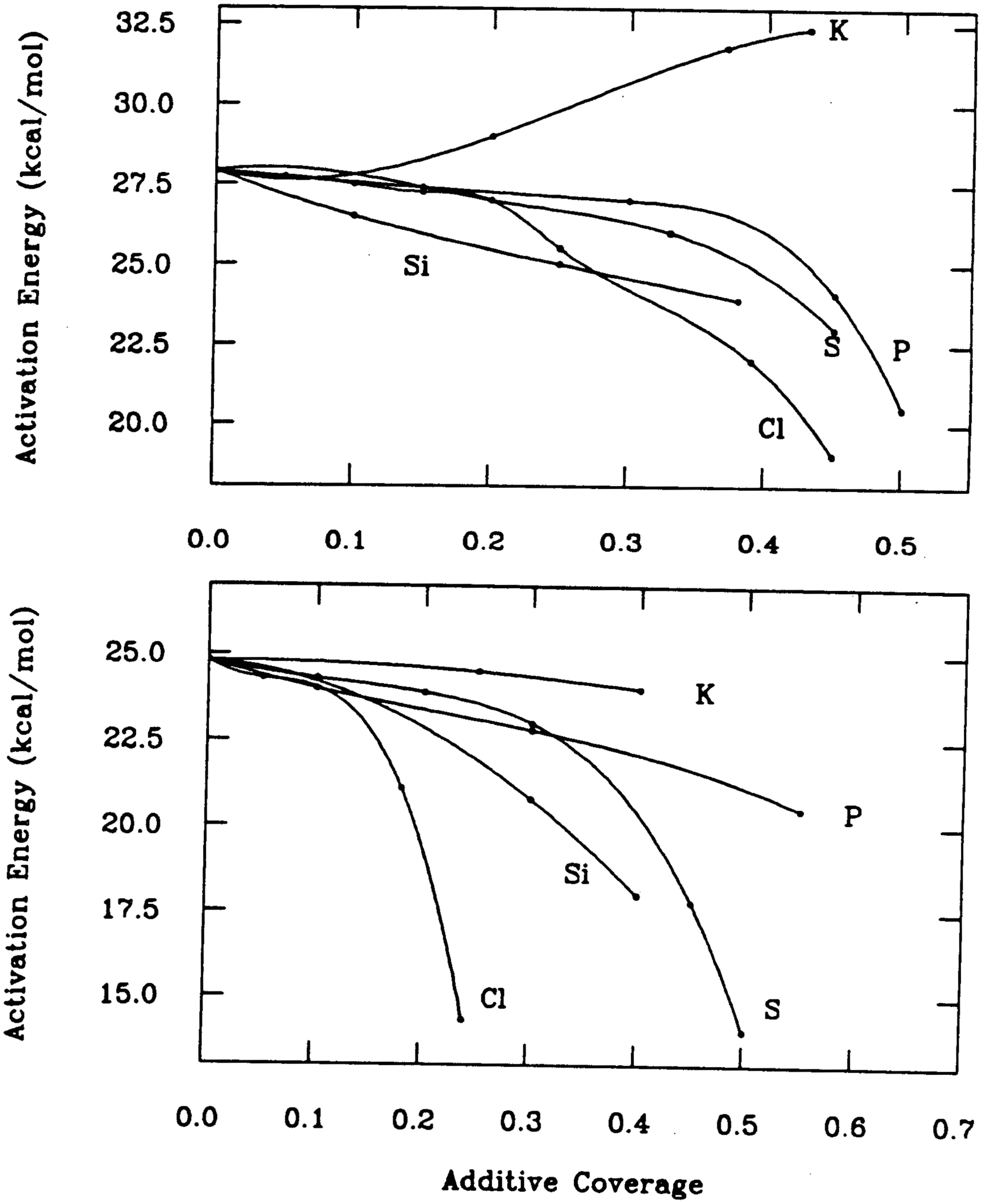

Figure 4.32: These two graphs show the activation energy of desorption of CO from additive covered Pd(111) and (110). In general, the more electronegative an additive, the larger the decrease in desorption temperature at a given coverage. The sharp changes in slope at higher coverages are due to the population of a new low temperature binding site.

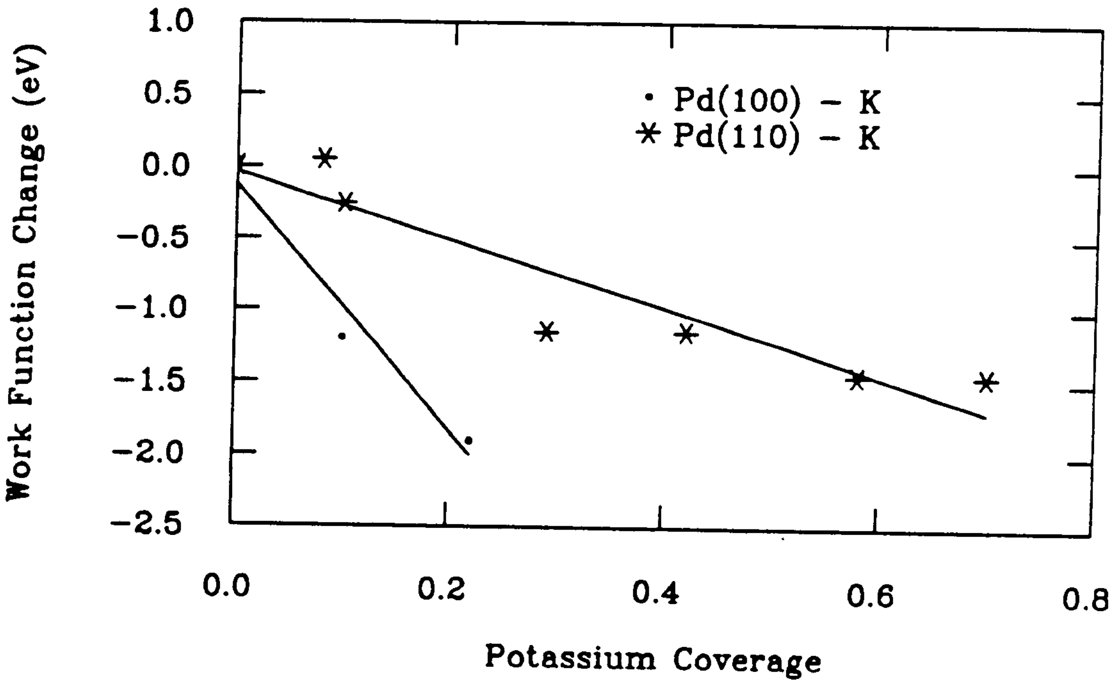

Figure 4.33: This figure shows the changes in work function for the Pd(110) and (100) surfaces as a function of increasing potassium coverage. On the more open (110) surface, potassium does not lower the work function as much as on the (100) surface.

undergo surface reconstruction. As the additive coverage increases, the number of large palladium clusters decreases, favoring less stable bonding configurations for the CO. These shifts have been observed in a Ag-Pd alloy by Soma-Noto and Sahtler [48]. They found a maximum in the IR bands of linearly bound species on a 70% - Pd alloy with a constant decrease in bridge bound species. The linear bound species had desorption energies $\sim$ 15 kcal/mol lower than the bridge bound species. On numerous modified palladium systems, a new low temperature CO desorption peak grows in at additive coverages between $\Theta = .25 - .45$ (Pd(111) - S, P, Cl; Pd(110) - S, Cl). At low CO exposures, it is possible that the additives force the CO into binding configurations accessible only under high CO exposures where there is CO crowding. Previous studies on Pd single crystals [49] indicate that CO desorption is a first order process, and that the desorption energy is coverage dependent due to CO - CO interactions. Therefore the shift in peak maximum at higher additive coverages could be attributed to these interactions. It does not seem that this perturbation is a major factor at low CO exposures. In most cases the desorption maximum shifts in differing amount relative to the clean surface which is dosed with higher CO exposures.

Another factor supporting a structural interaction of ensemble size effects is the cyclotrimerization of acetylene to form benzene. On the potassium-doped (110) surface benzene formation is hindered relative to the clean surface, in contrast to the (111) and (100) surfaces where the rate is enhanced by a factor of five. To form benzene, three acetylene molecules must be able to bond in close proximity to each other. On the (110) restructured surface, the palladium ensemble size has diminished to a point where the reaction cannot take place.

A fourth factor favoring the structure argument is the structure sensitivity in the CO desorption shift for the additives. Phosphorus on the three surfaces induces vastly different CO binding states. On the (111) surface at low coverages there is a gradual decrease ($\sim 20°$) in the desorption maximum followed by the appearance of a new binding state (50° lower) at phosphorus coverages above $\Theta =$ .35, whereas on the (110) surface there is a gradual decrease in the CO maximum with increasing phosphorus coverage. If the CO - metal - P interaction were purely electronic, similar trends in the CO trace would be expected (i.e. only shifts, or new CO TPD peaks forming on both surfaces) with only the magnitude being affected by the metal - phosphorus bonding orbital overlap.

The CO TPD traces do not undergo any shape changes or broadening as a function of additive coverage. This implies that the energies of the CO binding sites are relatively homogeneous at most additive coverages. After the CO molecules adsorb on the surface they must diffuse to a low energy binding site on the surface. On the surface additive systems where new peaks are resolvable, more than one binding site is energetically favorable and the activation barrier for diffusion is high. Arias *et al.*, using metastable quenching spectroscopy, found that at low CO exposures the CO molecules are adsorbed near potassium and at high potassium coverages the CO molecules lie flat on the surface or very much tilted from the surface normal [50]. The presence of only limited sites is supported by the EELS data for the Pd(111) - S surface, which shows two different binding sites for CO, a bridged species intense at low sulfur coverages and a tilted species which increases in intensity with increasing sulfur coverage. These two species have been assigned to the high temperature CO desorption (bridged) and low temperature CO desorption (tilted). The tilting may be due to either a steric interaction between the additive and CO or an electronic 'bonding' between the CO π orbitals and the additive.

Another effect these surface additives exhibit is the purely steric or site blocking effect. At high CO exposures the amount of CO desorbing decreases with increasing additive coverage.

Figure 4.34 shows some of the possible bonding configurations of CO in the presence of surface additives which correlate to the experimental results and interpretations. As seen by these changes in CO chemisorption, the additives modify CO bonding both structurally and electronically.

In the literature there has been extensive study of the long range vs. short range interactions of surface additives [51]. The easiest way to discern these effects is to study the change in CO binding as a function of additive coverage. If long range interactions are dominant there would be a continuous variation in the CO binding energy and broad peaks would be detected, since the additive's influence would decay over numerous CO binding sites. If short range interactions are dominant, then only the nearest CO binding states would be effected and the remaining sites would remain unperturbed. In this case CO might be expected to exhibit discreet binding states. Since only a few of the CO TPD traces showed any broadening, and in some cases this broadening was due to multiple sites, it can be said that the additives exhibit only a short range effect.

4.3.4 Effect of Additives on Hydrogen Bonding

The effect of the surface additives on hydrogen chemisorption on the palladium single crystals is very different than that seen for CO. The amount of hydrogen desorbing decreased as the additive concentration increased without changing the desorption temperature or activation energy of desorption. On all three surfaces, phosphorus, sulfur and chlorine, in that order, decreased the amount of hydrogen bound to the surface at a given coverage. Since there was no change in the desorption temperature this decrease can be attributed to site blocking by the additive. However, chlorine, which for a given coverage had the largest effect has the smallest ionic radius. Similar desorption temperatures for hydrogen from the clean surface were seen by other groups [4,52,35].

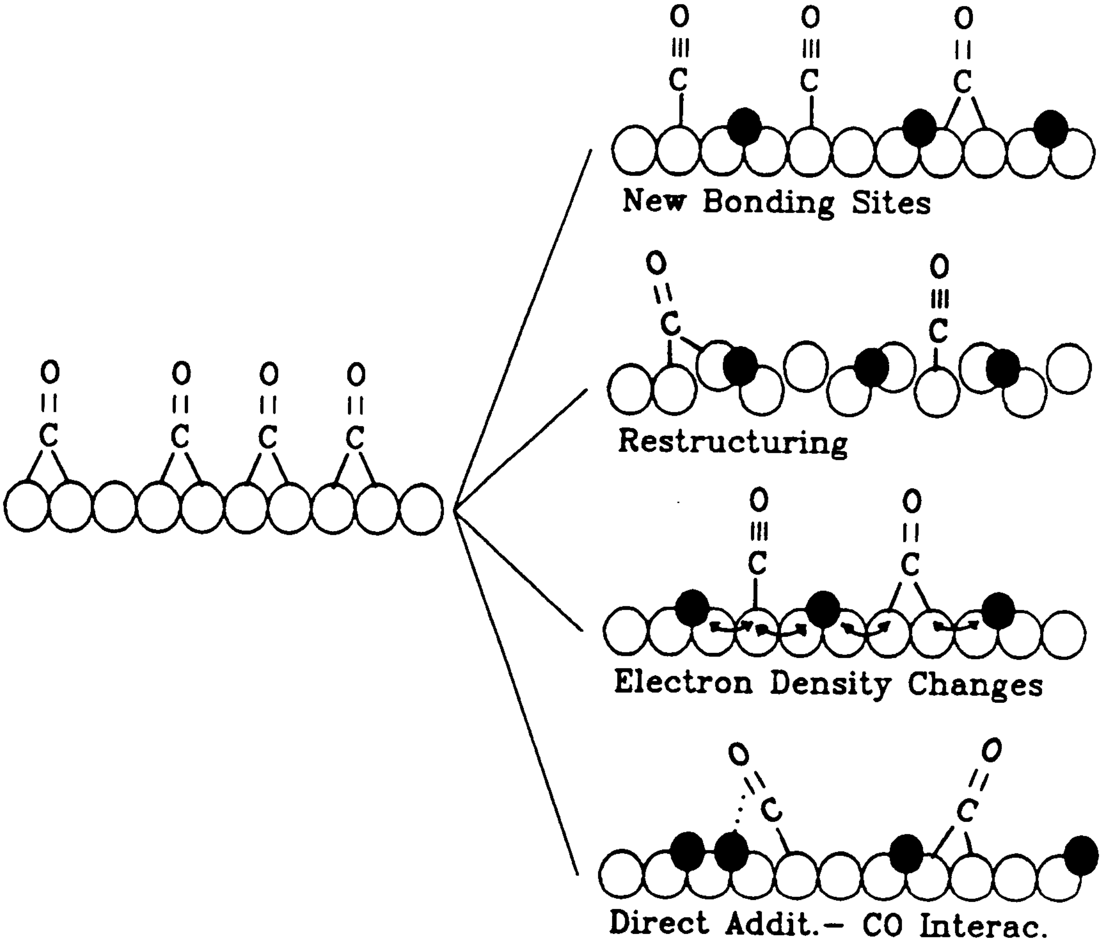

Figure 4.34: This figure shows some of the possible bonding configurations of CO in the presence of surface additives. These additives both structurally and electronically modify the bonding relative to the clean surface.

Hydrogen dissociatively adsorbs on palladium and it easily dissolves into the bulk [53,54,55]. At room temperature the metal has the unusual property of absorbing 900 times its own volume of hydrogen, possibly forming Pd_2H. Most likely the additives affect the adsorption process rather than the desorption process where the rate determining step is hydrogen recombination. Hydrogen also bonds in the four fold sites that are preferred by the additives. The additives lower the sticking coefficient of hydrogen, with the more electronegative additives having a larger effect. This decrease in the sticking coefficient is due an activated adsorption of hydrogen on the surface in a process that involves dissociation.

4.3.5 Palladium - Silicon

In studying the effects of the additives on work function changes, and on CO and H_2 bonding, K, P, S, and Cl followed each other, whereas silicon exhibited very unique and different effects. For instance, in hydrogen chemisorption on the (100) surface there was an increase in the hydrogen chemisorption relative to the clean surface while the other additives decreased the amount of hydrogen bonding. In CO bonding, silicon on all three surfaces gradually shifted the desorption maximum without forming a new peak. The other additives produced more varying features. Also, the decrease in the activation energy of desorption did not follow in the trends established by the other additives based on electronegativities. With silicon, unlike any of the other additives, annealing the surface, changed the work function by .75 eV (closer to clean Pd(100)), while only slightly decreasing the surface concentration as measured by AES. All this evidence of silicon's unique behavior suggests that silicon forms a palladium silicide in the near-surface region. Surface compound formation has been proposed on other systems [21,56,57,58,59,60,61,62,63,64]. Pd_xSi_y compounds do exist and are very stable [65]. The surface compound exhibits very different chemistry than a surface only decorated with an additive.

4.4 Conclusions

The following list of points summarize the results in studying the effect of additives on the surface chemistry of palladium single crystals ((111),(100) and (110)).

- The Pd - Additive bond strength ordering is Na $<$ Cl $<$ K $<<$ Si $<$ P $<$ S.
- The additives modify CO bonding through the convolution of both electronic and structural interactions with the surface and CO.
- The additives change only the relative sticking coefficient of hydrogen to the surface and do not change the desorption temperature.
- Palladium can form a surface palladium silicide which has different bonding properties than would be expected if silicon followed in the trends established by the other additives.

References

[1] H. P. Bonzel. *J. Vac. Sci. Tech* **A2** (1984) 866.

[2] D. W. Goodman. *J. Vac. Sci. Tech.* **20** (1982) 522.

[3] G. Ertl. *Catalysis, Science & Technology (Vol. 4).* Springer, 1983.

[4] H. Conrad, G. Ertl, and E. E. Latta. *Surf. Sci.* **41** (1974) 435.

[5] J. C. Tracey and P. W. Palmberg. *J. Chem. Phys.* **51** (1969) 4852.

[6] C. J. Barnes, M. Q. Ding, M. Lindroos, R. D. Diehl, and D. A. King. *Surf. Sci.* **162** (1985) 59.

[7] W. Berndt, R. Hora, and M. Scheftler. *Surf. Sci.* **117** (1982) 188.

[8] L. Perlata, Y. Berthier, and M. Huber. *Surf. Sci.* **104** (1981) 435.

[9] W. Erley. *Surf. Sci.* **94** (1980) 281.

[10] W. Erley. *Surf. Sci.* **114** (1982) 47.

[11] Y. Nakamoto. *Infrared & Raman Spectra of Inorganic and Coordination Compounds.* Wiley, 1978.

[12] I. A. Oxton. *J. Molec. Struct.* **78** (1982) 77.

[13] D. M. Adams and I. D. Taylor. *J. Chem. Soc. Faraday Trans.* **78** (1982) 1551.

[14] M. A. Logan, T. G. Rucker, T. M. Gentle, E. L. Muetterties, and G. A. Somorjai. *J. Phys. Chem.* **90** (1986) 2709.

[15] T. G. Rucker, M. A. Logan, T. M. Gentle, E. L. Muetterties, and G. A. Somorjai. *J. Phys. Chem.* **90** (1986) 2703.

[16] F. Weibke and J. Laar. *Z. Anorg. Chem.* **224** (1935) 49.

[17] J. Krustinsons. *Z. Elecktrochem.* **44** (1938) 537.

[18] G. Pirug, H. P. Bonzel, and G. Broden. *Surf. Sci.* **122** (1982) 1.

[19] E. L. Garfunkel and G. A. Somorjai. *Surf. Sci.* **115** (1982) 441.

[20] G. A. Somorjai. *Chemistry in Two Dimensions.* Cornell University Press, Ithaca, New York, 1981.

[21] G. Ertl and J. Kuppers. *Low Energy Electrons and Surface Chemistry.* Verlag Chemie, 1974.

[22] R. P. Eischens and W. A. Pliskin. *Advan. Catalysis* **10** (1958) 1.

[23] J. P. Biberian and M. A. van Hove. *Surf. Sci.* **118** (1982) 443.

[24] A. Ortega, F. M. Hoffman, and A. M. Bradshaw. *Surf. Sci.* **119** (1982) 79.

[25] H. Conrad, G. Ertl, J. Koch, and E. E. Latta. *Surf. Sci.* **43** (1974) 462.

[26] F. P. Netzer and M. M. El Gomati. *Surf. Sci.* **124** (1983) 26.

[27] S. Sung and R. Hoffmann. *J. Amer. Chem. Soc.* **107** (1985) 578.

[28] A. M. Bradshaw and F. Hoffmann. *Surf. Sci.* **52** (1975) 449.

[29] A. M. Bradshaw and J. Pritchard. *Proc. Roy. Soc. (London)* **A316** (1970) 169.

[30] F. Palazov. *J. Catalysis* **74** (1982) 44.

[31] I. P. Batra and P. S. Bagus. *Solid State Commun.* **16** (1975) 1097.

[32] G. Blyholder. *J. Phys. Chem.* **68** (1964) 2772.

[33] G. Blyholder. *J. Vac. Sci. Tech.* **11** (1974) 865.

[34] J. L. Gland, R. J. Madix, R. W. McCabe, and C. DeMaggio. *Surf. Sci.* **143** (1984) 46.

[35] M. Kiskinova, G. Bliznakov, and L. Surnev. *Surf. Sci.* **94** (1980) 169.

[36] T. Madey, J. T. Yates, A. M. Bradshaw Jr., and F. M. Hoffmann. *Surf. Sci.* **89** (1979) 370.

[37] V. S. Sundaram, S. P. da Cunha, and R. Landers. *Surf. Sci.* **119** (1982) L383.

[38] N. D. Lang, S. Holloway, and J. K. Norskov. *Surf. Sci.* **150** (1985) 24.

[39] J. K. Norskov, S. Holloway, and N. D. Lang. *Surf. Sci.* **137** (1984) 65.

[40] E. V. Albano. *Surf. Sci.* **141** (1984) 191.

[41] J. Benziger and R. J. Madix. *Surf. Sci.* **94** (1980) 119.

[42] J. M. Maclaren and J. B. Pendry. To be published.

[43] P. J. Feibelman and D. R. Hamann. *Surf. Sci.* **149** (1985) 48.

[44] P. A. Redhead. *Vacuum* **12** (1962) 203.

[45] C. N. Satterfield. *Heterogeneous Catalysis in Practice.* McGraw-Hill, 1980.

[46] R. Smoluchowski. *Phys. Rev.* **60** (1941) 661.

[47] F. P. Netzer, D. L. Doering, and T. E. Madey. *Surf. Sci.* **143** (1984) L363.

[48] Y. Soma-noto and W. M. H. Sachtler. *J. Catalysis* **32** (1974) 315.

[49] P. Ladas, H. Poppa, and M. Boudar. *Surf. Sci.* **102** (1981) 151.

[50] J. Arias, J. Lee, J. Dunaway, R. Martin, and H. Metiu. *Surf. Sci.* **159** (1985) L433.

[51] K. Markert and K. Wandelt. *Surf. Sci.* **159** (1985) 24.

[52] M. G. Cattania, V. Penka, R. J. Behm, K. Christmann, and G. Ertl. *Surf. Sci.* **126** (1983) 382.

[53] R. J. Behm, K. Christmann, and G. Ertl. *Surf. Sci.* **99** (1980) 320.

[54] J. P. Muscat and D. M. Newns. *Surf. Sci.* **80** (1979) 189.

[55] F. A. Lewis. *The Palladium - Hydrogen System.* Academic Press, 1967.

[56] E. Baner, H. Poppa, and V. Viswanath. *Surf. Sci.* **92** (1980) 53.

[57] E. Baner, H. Poppa, and V. Viswanath. *Surf. Sci.* **93** (1980) 407.

[58] H. M. Kramer and E. Bauer. *Surf. Sci.* **92** (1980) 53.

[59] H. M. Kramer and E. Bauer. *Surf. Sci.* **93** (1980) 407.

[60] Y. P. Zingermann and V. A. Ishchuk. *Fiz. Tver. Tela.* **9** (1967) 2529.

[61] P. H. Holloway and J. B. Hudson. *Surf. Sci.* **43** (1974) 123.

[62] J. E. Denath and T. N. Rhodin. *Surf. Sci.* **45** (1974) 249.

[63] K. Akimoto, Y. Sakisaka, and M. Onichi. *Surf. Sci.* **82** (1979) 349.

[64] C. A. Papageorgopoulos and C. A. Chen. *Surf. Sci.* **52** (1975) 40.

[65] *Handbook of Chemistry and Physics.* C. R. C. Press, 1983.

Chapter 5

PEROVSKITES

5.1 Introduction

Perovskite oxides are a class of compounds which are important in many areas of science and technology due to their physical properties, which include ferroelectricity, piezoelectricity, pyroelectricity, magnetism, high temperature superconductivity and electrooptic effects. This class of compounds has the general formula ABO_3, where A is a large ion with a filled d shell and B is a smaller transition metal. Figure 5.1 shows the crystal structure of a perovskite with the $CaTiO_3$ structure. Tetragonal and rhombohedral distortions are not uncommon, and it has been shown that small changes in structure and composition result in large changes in the electronic properties [1,2].

Only in the last sixteen years has there been any interest in these materials as catalysts [3]. Most of the catalytic research has centered on developing stable and active catalysts for the treatment of automobile exhaust in catalytic converters. Cobalt, platinum, ruthenium and manganese type perovskite compounds have shown activity in the oxidation of nitric oxide [4]. However their low conversions and sensitivity to sulfur poisoning limited their application in this field.

Concurrently there has been interest in producing two carbon oxygenate molecules from carbon monoxide and hydrogen such as ethanol, ethylene glycol and

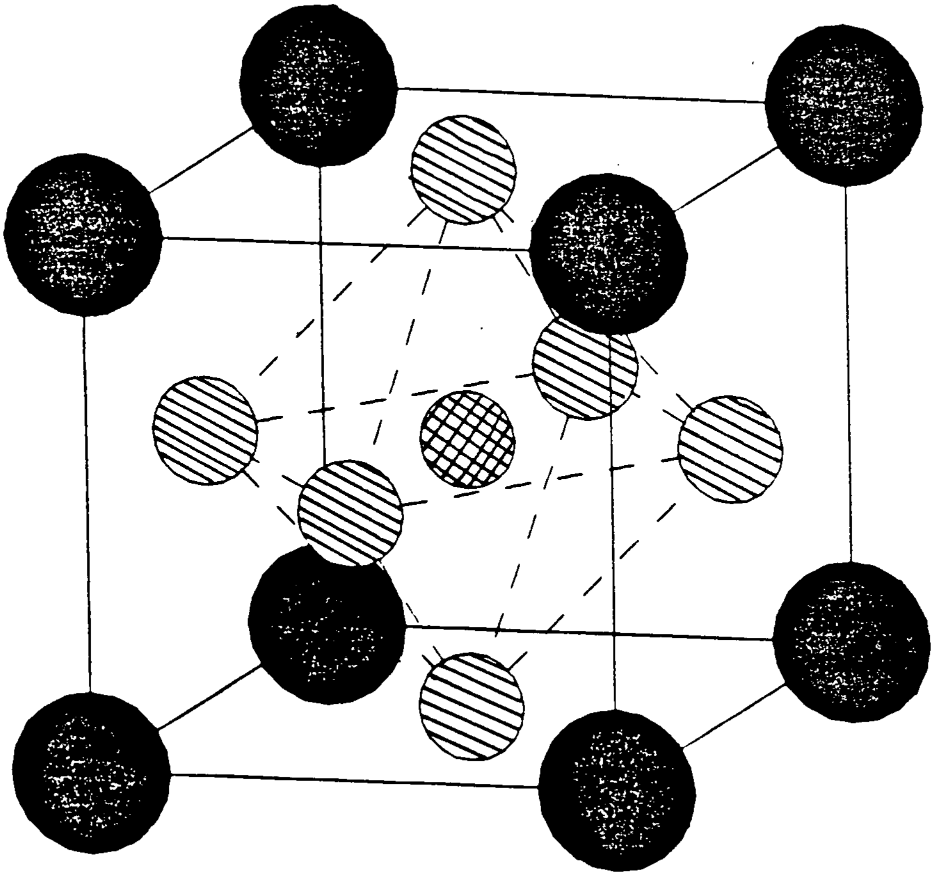

Figure 5.1: Crystal structure of perovskite compounds.

acetic acid. Supported rhodium catalysts have shown high activity in forming these molecules but the product distribution is very sensitive to the catalyst preparation [5,6,7,8,9]. It appears that the chemical state of the rhodium varied widely in these different samples. Previous research in our group has centered on modeling these supported rhodium catalysts with low-surface-area well-characterized rhodium single crystals and foils [10,11,12]. These studies found that metallic rhodium is a stable, but average methanation catalyst. Oxidation prior to a reaction activated the foil for ethanol formation but this surface was unstable in the reducing conditions of the CO + H_2 reaction. Under the same conditions rhodium sesquioxide reduced only slightly and lanthanum rhodate did not reduce. Both of these compounds had a relatively high yield of oxygenated (+25%) products.

The possibility that the perovskite structure could stabilize an oxidized form of a metal led us to study this class of compounds in the CO hydrogenation reaction. In this chapter the catalytic activity of perovskite compounds $LaMO_3$ (M = Rh, Cr, Mn, Co and Fe) is reported and compared to the catalytic behavior of the oxidized and reduced metal alone.

5.2 Results and Discussion

5.2.1 Introduction

This section presents and discusses the results obtained in the survey of the lanthanum perovskite compounds $LaMO_3$ (M = Cr, Mn, Co, Rh, and Fe). The powered samples were compressed into a .005 in gold mesh at ~ 25,000 psi. This mesh was then spotwelded to a 1 cm^2 .010 in gold foil which in turn was attached to the manipulator. All reactions were run at 250°C, 2:1 H_2:CO ratio with a total pressure of 300 psi (20 atm).

5.2.2 Catalytic Studies

The catalytic activity of first row transition metals in $LaMO_3$ perovskite structures was studied in the CO hydrogenation reaction. Figure 5.2 shows normalized product distributions for the five samples. In all cases methane is the major product ranging from 95+ mole-percent of the product distribution on $LaCrO_3$ down to 77 mole percent on $LaFeO_3$. Figure 5.3 shows an expanded view of the percentage of C_2, C_3, C_4 and alcohol molecules formed. $LaFeO_3$ produces almost 3 times as much ethane and ethylene as any of the other samples and $LaCrO_3$ is virtually inactive in forming any products other than methane. All the samples to some degree catalyze the formation of C_3 and C_4 hydrocarbons. No larger molecules were detected in the reaction loop. $LaFeO_3$, $LaCoO_3$ and $LaRhO_3$ showed some activity in alcohol formation, primarily methanol.

Table 5.1 summarizes the initial rate of product formation of the lanthanates expressed as molecules formed per site-second. Moving from left to right through the periodic table it can be seen that the rate of product formation increases: $LaCrO_3 > LaMnO_3 > LaFeO_3 > LaCoO_3 \sim LaRhO_3$. The differences in activity are tremendous and span 2 orders of magnitude. This shows that the metal (Cr, Mn, Fe, Co and Rh) both the selectivity and activity of the catalyst. The role of the lanthanum oxide cannot be elucidated from the data, but it might be either a structural support, a promoter providing a mixed catalytic site with the metal, or it may keep the metal in an oxidized state.

From CO chemisorption results, Cr and Mn dissociatively bond CO whereas Co and Rh exhibit CO bonding where there is some dissociation followed by recombination and desorption. Cr and Mn, in general, irreversibly bind hydrocarbons whereas Rh forms weaker bonds which leads to less decomposition [13]. On the samples with lower rates such as $LaCrO_3$ and $LaMnO_3$, a large carbon concentration was detected after the reaction. This suggests that during the reaction the

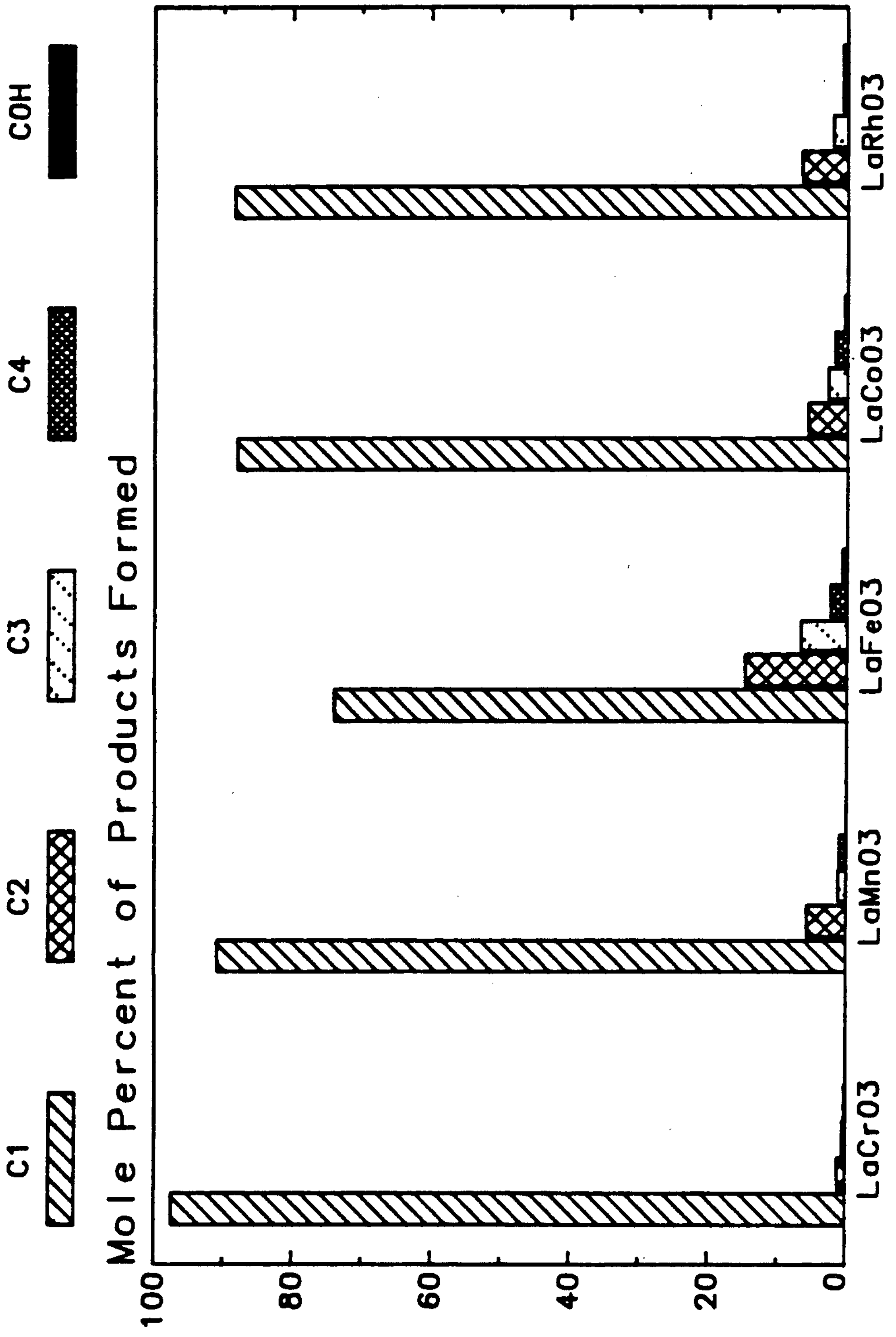

Figure 5.2: Product distribution in the CO hydrogenation reaction for the perovskites $LaRhO_3$, $LaMnO_3$, $LaCoO_3$, $LaFeO_3$ and $LaCrO_3$.

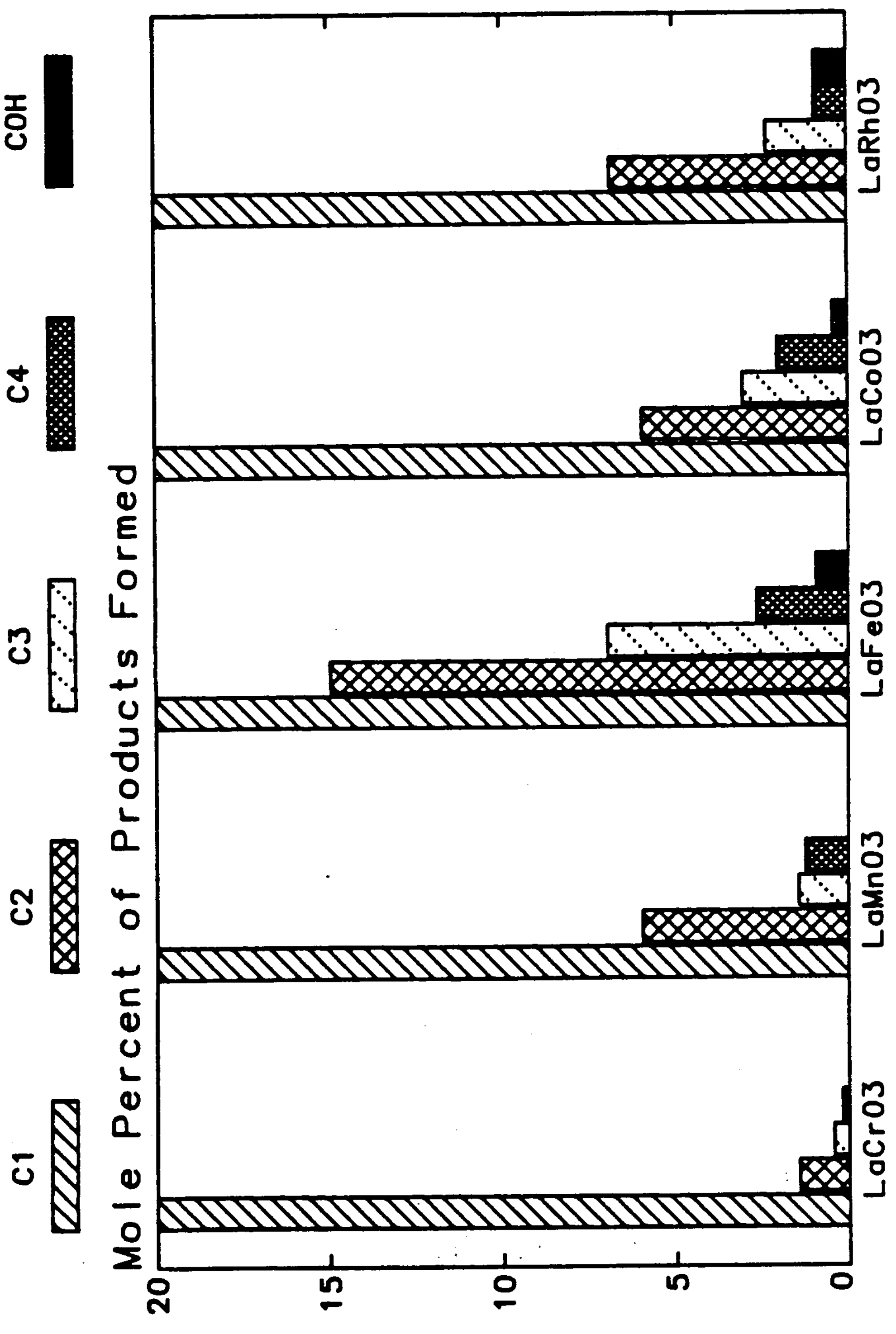

Figure 5.3: Product distribution of C_2, C_3, C_4 and Alcohols in the CO hydrogenation reaction for the perovskite compounds.

Cmpd.	**Reaction Product**					
	Methane	Ethane	Ethylene	C_3	C_4	COH
$LaCrO_3$	5.8×10^{-4}	5.1×10^{-5}	9.1×10^{-6}	2.2×10^{-5}	1.6×10^{-5}	–
$LaMnO_3$	1.2×10^{-3}	1.3×10^{-4}	1.6×10^{-5}	3.6×10^{-5}	4.6×10^{-5}	–
$LaFeO_3$	6.7×10^{-3}	7.2×10^{-4}	6.4×10^{-4}	9.6×10^{-4}	4.4×10^{-4}	$4.\times10^{-5}$
$LaCoO_3$	9.5×10^{-2}	4.7×10^{-3}	3.2×10^{-3}	1.5×10^{-3}	3.8×10^{-3}	$1.\times10^{-4}$
$LaRhO_3$	6.9×10^{-2}	5.3×10^{-3}	3.0×10^{-3}	3.9×10^{-3}	1.6×10^{-3}	$2.\times10^{-4}$

Table 5.1: Rate of hydrocarbon formation (molecules/site-sec) on perovskite compounds at 250°C, 20 atm.

surface sites were quickly blocked by dissociated CO and hydrocarbons, and that the reaction probably proceeded on the metal and not on a carbon overlayer.

5.2.3 XPS Results

XPS studies were done to probe the oxidation state of the perovskite surface before and after reactions, to determine the catalytically active species. Table 5.2 summarizes the 3d peak positions before and after reactions. In all four samples studied ($LaCrO_3$, $LaFeO_3$, $LaCoO_3$ and $LaRhO_3$), the metal was initially in a high oxidation state (+3) and during the reaction was reduced to the +1 state. This reduction occurred over a period of approximately 15 - 30 minutes after the start of the reaction. None of the samples reduced to the metallic (0) state even after 5 - 6 hours of reaction time. Without the lanthanum oxide matrix, the metals reduce to the metallic state. The perovskite lattice stabilized a slightly oxidized metal. No change in peak position was detected for lanthanum. Figure 5.4 shows a typical full scan obtained for a sample before and after reaction. Studies on other perovskite compounds ($LaMnO_3$, $BaTiO_3$, $LaCoO_3$, $SrTiO_3$, $La_{1-x}Sr_xCoO_3$) report that the

Compound	Binding Energy (eV)	
	Before Reaction	After Reaction
$LaCrO_3$	576.5	575.0
$LaFeO_3$	709.5	707.0
$LaCoO_3$	779.5	778.8
$LaRhO_3$	309.5	307.8

Table 5.2: XPS binding shifts for the perovskite compounds before and after reactions.

B metal can be reduced only at temperatures over 400°C and that this metallic species was slightly active in hydrocarbon hydrogenation and oxidation reactions [14,15,16,17].

5.2.4 $LaRhO_3$

The product accumulation curve (Figure 5.5) shows methane as the major product. Figure 5.6 shows an expansion of the longer ($> C_1$) hydrocarbon product accumulation curve. Ethylene, C_3 and C_4 show a steady state rate for over 6 hours of reaction time whereas the rate of ethane formation and that of the alcohols decreases after 4 - 5 hours. Interestingly, ethanol formation is initially negligible, but after 2 hours the rate increases and is only slightly less than that of ethylene. Ethanol is detected approximately the same time as the rate of ethane formation decreases and also after 6 - 7 hours when the ethane production starts to level off so does the ethanol production. Ethane may possibly oxidize to form ethanol. For all the hydrocarbons, the reaction rate was positive order in CO and negative order in hydrogen.

Oxidation of the catalyst sample (1 atm, 500°C) increased ethanol formation,

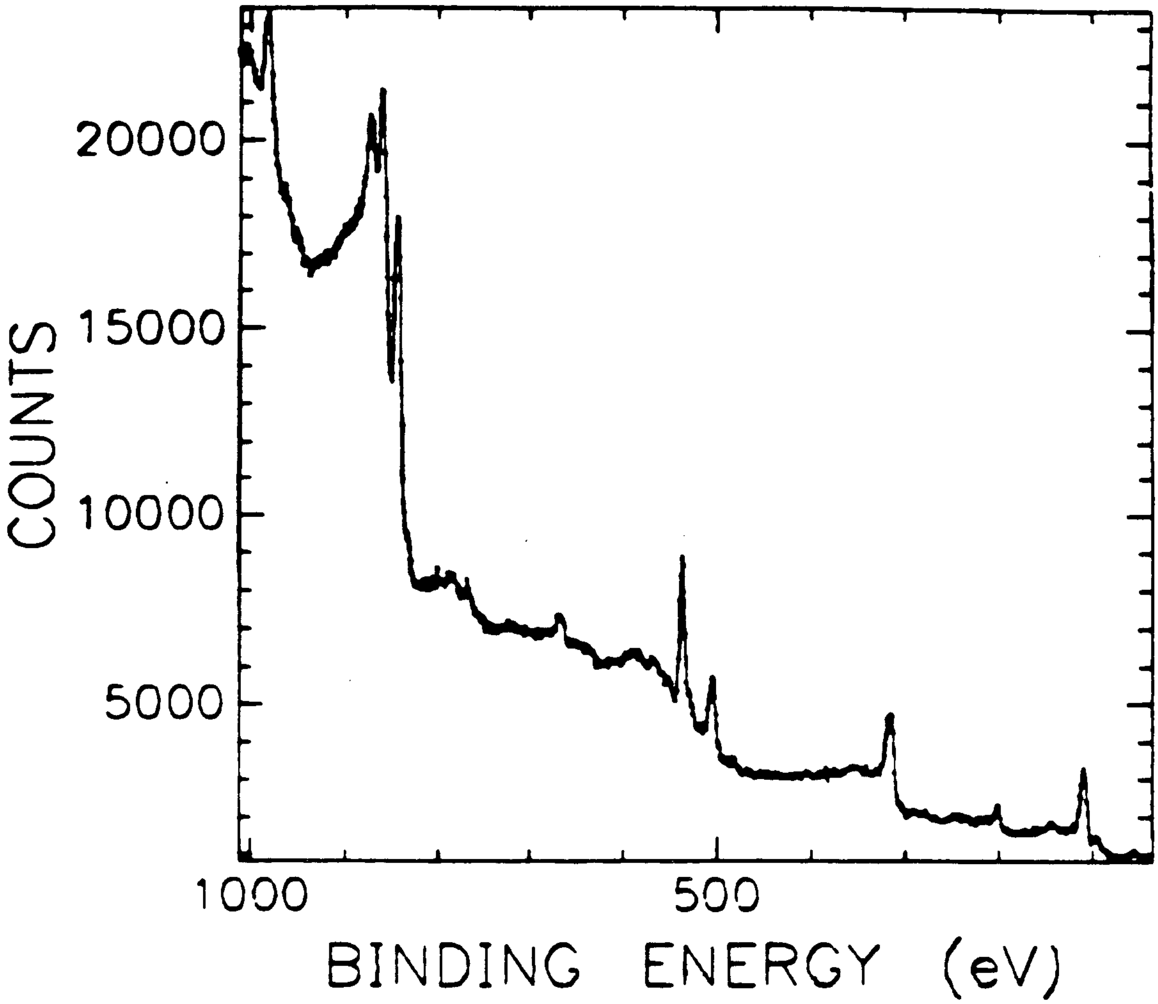

Figure 5.4: A full scan XPS spectra for $LaRhO_3$, after a reaction.

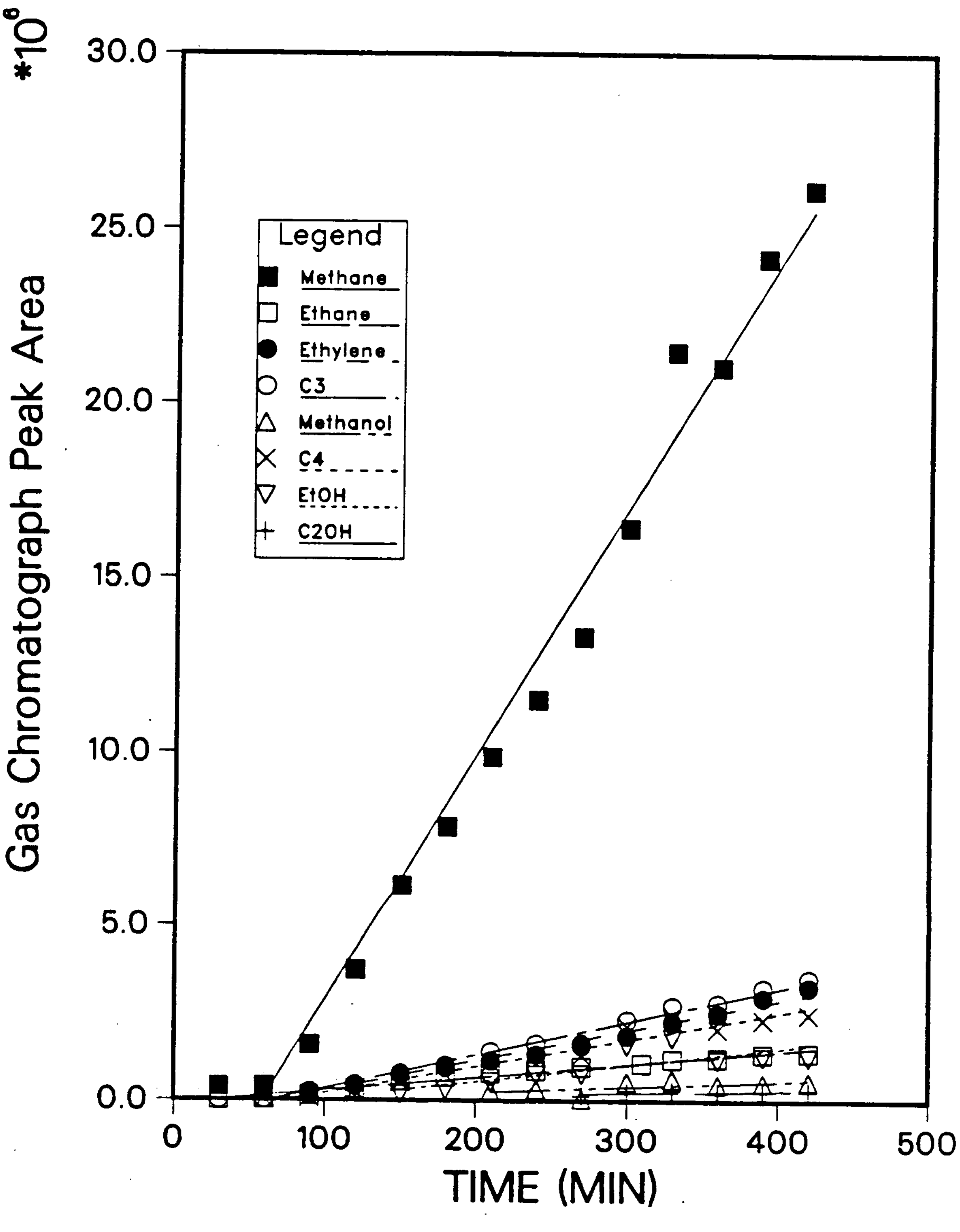

Figure 5.5: Product accumulation curve for $LaRhO_3$, with methane as the major product. Most products are produced for over 5 hours of reaction time.

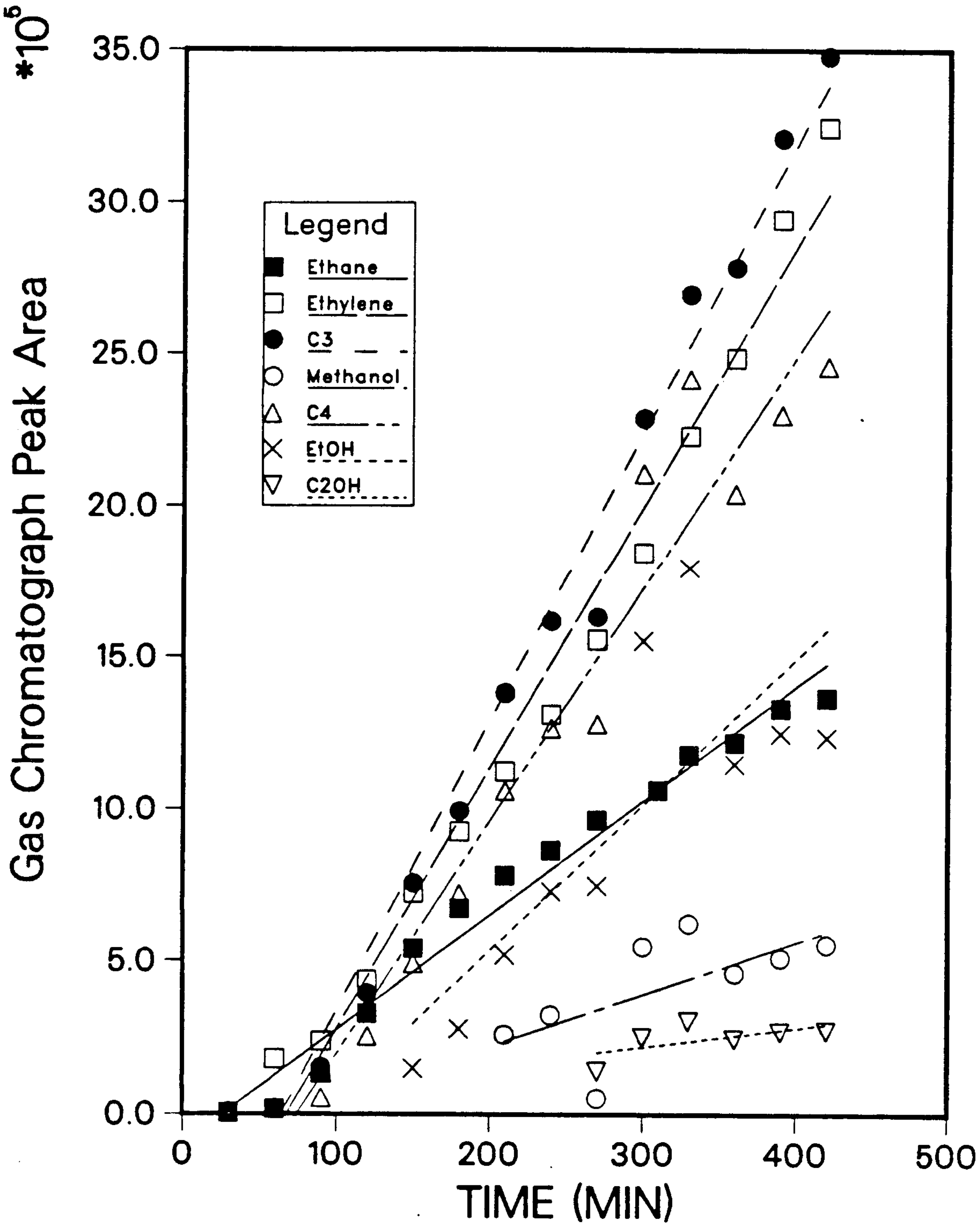

Figure 5.6: Expansion of the product accumulation curve for the longer hydrocarbons (> C_1) over $LaRhO_3$.

suppressed methanol formation, and lowered methane formation by ~ 20% (Figure 5.7). The effect of preoxidation on the other hydrocarbons was minimal.

Studies on the catalytic activity of lanthanum rhodate yielded results quite different than previously reported by Watson *et al.* [12]. They reported an 80 wt% yield of oxygenated products for the CO hydrogenation reaction at temperatures in the range of 225-375°C at 6 atm. In this study we find only a 5 - 9 wt% yield of oxygenates for a similar temperature range and only slightly higher pressures (20 atm). In both their study and ours, the rate of methane and methanol formation vary independently of the formation rate of the other products. This implies that the formation of methanol and methane are occuring by different mechanisms.

XPS characterization of $LaRhO_3$ showed that the initially oxidized (+3) rhodium surface reduced to a +1 state during the reaction (Figure 5.8). Being bonded in the lanthanum oxide matrix kept the rhodium from being completely reduced. After a reaction, cleaning by Ar^+ sputtering and by UHV oxidation (5×10^{-6} torr O_2, 400°C) the rhodium did not become completely oxidized. Only a 1 atm treatment with oxygen accomplished this oxidation.

From these results and other studies on rhodium, it can be concluded that methane forms on metallic or only slightly oxidized ($0 \rightarrow +1$) rhodium with a different mechanism than the other hydrocarbons. Ethanol forms on a more oxidized ($+1 \rightarrow +3$) surface, which the perovskite structure can stabilize under reaction conditions. Other than stabilizing oxidized rhodium, the role of the lanthanum is not well understood. It may also provide mixed interfacial binding sites for hydrocarbon formation, similar to the role of oxide overlayers on palladium (see Chapt. 3).

An important result of this work is that the perovskite compounds exhibit varying catalytic behavior which is critically dependent on the preparation method. We may have produced a different surface composition than Watson *et al.* by

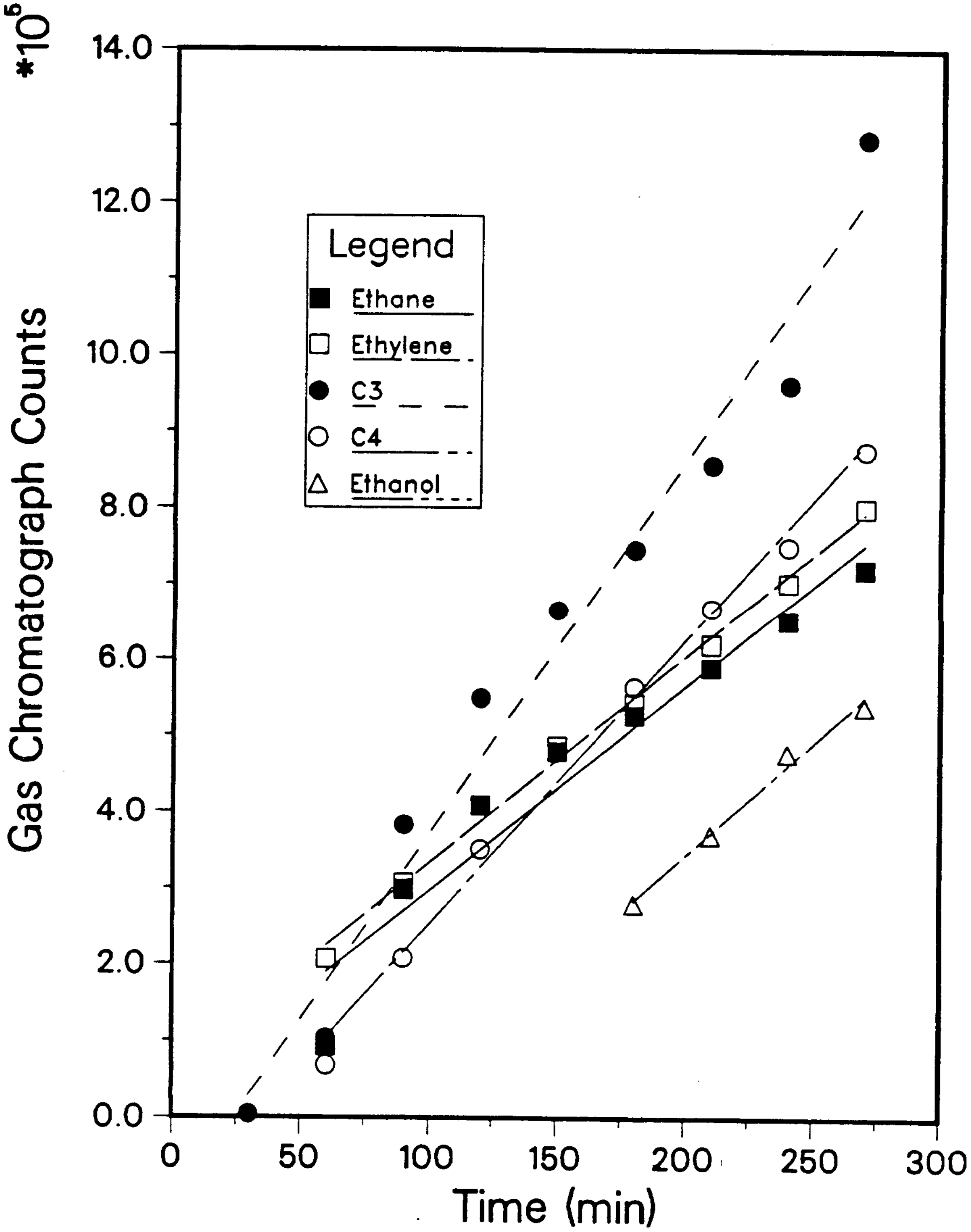

Figure 5.7: Product accumulation curve over $LaRhO_3$ after high pressure oxidation.

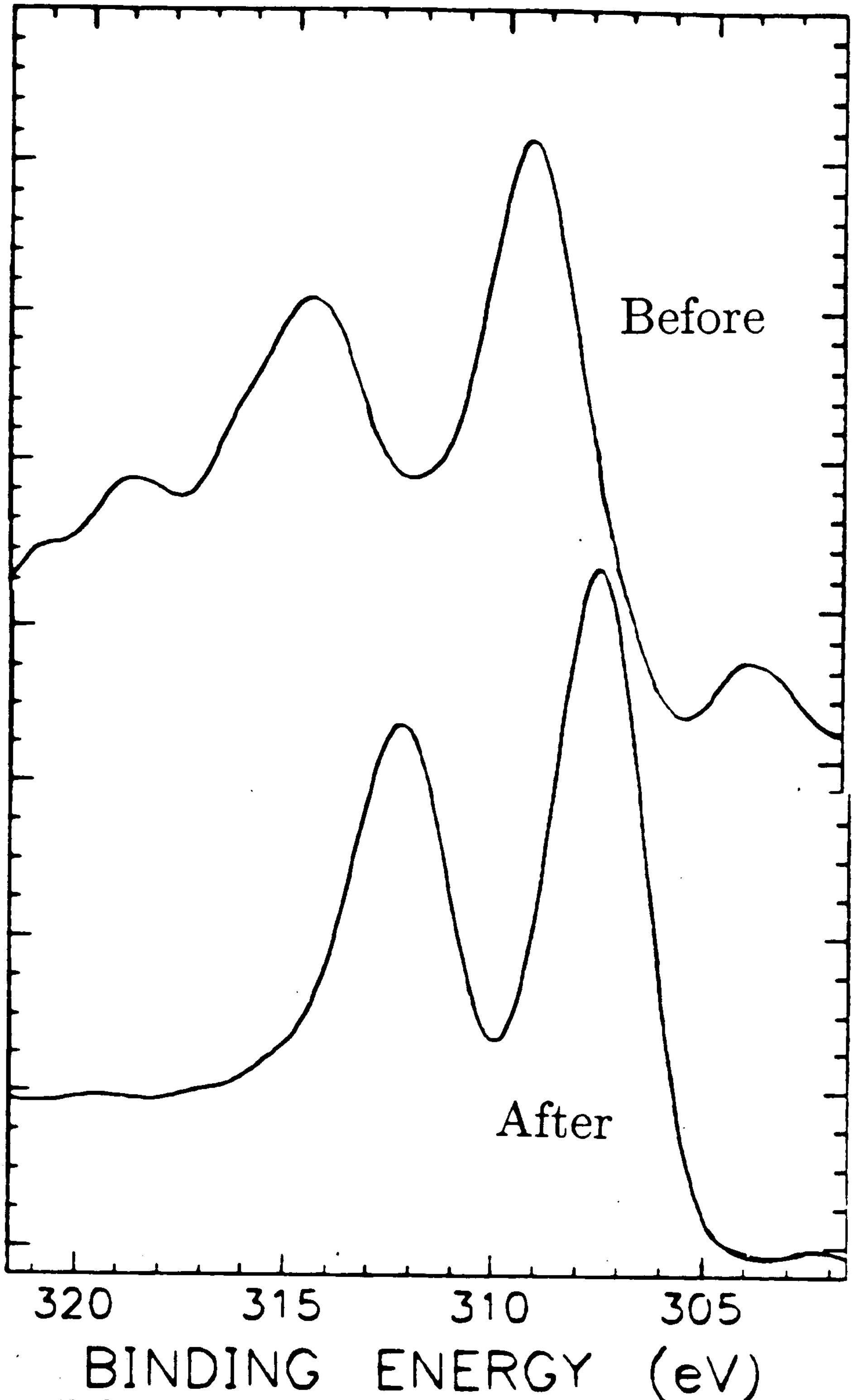

Figure 5.8: XPS spectra of LaRhO$_3$ before and after reaction. The rhodium is reduced from the +3 state but not completely to the metallic state.

pressing our sample into the gold mesh at high pressures rather than drying a wet slurry onto gold foil. The preparation method affects the surface stoichiometry and structure and thereby changes the catalytic behavior. The major difficulty in studying these perovskite compounds is the inhomogeneity of the surface and the difficulty in reproducibly forming a sample with the same surface composition. This was shown by the scatter in the initial rate studies. The ease of preparation and the large number of metals which can be incorporated into the perovskite lattice make this area of solid state chemistry and catalysis and important field for developing tailored stable catalysts.

5.3 Conclusions

The following points summarize the results obtained in this survey of the catalytic activity of perovskite compounds ($LaMO_3$).

- Catalytic activity increases from left to right in the periodic table ($Cr > Mn > Fe > Co \sim Rh$).
- The major product is methane for all samples.
- $LaFeO_3$ had a higher percentage of longer hydrocarbons in the product distribution.
- All the perovskite compounds reduced to the +1 state during the reaction.

For the $LaRhO_3$ samples studied:

- Alcohol formation does not need Rh^{+3} since catalytic activity remained constant for over 3 hours, even though XPS showed that the metal had been reduced to Rh^{+1}.
- Reoxidation of the sample (1 atm O_2, 450°C) increased the rate of ethanol formation and suppressed methanol formation.

References

[1] R. J. H. Voorhoeve. *Advanced Materials in Catalysis.* Academic Press, New York, 1977.

[2] M. Crespin and W. K. Hall. *J. Catalysis* **69** (1981) 359.

[3] R. J. H. Voorhoeve, D. W. Johnson, J. P. Remeika, and P. K. Gallagher. *Science* **195:4281** (1977) 827.

[4] A. Lauder (E. I. DuPont). *U. S. Patent* **3897367** (1975) .

[5] M. Ichikawa. *Bull. Chem. Soc. Chem. Commun.* (1978) 566.

[6] M. Ichikawa. *J. Catalysis* **56** (1979) 127.

[7] P. C. Ellgen, W. J. Bartley, M. M. Bhasin, and T. P. Wilson. *Advan. Chem. Ser.* **178** (1979) 147.

[8] F. Wunder, H. J. Arpe, E. I. Leupold, and H. J. Schmidt. *U.S. Patent* **4224236** (Hoescht AC) .

[9] M. A. Vannice. *J. Catalysis* **37** (1975) 449.

[10] D. G. Castner, R. L. Blackadar, and G. A. Somorjai. *J. Catalysis* **66** (1980) 257.

[11] P. R. Watson and G. A. Somorjai. *J. Catalysis* **74** (1982) 282.

[12] P. R. Watson and G. A. Somorjai. *J. Catalysis* **72** (1981) 347.

[13] B. Bent. PhD thesis, U. C. Berkeley, Berkeley, CA., 1986.

[14] J. O. Petunchi, M. A. Ulla, J. A. Maracos, and E. A. Lombardo. *J. Catalysis* **70** (1981) 356.

[15] J. L. G. Fierro, J. M. D. Tascon, and L. Gonzalaz Tejuca. *J. Catalysis* **89** (1984) 209.

[16] T. Nakamura, M. Misono, and Y. Yoneda. *J. Catalysis* **83** (1983) 151.

[17] E. Lombardo, K. Tanaka, and I. Toyoshima. *J. Catalysis* **80** (1983) 340.

Chapter 6

CONCLUSIONS AND FUTURE DIRECTIONS

This thesis research has studied the role of surface additives on the catalytic activity and chemisorption properties of palladium single crystals and foils. In particular, the effect of sodium, potassium, silicon, phosphorus, sulfur and chlorine on the bonding of carbon monoxide and hydrogen and on the cyclotrimerization of acetylene on the (111), (100) and (110) faces of palladium was studied in addition to the role of TiO_2 and SiO_2 overlayers deposited on palladium foils in the CO hydrogenation reaction.

The surface characterization and catalytic reactions were performed in a combined ultra-high vacuum/ high pressure chamber equipped with the standard surface analytical techniques. This chamber also included a new high pressure isolation cell mounted inside the chamber capable of attaining pressures of 1800 psi.

On palladium, only in the presence of oxide overlayers (TiO_x, SiO_x) are methane or methanol formed from CO and H_2. The maximum rate of methane formation is attained on a palladium foil where 30% of the surface is covered with titania. Methanol formation can be achieved only if the TiO_x/Pd surface is pretreated in 50 psi of oxygen at 550°C prior to the reaction. Carbon monoxide TPD showed a new high temperature shoulder on the 200°C CO/Pd desorption peak on the TiO_x/Pd surface which is not present on clean Pd. Pretreating the TiO_x/Pd surface in oxygen led to an additional high temperature (425°C) binding site. The titania overlayers stabilized the palladium oxide relative to the clean and silica covered surfaces in the presence of hydrogen. The TPD and XPS results and the reaction rate studies suggest that methane forms on a stable mixed TiO_x/Pd site whereas methanol, which is produced only during the first few minutes of the reaction, forms on an unstable heavily oxidized TiO_x/Pd surface. Subsequent work should be geared towards fully probing the active site and mechanism for methanol synthesis. From the results of this research it can be seen that an oxidized palladium ion is necessary for methanol formation and possibly the presence of lanthanum oxide or other oxide will stabilize this form of palladium.

The additives (Na, K, Si, P, S, & Cl) affect the bonding of CO and hydrogen and the cyclotrimerization of acetylene to benzene by both structural and electronic interactions. The structural interaction is seen by the structure sensitive bonding of CO on additive doped surfaces. Two examples are: (1) increasing K coverage on Pd(111) increases the CO desorption temperature whereas on the Pd(110) surface the desorption maximum shifts to lower temperature, (2) the differences in CO bonding on phosphorus covered Pd(111) (new peaks) and Pd(100) (slight shift in CO desorption maximum). Surface reconstruction, changes in palladium ensemble size and site blocking are some of the structural changes induced by the additives. The electronic interaction involves the donation or withdrawal of electron density based on the electronegativites of the additives relative to palladium. In general, the electron donating additives increase the desorption temperature of CO and increase the rate of acetylene cyclotrimerization and the electron withdrawing additives decrease the desorption temperature of CO and decrease the rate of benzene formation from acetylene. Further information on the role of additives can be obtained by expanding this study to different reactions and probing the bonding of small molecules using a variety of surface sensitive techniques.

The perovskite compounds ($LaCrO_3$, $LaMnO_3$, $LaFeO_3$, $LaCoO_3$ and $LaRhO_3$) are active catalysts in the CO + H_2 reaction producing methane, C_2, C_3 and alcohols. The catalytic activity increases moving from left to right in the periodic table (Cr>Mn>Fe>Co∼Rh) with $LaFe)_3$ producing the largest percentage of larger hydrocarbons ($>C_1$). The primary role of the lanthanum oxide matrix was in stabilizing the metal in a slightly oxidized (+1) state, which is most likely the active site for alcohol synthesis. Subsequent research in this field should study the effect of catalyst preparation on the surface composition, structure and catalytic activity.

In order to fully characterize and understand any surface chemical phenomena, a wide variety of analytical techniques must be employed. No single technique will answer the myriad of questions but a combination of numerous techniques may well accomplish this goal. The two techniques which would yield the largest amount and least ambiguous information in studying the oxide and additive covered palladium systems and the perovskites are listed below.

Vibrational Spectroscopy EELS or Infra-red Reflection Absorption Spectroscopy (IRRAS) would accurately determine the CO and hydrocarbon bonding configurations in the presence of the adatoms. The development of an in situ high pressure IR cell to monitor the surface species during a reaction would be extremely valuable. This capability would make it easier to determine reaction intermediates and mechanisms without having to infer from UHV measurements.

Scanning Tunneling Microscopy This relatively new technique which can image surfaces on the atomic scale holds great promise in determining the binding sites of adatoms and the growth mechanisms of overlayers. With this information the type and quantity of active catalytic surface sites can be determined.

Other techniques include Surface Enhanced X-ray Absorption Fine Structure (SEXAFS), Secondary Ion Mass Spectrometry (SIMS).

The goal in studying surface additives is not just to understand their role in specific catalytic systems, but to establish trends and generalized rules for catalysis. Future work should ultimately enhance the predictive power of surface science and catalysis and move the field from an art to a science.

Appendix A

HIGH PRESSURE CELL

This appendix has some pictures and a blueprint of the new high pressure isolation cell developed for studying catalytic reactions.

Figure A.1 Top view of the disassembled components of the high pressure isolation cell. Counterclockwise - 10 inch bottom flange with 4 mini-conflat flanges for connections to gases, pumping and water; 3 inch flange for bottom of outer housing; outer-housing; top of housing and connection for bayonet mount; flange for piston; high pressure cell; assorted o-rings and piston seals; piston; washer; mount for cell·onto 10 inch cell; stainless steel bulkhead and sample holder; spring to force piston up.

Figure A.2 Picture of components arranged in order they would be assembled. The piston seal is attached to groove on the piston which is inserted into the bottom of the cell. The spring and washer are inserted around bottom of the piston and above the flange which is bolted to the high pressure cell. The bottom of the piston, which goes through the flange attached to the cell, is bolted to another flange which is bolted to the outer housing (not shown). This unit sits on a small pedestal which is attached to the bottom flange.

Figure A.3 Side view of the high pressure cell. On the cell (l to r) the connections are for differential pumping, cooling jacket water in, cooling jacket water out to bottom jacket, reactant gas in, reactant gas out, nitrogen line for pressurizing piston, cooling jacket water in from top jacket, cooling jacket water out, differential pumping for volume below piston.

Figure A.4 Top view showing dove-tail grooves for viton o-rings which are the sealing surface for the manipulator against the cell. The differential pumping hole can be seen in the middle groove in the side where the lines are attached to the cell.

Figure A.5 View of the stainless steel bulkhead with thermocouple and electrical feedthroughs welded in. The four teeth of the manipulator are grabbed in the bayonet mount (right) attached to the outer housing.

Figure A.6 View of outer housing and bayonet mount. The housing was machined to minimize mass.

Figure A.7 Close up view of piston assembly used through which the nitrogen pulls down the outer housing sealing the manipulator against the o-rings of the high pressure cell.

Figure A.8 Assembled high pressure cell.

Figure A.9 Assembled high pressure cell.

Figure A.10 Blueprint of the manipulator and high pressure cell.

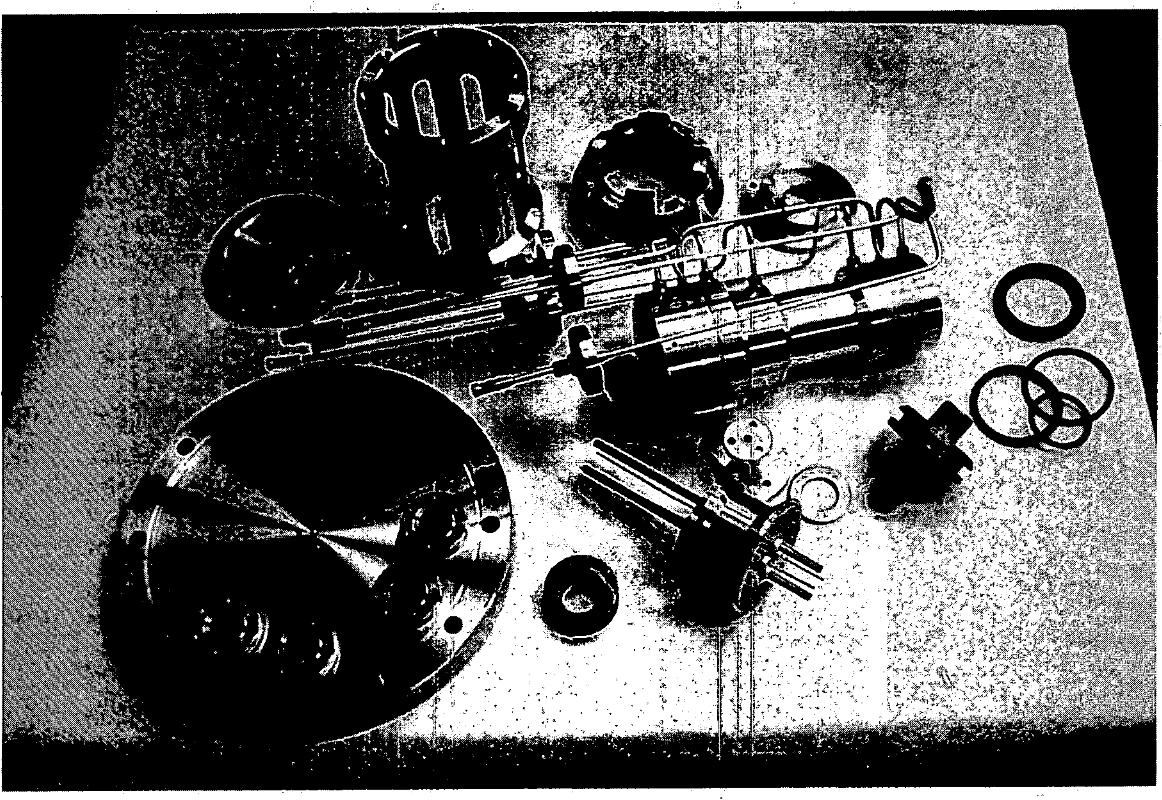

XBB 874-3321

Figure A.1:

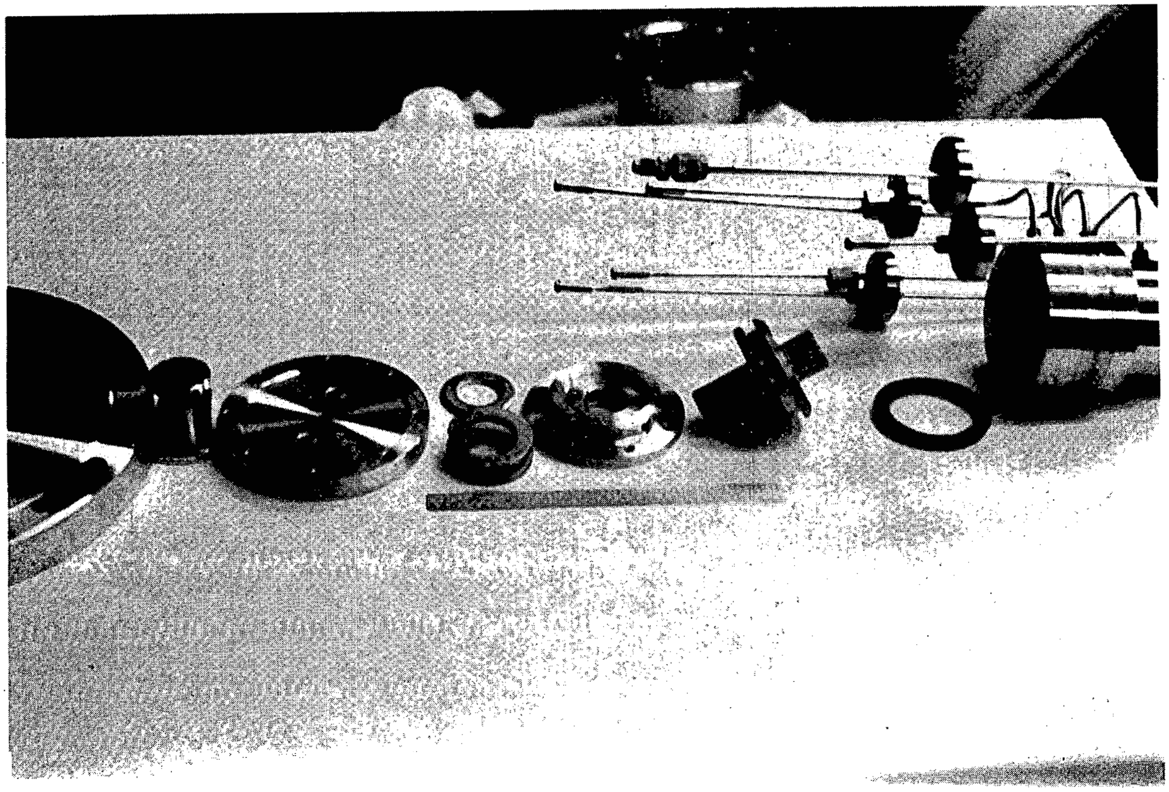

XBB 874-3318

Figure A.2:

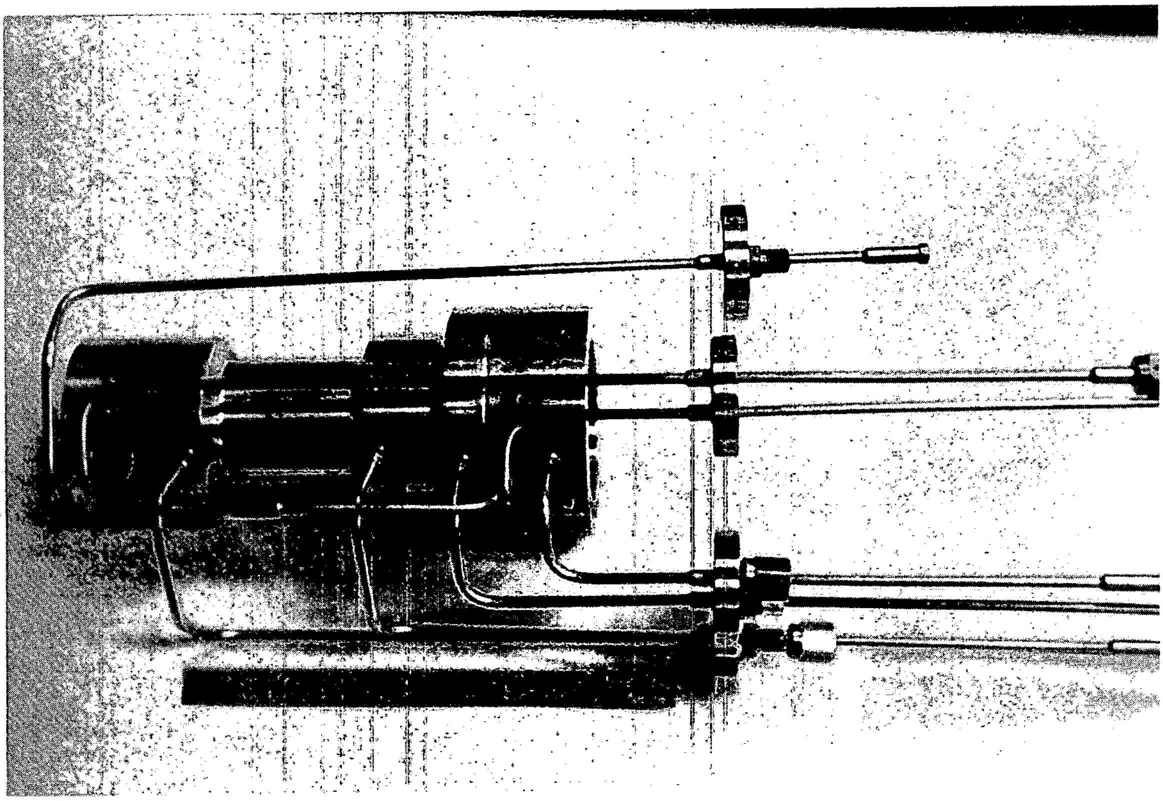

XBB 874-3319

Figure A.3:

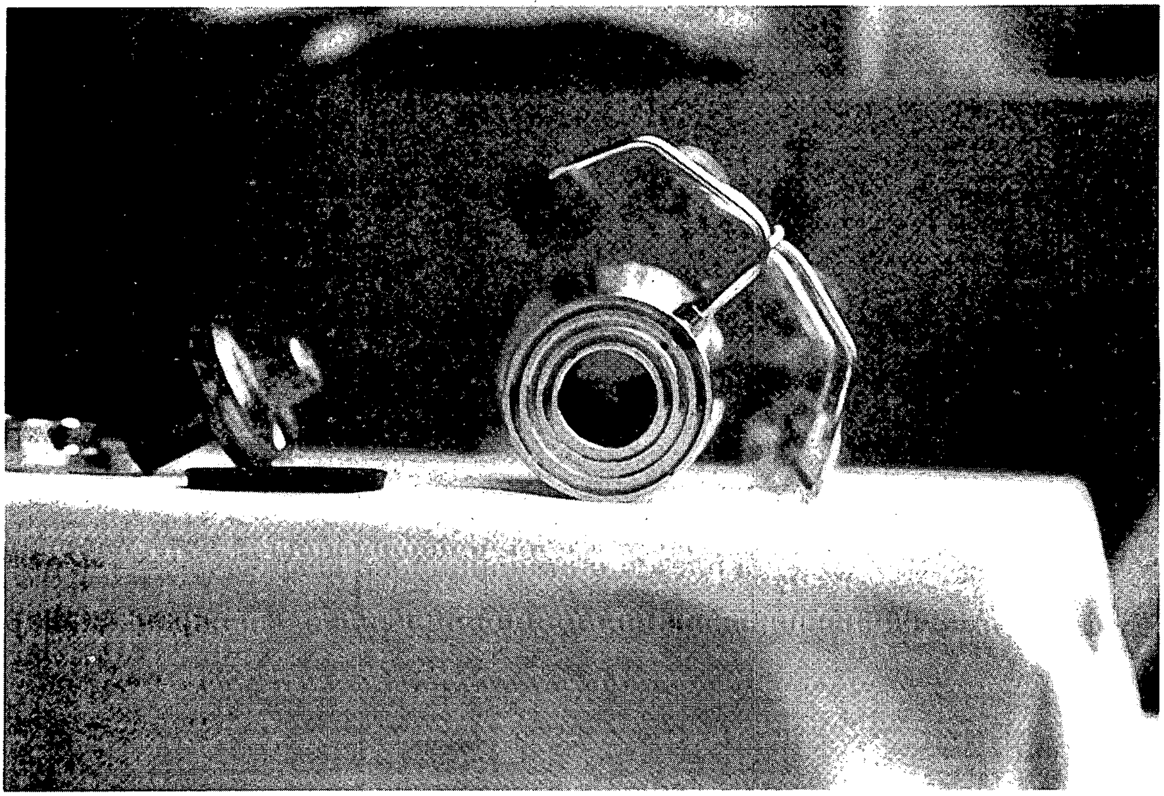

XBB 874-3317

Figure A.4:

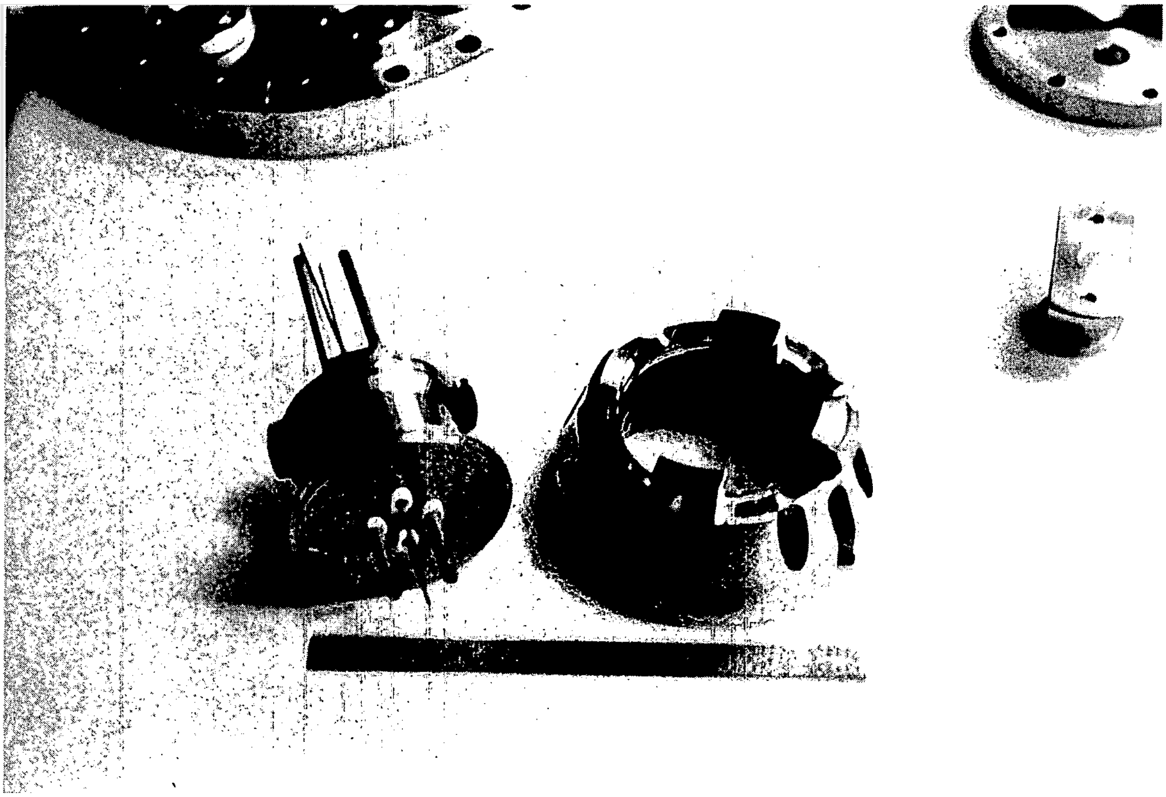

XBB 874-3315

Figure A.5:

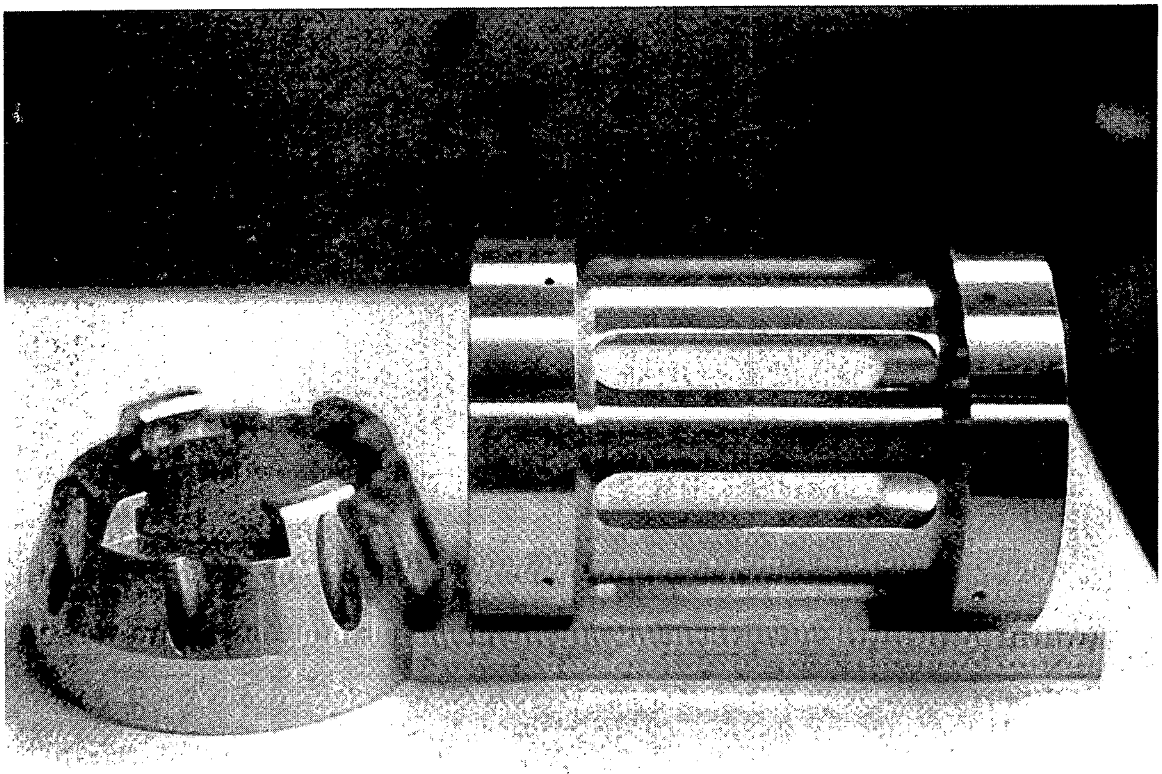

XBB 874-3320

Figure A.6:

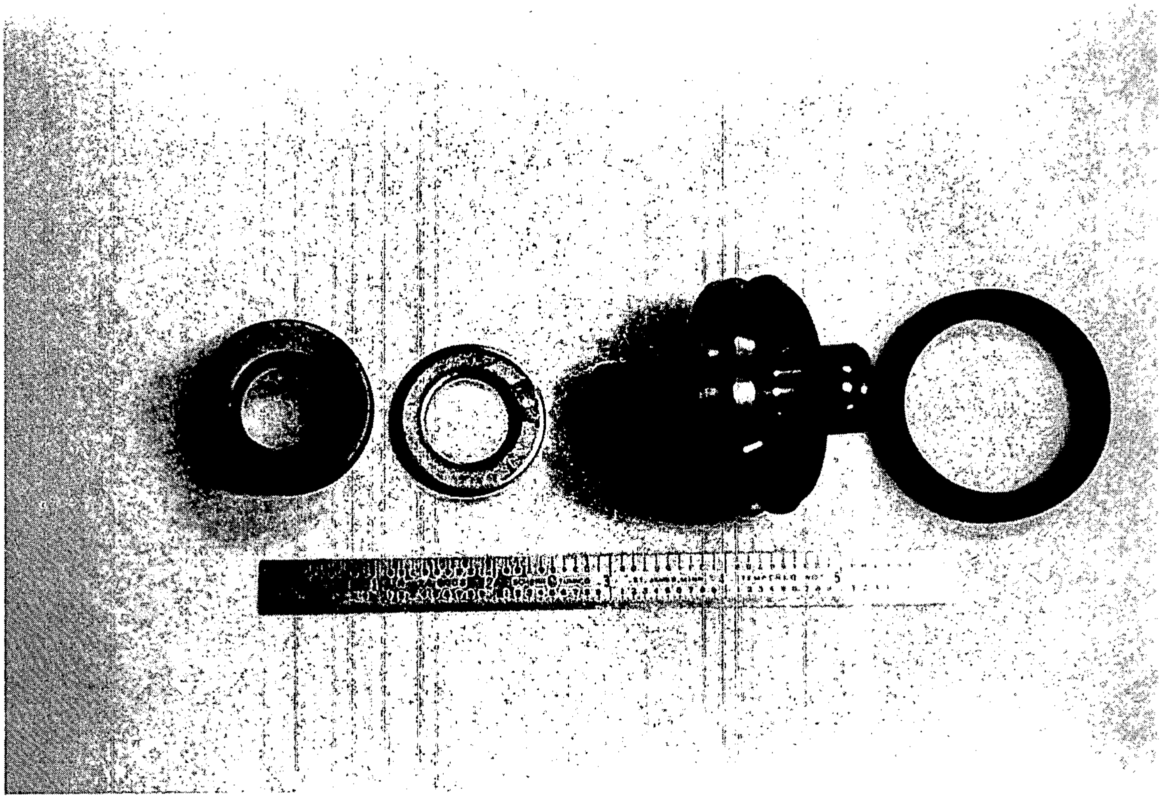

XBB 874-3316

Figure A.7:

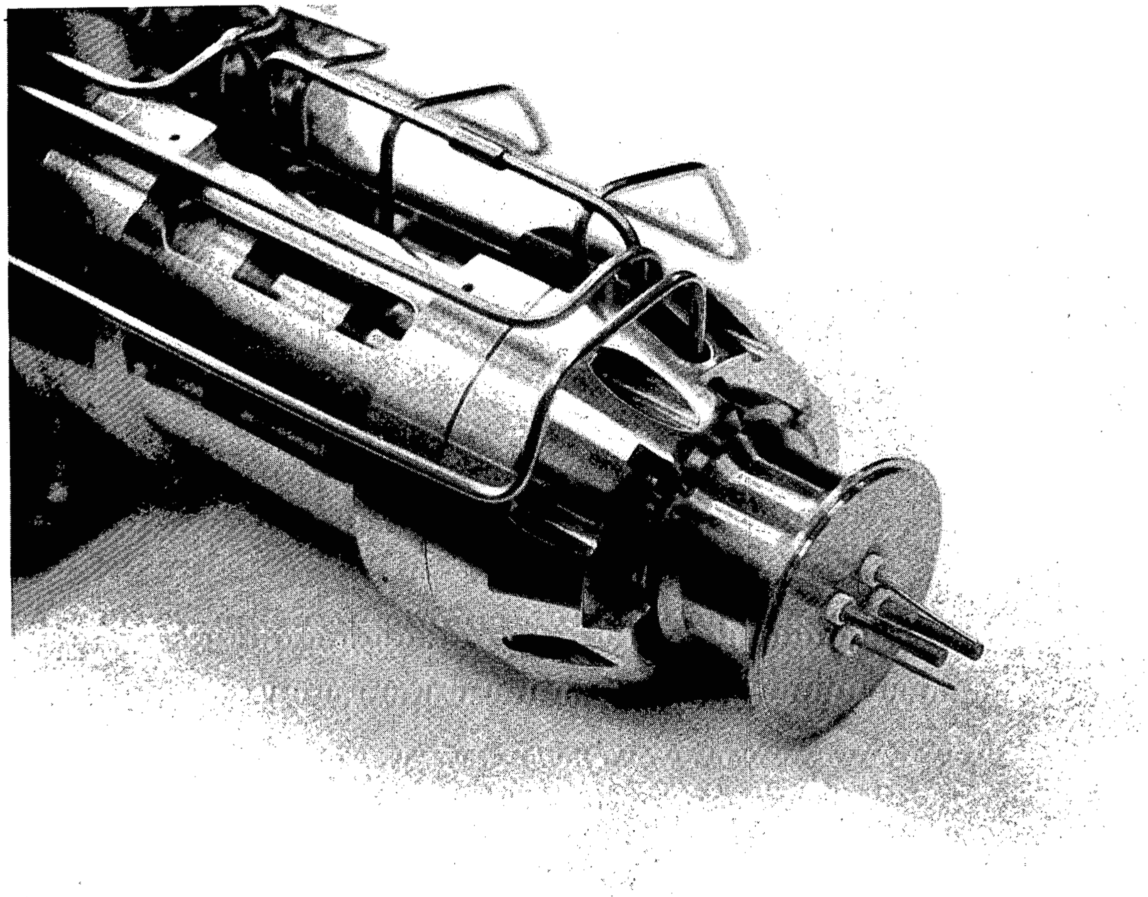

XBB 876-4909

Figure A.8:

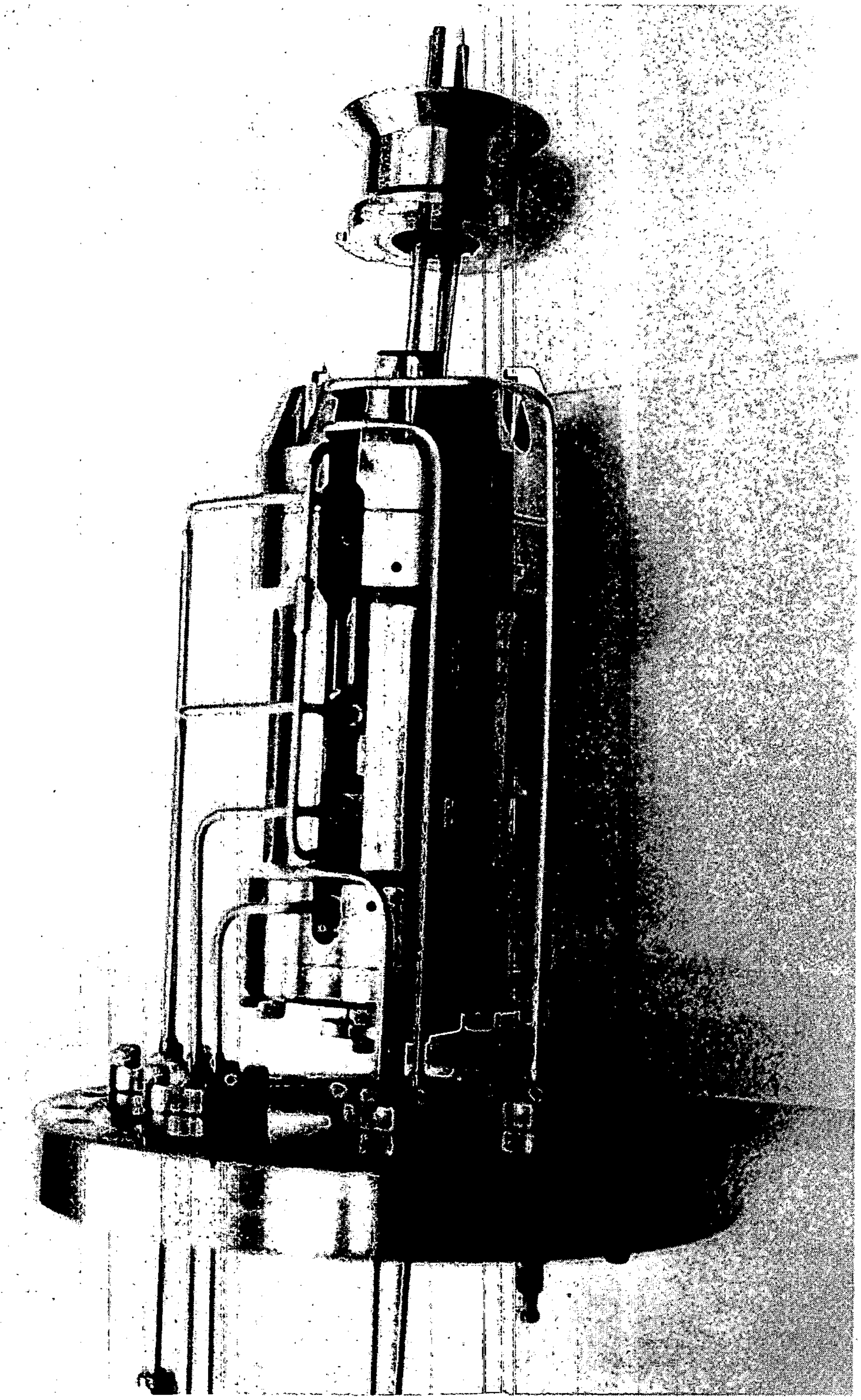

Figure A.9: XBB 876-4908

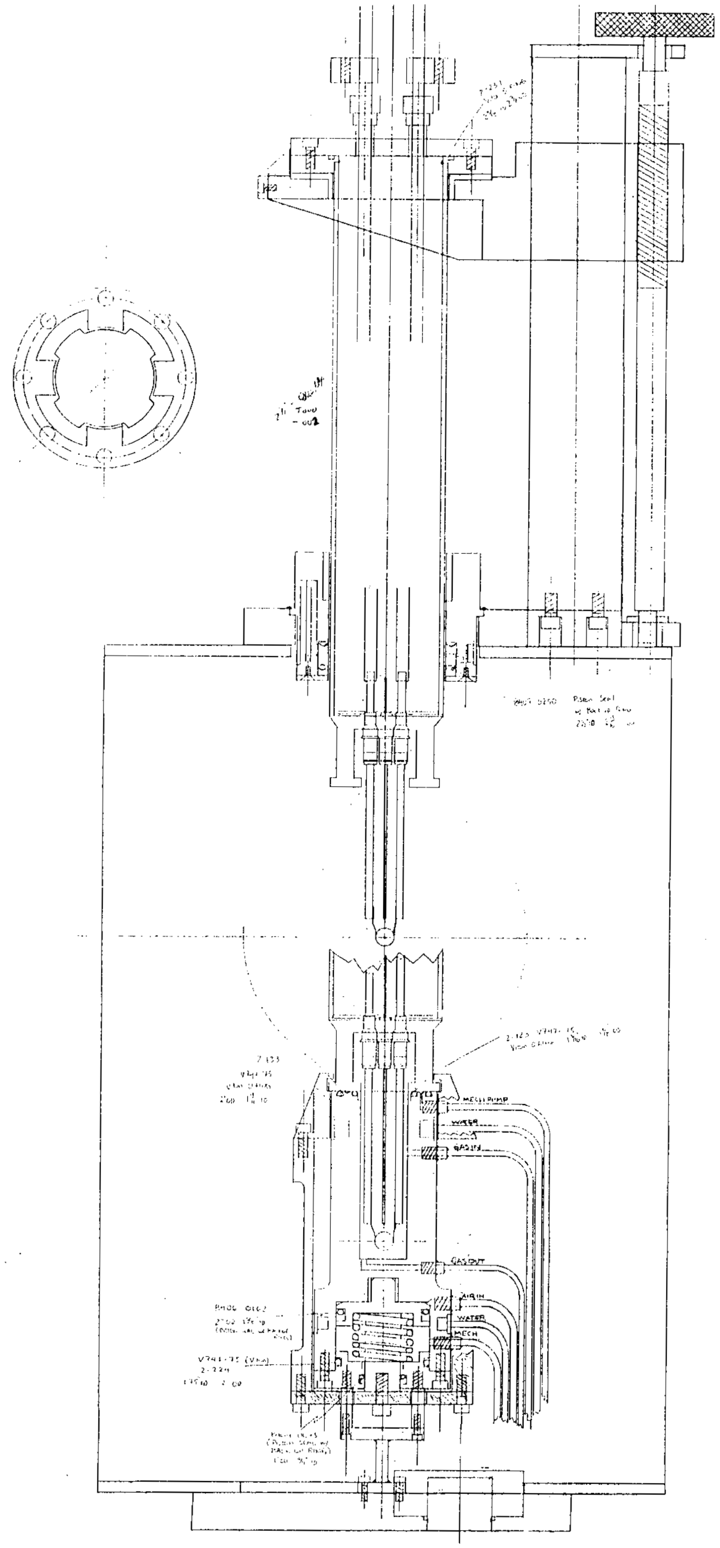

Figure A.10:

XBL 867-2921

Appendix B

CURVE FITTING ALGORITHM

The algorithm and program listing (RPLOT) [1] to fit gaussian peaks for the XPS peaks is presented below.

Known: f_i, g_i, h_i (functions) where i is index to points

Find: a, b, c

So that $e_i \cong af_i + bg_i + ch_i$

where e_i are the experimental data points.

Minimize error: $\xi = \sum_{i=0}^{300} [e_i - (af_i + bg_i + ch_i)]^2 = \sum \varepsilon^2$

with respect to unknowns a, b and c.

Three equations:

$$\begin{aligned}
\frac{\partial \xi}{\partial a} &= 2\sum_{i=0}^{300}(e_i + af_i - bg_i - ch_i)(-f_i) = 0 \\
\frac{\partial \xi}{\partial b} &= 2\sum_{i=0}^{300}(e_i + af_i - bg_i - ch_i)(-g_i) = 0
\end{aligned}$$

---

[1] Graphics and data manipulation program developed by Craig G. Shaefer, Rowland Institute of Science, Cambridge, MA

$$\frac{\partial \xi}{\partial c} = 2\sum_{i=0}^{300}(e_i + af_i - bg_i - ch_i)(-h_i) = 0$$

Work out three equations:

$$\begin{aligned}
a\sum_{i=0}^{300} f_i^2 + b\sum_{i=0}^{300} g_i f_i + c\sum_{i=0}^{300} h_i f_i &= \sum_{i=0}^{300} e_i f_i \\
a\sum_{i=0}^{300} f_i g_i + c\sum_{i=0}^{300} g_i^2 + c\sum_{i=0}^{300} h_i g_i &= \sum_{i=0}^{300} e_i g_i \\
a\sum_{i=0}^{300} f_i h_i + b\sum_{i=0}^{300} g_i h_i + c\sum_{i=0}^{300} h_i^2 &= \sum_{i=0}^{300} e_i h_i
\end{aligned}$$

In matrix form:

$$\begin{bmatrix} \sum f_i^2 & \sum g_i f_i & \sum h_i f_i \\ \sum f_i g_i & \sum g_i^2 & \sum h_i g_i \\ \sum f_i h_i & \sum g_i h_i & \sum h_i^2 \end{bmatrix} \begin{bmatrix} a \\ b \\ c \end{bmatrix} = \begin{bmatrix} \sum e_i f_i \\ \sum e_i g_i \\ \sum e_i h_i \end{bmatrix}$$

$$\mathrm{M} \quad \mathrm{A} = \mathrm{K}$$

$$\mathrm{A} = \mathrm{M}^{-1} \quad \mathrm{K}$$

Program Listing for RPLOT:

```
MAN CAL ”(1/($B1*2.4))*EXP(-1*(X-$X1)**2/(2*($B1**2)))” TO W

MAN COP W V

MAN POW W 2.

MAN INT W TO U

SET VAR ”$” R 1 U111


MAN CAL ”(1/($B2*2.4))*EXP(-1*(X-$X2)**2/(2*($B2**2)))” TO Z

MAN COP Z U

MAN POW Z 2.

MAN INT Z TO W

SET VAR ”$” R 2 W111
```

```
MAN CAL ”(1/($B1*2.4))*EXP(-1*(X-$X1)**2/(2*($B1**2)))” TO W
MAN CAL ”(1/($B2*2.4))*EXP(-1*(X-$X2)**2/(2*($B2**2)))” TO Z
MAN MUL W Z TO Z
MAN INT Z TO W
SET VAR ”$” R 3 W111

MAN CAL ”(1/($B1*2.4))*EXP(-1*(X-$X1)**2/(2*($B1**2)))” TO W
MAN MUL W Y TO W
MAN INT W TO V
SET VAR ”$” R 4 V111

MAN CAL ”(1/($B2*2.4))*EXP(-1*(X-$X2)**2/(2*($B2**2)))” TO Z
MAN MUL Z Y TO Z
MAN INT Z TO V
SET VAR ”$” R 5 V111

CAL
$S1=$R1
$S2=$R2
$S3=$R3
$S4=$R4
$S5=$R5

$T1=-1*($R4 * $R2 - $R5 * $R3)/($R3**2 - $R1 * $R2)
$T2= ($R4 * $R3 - $R5 * $R1)/($R3**2 - $R1 * $R2)
E
```

```
MAN CAL "(1/($B1*2.4))*EXP(-1*(X-$X1)**2/(2*($B1**2)))" TO W
MAN SCA W $T1 TO W
MAN CAL "(1/($B2*2.4))*EXP(-1*(X-$X2)**2/(2*($B2**2)))" TO Z
MAN SCA Z $T2 TO Z
MAN ADD W Z TO U
SYM +
PLO X W
SYM *
PLO X Z
SYM LIN
PLO X U
SYM DOT
PLO
LOG OFF
```